TECHNIQUES TO OVERCOME ENERGY STORAGE LIMITATIONS IN ELECTRIC VEHICLES

by

Matthew J. Hansen

A dissertation submitted in partial fulfillment
of the requirements for the degree

of

DOCTOR OF PHILOSOPHY

in

Electrical Engineering

Approved:

Abhilash Kamineni, Ph.D. Major Professor	Greg Droge, Ph.D. Co-Advising Professor
Regan Zane, Ph.D. Committee Member	Jake Gunther, Ph.D. Committee Member
Kevin Moon, Ph.D. Committee Member	D. Richard Cutler, Ph.D. Vice Provost of Graduate Studies

UTAH STATE UNIVERSITY
Logan, Utah

2024

ABSTRACT

Techniques to Overcome Energy Storage Limitations in Electric Vehicles

by

Matthew J. Hansen, Doctor of Philosophy

Utah State University, 2024

Major Professor: Abhilash Kamineni, Ph.D.
Co-Advising Professor: Greg Droge, Ph.D.
Department: Electrical and Computer Engineering

Electric vehicles are becoming increasingly popular, but battery cost, size, and weight limit electric vehicles' utility. Two approaches are detailed to overcome those limitations: improving battery health through an optimal charging strategy and minimizing necessary battery size through dynamic wireless power transfer. Three objectives focus research within those approaches. First, a planning tool is defined to reduce battery costs in an electric vehicle fleet by deferring battery replacement costs. This approach frames the optimization as a graph search problem, which can be solved with a mixed-integer linear program. Consideration for battery degradation costs and search space reductions are included. The second objective is to reduce the up-front and operational costs of dynamic wireless power transfer systems. One task in that objective is to describe a method to achieve load-independent zero-volt switching in a resonant system. This approach simplifies the nonlinear output capacitance of the power electronic switches and uses current harmonics to achieve zero-volt switching. The other task relating to lowering the cost of dynamic wireless power transfer systems is a secondary-driven synchronization and detection scheme. In this scheme, the primary pad operates its inverter to push power into the network. A control scheme to inject power may become unstable, so considerations are included to ensure system stability. The

third objective, to facilitate the adoption of dynamic wireless power transfer systems by improving the modeling of the same, also has two associated tasks. The first of those tasks is to describe a neural network trained to estimate the magnetic fields in a wireless power transfer system. This approach requires optimal cost functions, data representation, and neural network structure to achieve quality results. The second task describes a method to model a complex network of wireless power transfer pads with a graph, where each pad is given by a node and each mutual inductance by an edge value. With this model, power transfer can be optimized to exploit power flow through the network. Together, these three objectives, organized into five tasks, use similar methods and modeling-heavy analyses to address pressing needs to overcome energy storage limitations in electric vehicles.

(157 pages)

PUBLIC ABSTRACT

Techniques to Overcome Energy Storage Limitations in Electric Vehicles

Matthew J. Hansen

Electric vehicles are becoming increasingly popular, battery limitations (cost, size, and weight) complicate electric vehicle adoption. While important research on battery development is ongoing, this dissertation discusses two main approaches to overcome those limitations within the existing battery technology paradigm. Those thrusts are: improving battery health through an optimal charging strategy and minimizing necessary battery size through dynamic wireless power transfer. In this dissertation, relevant literature is discussed, with opportunities for further development considered. Within the two thrusts, three objectives sharpen the focus of the research presented here. First, a planning tool is defined for a battery electric bus fleet. This tool minimizes the summed cost of energy and battery replacement. The second objective is to improve the simplicity, availability, and cost of dynamic wireless power transfer systems. The third objective achieved in this dissertation is to facilitate the adoption of dynamic wireless power transfer systems by improving the modeling of the same.

To Hazel and Anders — I love you kiddos so much. I hope that in some small way, this work makes the world you inherit better and the air you breathe cleaner.

ACKNOWLEDGMENTS

I am grateful to many people who have guided, assisted, and influenced me along this journey. I owe gratitude to too many people to list, but I'll still name a few. First, I'd like to thank my Ph.D. advisors, Abhilash Kamineni and Greg Droge. Abhi, you mentored me through these past five years, giving me the right balance of guidance and independence. Greg, your mentorship brought an extra element to my research that made this project more valuable and interesting. I also owe thanks to Regan Zane, who started me on my research journey years ago, inspired me to pursue a Ph.D., and served as my main advisor through my undergraduate degree and into the first years of graduate school. I have had the great pleasure of collaborating with other colleagues, who have helped develop the content here with discussion and experimentation. Abdullah Baig, Andy Budge, Azmeer Zahid, Bryce Hesterman, Haris Ahmed, Josh Larsen, Justin Whitaker, and Mayank Chawla: thank you. I'd like to thank my parents for setting me on this academic path as a child, and my siblings and siblings-in-law for being the best I could have wished for. Most importantly, I need to thank my partner, sweetheart, and support: Cassidy, thank you for encouraging me and sharing the frustrations and joys of these past years. Technically, your ability of expression has led me to write more clearly and powerfully; you're my first and last edit, and you've helped me to see and aim higher. I appreciate every time you work to understand some technical problem I'm solving. More importantly, you see more in me than I see in myself, and I'm blessed to share this life with you.

Matthew J. Hansen

CONTENTS

LIST OF TABLES

LIST OF FIGURES

ACRONYMS

AC	alternating current
ADC	analog to digital converter
ANN	artificial neural network
BEB	battery electric bus
BHC	battery-health conscious
CCCV	constant current, constant voltage
CPT	capacitive power transfer
CSV	comma-separated values
CT	current transformer
DC	direct current
DoD	depth of discharge
DSRC	directed short-range communications
DWPT	dynamic wireless power transfer
ECCE	Energy Conversion Congress and Expo
EM	electromagnetic
EoL	end of life
EV	electric vehicle
EVPSE	EV power supply equipment
FEM	finite element method
GHG	green house gas
HDV	heavy-duty vehicle
IEEE	Institute of Electrical and Electronics Engineers
ICE	internal combustion engine
IPT	inductive power transfer
LDV	light-duty vehicle
MDV	medium-duty vehicle

PINN	physics-informed neural network
RNN	recursive neural network
SoC	state of charge
SWPT	static (or stationary) wireless power transfer
ToU	time of use
WPT	wireless power transfer
WPTCE	Wireless Power Technology Conference and Expo
ZCS	zero-current switching
ZVS	zero-volt switching

CHAPTER 1

INTRODUCTION AND OBJECTIVES

Electric vehicles (EVs) are increasingly popular, with the potential to reduce greenhouse gas (GHG) emissions and other pollutants [1]. In 2020, transportation accounted for 26 % of energy consumption in the United States, and petroleum accounted for 90 % of energy used in transportation [2]. Advancing EV technology can allow some of that GHG-emitting petroleum with cleaner, alternative energy sources. This dissertation aims to define current gaps in the technology and propose research into potential solutions. This chapter gives a brief overview of electric vehicles (EVs). A key limitation of current EV technology is given and, in Section 1.2, three objectives are identified to overcome current limitations in EV technology. This dissertation aims to complete those objectives and is organized around them.

1.1 Brief Overview of EV Technology and Limitations

EVs have experienced a surge in popularity in recent years, with adoption expected to continue to increase [3]. Increasing vehicle electrification promises several positive effects, including decreased greenhouse gas emissions and improved health benefits [4]. High adoption of light-duty EVs is feasible in most cases, but higher electrification rates of heavy-duty vehicles (HDVs) present more challenges, even while those heavy-duty vehicles disproportionately contribute to GHG and pollution emissions [5]. The battery is a significant obstacle to broader EV adoption, especially among HDVs. The battery energy storage is more expensive, bulkier, and heavier than the fuel tank in ICEs per mile of energy storage, limiting the range and size of EVs. Consumers are also wary of purchasing EVs due to concerns about charging length, charging frequency, EV cost (driven higher by battery costs), and deleterious effects of battery manufacturing [6]. Consequently, there is a need to address this limitation to enable higher adoption of EVs, with the associated environmental and

social benefits.

Therefore, this dissertation defines two broad research approaches to help overcome the battery limitations of EVs. First, an approach integrating battery costs when optimizing EV battery charging is considered; this approach works within the existing EV charging paradigm to reduce EV battery costs by deferring battery replacement costs. Second, enabling technologies for dynamic wireless power transfer (DWPT) are investigated. With widespread DWPT, more vehicles are electrifiable at a lower cost, requiring smaller batteries [7]. Two objectives advancing DWPT are considered.

These two approaches are innately linked to the battery problem for EVs. The first approach works within the existing EV paradigm. A rich body of literature on optimal charging has been developed, including significant work focused on developing an optimal fleet charging strategy [8–10] and a battery-health-conscious charging strategy for a single vehicle [11]. However, the literature body lacks an approach that optimizes total cost, including battery degradation costs, for an entire electric fleet. By considering battery health when making charging decisions, battery replacement costs can be deferred. This approach focuses on a heavy-duty fleet with a known schedule, a class of vehicles whose sometimes-regular schedules are easily modeled and have an outsize impact on emissions. The resulting algorithm could be implemented easily and would result in a longer battery lifetime.

However, there are many situations in which lengthening the battery lifetime is insufficient. First, many driving scenarios do not require the vehicles to return to a charging depot, including long-haul trucking; the work on optimizing charging to defer battery replacement costs has limited applicability here. Second, deferring battery replacement costs does not reduce the upfront cost. To complement that approach, work on DWPT is proposed. While several industrial solutions to DWPT are currently in development, they are disjointed and no approach yet applies to all vehicle classes. The goal of the second approach is to make DWPT feasible, ultimately reducing battery size and cost. Two objectives relating to DWPT are proposed; to reduce the up-front and operation costs of a DWPT system, and to improve the modeling of DWPT systems.

Significant research exists on wireless power transfer in general [12–14], including important work on reducing switching losses in resonant converters, a class of circuits that includes WPT systems [15–17]. Rich work on some DWPT systems already exists [18,19]. However, there exists a need for a simplified approach to vehicle detection in DWPT, that introduces no additional circuit elements. Further, none of the approaches in [15–17] are applicable for a general DWPT system at unity power factor. Consequently, there is a need to develop a method to lower switching losses in a DWPT circuit.

Improved modeling of complex WPT systems is also needed. Existing literature describes various methods of modeling magnetics, including those in a WPT system, with artificial neural networks [20–22]. Modeling of WPT systems can be improved by training a more powerful neural network, with more training data, and a sufficiently rich description output to aid optimization. Similarly, modeling a WPT system with more than two sub-circuits (sources or loads) exists in very limited literature [23]; however, the approach in [23] does not allow for sub-circuits to approach the maximum power. Consequently, a framework to consider such a complex system with sources and loads operating near maximum power is proposed here.

Although the two approaches may appear to be dissimilar, they aim to solve the same problem, and both approaches rely on similar fields of electrical engineering. Common threads of control theory, optimization, and graph theory run through all three objectives, although applied to different problems. The following section clarifies the proposed approaches into three objectives.

1.2 Objectives

Given the prominence of vehicle electrification at present, many research opportunities exist to alleviate the constraints batteries place on vehicle electrification. Two approaches to overcoming the battery constraints are considered. First, the optimal use of existing technology is considered; that is, maximizing battery utilization and minimizing battery cost. The second approach explores enabling WPT technologies that allow DWPT, potentially reducing battery size, weight, and cost. The specific objectives are as follows:

1. Define a planning tool to reduce battery costs in an EV bus fleet by reducing battery degradation and deferring battery replacement costs. This objective is described in a single task:

   (a) Formulate the allocation of chargers to an EV fleet as a MILP. The formulation considers time of use (ToU) energy costs and battery degradation costs with limited charging resources.

2. Reduce up-front and operational costs of DWPT systems, by reducing system complexity and system losses. The two tasks to achieve this objective are:

   (b) Describe a method to achieve ZVS in a resonant converter or WPT circuit without added reactive power.

   (c) Develop a synchronization and detection algorithm for DWPT. This algorithm:

      i. Allows active switching on both the primary and the secondary sides

      ii. Turns on the primary pad only in response to a secondary pad

      iii. Requires no additional sensing coils

      iv. Includes sufficient robustness for roadway deployment

3. Facilitate the adoption of DWPT systems by improving the modeling of DWPT systems. The two tasks corresponding to this objective are:

   (d) Train a neural network to describe the characteristics of a DD coil topology. Specifically, given nine variables describing the geometry of the primary and secondary coils and their locations relative to each other, the neural network will model

      i. Stray magnetic fields

      ii. Ferrite magnetic fields, from which ferrite losses are estimated

      iii. Copper magnetic fields, from which copper proximity losses are estimated

      iv. Primary and secondary self inductances and mutual inductance

(e) Develop a graph-based model to evaluate steady-state interactions between multiple primary and secondary coils, including possible benefits of parasitic coupling.

1.3 Dissertation Structure

This dissertation follows the multiple-paper format, and the dissertation is organized around five IEEE journal and conference papers.

Chapter 2 reviews existing scholarship relevant to the objectives discussed above, upon which the papers are built. Chapters 3 to 7 contain "photo-ready" replications of the papers. The work in Chapter 3 fulfills objective one, and is under review in the IEEE Transactions on Intelligent Transportation Systems [24]. The works in Chapters 4 and 5 discuss how objective two is met, with the work in Chapter 4 having been reviewed and presented at the 2021 IEEE Energy Conversion Congress and Expo (ECCE) [25] while the work in Chapter 5 is currently under review in the IEEE Open Journal of Power Electronics [26][1]. The work fulfilling objective three is included in Chapters 6 and 7, with the work in Chapter 6 having been submitted for review in the IEEE Transactions on Magnetics [29][2], and the work in Chapter 7 having been submitted in the journal *Electronics* [31]. While Chapters 3 to 7 replicate the work included in the research body, space and scope constraints limited discussion of various practical implementation notes. Those comments are discussed in Chapter 8. Chapter 9 concludes the body of this dissertation with a discussion on the implications of this work and avenues for further research.

[1] An earlier version of this work was presented as [27, 28]
[2] An earlier version of this work was presented as [30]

CHAPTER 2

LITERATURE REVIEW

Electric vehicles (EVs) are gaining an increasingly large penetration in the market, with the potential to reduce greenhouse gas (GHG) emissions and other pollutants. It has been predicted that 30 % of the worldwide passenger vehicle fleet will be electrified by 2032 [3]. Heavy-duty vehicles are also becoming increasingly feasible. The authors of [5] analyzed typical drive schedules of medium-duty vehicles (MDV) and heavy-duty vehicles (HDV) in California, concluding that roughly 70 % of current MDV vehicle-miles and roughly 8 % of HDV vehicle-miles can be electrified with current technology and charger locations. Given those results, the authors conclude that EVs present a strong possibility to reduce vehicle emissions. With the increasing penetration of EVs into the vehicle market, there is a need to improve EV technology. This literature reviews recent contributions to this field and identifies opportunities for further investigation.

The work discussed in this dissertation focuses on EV energy storage. Two principal EV energy storage techniques are commonly used, fuel cells and batteries; of those two, only battery energy storage is considered. At present, the EV charging paradigm reflects the ICE fueling paradigm, where EVs drive to a charging station, charge, and then continue driving. However, the limitations of this approach with battery energy storage have spurred significant research into novel charging strategies; the research discussed here exploits the inherent advantages and minimizes the disadvantages of EVs relative to ICE vehicles.

Several key disadvantages of batteries have been addressed, including cost [32] and battery degradation [33–35]. In [5], the authors conclude that improving EV fuel economy and increasing charging locations can overcome some battery limitations. According to current EV adoption models, the most significant hurdle is battery production, which needs to be increased by roughly a factor of 100 in coming years [3]; the cost of those batteries figures to be a significant portion of the total EV cost. In [36], the cost of a battery pack alone

in a passenger vehicle is estimated at $11,500 in 2017, dropping to $8,000 by 2025. For comparison, the cost of an entire ICE powertrain, including the engine and transmission, was estimated at only $6,800. There is a present need to optimize battery performance or reduce the need for batteries generally.

In this review of existing literature, current research is considered across three areas. First, in Section 2.1, current work on optimizing EV charging schedules, within the constraints presented by batteries, is considered. Objective 1 seeks to fill gaps in the literature considered in Section 2.1. Section 2.2 covers existing scholarship on wireless power transfer (WPT) as a technology to improve EV feasibility and decrease EV dependence on batteries; the work discussed in Objective 2 builds on that work. Section 2.3 details the use of machine learning and other modeling techniques relevant to WPT; Objective 3 focuses on overcoming limitations addressed in that section.

2.1 EV Charging Optimization

Relevant work on EV charging optimization covers two principal areas. First, recent work has improved the modeling of battery degradation. Second, various works have sought to overcome battery limitations by optimizing how vehicles are charged. Section 2.1.1 gives a brief overview of the current state of battery modeling, Section 2.1.2 describes current efforts to optimize how EVs are charged, and Section 2.1.3 surveys literature that includes battery degradation in an EV fleet charging schedule optimization. Finally, Section 2.1.4 describes how Objective 1 fills a gap in the literature.

2.1.1 Battery Degradation Modeling

To include the costs of battery degradation in an EV charging plan, a thorough understanding of battery degradation mechanisms is required; the work relevant to Objective 1 will leverage work on battery degradation discussed in this section.

Work reviewing battery technologies [37, 38] and their lifetime environmental effects [39] frames the need to reduce battery degradation. Early work in [33] gives a reasonable degradation model for Li-ion batteries, which requires only a few parameters to model a battery.

However, that work includes recursive relationships which make adaptation to an EV charging optimization program infeasible. More recent work presents a more complex model; in [35], a thorough degradation model is presented, which accounts for battery degradation effects due to cycling and calendar aging. This approach allows a planner to model battery degradation with arbitrary cycling conditions but requires experimentally determined parameters for each battery cell type. A more complex explanation for battery capacity fade is presented in [34], which, unlike [35], addresses coupling between various capacity loss mechanisms. While any recommendations on optimally charging an EV are beyond the scope of both [34, 35], the approach in [35] can be more easily applied to determine an optimal charging strategy because the degradation mechanisms are more independent. That approach represents battery degradation through two principal mechanisms, which are mostly dependent on battery cycling and calendar aging; the model in [35] presents a straightforward link between charging schedule characteristics and battery degradation. Critically, [35] also provides a floor for battery degradation, beyond which point reducing battery cycling does not improve battery life.

The two main battery degradation mechanisms discussed in [35] are lithium degradation and negative electrode site degradation. The model for lithium capacity [35, eq. (4)] is given as

$$Q_{Li} = d_0 \left[b_0 - \underbrace{b_1 t^{1/2}}_{\substack{SEI\ growth \\ with\ calendar \\ time}} - \underbrace{b_2 N}_{\substack{Loss\ with \\ cycling}} - \underbrace{b_3 (1 - \exp(-t/\tau_{b3}))}_{\substack{Break-in\ mechanism \\ at\ BOL}} \right], \tag{2.1}$$

where Q_{Li} is the lithium-limited battery capacity, t is the days since manufacturing, N is the number of cycles, and the remaining terms are temperature-dependent, experimentally-determined values. It will be shown in the full dissertation that the values in (2.1) are well-approximated by constants under certain assumptions. The authors of [35] note that (2.1) is dominated by the b_0 and $b_1 t^{1/2}$ terms. Further, the time constant τ_{b3} is much less than the battery lifetime. With minimal loss of accuracy, (2.1) near end-of-life (EoL) can

be approximated as

$$Q_{Li} = d_0 \left(b_0 - b_1 t^{1/2} \right), \tag{2.2}$$

from which the calendar-aging battery degradation can be determined, determining the minimum daily battery damage.

The negative electrode capacity is given by [35, eq. (9)] as

$$Q_{neg} = [c_0^2 - 2c_2 c_0 N]^{\frac{1}{2}}, \tag{2.3}$$

where Q_{neg} is the negative-electrode-limited battery capacity, c_0 is a temperature-dependent, experimentally-determined value, N is, again, the number of cycles, and c_2 is a temperature-dependent and cycling-depth-dependent parameter. Eq. (2.3) can be interpreted as subtracting some capacity every charging cycle, from which the battery degradation per charging cycle is determined. Given a daily minimum battery damage and per-cycle battery damage, an optimization can be formulated that accurately reflects battery degradation.

Powerful tools have been discussed that improve battery degradation modeling [33–35] and that suggest strategies for low-level charging control [40–42]. The works discussed in this section inform the tool used to complete Objective 1. However, additional work beyond that presented here is required to integrate battery degradation into constrained optimization. With current battery constraints, there is a need to ensure EVs charge intelligently, including multiple EVs in a resource-constrained scenario. This is addressed in Section 2.1.2.

2.1.2 EV Charging Optimization

Given the constraints batteries place on EVs, new approaches to charging need to be defined and evaluated. Here, we give a brief overview of approaches to planning EV charging, where EV schedules are included in the optimization.

A brief overview of work regarding optimally charging private vehicles is considered here; the purpose of this portion is to 1) highlight related work, and 2) show that the question

of private vehicles has been sufficiently studied to justify a focus on a battery electric bus (BEB) fleet in this proposal. Work discussed in [43] determines where chargers can be placed for various objectives while [44, 45] present algorithms to minimize wait time at EV chargers. Related work in [46, 47] determines how to allocate power to various private vehicles. Given the high variability of private vehicle behavior, limited further development remains. Instead, a focus on improving heavy-duty fleets, like BEBs, is justified.

Before the charging schedule for a BEB fleet can be optimized, a planner must know the approximate EV energy consumption. The work in [48] describes a method to generate such data. The model stochastically simulates stops, powertrain loads, and auxiliary loads in a fleet of electric buses. This model can then inform a charging optimization algorithm. An approach to optimal charging can use the work in [48] or similar work to generate realistic values.

In [32], the cost savings associated with bus fleet electrification are considered, with typical savings between \$0.1 and \$3.6 billion for bus fleets in California. However, the authors of [32] note that, while EV bus fleets present a cost-saving opportunity, bus planners need tools to better optimize deployment and charging. A brief overview of such contributions follows. In [8], an algorithm is presented to optimize hold times, where a bus waits before proceeding to the subsequent stop to maintain a schedule, to minimize charging delays. Using this approach, an EV bus driver can determine, in real-time, how long to hold at each stop to more seamlessly integrate charging times into the bus schedule.

One approach to optimizing bus scheduling is assigning which EV buses are assigned to which routes. The work in [49] approaches this on a daily frequency, assigning buses to routes each day, to minimize total battery capacity fade. A major draw of bus electrification is reduced emissions; [50] presents the choice of which bus routes to electrify as a bi-objective optimization, which considers environmental equity, i.e., reduced emissions, and initial investment costs, e.g., battery costs and power supply costs. Another approach is explored in [51], in which the system parameters, e.g., EV bus battery capacity and charger number, are optimized in a nonlinear program. However, [49–51] do not consider how the

charging schedule for a BEB fleet can be optimized.

Sufficient research on optimizing BEB system parameters exists to warrant a focus on low-level operations planning. Four works considered here represent current literature on low-level charging scheduling. The work in [10] includes battery capacity, fleet size, and charging infrastructure as variables of optimization, and makes assumptions on low-level charging planning. However, while limits on bus battery state of charge (SoC, a fraction representing the battery stored energy relative to battery capacity) are included to improve reliability, battery degradation is assumed to be fixed.

The work in [52] addresses both high-level decisions on which routes to electrify and low-level decisions on how to charge BEBs on the electrified routes to minimize time-of-use (ToU) electricity costs. The low-level planning approach greedily assigns charging during low-cost times, including higher-cost charging intervals only enough to meet charging constraints. The work in [53] also addresses low-level decisions on where to charge, but that work includes a focus on power grid interactions with BEB charging. The cost of charging is assumed to be determined for each grid connection. Power drawn from each grid connection at each BEB stop is optimized to reduce total cost. The work in [54] also addresses low-level charging optimization, but the approach is simplified by assuming each bus is charged to 100 % SoC each time it charges. In effect, [54] optimizes over a binary search space.

Especially pertinent is the work in [9], which frames the charging optimization problem as a network search problem, where network edges are chosen to allocate chargers throughout a planning horizon. That approach allows essentially seamless integration with battery degradation costs — the costs for variable charging depths can be assessed along the edges of the network. The work in [9] also includes tools to optimize the charging infrastructure configuration, as many other works do [10, 52]. However, like other works [52–55], considerations to maximize battery lifetime are beyond the scope of this scholarship.

2.1.3 Battery Degradation in Optimal EV Charging

Other scholarship has focused on methods to improve EV battery life. The work in [56] is also relevant to a discussion on recent contributions to battery science, in [56], several

techniques to cool EV battery packs under use are considered, which is essential to extend EV battery life. The authors of [40] conclude that an optimal algorithm to charge a battery can be approximated by a constant-current constant-voltage (CCCV) charging law, and defines the voltage and current parameters. In [41], an improvement to the CCCV charging algorithm is introduced, which improves charging speed and charging efficiency. While [40, 41] address how a battery is charged, the work in [42] describes a method to optimally discharge a battery. The work in [42] also allows pulsed charging, rather than exclusively considering DC charging/discharging, resulting in improvements in discharging capacity, efficiency, and battery temperature.

An early approach to EV charging optimization is discussed in [11], where an algorithm to minimize the total cost for a single electric vehicle is developed. An iterative approach minimizes both battery degradation costs and energy costs, which very nearly satisfies Objective 1. The two significant exclusions from the scope of [11] are 1) balancing the needs of multiple EVs and 2) a guarantee of optimality; those exclusions are addressed in Objective 1. Multi-EV fleets are considered in other work, but without the same consideration of battery health in [11].

The recent work in [55] is especially pertinent to the research completed for Objective 1. In [55], a formulation to optimize BEB lifetime cost, including electricity and battery replacement costs. The approach is solid, but while the battery degradation model does distinguish between fast and slow charging, the battery degradation does not account for specific battery degradation mechanisms. A potentially more accurate model can be developed that explicitly accounts for various battery degradation mechanisms, which is an essential part of the work of Objective 1.

2.1.4 Opportunities for Further Research

Many tools to determine an optimal EV charging strategy are considered. In [43–47], powerful tools are determined to smartly charge private EVs. The work in [8] discusses strategies for making optimal timing decisions for en-route buses, and the work in [11] includes battery health in determining an optimal charging strategy, although there is no

guarantee of optimality. The research in [32, 49, 50] addresses which bus routes should be electrified. Finally, the works in [9, 10, 51] address a master plan for an EV fleet. Given the rich background in EV bus fleet optimization, there exists a need to determine an algorithm to determine an optimal charging plan for a fleet of EVs that includes battery degradation costs and guaranteed optimality. This is the aim of Objective 1.

2.2 Wireless Power Transfer

One well-explored approach to circumventing battery limitations in EVs is WPT, where power is transferred from a primary to a secondary across an air gap. With WPT, vehicles can charge easily and frequently, including while a vehicle is in motion; this approach minimizes EV reliance on batteries. Objectives 3 and 2 both explore improvements to DWPT for EVs, although the contributions discussed here could also apply to stationary WPT (SWPT). Significant research has been done in this field, especially concerning EVs. In this section, a brief overview of relevant scholarship in this space is provided.

Section 2.2.1 gives an overview of WPT in EVs, while Sections 2.2.2 and 2.2.3 give an overview of the current state of capacitive power transfer and inductive power transfer, respectively. Adaptations of WPT technology for DWPT are addressed in Section 2.2.4, and methods to minimize losses in resonant converters are discussed in Section 2.2.5. Finally, gaps in the current literature are discussed in Section 2.2.6.

2.2.1 Overview and Approaches of WPT in Vehicle Electrification

A thorough consideration of the potential benefits of WPT is given in [7]. That work seeks to quantify the economics, environmental impact, and infrastructure rollout of in-motion WPT. While the benefits of SWPT are mostly convenience (SWPT and wired charging both require the same sizes of batteries, and the same vehicle charging time), broad implementation of DWPT could decrease EV battery size and increase the number of routes achievable by EVs. Another benefit of advanced WPT systems in vehicles is the inherent energy storage capacity provided. In [57], such a benefit of bi-directional enabled WPT EVs is explored. A strategy is proposed where the EVs act as a backup during power

outages, wirelessly transferring power back to the grid to improve stability.

A review [58] of advances in wireless power transfer differentiates between SWPT and DWPT; both approaches will be addressed here. The review conducted in [13] also gives an excellent overview of current approaches to WPT in EVs. In [13], the technology is divided into near-field (where the primary and secondary coils are coupled) and far-field (where the power is radiated from the primary to the secondary) applications. Work is also divided into SWPT, quasi-dynamic WPT, and DWPT. The differences between DWPT and SWPT are more fully analyzed in Section 2.2.4, while an overview of near- and far-field WPT technologies is given here.

Although less recent, the work in [59] gives a good overview of the strengths and weaknesses of two approaches to near-field WPT: inductive power transfer (IPT, where power is transferred through a magnetic field) and capacitive power transfer (CPT, where power is transferred through an electric field). Key conclusions from that work are that CPT can require higher frequencies and much smaller air gaps. While CPT is considered here, the limitations of CPT make IPT more attractive for EVs.

While the most obvious application of WPT to vehicle electrification is in charging the powertrain battery, a commonly-studied WPT application relates to the literature discussed in Section 2.1.1, where WPT is used to balance the cells in an EV battery. As the cells inside a battery pack age, they degrade at different rates. The capacity (in A h) of a series of battery cells is limited by the lowest-capacity cell in that series. To that end, [60,61] both propose algorithms to actively balance battery pack cell capacities with WPT. WPT works well in this application because while each cell is at a different voltage potential, WPT allows any or all of the cells to be charged from a low-voltage-potential source. Of [60, 61], the work in [61] presents a more complete design.

As IPT is the focus of Objectives 3 and 2; special attention is given to current scholarship in IPT in Section 2.2.3, while Section 2.2.2 reviews research on CPT.

2.2.2 Capacitive Power Transfer

In CPT, power is transferred through a near-field electric field. Two plates on the primary, or transmission side, generate an electric field, which is then picked up by the secondary, or receiving side. Typically, CPT requires high voltages and high frequencies for effective power transfer. Significant recent scholarship has focused on advancing CPT to suitable power levels for EVs.

Early work on CPT includes [62], which presents a design approach to overcome the high voltage requirement. A compensation approach is described, which increases the voltage and decreases the current across the capacitive link, thereby limiting current through lossy components. The circuit topology used in [62] is frequently used in other CPT designs. A simple approach to modeling CPT is through the concept of a gyrator, discussed in [63]. A gyrator is an ideal circuit component where the current on one set of ports corresponds to the voltage on the complementary set of ports. In [63], the CPT network is simplified to a gyrator, which simplifies modeling and design.

In [64], a three-loop control algorithm for CPT is introduced. This this approach, the fastest loop regulates the frequency to ensure gyrator operation. The middle loop regulates primary inductance to regulate link capacitor current, and the slowest loop regulates secondary inductance to regulate secondary power. The major weakness of this approach is that some regulation is achieved through inductor bias current, which can be lossy. However, a good control law for any system, including CPT systems, requires good knowledge of the system; in a CPT system, the secondary is potentially unknown. Chen *et. al.* introduce a fitting algorithm in [65] to overcome this limitation, where a spectrum analysis is used to estimate system parameters. However, this approach does require conducting a spectrum analysis for every secondary.

As noted in [59], CPT tends to work only over limited air gaps. However, the work in [66] introduces a repeater capacitor into the airgap to extend the airgap, with equivalent circuit models. The main limitation of this approach is that it requires a repeater in the airgap, and does not present a significant advantage over simply replacing the repeater capacitor with the receiver capacitor.

The work in [67] introduces a CPT system for a railway application. A CPT model is tested on a smaller scale, with a 23 −cm train charged with 91 % efficiency. However, the switching frequency is very high (2 MHz), which introduces other complications. Because most CPT systems operate at higher frequencies, above 1 MHz, there is a need to develop better high-frequency inductors, which is addressed in [68], where an interleaved foil inductor is implemented. Typically, high-frequency inductors are solenoidal, but the design in [68] replaces the common Litz wire with foil and winds the inductor in a toroidal or semi-toroidal shape. The resulting inductor allows more dense power transfer but is applicable mostly for high-frequency CPT systems.

2.2.3 Inductive Power Transfer

Currently, IPT for EVs is supported by SAE J2954 standard [69], while CPT for EVs has no such standard. Deployed efforts to design IPT systems must also comply with IEEE (Institute of Electrical and Electronics Engineers) standard C95.1-2019, which limits human exposure to the magnetic fields, including those required to transfer power inductively [70]. Because IPT is more common than CPT for EVs, methods of IPT are addressed here. Near-field WPT is advantageous because it can be inherently bidirectional. Early work in [71] gives a control algorithm for a bidirectional IPT system, where a vehicle can wireless transfer power from the grid to charge its battery, or to the grid to reduce peak load.

One challenge in WPT is power regulation; in many cases, power delivery is measured at the secondary but regulated at the primary. The work in [72] attempts to solve this problem; the authors define an algorithm to communicate over the power link using distinct frequencies for primary–secondary communication and WPT. Buja *et. al.* [12] developed a scheme to regulate power transfer while ignoring primary–secondary communication; the circuit is designed and optimized, and an additional converter is placed between a passive secondary rectifier and the load. While effective, this approach unnecessarily increases complexity and potentially increases losses.

Excellent work by Chu *et. al.* describes power metering, an important aspect of IPT [14]. Currently, many plug-in charging systems charge for the power transmitted, which can be

fairly measured in the charging cable. However, when losses are present in either the primary or secondary, there is not a standard practice to measure power transferred, rather than power received or power drawn by the primary. The work in [14] measures the magnetic field strength to determine power transferred and is accurate to 0.1 %. This work is an important step towards commercialization and widespread adoption of IPT technology.

A major consideration in IPT is coil design. Several designs have been proposed in recent literature. In [73], a four-coil design is proposed. A major strength of such a coil design is interoperability, as the coil design is compatible with many other coil designs. However, a limitation of this approach is its applicability to DWPT. Similarly, the work in [74] proposes a three-phase system, where the magnetic field rotates about an axis. While this approach increases power density, the three-phase, rotating field is incompatible with DWPT. Essentially, the approaches in [73, 74] improve SWPT, but are not directly applicable to DWPT.

One motivation for improved IPT coil design is to overcome the air gap limitation. At larger air gaps, the primary–secondary coupling decreases, and transferring the same power requires higher voltages or currents. As discussed previously, [66] introduces a repeater capacitor; a similar approach for IPT can be developed. In [75], a repeater coil design is proposed, where each repeater coil has a transmitting and a receiving side, separated by a plane of ferrite, and oriented orthogonal to each other. With this approach, each repeater coil can extract power, and the range of feasible air gaps is extended. While this contribution shows the present research interest in IPT, its applicability to EVs is limited. First, EVs are not among the applications where each repeater coil would need to power a load. Second, adding repeater coils to the underside of an EV increases weight, and low-hanging charging coils could be more likely to break. As with other contributions, this demonstrates scholarly interest in WPT without significantly advancing EV technology.

In many WPT systems, including EV applications, it is desired to maximize the utilization of a single inverter — inverters can be bulky, lossy, and expensive. Work on consumer electronics [76] provides a pattern for powering multiple secondary loads from a single transmission coil. In this approach, each secondary coupled with the primary is modeled as

a load in series. The frequency is higher than is typical for EV applications (7 MHz), and the efficiency is lower than has been achieved in lower-frequency systems (between 70 % and 86 %).

2.2.4 Considerations in DWPT Systems

One of the major struggles of DWPT is achieving rapid detection time. In a fraction of a second, either the primary or secondary pad needs to detect the other, power on, and power off after the coupling is reduced. The work in [77] adapts a SWPT system for DWPT by sensing an approaching EV (in this case, a scooter) with ultrasonic sensors. The applicability of this approach to larger EVs is limited; road debris is likely to limit the effectiveness of this approach on a roadway.

A similar approach is presented in [78]. Although the goal of [78] is to track vehicles, a logical extension is detecting vehicles for DWPT. That approach uses dedicated short-range communications (DSRC), defined in [79], to locate vehicles and report their location to a mobile device. While this approach could be extended to vehicle detection for DWPT, two limitations hinder the effectiveness of DSRC for DWPT. First, DSRC is omnidirectional, so any primary pads within the DSRC range could be activated, including pads that are uncoupled with the vehicle's pad. Second, DSRC is too slow for DWPT; the frequency of DSRC messages could be much less than the frequency with which a vehicle passes primary pads. Therefore, other detection methods are needed.

The work detailed in [80] is another, more robust approach to sensing an approaching vehicle for WPT. Because an ultrasonic sensor could break, and lose effectiveness in noisy environments, sensing with the magnetic field itself is desirable. In [80], a detection scheme is presented that requires an additional sensing coil but is otherwise more robust than the approach in [77]. A simpler approach, requiring less hardware, is introduced in [18]. In this approach, a primary detects resonant current and begins switching when the resonant current exceeds a threshold. The primary stops switching when the bridge current drops below a given threshold. This approach applies to a number of converter topologies. In this approach, no additional sensors or equipment are required, and the response is very

fast. However, this approach does require all primaries to be synchronized. Further, if the secondary has passive rectification, no method to begin power transfer is considered. If the secondary has active rectification, it must synchronize to the primary. Those questions, outside the scope of [18], are considered in Objective 2c.

A related complication is vehicle localization, which is the major consideration in [19]. A design is proposed to aid the driver in achieving correct alignment; the design requires the introduction of three new pads. With this approach, feedback is given to the driver to achieve good alignment and transfer maximum power.

The last potential issue with the broad adoption of DWPT technology discussed here is the pulsed load demanded from the grid, analyzed in [81]. A control strategy is proposed for a system of DWPT pads, which regulates the transient response of the DWPT system on the grid. The effectiveness of the control strategy is also validated.

Zhang *et.al.* addresses power regulation in DWPT, with applications in EVs in [82]. In that work, a hovering drone is wirelessly charged; as with DWPT for EVs, the primary–secondary coupling varies. It is desired to charge the drone with constant current, for this, an RL approach is considered. A recursive neural network (RNN), where past values inform the network, is developed to regulate power transfer.

2.2.5 Bridge Loss Minimization in Resonant Circuits

Switching loss is a major consideration, especially as the frequency increases for WPT. This section considers some of the advances in low-loss switching in resonant circuits, a broad class that includes WPT circuits. Two methods to achieve lower losses are considered, zero-volt switching (ZVS) and zero-current switching (ZCS).

Every semiconductor switch has some parasitic output capacitance; when a switch closes while a voltage is present across the switch, the capacitive charge dissipates through the switch as a loss. This lowers overall efficiency and heats the switch. However, if the body diode of a switch is conducting when the switch closes, the voltage across the parasitic capacitance is negligible and minimal energy loss occurs. This is the goal of ZVS. Note that ZVS requires deadtime, where no switches on a half-bridge are conducting. The work

presented in [16] describes a modification to an isolated DC-DC conversion circuit, which is similar to a WPT circuit, the ensure ZVS. In this method, a capacitive link is inserted between the source and the load. This method effectively reduces switching losses and allows primary–secondary isolation, but the physical capacitive link renders this approach ineffective for WPT, as the capacitive link cannot be established in a DWPT system.

Especially relevant to the work discussed here is the work in [15]. In that excellent work, an approach similar to the approach used in Task 2, where the higher-order harmonics of the switching voltage waveform are used to achieve ZVS. This approach is excellent, but the method proposed in [15] requires the circuit to be designed for ZVS. In a WPT circuit, the component values may not be changeable; it is desired to define an algorithm to achieve ZVS for any resonant circuit, where the deadtime can be calculated from circuit components.

In contrast to ZVS, ZCS seeks to minimize turn-off losses in the switches, this is achieved by turning off the switches while the body diodes conduct. While ZVS requires the body diode to conduct before the switch, ZCS requires the body diode to conduct after the switch. For MOSFET designs, the losses avoided by ZVS are more significant than the losses avoided by ZCS. Nevertheless, some relevant work on ZCS is considered. In [83], a design is proposed to transfer maximum power, minimize converter requirements, and achieve ZCS. The design is verified both in simulation and experimentally. While this work is effective at its aims, the most significant drawback is that ZCS is generally not the most important component of switching loss.

Another approach to loss minimization is synchronous rectification. In WPT and other resonant circuits, the load side rectifies a current. Passive rectification is the simplest approach, where a diode bridge converts the AC to DC. However, active switching or rectification can minimize bridge losses. Active rectification has been well-studied. For example, in [84,85], a new approach to synchronous rectification is introduced, where many switches are operated in parallel to improve efficiency. By sequentially commuting the parallel switch, the overall losses are reduced.

Critical, early research on modeling resonant converters also merits mention here. The work

in [86] simplifies the approach to modeling resonant circuits. In [86], a method is presented to model perturbations in the phasor domain, rather than the time domain. The method is sufficiently robust to account for frequency, phase, and magnitude perturbations of the excitation. In designing resonant circuits, phasor or envelope modeling allows complex reactions to be analyzed.

2.2.6 Opportunities for Further Research

Significant research has been completed in the field of WPT, but a few key limitations remain. Control and modeling of WPT systems are well understood, but limitations exist for adapting existing WPT systems for multi-vehicle-class DWPT systems. While some detection algorithms have been proposed, the detection methods in the literature are frequently too slow, too lossy, too complicated, or insufficiently robust for a roadway application. There is a need for an efficient, simple, detection scheme that allows secondary power regulation in the rectifier.

Further, reducing switching losses is essential to the broader adoption of DWPT. Again, numerous algorithms to reduce switching losses have been proposed, but the literature surveyed did not include a method that 1) does not add reactive power and 2) allows no physical connection between the primary and secondary. The relevant tasks are chosen to fill both of those gaps identified in the existing literature.

2.3 Machine Learning and Other Modeling Techniques

A literature review of all recent contributions to machine learning is beyond the scope of this review. Here, we give a brief overview of relevant machine learning development and consider recent applications of ANNs to WPT systems; discuss other modeling techniques, including for graph-based systems; and discuss opportunities for further research. Section 2.3.1 discusses contributions to machine learning, Section 2.3.2 discusses other advances in modeling WPT systems, and Section 2.3.3 addresses existing gaps in the literature.

2.3.1 Machine Learning

In ANNs, a network uses a gradient descent algorithm to minimize a cost, causing the ANN to represent a target function. A powerful gradient descent algorithm (Adam) was introduced in [87], which is proposed to be used in the ANN tasks. The Adam algorithm uses both the present gradient and past gradients to quickly approach a minimum, where the ANN represents the target function well.

Reinforcement learning (RL), using ANNs, trains an agent to interact to maximize some reward. In WPT, the control space is generally continuous, where the phase or frequency of switching can be modulated. In [88], an algorithm to stably train an agent with a continuous action space is presented. This requires training four neural networks and requires the agent to learn the value of a given action-state combination. In [89], a different approach to training an agent to act on a continuous actions space is presented, where the agent leverages the differentiability of the environment to learn. This algorithm could easily be applied to a resonant converter, where the environment (circuit) dynamics are well-understood and easily differentiable.

One last contribution to the machine learning field bears mentioning here. In [90], the concept of convolutional neural networks is introduced, which are especially powerful for processing images. When using a neural network to model magnetic fields, those fields may be represented as images, and an approach similar to that in [90] may be useful.

Perhaps the simplest application of an ANN to WPT is in estimating self-inductances of the primary and secondary coils, and their mutual inductance. Those inductance values are the minimum required to simulate a system. Perhaps unsurprisingly, much of the work applying ANNs to WPT involves inductance estimation. In [21], an ANN is trained to estimate the mutual inductance between a primary and secondary coil. The proposed ANN runs online, meaning that it generates new estimates of the mutual inductance as the primary–secondary alignment varies. Objective 3 replicates the utility of the approach in [21], but will use system geometry, rather than measured values, to estimate coupling. Similarly, in [20], an ANN is presented that has been trained to model an inductor. The model is very robust, with 30 input variables and 40 output variables, and accurate to

within 3 %. The large number of input variables is impressive, but the number of output variables is too few to fully model the WPT magnetic fields, and only a single inductor is considered, rather than a pair of coupled inductors. While the work in [20] is a strong starting point, more work is needed to model WPT coils with ANNs.

Hariri *et. al.* propose an ANN to optimize the WPT coil link [91], which, again, is similar to the work discussed here. The ANN was trained to represent the WPT coils, while a genetic algorithm optimized the coil design. While this early work presents a solid approach to WPT optimization with machine learning, the number of data points used in the work and the limitations on the coil design (circular coils with no ferrite) limit the applicability of this work for current WPT designs. A similar approach is used in [92], where an ANN is used to create an optimal design. In that work, an ANN is trained to represent converter efficiency and power density as a function of switching frequency, inductor current ripple, switch physical area, and junction area. This work is especially relevant to the approach presented here.

Similarly, [93] considers a WPT system with multiple primary coils and multiple secondary coils, where the positions of multiple secondary coils are unknown. A control law is known to transfer power optimally when the locations of the secondary coils are known. The ANN in [93] estimates the position of the secondary coils; because this ANN is used in a controller, the approach is similar to a reinforcement learning (RL) agent. However, unlike an RL agent, knowledge of the system is used to design the controller.

In [94], a small WPT system used for medical devices is modeled and optimized for maximum power transfer with a fixed magnetic field strength. This work does not use machine learning but uses analytic descriptions of the system to perform the optimization. Relationships between coil size, power transfer, field strength, and frequency are analyzed. While this is related to the goal of optimizing WPT coil design for EVs, the focus on constrained magnetic fields means that the solution described here operates at high frequency and low efficiency (less than 23 %).

While machine learning in general has advanced significantly in recent years, much less

computational power has been devoted to modeling complex magnetic field interactions. There is a need to apply more computing resources to modeling magnetic fields in WPT systems, to develop a comprehensive modeling tool.

2.3.2 Other Modeling Techniques in WPT Systems

It is also necessary to devise a modeling strategy for a multi-primary, multi-secondary system. The field of power electronics has developed numerous solutions for transferring power from one point to another through a variety of power converters, as modeled by the graph depicted in Fig. 2.1. In that approach, power moves between two nodes. Efforts to model more complex interactions have used a bus approach, depicted in Fig. 2.2. Again, too many contributions using this modeling approach exist for consideration here. However, this requires a central bus, which is not possible in a WPT system.

Efforts to model multi-primary, multi-secondary WPT systems, as depicted in Fig. 2.3, are still under early development. Although power electronics generally approaches this problem with a bus for conductive power transfer, very little work has been done on complex WPT systems. The only works reviewed used the approach in [23], where each element in the system has a unique, orthogonal key. An element in the system can then transfer power to or from another element by using the respective key. The approach is based on communication networks.

While the work in [23] is laudable for beginning to consider multi-agent WPT systems, a few areas outside the scope of that work are necessary. First, the approach in [23] does not operate each converter all the time, so power transfer rates are limited. Second, the approach requires some synchronization. Third, additional benefits easily intuited with a different modeling scheme may be available. It is necessary to develop a new modeling tool to address those opportunities for further study.

Another approach that addresses a multi-primary, multi-secondary system is the repeater method used in [66, 75]. Although [75] aims to transfer power from one point to one other point, the repeater coils act as both primary and secondary: each repeater coil transmits an equal quantity of power as it absorbs. The work in [66] is the CPT analog of the work in [75],

using booster capacitors rather than booster coils. Of course, the boosters in [66, 75] are passive, and the WPT graph is singly connected. Nevertheless, the booster coil approach paves the way for the introduction of hybrid booster/primary coils.

Fig. 2.1: One-to-one model of a power electronics system. Power transfers from one source to one load.

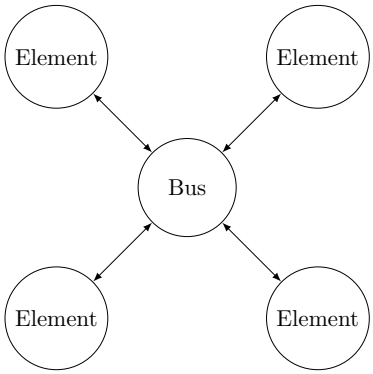

Fig. 2.2: Bus model of a power electronics system. Power transfers between many elements, which can function as either sources or loads and a bus.

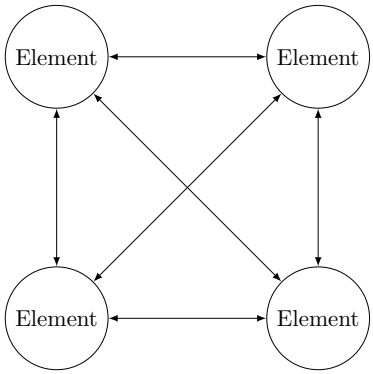

Fig. 2.3: Complex model of a power electronics system. Power transfers among many elements, which can function as either sources or loads.

One modeling tool, developed to determine current distribution in multi-filar WPT coils, is very relevant to this approach [95]. That work allows a single simulation to quickly evaluate the tradeoffs between a high number of turns and a high number of parallel windings. The thesis of [95] is summarized here. In that approach, an inductance matrix is defined for an n-filar WPT coil, which is then manipulated. Let L be the inductance matrix:

$$L = \begin{bmatrix} L_1 & M_{12} & \cdots & M_{1n} \\ M_{21} & L_2 & \cdots & M_{2n} \\ \vdots & \vdots & \ddots & \vdots \\ M_{n1} & M_{n2} & \cdots & L_n \end{bmatrix} \tag{2.4}$$

Consider a 2-winding, bifilar structure as in Fig. 2.4. It is desired to determine the total effective inductance and the currents through each bifilar portion, $\bar{I}_1$ and $\bar{I}_2$ in the figure.

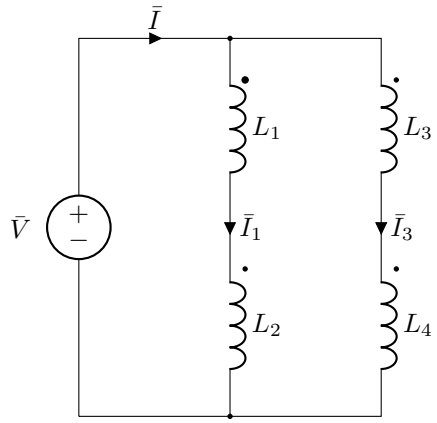

Fig. 2.4: Example circuit diagram of mutlifilar, multi-winding coil

Express L as a block matrix

$$L = \begin{bmatrix} [L_\alpha] & [L_\beta] \\ \left[L_\beta^T\right] & [L_\gamma] \end{bmatrix} \tag{2.5}$$

Further, let $\bar{V}_n$ and $\bar{I}_n$ be the voltage across and current through each inductor, and let those quantities be gathered into vectors $\mathbf{v}$ and $\mathbf{i}$. The governing equations are:

$$\begin{aligned} \mathbf{v} &= j\omega L\mathbf{i} \\ \bar{V} &= \bar{V}_1 + \bar{V}_2 \quad = \bar{V}_3 + \bar{V}_4 \\ \bar{I}_1 &= \bar{I}_2 \\ \bar{I}_3 &= \bar{I}_4 \\ \bar{I} &= \bar{I}_1 + \bar{I}_3 \end{aligned} \tag{2.6}$$

Adding rows of $\mathbf{v}$ and using only $\bar{I}_1$ and $\bar{I}_3$, the governing equations can be expressed as

$$\begin{bmatrix} \bar{V} \\ \bar{V} \end{bmatrix} = j\omega \begin{bmatrix} L_1 + M_{21} + M_{12} + L_2 & M_{13} + M_{23} + M_{14} + M_{24} \\ M_{31} + M_{41} + M_{32} + M_{42} & L_3 + M_{43} + M_{32} + L_4 \end{bmatrix} \begin{bmatrix} \bar{I}_1 \\ \bar{I}_2 \end{bmatrix} \tag{2.7}$$

Expressing the sum of all elements in a matrix as $\sum(\cdot)$, (2.7) can be written as

$$\begin{bmatrix} \bar{V} \\ \bar{V} \end{bmatrix} = j\omega \begin{bmatrix} \sum(L_\alpha) & \sum(L_\beta) \\ \sum(L_\beta) & \sum(L_\gamma) \end{bmatrix} \begin{bmatrix} \bar{I}_1 \\ \bar{I}_2 \end{bmatrix} \tag{2.8}$$

For convenience, let

$$L_{reduc} = \begin{bmatrix} \sum(L_\alpha) & \sum(L_\beta) \\ \sum(L_\beta) & \sum(L_\gamma) \end{bmatrix} \tag{2.9}$$

Essentially, the inductance matrix should be sorted into blocks corresponding to each filar set, and each block matrix summed to generate the reduced inductance matrix L_{reduc}. The current distribution is given by

$$\begin{bmatrix} \bar{I}_1 \\ \bar{I}_3 \end{bmatrix} = \frac{-j}{\omega} L_{reduc}^{-1} \begin{bmatrix} \bar{V} \\ \bar{V} \end{bmatrix}, \tag{2.10}$$

which can be simplified by summing the columns of L_{reduc}^{-1}

This method, discussed in [95] is used to evaluate the complex interactions between WPT pads with excitations. The approach in [95] is not general enough to allow different excitations on each coil, and does not consider power transfer between the multi-filar windings. Further, it does not account for any compensation on each coil, which is outside the typical multi-filar coil design. Regardless, conceptually and mathematically, this approach bears a strong resemblance to the full graph-based modeling problem discussed in Chapter 7.

2.3.3 Opportunities for Further Research

The most salient gap in the scholarship on ANNs for magnetics modeling is a more powerful network. Powerful tools for ANN modeling have been developed [96, 97] and there exists an opportunity to leverage those advances from computer science to WPT. A single ANN that can model all the relevant magnetic parameters for a WPT system is needed to develop good coil designs; many different actors developing WPT technologies have developed good designs for a single application, but an interoperable standard will require more simulation

power. Therefore, addressing this gap constitutes a portion of Objective 3.

Further, there is a need for a framework that addresses complex primary–primary and primary–secondary interactions. Work addressing more complicated WPT networks has been introduced [23], but that approach does not allow the agents to approach full power. There is a need for a more powerful framework to model complex WPT systems operating near full power.

CHAPTER 3

A NETWORK FLOW APPROACH TO BATTERY ELECTRIC BUS SCHEDULING AND BATTERY HEALTH CONSCIOUS OPTIMIZATION

This chapter is a replication of a journal article currently under review, submitted to IEEE Transactions on Intelligent Transportation Systems [24].

A Network Flow Approach to Battery Electric Bus Scheduling and Battery Health Conscious Optimization

Matthew Hansen, Greg Droge, Jacob Gunther

***Abstract*—A battery-health-conscious (BHC) approach is introduced to determine a least-cost charging solution for a fleet of battery electric buses (BEB). The optimal solution is defined as that which minimizes total daily cost, comprised of both energy cost and a monetary value of battery degradation. The approach models flow through a circular graph to assign chargers to buses throughout the day. A formulation to translate a given bus schedule to a graph, and a graph to a mixed-integer nonlinear program is presented. The framework is demonstrated with 14 buses and two different optimization strategies, the battery health conscious approach and a baseline approach.**

I. Introduction

BATTERY-electric buses (BEBs) are becoming increasingly popular as a way to eliminate tailpipe emissions, reduce vehicle noise, and lower maintenance costs [1], [2], [3], [4]. The introduction of BEB into a fleet presents new restrictions and opportunities for cost savings with no parallel in internal-combustion engine (ICE) fleets; a large body of recent research seeks to optimize fleet electrification across a variety of parameters. As batteries are among the most expensive components in battery electric vehicles [5], there is a need to better optimize total daily cost for an EV fleet owner, including both energy costs and battery degradation costs for multiple vehicles. However, previous contributions to the bus-scheduling problem have ignored or simplified battery health as a variable of optimization. In this work, we present a method to optimize a BEB fleet charging schedule while considering both energy and degradation costs.

Recent research in the space has attempted to aid deployment of electric vehicles by lowering battery degradation. In [6], a strategy for optimizing battery health by splitting power between a battery/fuel cell and an ICE is proposed. In [7], battery swapping is proposed to reduce upfront costs and increase efficiency, without posing an optimal charging problem. Battery health contributes to the objective function in [8], but the approach does not guarantee an optimal solution and does not consider multiple EVs. Expanding an approach to consider a fleet of BEBs, rather than a single vehicle, is non-trivial; typically, a fleet will have more vehicles than EV power supply equipment (EVPSE). This requires solving a problem of limited resource allocation, which is the central issue of fleet schedule optimization. Although existing work considers battery health, we are aware of no work that considers battery health along with charging costs for scheduling the charging for a fleet of EVs.

Significant work has been done to simultaneously optimize BEB scheduling. Within those and other approaches, fidelity to battery health dynamics varies widely in the literature. However, a robust consideration of battery health is outside the scope of many previous contributions. A brief overview of existing approaches follow. Some work on optimizing BEB charging schedules assumes batteries are completely charged every time a bus stops at a charging station [9], [10]. Others do consider battery state of charge (SoC, defined as stored energy divided by energy capacity), but do not consider battery health [8], [11], [12], [13], [14], [15]. In those cases, battery degradation costs are either modeled as a single upfront cost or a recurring cost but are not involved in the optimization.

Of the previous approaches considered here, the work in [15] is especially relevant. In that work, the allocation of EV power supply equipment (EVPSE) to BEBs is expressed as a graph search problem, which can be solved as a mixed-integer linear program (MILP) to minimize daily energy costs. The primary contribution of this work is an improvement to the MILP graph search in [15] that includes the cost of battery degradation in the optimization. An important secondary contribution of this work is the introduction of a strategy to reduce the optimization space and eliminate a constraint, improving the MILP runtime. We are unaware of any work that has developed a framework to simultaneously consider battery degradation costs, fleet charging resource allocation, and charging costs when planning the daily charging schedule.

Section II introduces the battery degradation model used in the present work. In Section III, a graph is introduced to model the decision space. In Section IV, the graph search is presented as a MILP. In Section V, an algorithm to decrease the variables of optimization, remove a constraint, and improve processing speed is described. Key modifications to the algorithm described in Section IV that allow multiple charger power levels are detailed in Section VI. Section VII demonstrates the planning framework and Section VIII summarizes the key points of this work.

II. Battery Basics

In this section, a battery health model is introduced and adapted for modeling battery degradation within a MILP. Section II-A describes the battery degradation model; in Sections II-B and II-C, two components of the degradation model are quantified.

TABLE I: Notation Used

Variable	Description	Variable	Description
Battery Health and EVPSE Parameters and Variables			
t	Battery time, in days	N	Number of battery cycles
Q_{Li}	Lithium available for energy storage	Q_{neg}	Negative electrode capacity for energy storage
Q_{pos}	Positive electrode capacity for energy storage	Q_{min}	Battery capacity, $Q_{Li}Q_{neg}$
d_0	Lithium degradation parameter	$d_{0,ref}$	Reference value of d_0
b_0	Lithium constant degradation parameter	b_1	Lithium time-based degradation parameter
$b_{1,ref}$	Reference value of b_1	b_2	Lithium cycling-based degradation parameter
$b_{2,ref}$	Reference value of b_2	b_3	Lithium BoL break-in parameter
$b_{3,ref}$	Reference value of b_3	τ_{b3}	Time constant corresponding to b_3
T_{ref}	Reference temperature, 25 °C	Q_{eol}	End-of-life battery capacity
B_{cost}	Battery cost	$bat_{d,Li}$	Daily battery damage costs due to Q_{Li} degradation
c_0	Negative electrode degradation parameter	$c_{0,ref}$	Reference value of c_0
c_2	Negative electrode cycling-based degradation parameter	$c_{2,ref}$	Reference value of c_2
DoD	Cycling depth	β_{c2}	DoD dependence coefficient of c_2
$bat_{d,neg}(DoD)$	Battery damage costs due to Q_{neg} degradation per cycle	$r_{(l)}$	C-rate of PSE type l (units of h^{-1})
B_{cap}	Battery capacity (units of kW h)		
Graph variables			
$\mathcal{G}_{(l)}$	A graph corresponding to charger type l	$\mathcal{V}_{(l)}$	A set of vertices corresponding to charger type l
$\mathcal{E}_{(l)}$	A set of edges corresponding to charger type l	$\mathcal{R}_{(l)}$	The subset of $\mathcal{V}_{(l)}$ corresponding to rest nodes
$\mathcal{C}_{(l)}$	The complement of $\mathcal{I}_{(l)}$, set of charging nodes	$\mathcal{U}_{(l)}$	The set of edges leading from idle nodes to charging nodes
$\mathcal{D}_{(l)}$	The set of edges leading from charging nodes	$v_{(l)q}$	The q^{th} vertex of graph l
$e_{(l)i}$	The i^{th} edge of graph l	$D_{(l)}$	Incidence matrix for graph l
$d_{(l)mn}$	Element in row m, column n of $D_{(l)}$	Δ_t	The time interval resolution; fraction of an hour
$\delta(v)$	Duration value of a node v	$\mathcal{V}_{(l)p}$	Subset p of $\mathcal{C}_{(l)}$ corresponding to a bus stop at the depot
$\mathcal{I}_{(l)p}$	The index set of the edges leading into group p	$j(v)$	Bus corresponding to node v
Counters and Indices			
n_b	Number of buses	$n_{(l)c}$	Number of chargers of type l
$n_{(l)v}$	Number of vertices in subgraph l	$n_{(l)e}$	Number of edges in subgraph l
n_t	Number of time steps	n_g	Number of groups
n_l	Number of types of chargers	$n_{(1)vc}$	Number of charging vertices of graph l
i	Edge index	q	Vertex index
k	Time index	j	Bus index
p	Group index	m, n	General matrix indices
l	Charger type and graph number index		
Optimization Variables and Constraints			
$x_{(l)i}$	Integer variable for using edge i with charger type l	$\mathbf{x}_{(l)}$	Vector of integer decision variables $x_{(l)i}$
y_j	Value of initial SoC of bus j	$\mathbf{y}$	Vector of initial battery SoC values
$d_{(l)}$	Charger number constraint vector for type (l)	$D_{(l)}$	Incidence matrix for subgraph of charger type l
$\mathbf{0}_m$	Vector of zeros with m rows	$\mathbf{1}_m$	Vector of ones with m rows
$A_{(1)g}$	The group constraint matrix for charger type l	soc_{min}	minimum SoC allowed
soc_{max}	maximum SoC allowed	$w_{j,k}$	SoC of bus j at time k
$\mathbf{w}_j$	Concatenation of $w_{j,k}$ for all k	$\mathbf{w}$	Vector of charge variables $w_{j,k}$ for all j and k
$\mathbf{s}_{min}$	Vector setting lower bounds on SoC	$\mathbf{s}_{max}$	Vector setting upper bounds on SoC
$S_{(l)j}$	SoC matrix for bus j and charger type l	$S_{(l)}$	Concatenation of $S_{(l)j}$ for all j
T	Matrix mapping y_j to the corresponding rows of $S_{(l)}$	$S_{(l)}$	Concatenation of $S_{(l)j}$ for all j
$S_{(l)[n_t]}$	Concatenation of every n_t^{th} row of $S_{(l)}$	$N_{(l)}$	Integer matrix whose image is the kernel of $D_{(l)}$
α_i	Coefficient of reconstruct $\mathbf{x}_{(l)}$ from columns of $N_{(l)}$	$\mathbf{x}'_{(l)}$	Vector of decision variables α_i
$n_{(l)events}$	Number of charging events of charger type l	$N'_{(l)}$	Rows of $N_{(l)}$ corresponding to rest edges
Optimization Costs			
$c_{(l)i}$	Graph edge costs for charger type l	$\mathbf{c}_{(l)}$	Vector of edge costs $c_{(l)i}$
$C_{(l)b}$	Charging event cost matrix of charger type l	$\mathbf{z}$	Charging event cost vector

A. A Brief Overview of Battery Degradation Factors

As batteries are used, their capacity fades. Although some applications for battery after first end-of-life exist, [16], here we only consider first life use, the time that the battery is installed in a BEB. Typically, first end-of-life (EoL) is when the battery capacity reaches 80% of the nameplate capacity. The battery lifetime can depend on variables such as charge rate (C-rate), depth of discharge (DoD), daily use, time since manufacture, SoC, and temperature [17], [18], [16]. Due to the complex interactions among the variables, a simplified model is needed to estimate loss within a MILP. In this paper, we consider a battery degradation model dominated either by calendar aging or cycling.

Battery packs are comprised of cells in series and parallel. The battery pack capacity is limited by the lowest-capacity cell in the battery. While cells within a pack naturally have some imbalance, we use a battery cell degradation model to estimate overall pack health.

Typically, BEBs use a lithium-ion (Li-ion) battery due to the lighter weight relative to other battery chemistries [19], [20], [21]. Three major phenomena affecting battery capacity are addressed in the battery life predictive model (BLPM) developed in [18], namely lithium degradation, negative electrode site capacity, and positive electrode site capacity.

Energy is stored and released in a Li-ion battery as the ions move between the positive and negative electrodes; the

minimum of three values determines battery capacity:

1) Cyclable Li, Q_{Li}, noted to be dominated by calendar aging in [18].
2) Negative electrode site capacity, Q_{neg}, noted to be dominated by cycling in [18]
3) Positive electrode site capacity, Q_{pos}, which does not significantly affect battery life[1]

In the BLPM, EoL would either be when cyclable Li decreases to $80\,\%$ of the original value, or when the number of negative electrode sites decreases to $80\,\%$ of the original value, whichever occurs first.

A simplistic example of this is illustrated in Fig. 1, where there are different capacities for each the states listed above. Because energy is stored and released by Li ions moving between the electrodes, capacity is limited by whichever state (Q_{Li}, Q_{neg}, or Q_{pos}) limits the quantity of Li ions that can cycle between electrodes. In Fig. 1, there are 4 ions, 8 positive electrode sites, and 6 negative electrode sites; the capacity is only limited by the lithium ions available and a marginal loss of sites on either electrode has no direct effect on battery capacity.

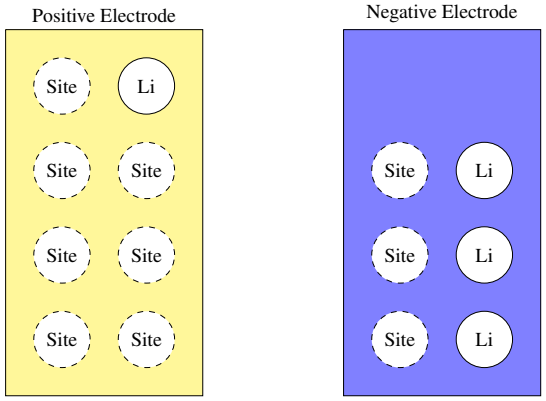

Fig. 1: Diagram of battery capacity. The battery capacity in Ampere-seconds is equal to the charge that can be moved from one electrode to another by the lithium ions.

B. Lithium Degradation

Battery degradation corresponding to a reduced Q_{Li} is now discussed. In [18], lithium capacity is expressed as a function of a nominal capacity d_0, time in days since cell manufacture t, number of cycles N, experimentally-determined values b_0, b_1, b_2, b_3, and a break-in time constant τ_{b3}. The capacity fade equation from the BLPM is stated as follows [18, eq. (5)].

$$Q_{Li}(t) = d_0 \left[b_0 - b_1 t^{1/2} - b_2 N - b_3 (1 - \exp(-t/\tau_{b3})) \right] \tag{1}$$

The value b_0 is an experimentally-determined constant; each of the other coefficients in (1) is the product of a nominal value; i.e., $d_{0,ref}$, $b_{1,ref}$, $b_{2,ref}$, and $b_{3,ref}$; and a temperature-dependent correction factor. With $T(t)$ defined as the temperature, T_{RPT} as the temperature during battery capacity testing, T_{ref} as a reference temperature, V_{OC} as the cell open-circuit voltage, V_{ref} as a reference voltage, $U_{\_}$ as terminal voltage, θ as an experimentally-determined constant, and U_{ref} as a reference voltage, the coefficients are defined as

$$d_0 = d_{0,ref} \left(\exp \left[- \frac{E_{a,d_0,1}}{R_{ug}} \left(\frac{1}{T_{RPT}(t)} - \frac{1}{T_{ref}} \right) - \left(\frac{E_{a,d_0,2}}{R_{ug}} \right)^2 \left(\frac{1}{T_{RPT}(t)} - \frac{1}{T_{ref}} \right)^2 \right] \right) \tag{2}$$

$$b_1 = b_{1,ref} \exp \left[- \frac{E_{a,b_1}}{R_{ug}} \left(\frac{1}{T(t)} - \frac{1}{T_{ref}} \right) \right] \times \exp \left[\frac{\alpha_{b_1} F}{R_{ug}} \left(\frac{U_{\_}(t)}{T(t)} - \frac{U_{ref}}{T_{ref}} \right) \right] \times \exp[\gamma_{b_1} (DoD_{\max})^{\beta_{b1}}] \tag{3}$$

$$b_2 = b_{2,ref} \exp \left[- \frac{E_{a,b_2}}{R_{ug}} \left(\frac{1}{T(t)} - \frac{1}{T_{ref}} \right) \right] \tag{4}$$

$$b_3 = b_{3,ref} \exp \left[- \frac{E_{a,b_3}}{R_{ug}} \left(\frac{1}{T(t)} - \frac{1}{T_{ref}} \right) \right] \times \exp \left[\frac{\alpha_{b_3} F}{R_{ug}} \left(\frac{V_{OC}(t)}{T(t)} - \frac{V_{ref}}{T_{ref}} \right) \right] (1 + \theta DoD_{\max}) \tag{5}$$

Many constants appear in the initial expressions, but are quickly eliminated by some simplifying assumptions; given the following assumptions, the lithium degradation model given in [18] can be simplified.

- $\tau_{b3} \ll t$. In [18], $\tau_{b3} = 5$, which is negligible compared to battery lifetime. This implies that, at the EoL condition, $b_3(1 - \exp(-t/\tau_{b3}))$ is approximated by b_3.
- A well-cooled battery. A well-cooled battery has a longer lifetime, and recent research has investigated new techniques to cool EV batteries [17]. With this assumption, all temperatures referenced in (2)–(5) are equal to T_{ref}. This causes (2) to simplify to $d_0 = d_{0,ref}$.
- Cycling degradation is manifested only through Q_{neg} degradation, not through Q_{Li} degradation. In [18], it is noted that Q_{Li} degradation is dominated by time, and the cycling dependence of Q_{Li} is not fundamental to the model, while Q_{neg} degradation is dominated by cycling. When cycling is a dominant degradation mechanism, we expect Q_{neg} to limit battery capacity. Thus, we drop the the cycling terms and approximate $DoD_{\max} = 0$ in (3) and (5). This also approximates $b_0 - b_1 t^{1/2} - b_2 N - b_3$ by $b_0 - b_1 t^{1/2} - b_3$.
- Battery SoC is constant at the reference. The voltages $U_{\_}$ and V_{OC} are related to SoC; neglecting the effects of cycling on Q_{Li} implies that $U_{\_} \approx U_{ref}$ and $V_{OC} \approx V_{ref}$. This further implies that the DoD_{max} is 0. Together with the assumption of a well-cooled battery and the disregard of the battery cycling, this assumption implies that $b_1 = b_{1,ref}$ and $b_3 = b_{3,ref}$.

[1]In [18], it is noted that the positive electrode site capacity increases slightly at beginning-of-life, and then stabilizes. As Q_{pos} does not degrade and therefore does not affect battery capacity at EoL, further discussion of Q_{pos} is omitted.

The above assumptions force the exponential terms in (2)–(5) to unity. With those simplifications, the lithium degradation equation (1) is simplified as:

$$Q_{Li}(t) \approx d_{0,ref}\left[b_{0,ref} - b_{1,ref}t^{1/2} - b_{3,ref}\right]. \quad (6)$$

In [18], the full equation (1) is fine-tuned version of an equation like (6). This lends credence to (6) as a simplified, reasonable form of (1)

Given (6), it is desired to measure average daily cost from degradation due to lithium degradation, measured from manufacture until first EoL. Note that the only variable in (6) is t; the other quantities are constants. To measure average daily battery cost, (6) is solved for the days t_{max} to the EoL capacity Q_{eol}, which is $80\,\%$ of the initial capacity.[2] Solving (6) for t_{max} yields

$$Q_{eol} = d_{0,ref}\left[b_{0,ref} - b_{1,ref}t_{max}^{1/2} - b_{3,ref}\right] \quad (7)$$

The solution gives the time in days, t_{max}, the battery can sit idle before end-of-life. With a battery replacement cost of B_{cost}, the average daily battery replacement cost $bat_{d,Li}$ is then the lifetime cost in dollars divided by the lifetime length in days.

$$bat_{d,Li} = \frac{B_{cost}}{t_{max}}, \quad (8)$$

with units of dollars per day.

Regardless of how the battery is cycled, the lithium degradation sets a lower daily bound for battery damage. With light cycling, the battery degradation will be dominated by calendar aging leading to degradation in Q_{Li}, described in this section. With heavier cycling, battery degradation will be dominated by degradation in Q_{neg}, which is addressed in continuation.

C. Negative Electrode Degradation

Battery degradation corresponding to a reduction in Q_{neg} is now discussed. In [18], negative electrode capacity is expressed as a function of experimentally-determined values c_0, c_2, and number of cycles N. The Q_{neg} capacity fade equation from the BLPM is stated as follows [18, eq. (9)].

$$Q_{neg}(N, DoD) = \left[c_0^2 - 2c_2c_0N\right]^{\frac{1}{2}} \quad (9)$$

The values c_0 and c_2 are products of nominal values, i. e., $c_{0,ref}$ and $c_{2,ref}$ a temperature-dependent correction factor, and, for c_2, a DoD-dependent term. As in Section II-B, various constants appear in the initial expressions, but are quickly eliminated by some simplifying assumptions. The value β_{c2} is an experimentally-determined constant and, as before, $T(t)$ is defined as the battery temperature. The values c_0 and c_2 are given by

$$c_0 = c_{0,ref}\exp\left[-\frac{E_{a,c0}}{R_{ug}}\left(\frac{1}{T(t)} - \frac{1}{T_{ref}}\right)\right] \quad (10)$$

$$c_2 = c_{2,ref}\exp\left[-\frac{E_{a,c_2}}{R_{ug}}\left(\frac{1}{T(t)} - \frac{1}{T_{ref}}\right)\right](DoD)^{\beta_{c2}} \quad (11)$$

[2]Note that $Q_{Li}(0)$ is greater than the initial capacity when the initial capacity is limited by either Q_{neg} or Q_{pos}. In that case, $0.8Q_{Li} \geq Q_{eol}$.

As in Section II-B, the assumption of a well-cooled battery implies that $T(t) = T_{ref}$, which reduces (10) and (11) to

$$c_0 = c_{0,ref} \quad (12)$$

and

$$c_2 = c_{2,ref}(DoD)^{\beta_{c2}} \quad (13)$$

Substituting (12) and (13) into (9) yields

$$Q_{neg}(N, DoD) = \left[c_{0,ref}^2 - 2c_{2,ref}\left(DoD\right)^{\beta_{c2}}c_{0,ref}N\right]^{\frac{1}{2}} \quad (14)$$

Given (14), it is desired to determine the average cost per charging cycle with a given DoD, measured from manufacture until first EoL. Note that because N and DoD are the only variables in (14), it is possible to express N as a function of DoD. To that end, (14) is solved for the number of charging cycles N_{max} until Q_{neg} equals the EoL capacity Q_{eol}. This yields

$$N_{max}(DoD) = \frac{c_{0,ref}^2 - Q_{eol}^2}{2c_{2,ref}c_{0,ref}\left(DoD\right)^{\beta_{c2}}}. \quad (15)$$

The average cost per charging cycle[3], as a function of DoD $bat_{d,neg}(DoD)$, is determined by dividing the battery replacement cost B_{cost} by $N_{max}(DoD)$, so

$$bat_{d,neg}(DoD) = \frac{2c_{2,ref}c_{0,ref}\left(DoD\right)^{\beta_{c2}}B_{cost}}{c_{0,ref}^2 - Q_{eol}^2}. \quad (16)$$

In (8) and (16), damage was assumed to be dominated by either Q_{Li} degradation or Q_{neg} degradation, respectively. When the EoL condition is reached through either degradation mechanism, any degradation through the other mechanism will have had no effect on battery lifetime. Therefore, because battery capacity is limited by either Li availability or negative electrode site availability, battery degradation during a given day is the greater of either the minimum daily cost, due to Q_{Li} reduction, or the sum of the cycling damages, due to Q_{neg} degradation. Degradation costs do not sum.

III. Graph Preliminaries and Basic Approach

This section gives a brief overview of the relevant graph theory upon which this work builds, then formulates a graph search problem. A graph is built to model EVPSE allocation throughout a day, with nodes representing EVPSE allocation and edges representing changes in EVPSE allocation.

A MILP is then formulated to chart an optimal path through the graph along the edges, which determines how EVPSEs should be allocated to buses throughout the planning horizon. Rather than assigning a specific EVPSE to a specific action, the network flow formulation models how EVPSEs transition from one assignment to another by letting the edge flow variable represent the number of EVPSEs transitioning between the two assignments, or nodes, without specifying which

[3]Here, all the charging cycling is expressed through the commonly-used DoD metric, although in later sections, the damage is assumed to occur during the charging event. We are unaware of any literature separating the effects of charging depth and discharging depth on battery degradation; further, a large charging event typically corresponds to a similarly-large discharging event.

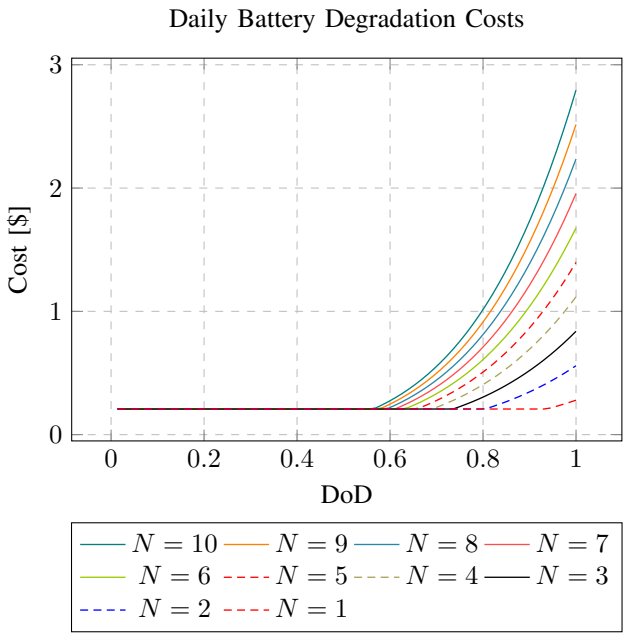

Fig. 2: Sample daily battery degradation costs with varying DoD values and N cycles per day. It is assumed that B_{cost} is \$1000. With few daily cycles or low DoD, battery damage is dominated by $bat_{d,Li}$, heavier cycling implies that Q_{neg} dominates batter degradation. Battery characteristics found in [18] and Section VII.

EVPSEs are allocated. Constraints are included to ensure that the charge on each bus remains within the maximum bounds, that each bus only charges once per visit to the station, that each bus is only serviced by at most one EVPSE at a time, and that the number of EVPSE remains constant throughout the day. We assume constant current charging control here; that is, the energy deposited on a battery while charging is proportional to the time spent charging.

Sections IV to VI define how the graph search problem is translated to a mixed-integer program, expressing costs and constraints of the graph search as a MILP. The fundamental approach presented in [15] has been adapted to account for battery degradation costs in the optimization.

A. Graph Preliminaries

A network is a directed graph whose edges move some quantifiable element [22], [23]; in this case, the assignment of EVPSEs. Given a set of bus schedules and EVPSEs of type l, a graph $\mathcal{G}_{(l)}$ is defined. The graph comprises a set of vertices or nodes, $\mathcal{V}_{(l)}$, and edges connecting pairs of nodes, $\mathcal{E}_{(l)} \subset \mathcal{V}_{(l)} \times \mathcal{V}_{(l)}$, i.e. $\mathcal{G}_{(l)} = \{\mathcal{V}_{(l)}, \mathcal{E}_{(l)}\}$. Let the edges be indexed by $i = \{1, 2, \ldots, n_{(l)e}\}$ and let the vertices be indexed by $q = \{1, 2, \ldots, n_{(l)v}\}$.

As defined in [24], the incidence matrix, $D_{(l)}$, can be used to represent the vertices and edges in matrix form. The incidence matrix is of dimension $n_{(l)v} \times n_{(l)e}$, where $|\mathcal{V}_{(l)}| = n_{(l)v}$ and $|\mathcal{E}_{(l)}| = n_{(l)e}$. Each column of $D_{(l)}$ is used to represent an edge, while each row of $D_{(l)}$ corresponds to a specific vertex. Writing the element of $D_{(l)}$ in the m^{th} row and n^{th} column as $d_{(l)mn}$, the incidence matrix is defined as:

$$D_{(l)} = [d_{(l)mn}],\ d_{(l)mn} = \begin{cases} 1 & \text{Edge } n \text{ begins at vertex } m \\ -1 & \text{Edge } n \text{ ends at vertex } m \\ 0 & \text{Otherwise} \end{cases} \tag{17}$$

Edge indices are taken directly from the incidence matrix using the notation $e_{(l)i}$ to represent the edge corresponding to the i^{th} column of $D_{(l)}$. Similarly, $v_{(l)q}$ represents the vertex corresponding to the q^{th} row of $D_{(l)}$.

B. Network Generation

This section describes how a network is defined. Each node represents an EVPSE action during a time interval, and the edges represent allowed transitions between actions; the characteristics of edges and nodes are also defined here.

Two types of nodes are included: charging nodes in the set $\mathcal{C}_{(l)}$ allocate an EVPSE to a bus, rest nodes in the set $\mathcal{R}_{(l)}$ represent EVPSEs at rest, i.e., a state indicating that the EVPSE is not charging a bus, and flow values represent changes in EVPSE allocation between subsequent time intervals, or *flow* of EVPSE allocation. For example, if three EVPSEs move from one allocation to another (or from one node to another) along an edge, the flow along that edge is three.

Each node is assigned with the properties defined in Table II and each edge is assigned with the properties defined in Table III, where n_b is the number of buses, Δ_t is the time resolution (the length of time represented by a single node), and $r_{(l)}$ is the charging rate of the l^{th} EVPSE type, given by the ratio of charging power in kW to battery pack size in kW h. The charging rate is assumed constant, regardless of the battery SoC.

TABLE II: Node Attributes

Node Attribute	Type	Minimum	Maximum
Node ID	Integer	1	$n_{(l)v}$
Bus ID	Integer	0	n_b
Time Interval Start	Time	00:00	24:00 - Δ_t
Time Interval End	Time	Δ_t	24:00
Duration	Integer	0 (Idle)	$\left\lfloor \frac{r_{(l)}}{\Delta_t} \right\rfloor$

TABLE III: Edge Attributes

Edge Attribute	Type	Minimum	Maximum
Edge ID	Integer	1	$n_{(l)e}$
Time	Time	00:00	24:00 - Δ_t
From Bus	Integer	0	n_b
To Bus	Integer	0	n_b

Buses are assigned an index from 1 to n_b, inclusive. The index 0 is used to represent the rest assignment, or nodes in set $\mathcal{R}_{(l)}$; the charging nodes $\mathcal{C}_{(l)}$ are the complementary set.

Let $j(v)$ be a function that returns the bus index corresponding to node v. Then

$$\begin{aligned} &\mathcal{R}_{(l)} \subset \mathcal{V}_{(l)}, \mathcal{C}_{(l)} \subset \mathcal{V}_{(l)} \\ &\mathcal{R}_{(l)} = \left\{v \in \mathcal{V}_{(l)} | j\left(v\right) = 0\right\}, \\ &\mathcal{C}_{(l)} = \mathcal{R}_{(l)}^{\complement} \end{aligned} \tag{18}$$

with

$$|\mathcal{R}| = n_t. \tag{19}$$

Figure 3 shows a sample portion of a graph with a single bus. The rest nodes in set $\mathcal{R}_{(l)}$ are shown as black circles along the bottom row, while charging nodes are shown as red circles in the other rows. Edges connect subsequent nodes; the *duration* property referenced in Fig. 3 is defined later in this section. The figures shows two bus stops at the depot.

Using nomenclature that refers to the structure drawn in Fig. 3, an *upward* edge leads from a rest node to a charging node, and a *downward* edge leads from a charging node. Each charging node has exactly one downward edge leading from it, to the node with the same bus number (or 0), at the following time interval. Each charging node also has exactly one upward edges leading to it from the previous rest state, and possibly one from the previous, longer-duration charger node. Then let the set of upward edges $\mathcal{U}_{(l)}$ be defined by

$$\begin{aligned} \mathcal{U}_{(l)} \subset &\mathcal{E}_{(l)} \\ \mathcal{U}_{(l)} = &\{e \in \mathcal{E}_{(l)} \text{ where } e = (v_m, v_n) \\ &|j\left(v_m\right) = 0, j\left(v_n\right) > 0\}, \end{aligned} \tag{20}$$

with the set of downward edges $\mathcal{D}_{(l)}$ given by

$$\begin{aligned} \mathcal{D}_{(l)} \subset &\mathcal{E}_{(l)} \\ \mathcal{D}_{(l)} = &\{e \in \mathcal{E}_{(l)} \text{ where } e = (v_m, v_n) \\ &|j\left(v_m\right) > 0\}, \end{aligned} \tag{21}$$

Each charging node has exactly one upward edge leading to it, and exactly one downward edge leading from it. Using the notation $\exists!$ to indicate "there exists exactly one", this can be expressed mathematically as:

$$\begin{aligned} &\forall v \in \mathcal{C}_{(l)} \exists! e \in \mathcal{D}_{(l)} \text{ s.t. } e = (v_m, v_n) \, | v_m = v \\ &\forall v \in \mathcal{C}_{(l)} \exists! e \in \mathcal{U}_{(l)} \text{ s.t. } e = (v_m, v_n) \, | v_n = v. \end{aligned} \tag{22}$$

That is, an EVPSE may transition from rest to charge, and once charging, there is only one next allocation transition for that EVPSE. The cardinality of the charging node set, upward edge set, and downward edge set is the same:

$$|\mathcal{C}_{(l)}| = |\mathcal{U}_{(l)}| = |\mathcal{D}_{(l)}| \tag{23}$$

To accurately measure the battery damage due to cycling, we associate a *duration* value δ with each node. This integer describes the number of time intervals between the charging node and the next rest node, inclusive. The duration property indicates how long a bus will be charging and is related to the battery cycling depth; the duration property of all rest nodes is 0. Multiple charging nodes may exist for the same bus at the same time, provided each node has a different duration value. Downward edges lead to the same bus (or bus 0) at the subsequent time interval with a decreased duration. To express that statement mathematically, let $\delta\left(v\right)$ return duration of node v and let $t\left(v\right)$ represent the start time of the interval node v exists on. Then,

$$\begin{aligned} \forall e \in \mathcal{D}_{(l)} \text{ where } e = (v_m, v_n), j\left(v_n\right) \in \{j\left(v_m\right), 0\}, \\ \delta\left(v_n\right) = \delta\left(v_m\right) - 1 \end{aligned} \tag{24}$$

Practically, the duration for all nodes is limited by the charging rate of the EVPSE and the time interval resolution; the duration cannot be so high that a battery could charge from less than $0\,\%$ SoC to greater than $100\,\%$ by charging for a given duration. That is,

$$\max \delta \leq \frac{1}{\Delta_t r_{(l)}}, \tag{25}$$

where $r_{(l)}$ is the charging rate of PSE type l, in units of inverse hours. The maximum duration for a given time interval is also limited by the remaining time the bus will be in the depot.

Charging nodes are sorted into mutually-exclusive groups $\mathcal{V}_{(l),p}$, each representing a stop by a bus at the charging depot. Figure 3 shows two such groups. Note that such that each group corresponds to a single bus, each group is mutually exclusive, and the union of all groups $\mathcal{V}_{(l),p}$ is the charging node set. With n_g groups,

$$\begin{aligned} \mathcal{V}_{(l),p_1} \cap \mathcal{V}_{(l)p_2} = \varnothing, p_1 \neq p_2 \\ \bigcup_{p=1}^{n_g} \mathcal{V}_{(l),p} = \mathcal{C}_{(l)}. \end{aligned} \tag{26}$$

A portion of an example graph is illustrated in Fig. 3. Consider a bus that arrives at the depot twice, at t_0 and t_x. Charging nodes are red, and rest nodes are black. All of the charging nodes correspond to the same bus. Each row represents nodes with distinct duration values. Each charging node has exactly one incoming upward edge, or edge from a rest node to a charging node. Each charging node has exactly one leaving edge.

As seen in Fig. 3, the bus arrives at time t_1, and can begin charging at the time interval between t_1 and t_2. Note that before t_1, there are no charging nodes, so an EVPSE must be rest. From there, all of the EVPSEs allocated to be resting between t_0 and t_1 must flow to one of the subsequent nodes. When flow is conserved through the graph, the number of EVPSEs allocated at each time step remains consistent throughout the planning horizon. Because the number of EVPSEs is fixed, the flow formulation is a convenient way to express the problem.

Because each charging node has only one exiting edge, each upward edge $e \in \mathcal{U}_{(l)}$, forces subsequent edges to be taken; the flow along each edge in $\mathcal{D}_{(l)}$ can be calculated from the flow allocated to each edge in $\mathcal{U}_{(l)}$. As described in Section II, the battery damage depends on the energy deposited on a battery during a charging event, expressed as the DoD[4]. The battery degradation cost in (16) is a nonlinear function of DoD, so the cost assessed for charging during each node depends on the the total number of charging nodes in a charging event. This graph structure allows a single edge to convey all the information from each charging event, transforming the nonlinear function

[4]As described here, this would be the depth of charge, rather than DoD. However, to be consistent with existing terminology, the term DoD is used.

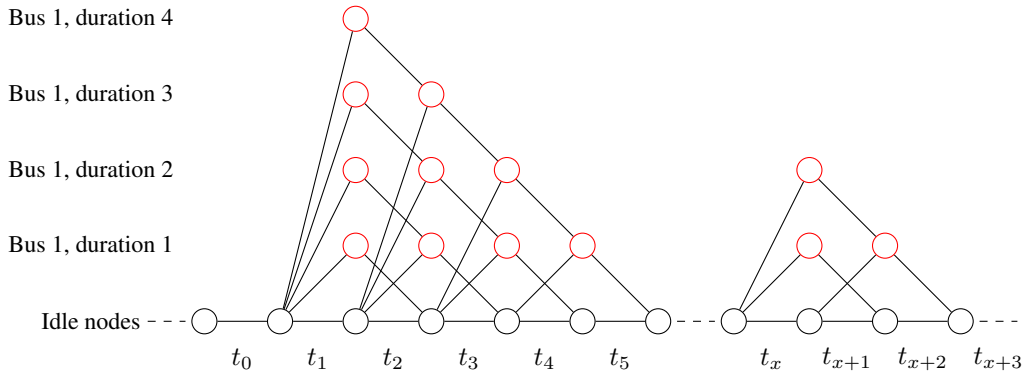

Fig. 3: Two subgraphs depicting a total of 13 charging nodes (red) together with the 11 neighboring rest nodes (black). Note that once a red vertex is selected, a charge is initiated and the rest of the edges through the subgraph, or group, are fixed. In this formulation, some nodes are redundant, but those are removed in Section V.

in (16) to a lookup table in the MILP implementation. A constraint included in Sections IV and VI prevents multiple charging events in a single stop.

To allow a charging event to continue through the beginning/end of a day, the graph is circular, reflecting the arbitrary definition of when a day ends. That is, all edges have at least one entry edge and at least one exit edge, and where appropriate, there exist edges between nodes at the end of the day and nodes at the beginning of the day. While the planning day could arbitrarily be chosen to start at any time, and a start time for the planning day must be selected for some constraints, the underlying network structure ignores that start time.

The graph structure seen in Fig. 3 introduces more edges and nodes than [15], which increases the complexity of the problem. Some simpler structures could be imagined that would reduce the cardinality of edges and nodes, for example, forcing all downward edges to lead directly to some time interval. This complexity can be addressed through one of two approaches. First, the network could be simplified first, with constraints and costs then developed on the simplified network. Alternatively, constraints and costs could be developed on the full graph with the resulting MILP subsequently simplified. Both approaches are fundamentally identical, and a simplification to the MILP is addressed in Section V. With that simplification, the MILP only selects upward or rest–rest edges

The graph structure presented here allows a simple yet powerful network that allows an accurate battery cycle count. Such a structure is required to accurately model physical realities, and can be passed into a MILP solver to select which edges are taken.

IV. Network Flow Bus Scheduling Formulation

This section defines the network search problem in terms of a MILP for only charger type 1. As described in Section III, the MILP assigns a flow value to each edge. An integer decision variable is introduced for each edge in the graph, denoted as $x_{(1)i}$ for $i \in \mathcal{I}_{(1)}$, with the value of $x_{(1)i}$ representing the number of chargers taking an edge; all the values $x_{(1)i}$ are gathered into the vector $\mathbf{x}_{(l)}$. The minimum value of $x_{(1)i}$ is 0, so letting $mathbf0_n$ represent a zero-vector of length n, we constrain

$$\mathbf{x}_{(1)} \geq \mathbf{0}_{n_{(1)e}}. \tag{27}$$

The balance of this section describes the constraints and costs on the graph search and how they can be implemented in a MILP. Section IV-A addresses conservation of flow constraints, ensuring that the correct number of EVPSE are allocated throughout the planning horizon; Section IV-B develops constraints to ensure that each bus is only charged at most once each time it stops at the depot. Section IV-C details constraints to the batteries' state of charge. Section IV-D then defines the objective function to be minimized in the MILP.

Throughout this section, many variables have a subscript (1), denoting correspondence to the first charger type. The subscript makes the adaptation to multiple charger types presented in Section VI more straightforward.

A. Conservation of Flow Constraint

All chargers at a time interval must be allocated at the subsequent time interval; constraints must be introduced to balance the flow through the network so that flow moves continuously from one vertex to another through the graph. All nodes must have the same outgoing flow as incoming flow. Further, the total flow at any moment in time must be exactly the number of chargers at the depot.

This balance of flow can be represented as a constraint using the incidence matrix. Recall that the edge directionality is encoded into the incidence matrix. Summing across row q of $D_{(1)}$ will give the number of edges originating at vertex $v_{(1)q}$ minus the number of edges ending at vertex $v_{(1)q}$. As $\mathbf{x}_{(1)}$ represents the charger assignment flow quantity along each edge in the graph representing the first charger type, $D_{(1)}\mathbf{x}_{(1)}$ is a column vector where each row i corresponds to the net flow out of vertex i.

The conservation of flow constraint with a single type of charger can be written as:

$$D_{(1)}\mathbf{x}_{(1)} = \mathbf{0}_{n_{(1)v}} \quad , \tag{28}$$

where $\mathbf{0}_n$ is a zero vector with n elements.

The conservation of flow constraint in (28) enforces the conservation of flow in all vertices, but it does not dictate the number of chargers available. Note that $\mathbf{x}_{(1)} = \mathbf{0}_{n_{(1)e}}$, where no EVPSE are allocated, is a trivial solution to (28). To fix the number of EVPSE, we introduce another constraint. Let a vector $d_{(1)}$ have a 1 corresponding to each edge flowing out of all nodes at any given time. Since $n_{(1)c}$ is constant for all time, the following relation must hold:

$$d_{(1)}\mathbf{x}_{(1)} = n_{(1)c}, \tag{29}$$

where $n_{(1)c}$ is the number of chargers of type 1. When (29) is combined with the conservation of flow constraint in (29), this ensures that $n_{(1)c}$ EVPSEs will be accounted for at every point in time.

B. Group Constraints

As mentioned previously, there should be a constraint that each bus only charge at most once each time it stops at the depot. Let a *visit* be all charging nodes corresponding to a given bus between when that bus arrives at the depot and its next departure, corresponding to the nodes in $\mathcal{V}_{(l)p}$. A constraint can be introduced to limit the aggregate inflow to the group, which limits the total number of charging events initiated during a visit by a bus to the depot. Given a constraint on the input flow, the balancing property of the network flow constraint will enforce that the output flow be constrained to the same value. This section develops that constraint.

For each vertex group, the index set of the edges leading into group p is defined as

$$\mathcal{I}_{(1)p} = \{i | e_{(1)i} \in \mathcal{E}_{(1)} \text{ where } e_{(1)i} = (v_m, v_n), \\ v_n \in \mathcal{V}_p, \text{ and } v_m \notin \mathcal{V}_p\}. \tag{30}$$

The constraint effectively limits the total number of upward edges leading into $\mathcal{V}_p$ to be at most 1. Let n_g be the number of groups, then the constraint can be expressed

$$\sum_{i \in \mathcal{I}_{(1)p}} x_{(1)i} \leq 1,\ p = 1, ..., n_g, \tag{31}$$

The definition of $\mathcal{I}_{(1)p}$ can be used to write the constraint in matrix form, with a row corresponding to each group. Allowing $a_{pn}^{(1)g}$ to be the entry of a matrix $A_{(1)g}$ in the p^{th} row and n^{th} column, the matrix $A_{(1)}$ for EVPSE type 1 can be expressed as:

$$A_{(1)} = \left[a_{pn}^{(1)}\right],\ a_{pi}^{(1)} = \begin{cases} 1 & i \in \mathcal{I}_{(1)p} \\ 0 & \text{otherwise} \end{cases} \tag{32}$$

Letting $\mathbf{1}_n$ represent a vector of length n with all entries being 1, the group constraint is then defined as:

$$A_{(1)}\mathbf{x}_{(1)} \leq \mathbf{1}_{n_g}. \tag{33}$$

C. Charging Constraints

Three constraints exist to limit SoC of the batteries. First, the SoC can never pass below a minimum value, soc_{min}. Second, the SoC can never pass above a maximum value, soc_{max}. Finally, the net energy deposited on the battery in a 24-hour window must equal or exceed the net energy drawn from the battery in the same window. Without the third constraint, the least-cost solution would discharge the bus batteries with no plan to recharge them. In this section, the SoC for each bus at every time during the planning horizon is expressed as a linear function of $\mathbf{x}_{(1)}$. In this section, the expressions constraining the SoC are developed for a single bus first, and then expanded to constrain all buses in a single expression.

First, consider a discharge vector $\mathbf{w}_j$ for each bus j, representing the energy drawn from the battery as a percentage of battery capacity from the beginning of the planning horizon. Let $w_{j,k}$ be the k^{th} element of $\mathbf{w}_j$, where k is the time index. The convention used here requires that each element in $\mathbf{w}_j$ is strictly non-positive as the bus discharges the battery to complete its route. Each element $w_{j,k}$ expresses the negative of energy drawn from bus battery j from the beginning of the planning horizon to time k, thus, the elements in $\mathbf{w}_j$ monotonically decrease.

To map the chosen edges to their effect on battery charge, we introduce a matrix $S_{(1)j}$. Each column of $S_{(1)j}$ corresponds to a an edge in $\mathcal{E}_{(1)}$, while each row of $S_{(1)j}$ corresponds to a time index, given as the number of time intervals since the reference time t_0. Using the notation $S_{(1)j} = [s_{(1)j,ki}]$ to denote the matrix such that the element of $S_{(1)j}$ in row k and column i is $s_{(1)j,ki}$

$$S_{(1)j} = [s_{(1)j,ki}]$$
$$s_{(1)j,ki} = \begin{cases} R_{(1)}\Delta_t & e_i \text{ leads to a charging vertex with bus } j \text{ and time } t_0 < k \\ 0 & \text{otherwise} \end{cases}. \tag{34}$$

The first row of $S_{(1)j}$ corresponds to t_0 where $k = 0$; since no edges lead to charging nodes before t_0, the first row is filled by 0. The last row corresponds to the end of the planning horizon, where $k = n_t$. Thus, $S_{(1)j}$ has $n_t + 1$ rows.

There is also a need to introduce a continuous slack variable corresponding to the SoC of bus j at t_0, noted here as y_j. Then, the vector of SoC for bus j at every time is given by the sum of the initial SoC, y_j; energy deposited on the bus, $S_{(1)j}\mathbf{x}_{(1)}$; and energy drawn from the bus $\mathbf{x}_{(1)}\mathbf{w}_j$. That sum is constrained to be between soc_{min} and soc_{max}:

$$\mathbf{1}_{n_t} soc_{min} \leq \mathbf{1}_{n_t} y_j + S_{(1)j}\mathbf{x}_{(1)} + \mathbf{w}_j \leq \mathbf{1}_{n_t} soc_{max}. \tag{35}$$

It is more convenient to express (35) as a single constraint for all buses. Most of the matrices and vectors defined in this section can be concatenated, where the j subscript is dropped to show the concatenation:

$$S_{(1)} = \begin{bmatrix} S_{(1)1} \\ S_{(1)2} \\ \vdots \\ S_{(1)n_b} \end{bmatrix}, \mathbf{w} = \begin{bmatrix} \mathbf{w}_1 \\ \mathbf{w}_2 \\ \vdots \\ \mathbf{w}_{n_b} \end{bmatrix}, \mathbf{y} = \begin{bmatrix} y_1 \\ y_2 \\ \vdots \\ y_{n_b} \end{bmatrix} \tag{36}$$

Before expressing the charging constraints for all buses as a single constraint, we define a matrix T that selects the

appropriate value of $\mathbf{y}$. Using similar notation as before to define each element of the matrix $T \in \mathbb{R}^{n_b n_t \times n_b}$, let

$$T = [t_{mn}],\ t_{mn} = \begin{cases} 1 & (n-1)n_t < m \leq (n)n_t \\ 0 & \text{otherwise} \end{cases}, \quad (37)$$

letting the indices m and n begin at 1. With the concatenated values defined in (36) and the selector matrix defined in (37), we concatenate the constraint in (35) for each bus, as

$$\mathbf{1}_{n_t n_b} soc_{min} \leq T\mathbf{y} + S_{(1)}\mathbf{x}_{(1)} + \mathbf{w} \leq \mathbf{1}_{n_t n_b} soc_{max}. \quad (38)$$

(38) addresses the first two constraints, on the maximum and minimum SoC at any point. As mentioned previously, there also must be a constraint that the net change in over the 24-hour planning horizon be non-negative. To enforce this constraint, the total energy deposited on bus j at time $k = n_t$ is compared with and total energy drawn from bus j at time $k = n_t$. For bus j, that constraint is expressed as

$$S_{(1)j,n_t}\mathbf{x}_{(1)} \geq -w_{j,n_t} \quad (39)$$

where $S_{(1)j,n_t}$ is the n_t^{th} row of $S_{(1)j}$. Further, let $S_{(1)[n_t]}$ and $\mathbf{w}_{[n_t]}$ be the concatenation of all $S_{(1)j,n_t}$ and w_{j,n_t}, respectively. Effectively, $S_{(1)[n_t]}$ and $\mathbf{w}_{[n_t]}$ represent every n_t^{th} row of $S_{(1)}$ and $\mathbf{w}$. The constraint in (39) can be expressed compactly for all buses by

$$S_{(1)[n_t]}\mathbf{x}_{(1)} \geq -\mathbf{w}_{[n_t]} \quad (40)$$

The SoC constraints can then be defined as:

$$\begin{aligned} \mathbf{s}_{min} \leq S_{(1)}\mathbf{x}_{(1)} \ + T\mathbf{y} \leq \mathbf{s}_{max} \\ -\mathbf{w}_{[n_t]} \leq S_{(1)[n_t]}\mathbf{x}_{(1)} \end{aligned} \quad (41)$$

D. Charging Cost

Recall that the variables of optimization at $\mathbf{x}_{(1)}$ and $\mathbf{y}$, which describe EVPSE allocation and bus SoC at the beginning of the planning horizon. There are two components to the operational cost for a bus fleet. For simplicity, both are treated separately and then summed.

First, the energy used to charge the batteries incurs a cost, which can be dependent on time. For edge $e_i \in \mathcal{E}_{(1)}$ with $e_i = (v_m, v_n)$, let $cost_i$ be the cost of energy (in \$/kW h) during time interval of the node v_n, with 0 if $v_n \in \mathcal{I}_{(1)}$. Further let $R_{(l)}$ again be the power level in C-rate of the charger for charger type l. B_{cap} is defined as battery capacity in kW h. Then we define the energy cost vector $\mathbf{c}_{(1)}$ element-wise on each edge as

$$c_{(1)i} = B_{cap}\Delta_t cost_i R_{(1)}, \quad (42)$$

where $c_{(1)i}$ is the i^{th} element of $\mathbf{c}_{(1)}$. Then $\mathbf{c}_{(1)}^T\mathbf{x}_{(\mathbf{1})}$ sums the energy cost for all selected charging nodes. Recall that Δ_t is the time interval represented by each nodes. There is no cost directly associated with the slack variable vector $\mathbf{y}$.

The other cost component is determined by battery degradation. As seen in Section II, we can model the battery damage of a charging event as a function of the DoD, which is fully defined when a charging event is initiated.

Given the constraint that $A_{(1)g}\mathbf{x}_{(1)} \leq \mathbf{1}_{n_g}$, only one upward edge is taken in each group. When at most a single upward edge is taken in each group, the optimization vector $\mathbf{x}_{(1)}$ selects which battery damage is included. We can define a battery cost matrix $C_{(1)b} \in \mathbb{R}^{n_b \times n_e}$ that maps the damage for the charging event initiated by each edge to a battery degradation cost, for charger type 1.

$$\begin{aligned} C_{(1)b} =& [c_{b,ji}],\ c_{b,ji} = f(e_i, j) \\ f(e_i, j) =& \begin{cases} bat_{d,i}(R_l\Delta_t w) & v_m \in \mathcal{I}_{(1)}, v_n \in \mathcal{C}_{(1)} \\ 0 & \text{Otherwise} \end{cases}, \\ & \text{where } e_i = (v_m, v_n), v_n \text{ has a duration } w, \\ & \text{and } v_n \text{ corresponds to bus } j \end{aligned} \quad (43)$$

where $bat_{d,i}(DoD)$ is defined in (16). The cost due to battery cycling for each bus can be expressed as

$$C_{(1)b}\mathbf{x}_{(1)}. \quad (44)$$

However, as described in Section II, the battery damage is the minimum of Q_{neg}, largely determined by battery cycling, and Q_{Li}, dominated by calendar aging. In the total daily battery cost $\mathbf{z}$, each element corresponds to the battery damage of each bus per day. Note that each element of $\mathbf{z}$ must be greater than or equal to the minimum battery degradation $bat_{d,min}$ and the cycling battery degradation, $C_{(1)b}\mathbf{x}_{(1)}$.

$$\begin{aligned} \mathbf{z} &\geq C_{(1)b}\mathbf{x}_{(1)} \\ \mathbf{z} &\geq bat_{d,min}\mathbf{1}_{n_b} \end{aligned} \quad (45)$$

Given the constraints defined in (43)–(45) and the energy cost vector defined in (45), we arrive at the full optimization problem, where B_{cost} is the battery cost. The total cost is given in dollars, and includes costs incurred by daily energy usage and the costs incurred each day due to battery degradation. Recall that the flow values are constrained to be integers.

$$\begin{aligned} \min_{\mathbf{x}_{(1)}} \ & \mathbf{c}_{(1)}^T\mathbf{x}_{(1)} + \mathbf{1}_{n_b}^T\mathbf{z}B_{cost} \\ \text{s.t. } & \mathbf{x}_{(1)} \in \mathbb{Z}^{n_{(1)e}} \\ & C_{(1)b}\mathbf{x}_{(1)} \leq \mathbf{z} \\ & bat_{d,Li} \leq \mathbf{z} \\ & \mathbf{x}_{(1)} \geq \mathbf{0}_{n_{(1)e}} \\ & D_{(1)}\mathbf{x}_{(1)} = \mathbf{0}_{n_{(1)v}} \\ & d_{(1)}\mathbf{x}_{(1)} = n_{(1)c} \\ & A_{(1)g}\mathbf{x}_{(1)} \leq \mathbf{1}_{n_g} \\ & S_{(1)}\mathbf{x}_{(1)} \ + T\mathbf{y} \geq \mathbf{s}_{min} \\ & S_{(1)}\mathbf{x}_{(1)} \ + T\mathbf{y} \leq \mathbf{s}_{max} \\ & S_{(1)[n_t]}\mathbf{x}_{(1)} \geq -\mathbf{w}_{[n_t]} \end{aligned} \quad (46)$$

V. Simplifying Formulation using Incidence Kernel

As discussed in Section III, a graph search could be conducted over a smaller, simpler graph. In this section, a linear transformation of the MILP is developed to the same effect. This section expresses $\mathbf{x}_{(1)}$ as the product of a matrix and a smaller vector, reducing the MILP search space.

Note that the conservation of flow constraint requires that $\mathbf{x}_{(1)} \in \mathcal{N}\left(D_{(1)}\right)$, where $\mathcal{N}(\cdot)$ is the kernel of a matrix. If there exists some matrix

$$N_{(1)} \in \mathbb{Z}^{\left(n_{(1)e}\right)\times\left(n_{(1)vc}+1\right)} \tag{47}$$

whose columns form a basis for the kernel of $D_{(1)}$, then the search space can be reduced by optimizing over a reduced search space $\mathbf{x}'_{(1)}$, where

$$\mathbf{x}_{(1)} = N_{(1)}\mathbf{x}'_{(1)}. \tag{48}$$

Thus, the optimization space is reduced and the constraint in (28) is removed. This section defines a satisfactory $N_{(1)}$ that preserves the integer constraints, and describes how $N_{(1)}$ simplifies the MILP. This section proves that such a definition of $N_{(1)}$ exists by describing an algorithm to generate it from the graph.

A definition of $N_{(1)}$ is required that will preserve the integer constraints of the problem, that is,

$$\mathbf{x}_{(1)} \in \mathbb{Z}^{n_{(1)e}} \iff \mathbf{x}'_{(1)} \in \mathbb{Z}^{n_{(1)vc}+1} \tag{49}$$

First, it is necessary to prove (47). As $\mathcal{G}_{(1)}$ is a connected graph, the rank of the incidence matrix $D_{(1)}$ is $n_{(1)v}-1$ [24], so the row space of $D_{(1)}$ is has dimension $n_{(1)v}-1$. The column space of $N_{(1)}$ is the orthogonal complement of the row space of $D_{(1)}$ in $\mathbb{R}^{n_{(1)e}}$, so the rank and number of columns in $N_{(1)}$ is $n_{(1)e}-(n_{(1)v}-1)$. Thus, there must be $n_{(1)e}-n_{(1)v}+1$ basis vectors for $\mathcal{N}\left(D_{(1)}\right)$.

The number of edges between rest nodes is n_t, and the number of rest nodes is also n_t. Define the number of charging nodes $n_{(1)vc}$ as

$$n_{(1)vc} = |\mathcal{C}_{(1)}| = |\mathcal{U}_{(1)}| = |\mathcal{D}_{(1)}|. \tag{50}$$

The total number of edges in the graph is the sum of the number of edges between rest nodes, the number of upward edges, and the number of downward edges.

$$\begin{aligned} |\mathcal{E}_{(1)}| &= n_t + |\mathcal{U}_{(1)}| + |\mathcal{D}_{(1)}| \\ n_{(1)e} &= n_t + 2n_{(1)vc}. \end{aligned} \tag{51}$$

The number of nodes $n_{(1)v}$ is the sum of the charging nodes and rest nodes; there are n_t rest nodes.

$$n_{(1)v} = n_t + n_{(1)vc} \tag{52}$$

The number of basis vectors is given by

$$\begin{aligned} n_{(1)e} - n_{(1)v} + 1 &= n_t + 2n_{(1)vc} - n_t - n_{(1)vc} + 1 \\ &= n_{(1)vc} + 1. \end{aligned} \tag{53}$$

Each basis vector represents a unique path through the network. Note that the meaning of (28) is a conservation of flow through the network; any selection of edges that conserves flow must exist in the kernel of the incidence matrix. Note that because the planning horizon is $24\,\mathrm{h}$, and each time interval is Δ_t hours, each path that conserves flow will take $24/\Delta_t$ edges.

To that end, we define the first basis vector $\mathbf{b}_{(1)0}$ for the kernel as the path that only flows through edges in $\mathcal{R}_{(1)}$. Flow is conserved, so such a vector is in the kernel. We define each subsequent basis vector $\mathbf{b}_{(1)q}$ to conserve flow and only select one edge in $\mathcal{C}_{(1)}$. Because conservation of flow is achieved through each of these basis vectors, each vector exists in the kernel of $D_{(1)}$.

Further, each edge in $\mathcal{C}_{(1)}$ is represented in only one basis vector, so the vectors are linearly independent. Finally, any integer path through the network that conserves flow is in the image of the basis vectors.

We can express $\mathbf{x}_{(1)}$ as

$$\mathbf{x}_{(1)} = \sum_{q=0}^{n_{(1)vc}} \alpha_q \mathbf{b}_{(1)q}, \tag{54}$$

where α_q are integer values. When

$$\mathbf{x}'_{(1)} = \begin{bmatrix} \alpha_0 & \alpha_1 & \alpha_2 & \dots & \alpha_{n_{(1)vc}} \end{bmatrix}^T \tag{55}$$

and

$$N_{(1)} = \begin{bmatrix} \mathbf{b}_{(1)0} & \mathbf{b}_{(1)0} & \mathbf{b}_{(1)1} & \dots & \mathbf{b}_{(1)n_{(1)vc}} \end{bmatrix}, \tag{56}$$

it is observed that (54) is equivalent to (48).

The relationship in (49) holds in this formulation. To prove

$$\mathbf{x}_{(1)} \in \mathbb{Z}^{n_{(1)e}} \implies \mathbf{x}'_{(1)} \in \mathbb{Z}^{n_{(1)vc}+1}, \tag{57}$$

note that the flow value along each upward edge in $\mathcal{U}_{(1)}$ is in $\mathbb{Z}$. That flow value is the product of the entry in $\mathbf{b}_{(1)q}$ and α_q that corresponds to the upward edge. Therefore,

$$\mathbf{x}_{(1)} \in \mathbb{Z}^{n_{(1)e}} \implies \forall q, 1\alpha_q \in \mathbb{Z} \implies \mathbf{x}'_{(1)} \in \mathbb{Z}^{n_{(1)vc}+1}. \tag{58}$$

Further,

$$\begin{aligned} N_{(1)} \in \mathbb{Z}^{\left(n_{(1)e}\right)\times\left(n_{(1)vc}+1\right)}, \mathbf{x}'_{(1)} \in \mathbb{Z}^{n_{(1)vc}+1} \\ \implies N_{(1)}\mathbf{x}'_{(1)} \in \mathbb{Z}^{n_{(1)e}}. \end{aligned} \tag{59}$$

Thus, the matrix $N_{(1)}$ developed here is apt for the MILP space-reduction algorithm.

Besides the integer constraints already discussed, the constraint (27) ensures that flow through the graph is non-negative; such an assumption is default in many MILP solvers. An equivalent formulation is required for the MILP space-reduction algorithm. Because each basis vector allocates one charger at each time along the planning horizon,

$$\sum_{i=0}^{n_{(1)vc}} \alpha_i = n_{(1)c}, \tag{60}$$

as there are be $n_{(1)c}$ charger assignments at any point throughout the day. We define the number of charging events of the first charger type $n_{(1)events}$ as the number of upward edges, or

$$\sum_{i=1}^{n_{vc}} \alpha_i = n_{(1)events} \tag{61}$$

From (60) and (61) it is observed that

$$\alpha_0 = n_{(1)c} - n_{(1)events}. \tag{62}$$

In many scenarios, each EVPSE is used at least once each planning horizon, otherwise, the infrastructure is overbuilt. Note that when each bus charges at least once and there are more buses than EVPSEs, $\alpha_0 \leq 0$. However, each bus is not

guaranteed to charge at least once with each EVPSE type, so there is no general upper or lower limit on α_0. Nevertheless, positive flow through all charging edges in $\mathcal{C}_{(1)}$ is guaranteed by

$$\alpha_i \geq 0, \quad \forall i > 0. \tag{63}$$

However, all rest edges must also be constrained to be non-negative. Let $N'_{(1)}$ be the rows of $N_{(1)}$ corresponding to rest edges. Then, the constraint

$$N'_{(1)}\mathbf{x}'_{(1)} \geq \mathbf{0}_{n_t} \tag{64}$$

ensures that all rest edges are also non-negative.

With this formulation, the optimization space is reduced by roughly a factor of two, the lower bound constraint on the variable of optimization applies to roughly half as many variables, and the conservation of flow equality constraint with $n_{(1)v}$ rows is replaced by an inequality constraint with only n_t rows.

The implemented optimization is then given as:

$$\begin{aligned}
\min_{\mathbf{x}'_{(1)}} \ & \mathbf{c}_{(1)}^T N_{(1)}\mathbf{x}'_{(1)} + \mathbf{1}_{n_b}^T \mathbf{z} B_{cost} \\
\text{s.t. } & \mathbf{x}'_{(1)} \in \mathbb{Z}^{n_{(1)vc}+1} \\
& C_{(1)b}N_{(1)}\mathbf{x}'_{(1)} \leq \mathbf{z} \\
& bat_d \leq \mathbf{z} \\
& \mathbf{x}'_{(1)} \geq \mathbf{0}_{n_{(1)vc}+1} \\
& N'_{(1)}\mathbf{x}'_{(1)} \geq \mathbf{0}_{n_t} \\
& d_{(1)}N_{(1)}\mathbf{x}'_{(1)} = n_{(1)c} \\
& A_{(1)g}N_{(1)}\mathbf{x}'_{(1)} \leq \mathbf{1}_{n_g} \\
& S_{(1)}N_{(1)}\mathbf{x}'_{(1)} + T\mathbf{y} \geq \mathbf{s}_{min} \\
& S_{(1)}N_{(1)}\mathbf{x}'_{(1)} + T\mathbf{y} \leq \mathbf{s}_{max} \\
& S_{(1)[n_t]}N_{(1)}\mathbf{x}'_{(1)} \geq -\mathbf{w}_{[n_t]}
\end{aligned} \tag{65}$$

VI. Extensions for Multiple Charger Types

Multiple types of EVPSE, such as Level 2 chargers and DC fast chargers, are typically available to a fleet of BEBs. When available, the least-cost charging solution would likely employ a combination of all available charger types. Thus, the program presented in Section IV is expanded to include multiple charger types. In Section IV, the variables of optimization were defined as $\mathbf{x}_{(1)}$ and $\mathbf{y}$; we introduce $\mathbf{x}_{(2)}$ representing edges taken corresponding to the second charger type. As noted in Section V, we can express $\mathbf{x}_{(l)}$ as $N_{(l)}\mathbf{x}'_{(l)}$. This approach is then easily extended to an arbitrary number of charger types.

For each charger type, the network is extended by generating another graph, as in Section III-B, creating a nearly identical graph. There are no interconnections between the graphs corresponding to different charger types.

The search through both graphs and their mapping to a MILP is a simple expansion of the single-charger-type problem. Subsequent sections detail the requisite modifications for each constraint. In those sections, a subscript (l) indicates a matrix, vector, or scalar corresponding to the charger type l, otherwise defined as in Section IV. The structure of this section reflects that of Section IV.

A. Conservation of Flow Constraint

As noted in Section V, by expressing $\mathbf{x}_{(l)}$ as $N_{(l)}\mathbf{x}'_{(l)}$, we force the conservation of flow constraint to be met. No further consideration is needed to ensure conservation of flow. To ensure the correct number of chargers, we simply apply the constraint for all charger types:

$$d_{(l)}N_{(l)}\mathbf{x}'_{(l)} = n_{(l)c} \forall l. \tag{66}$$

B. Group Constraints

The group constraints ensure that a single bus charges at most once each time it stops at the depot, by limiting the total number of upward edges to one per group. While that charging event can occur at any power level, ensuring that only one charging event is initiated per stop also ensure at most one charger is assigned to each bus at a time.

All types of chargers count towards the group constraint, or a bus charging at one time precludes that same bus charging during the same stop at a different power level. Thus, the constraints are summed across power levels, as in

$$\sum_l A_{(l)g}N_{(l)}\mathbf{x}'_{(l)} \leq \mathbf{1}_{n_g}. \tag{67}$$

Again, this constraint can be logically expanded to an arbitrary number of charger types.

C. Charging Constraints

The SoC at any time is constrained to be greater than $0\,\%$ and less than $100\,\%$. The matrix $S_{(1)}$ as used in (46) includes charge contributed only by the first type of charger; charge added from each type of charger is summed. Including the effects of the second type of charger affects the battery charge, but not the limits; the batteries can still only have SoC on the range $[0, 1]$. Thus, the multi-charger analogue to the inequality introduced in (41) is given as

$$\begin{aligned}
\mathbf{s}_{min} \leq \sum_l \left(S_{(l)}N_{(l)}\mathbf{x}'_{(l)} \right) + T\mathbf{y} \leq \mathbf{s}_{max} \\
-\mathbf{w}_{[n_t]} \leq \sum_l S_{(l)[n_t]}N_{(l)}\mathbf{x}_{(l)}
\end{aligned} \tag{68}$$

Again, the constraint can be easily expanded to an arbitrary number of charger types.

D. Charging Cost

Consider the cost described in Section IV-D, with two principle components. First, $\mathbf{c}_{(1)}$ expresses the cost of energy throughout the day; the concept is easily extended to the multiple charging types by using the appropriate $R_{(l)}$.

Consider now the battery degradation cost. In Section IV-D, the matrix $C_{(1)b}$ is introduced. Here, with multiple types of chargers, the matrix $C_{(2)b}$ is defined as in Section IV-D, but with the appropriate charging rate. Due to the group constraint, each element of $\mathbf{z}$ is defined only by either $C_{(1)b}\mathbf{x}_{(1)}$ or $C_{(2)b}\mathbf{x}_{(2)}$. Again, this cost is easily extended to an arbitrary

number of charger types. Then the battery cost vector is defined as

$$\begin{aligned} \mathbf{z} &\geq \sum_l C_{(l)b} N_{(l)} \mathbf{x}'_{(l)} \\ \mathbf{z} &\geq bat_{d,min} \end{aligned} . \tag{69}$$

This leads to the cost

$$\sum_l \mathbf{c}_{(l)}^T N_{(l)} \mathbf{x}_{(l)} + \mathbf{1}_{n_b}^T \mathbf{z} B_{cost} \tag{70}$$

VII. Example

An example is now presented to illustrate the improvement of the present optimization scheme relative to a baseline solution. Three different bus sizes are used with both the naive approach and the BHC approach. First, a description of the station scenario is presented. The results from both the baseline and the BHC strategies are then compared for various bus battery sizes.

A. Battery Electric Bus Station Scenario

The bus station is required to charge 14 BEBs using a combination of slow and fast battery chargers. The battery packs are assumed to degrade according to the model in [18], with some experimentally-determined values for a $75\,\mathrm{A\,h}$ Kokam NMC cell. End of first life is assumed to be at $60\,\mathrm{A\,h}$. While aging characteristics vary among different cells, the model can be adapted to other cell chemistries and sizes by modifying the values in Table IV. Those values and the model presented in Section II yield

$$bat_{d,Li} = 2.08 \times 10^{-4} \tag{71}$$

TABLE IV: Experimentally-determined lithium reference battery parameters given in [18]

Parameter	Value	Parameter	Value
$d_{0,ref}$	0.46 A h	$b_{0,ref}$	1.07
$b_{1,ref}$	3.503e-3 day$^{-0.5}$	$b_{3,ref}$	2.805e-2
$c_{0,ref}$	75.64 A h	$c_{2,ref}$	3.9193e-3
β_{c2}	4.54		

Planning occurs on 10-minute intervals over a 24-hour period. Slow, low-cost charging can take several hours while fast, high-cost charging can be a fraction of an hour [4]. The EVPSE configuration is given in Table V. In this example, there are 5 fast chargers and 14 slow chargers, one slow charger for each bus. While each fleet could have a unique battery size and EVPSE power levels, the battery size assumed here are roughly in line with existing literature [14], [25] and the power levels are roughly in line with existing BEB technology [4]. The time-of-use energy cost is reflected directly in $\mathbf{c}_{(1)}$ and $\mathbf{c}_{(2)}$. In this scenario, the slow EVPSE are only available during the night break, when the buses return to a depot. Conversely, the fast EVPSE are only available during the day, between the first route and last route of the day. The planning horizon runs from midnight one day to midnight the next day, although the circular graph structure allows a charging event to wrap from the end of the planning horizon to the beginning.

TABLE V: EVPSE Configuration

Type	Power Level	Quantity
Type 1	240 kW	5
Type 2	20 kW	14

The bus schedules are taken from Utah Transit Authority (UTA) bus schedules. Of the given 15 routes, the 7 most easily electrified are considered, i.e., those with the lowest bound on drive time away from the depot. Those 7 routes are expanded to 14 by duplicating the original schedules and offsetting the time by 1 hour. The energy cost throughout the day is time-dependent.

The three scenarios use large batteries of $240\,\mathrm{kW\,h}$, mid-sized batteries of $180\,\mathrm{kW\,h}$, and small batteries of $120\,\mathrm{kW\,h}$. All three scenarios, which use the same bus schedules, will be based on very similar graphs and have similar costs. However, the different battery sizes will affect charging limit, maximum charging time, and battery degradation costs.

In all cases, the optimization is performed using the Gurobi MILP solver [26] on a machine running a Intel(R) Core(TM) i5-6200U CPU at $2.4\,\mathrm{GHz}$ with $12\,\mathrm{GB}$ of RAM, with the optimality gap cooinvergence set to $0.1\,\%$, and maximum optimization runtime of $300\,\mathrm{s}$.

For all three battery sizes, two different optimizations are performed, to measure the effects of including battery health in the optimization. First, a baseline solution using the objective function

$$\min \ \mathbf{c}_1^T N_{(1)} \mathbf{x}'_{(1)} + \mathbf{c}_2^T N_{(2)} \mathbf{x}'_{(2)} \tag{72}$$

is calculated. This approach neglects the battery degradation cost. The value for $\mathbf{z}$ is then minimized according to the constraints in (69), and the full cost is calculated. Second, the battery-health conscious (BHC) solution using the full cost described in (70) is calculated.

The two different objective functions and three different battery sizes create 6 scenarios for each set of assumptions. Additionally, each optimization was also performed without the optimization space reduction in Section V, to assess the performance improvement provided by the simplified formulation. The number of nodes, edges, continuous variables, and reduced integer variables for all three battery sizes are given in Table VI. Recall that without the speed improvement described in Section V, the number of integer variables is the number of edges. Note that, in line with (25), a larger battery size allows nodes with a higher duration value, resulting in moderate increases in the number of nodes and edges.

TABLE VI: Network Search Space Sizes

Battery Size	Nodes	Edges	Continuous Variables	Reduced Integer Variables
240 kW h	18 769	37 250	28	18 483
180 kW h	18 615	36 942	28	18 392
120 kW h	17 012	33 736	28	16 726

B. Example Results, Assumption Set 1

The first set of assumptions are listed in Table VII, with the assumed electricity rate table Table VIII

TABLE VII: Assumption Set 1

Assumption	Value
Power use while away from depot	30 kW
Battery cost per kW h	$150

TABLE VIII: Electricity Rate Structure 1

Beginning Time	End Time	Cost per kW h
12:00 AM	10:00 AM	$0.05
10:00 AM	4:00 PM	$0.08
4:00 PM	12:00 AM	$0.05

The baseline solution, where the battery health is neglected, favors using more of the battery capacity to charge at low-cost times. However, this incurs greater battery damage. Each component of the cost is detailed in Table IX, which are summarized visually in Fig. 4.

TABLE IX: Optimization Performance for Assumption Set 1

Approach, Battery Size	Battery Cost	Energy Cost	Total Cost	Runtime (Reduced/Full)
BHC, 240 kW h	$104.72	$217.33	$322.06	10.9 s / 25.1 s
Naive, 240 kW h	$104.72	$217.33	$322.06	11.2 s / 37.8 s
BHC, 180 kW h	$78.55	$217.33	$295.88	10.4 s / 36.9 s
Naive, 180 kW h	$81.69	$217.33	$299.03	10.9 s / 23.7 s
BHC, 120 kW h	$53.41	$224.53	$277.94	12.7 s / 300 s
Naive, 120 kW h	$106.89	$218.53	$325.42	10.2 s / 31.7 s

Note that in one case, the optimization without the search space reduction algorithm from Section V failed to converge within the time limit. In that case, the optimality gap was 0.52 %.

As seen in Table IX, the cost savings for using a BHC approach varies from 0 % to 14.6 %. Several observations merit further discussion. First, there is generally some cost saving for considering battery health, that effect is more pronounced with smaller batteries and more pronounced with larger batteries. The larger battery packs are more expensive, but the degradation in large battery packs is less likely to be dominated by cycling. In fact, with the largest battery size, the effect of cycling degradation is so minimal that including it in the optimization has no effect. Second, without the BHC approach, the small batteries are actually the most expensive; while the upfront cost is low the smaller batteries are cycled excessively and degrade quickly. However, if the batteries are charged with the BHC approach, the smallest battery size becomes the most cost-effective. Finally, using the simplification algorithm discussed in Section V improves the optimization time by at least 54 %.

C. Example Results, Assumption Set 2

The first set of assumptions are listed in Table X, with the assumed electricity rate table Table XI. This assumes more energy-consuming buses, maybe traveling at a higher speed or with a heavier load than the buses in Section VII-B. The energy rate is also flatter, with a lower peak cost per kW h and a longer on-peak time than in Section VII-B. Finally, the assumed cost of battery replacement is increased.

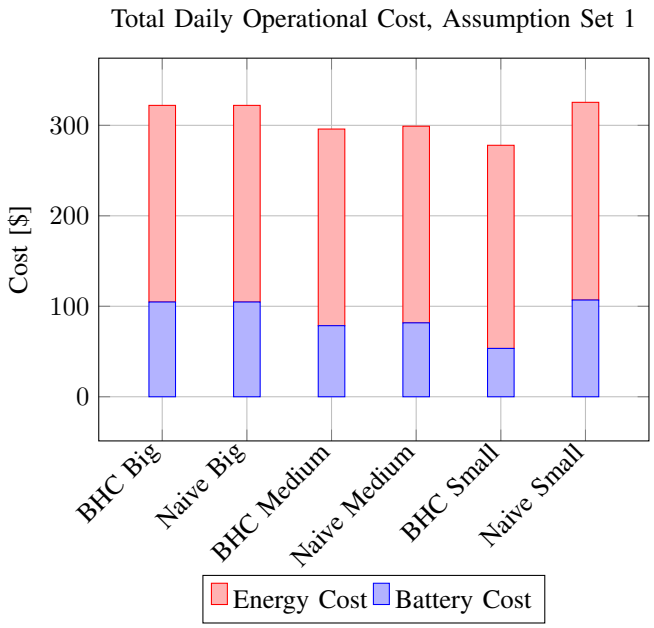

Fig. 4: Operational cost for the naive approach and BHC approach for three battery sizes for assumption set 1. Recall that "big" refers to a 240 kW h battery pack, "medium" refers to a 180 kW h battery pack, and "small" refers to a 120 kW h battery pack.

TABLE X: Assumption Set 2

Assumption	Value
Power use while away from depot	45 kW
Battery cost per kW h	$180

TABLE XI: Electricity Rate Structure 2

Beginning Time	End Time	Cost per kW h
12:00 AM	5:00 AM	$0.05
5:00 AM	6:00 PM	$0.06
6:00 PM	12:00 AM	$0.05

As with the first set of assumptions, the baseline solution favors using more of the battery capacity to charge at low-cost times, even when that approach may increase battery degradation. Each component of the cost is detailed in Table XII, which are summarized visually in Fig. 5.

Note that in two cases without the search space reduction algorithm, the optimization timed out before an optimality gap of 0.1 % was reached; in those cases, the optimality gap was between 0.21 percent and 0.25 %.

As seen in Table XII, the cost savings for using a BHC approach varies from less than 6 % to 14.7 %. Several observations merit further consideration. Interestingly, the optimized

TABLE XII: Optimization Performance for Assumption Set 2

Approach, Battery Size	Battery Cost	Energy Cost	Total Cost	Runtime (Reduced/Full)
BHC, 240 kW h	$116.69	$321.97	$438.66	9.48 s / 32.5 s
Naive, 240 kW h	$116.69	$321.97	$438.66	9.87 s / 52.9 s
BHC, 180 kW h	$87.52	$323.83	$411.35	11.6 s / 300 s
Naive, 180 kW h	$106.74	$321.97	$428.70	10.1 s / 34.4 s
BHC, 120 kW h	$109.15	$331.23	$440.39	11.8 s / 300 s
Naive, 120 kW h	$189.27	$327.23	$516.51	9.23 s / 95 s

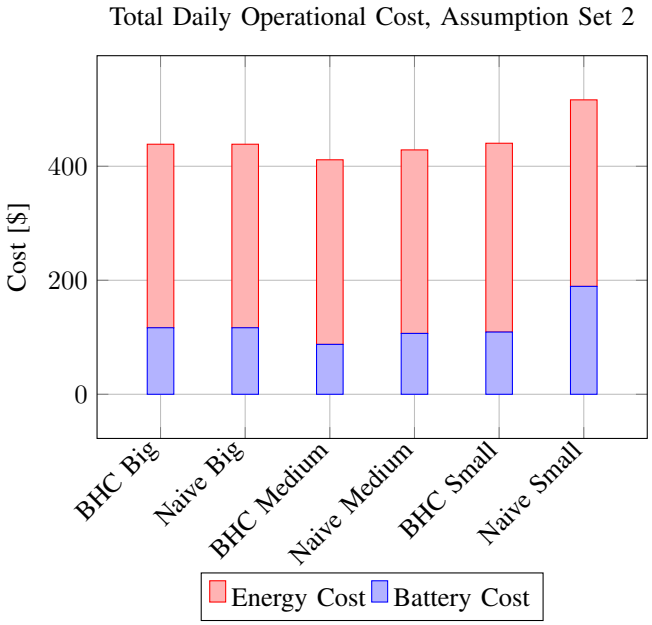

Fig. 5: Operational cost for the naive approach and BHC approach for three battery sizes with assumption set 2. Recall that "big" refers to a 240 kW h battery pack, "medium" refers to a 180 kW h battery pack, and "small" refers to a 120 kW h battery pack.

BHC cost is nearly the same for all battery sizes considered, as energy costs tend to increase when battery degradation costs decrease. As before, the baseline scenario with the smallest battery size is the most expensive; not only are the batteries degraded quickly through excessive cycling, but the smallest battery size forces charging at on-peak times. The large battery size had no cost difference when considering battery health; the batteries are likely large enough to avoid significant cycling degradation. Finally, note that the simplified formula with the incidence matrix kernel reduced computational time by at least 71 %.

VIII. Conclusion

This work develops a scheduling framework to balance the use of slow and fast chargers assuming the bus routes and EVPSE configuration are fixed. A circular graph was used to model the available charge times and possible charging durations for buses that routinely visit a station for charging. The incidence matrix of the DAG was used to formulate a network flow constraint; group constraints were used to enforce the natural progression of the bus through the station at each visit. The graph structure is circular, reflecting the repetition of bus schedules and accurately measuring number of discrete charging events, even when a single charging event crosses beyond the 24-hour planning horizon.

An example is presented that demonstrated the the ability of the MILP formulation to utilize slow chargers when possible and fast chargers when needed to accommodate timing constraints and ensure a sufficient charge for route execution. Further, the optimization formulation presented here allows the sum of the daily energy cost and the daily amortized battery replacement cost to be accurately minimized.

The results suggest that frequent, slow, shallow DoD charging events may result in a lower total cost, even when such an approach necessitates charging during on-peak times. While such a generalization may not always hold, this work suggests that a BHC optimization provides greater insights and savings opportunities than a naive approach, which does not consider the cost of battery degradation. Further, this work demonstrates that such a consideration is possible and effective.

One other use of this approach is to estimate the total cost of various battery sizes for an electrified bus fleet. As seen in the example, a smaller battery requires higher energy costs, but incurs a smaller battery degradation cost, while a larger battery requires a lower energy costs but higher batter degradation cost. The approach presented here is a powerful framework to optimize and compare energy and battery costs and energy costs for an entire electric vehicle fleet.

Acknowledgment

This material is based in part upon work supported by the National Science Foundation through the ASPIRE Engineering Research Center under Grant No. EEC-1941524.

References

[1] G. De Filippo, V. Marano, and R. Sioshansi, "Simulation of an electric transportation system at The Ohio State University," *Applied Energy*, vol. 113, pp. 1686–1691, 2014.

[2] M. Xylia and S. Silveira, "The role of charging technologies in upscaling the use of electric buses in public transport: Experiences from demonstration projects," *Transportation Research Part A: Policy and Practice*, vol. 118, pp. 399–415, 2018.

[3] U. Guida and A. Abdulah, "ZeEUS eBus Report #2 - An updated overview of electric buses in Europe," International Association of Public Transport (UITP), Tech. Rep. 2, 2017. [Online]. Available: http://zeeus.eu/uploads/publications/documents/zeeus-ebus-report-2.pdf

[4] J.-Q. Li, "Battery-electric transit bus developments and operations: A review," *International Journal of Sustainable Transportation*, vol. 10, no. 3, pp. 157–169, 2016. [Online]. Available: https://doi.org/10.1080/15568318.2013.872737

[5] N. Lutsey and M. Nicholas, "Update on electric vehicle costs in the United States through 2030," *The International Council on Clean Transportation*, vol. 2, 04 2019.

[6] X. Hu, C. Zou, X. Tang, T. Liu, and L. Hu, "Cost-optimal energy management of hybrid electric vehicles using fuel cell/battery health-aware predictive control," *IEEE Transactions on Power Electronics*, vol. 35, no. 1, pp. 382–392, Jan 2020.

[7] J. V. Barreras, C. Pinto, R. de Castro, E. Schaltz, S. J. Andreasen, P. O. Rasmussen, and R. E. Araújo, "Evaluation of a novel bev concept based on fixed and swappable li-ion battery packs," *IEEE Transactions on Industry Applications*, vol. 52, no. 6, pp. 5073–5085, Nov 2016.

[8] A. Hoke, A. Brissette, K. Smith, A. Pratt, and D. Maksimovic, "Accounting for lithium-ion battery degradation in electric vehicle charging optimization," *IEEE Journal of Emerging and Selected Topics in Power Electronics*, vol. 2, no. 3, pp. 691–700, 2014.

[9] Y. Zhou, X. C. Liu, R. Wei, and A. Golub, "Bi-objective optimization for battery electric bus deployment considering cost and environmental equity," *IEEE Transactions on Intelligent Transportation Systems*, vol. 22, no. 4, pp. 2487–2497, 2020.

[10] R. Wei, X. Liu, Y. Ou, and S. K. Fayyaz, "Optimizing the spatio-temporal deployment of battery electric bus system," *Journal of Transport Geography*, vol. 68, pp. 160–168, 2018.

[11] M. T. Sebastiani, R. Lüders, and K. V. O. Fonseca, "Evaluating electric bus operation for a real-world BRT public transportation using simulation optimization," *IEEE Transactions on Intelligent Transportation Systems*, vol. 17, no. 10, pp. 2777–2786, 2016.

[12] Y. Wang, Y. Huang, J. Xu, and N. Barclay, "Optimal recharging scheduling for urban electric buses: A case study in Davis," *Transportation Research Part E: Logistics and Transportation Review*, vol. 100, pp. 115–132, 2017. [Online]. Available: https://www.sciencedirect.com/science/article/pii/S1366554516305725

[13] H. Ambrose, N. Pappas, and A. Kendall, "Exploring the costs of electrification for california's transit agencies," *ITS Reports, 2017(03)*, vol. 03, Oct 2017.

[14] J. Lee, H. Shon, I. Papakonstantinou, and S. Son, "Optimal fleet, battery, and charging infrastructure planning for reliable electric bus operations," *Transportation Research Part D: Transport and Environment*, vol. 100, p. 103066, 2021. [Online]. Available: https://www.sciencedirect.com/science/article/pii/S1361920921003631

[15] J. Whitaker, G. Droge, M. Hansen, D. Mortensen, and J. Gunther, "A network flow approach to battery electric bus scheduling," *IEEE Trans. Intell. Transp. Syst.*, pp. 1–12, 2023.

[16] M. Rasheed, M. Kamel, H. Wang, R. Zane, and K. Smith, "Investigation of active life balancing to recondition li-ion battery packs for 2nd life," in *2020 IEEE 21st Workshop on Control and Modeling for Power Electronics (COMPEL)*, Nov 2020, pp. 1–7.

[17] M. Lu, X. Zhang, J. Ji, X. Xu, and Y. Zhang, "Research progress on power battery cooling technology for electric vehicles," *Journal of Energy Storage*, vol. 27, p. 101155, 2020. [Online]. Available: https://www.sciencedirect.com/science/article/pii/S2352152X19311193

[18] K. Smith, A. Saxon, M. Keyser, B. Lundstrom, Z. Cao, and A. Roc, "Life prediction model for grid-connected li-ion battery energy storage system," in *2017 American Control Conference (ACC)*, 2017, pp. 4062–4068.

[19] X. Chen, W. Shen, T. T. Vo, Z. Cao, and A. Kapoor, "An overview of lithium-ion batteries for electric vehicles," in *2012 10th International Power & Energy Conference (IPEC)*, Dec 2012, pp. 230–235.

[20] S. Manzetti and F. Mariasiu, "Electric vehicle battery technologies: From present state to future systems," *Renewable and Sustainable Energy Reviews*, vol. 51, pp. 1004–1012, 2015. [Online]. Available: https://www.sciencedirect.com/science/article/pii/S1364032115006577

[21] A. Fotouhi, D. J. Auger, K. Propp, S. Longo, and M. Wild, "A review on electric vehicle battery modelling: From lithium-ion toward lithium–sulphur," *Renewable and Sustainable Energy Reviews*, vol. 56, pp. 1008–1021, 2016. [Online]. Available: https://www.sciencedirect.com/science/article/pii/S1364032115013921

[22] R. Burkard, M. Dell'Amico, and S. Martello, *Assignment problems: revised reprint*. SIAM, 2012.

[23] D.-S. Chen, R. G. Batson, and Y. Dang, *Applied integer programming*. Wiley, 2010.

[24] M. Mesbahi and M. Egerstedt, *Graph Theoretic Methods in Multiagent Networks*. Princeton Univ Pr, 2010.

[25] N. A. El-Taweel, H. E. Z. Farag, and M. Mohamed, "Integrated utility-transit model for optimal configuration of battery electric bus systems," *IEEE Systems Journal*, vol. 14, no. 1, pp. 738–748, March 2020.

[26] Gurobi Optimization, LLC, "Gurobi Optimizer Reference Manual," 2021. [Online]. Available: https://www.gurobi.com

CHAPTER 4

CURRENT HARMONICS DEAD TIME DESIGN METHOD TO ACHIEVE ZVS WITH NON-LINEAR OUTPUT CAPACITANCE

This chapter is a replication of a paper presented at the 2021 IEEE Energy Conversion Congress and Expo (ECCE). In this replication, some minor edits are included to some equations. A slight modification is made to (10) and (11) to improve readability. An error appeared in (7) in the original, which did not propagate through to subsequent equations. That error has been corrected here.

Current Harmonics Dead Time Design Method to Achieve ZVS with Non-Linear Output Capacitance

Matthew Hansen
ECE Department
Utah State University
Logan, Utah, USA
matthew.hansen@usu.edu

Abhilash Kamineni
ECE Department
Utah State University
Logan, Utah, USA
abhilash.kamineni@usu.edu

Regan Zane
ECE Department
Utah State University
Logan, Utah, USA
regan.zane@usu.edu

***Abstract*—A novel current harmonic dead time design method is presented to guarantee zero-volt switching (ZVS) of a resonant LCCL network, regardless of loading condition, accounting for non-linear characteristics of the parasitic output capacitance. Dead time voltage modeling is omitted; an upper bound on necessary dead time to achieve ZVS is instead developed with a charge-based approach to modeling parasitic capacitance. The harmonic dead time design method is shown to conservatively estimate the necessary dead time, using only the harmonics created by all full-bridge inverters. The calculated dead time criterion is shown to be conservative for many loading conditions. Considerations are made for a mistuned systems and parasitic effects. Simulation validation of the design method is presented. A full hardware test also demonstrates the validity of the design technique. The harmonic design method can be applied to nearly any LCCL resonant converter designs to guarantee ZVS at all load conditions.**

***Index Terms*—wireless power transfer, resonant converter, soft switching, ZVS, output capacitance, parasitic capacitance, non-linear capacitance, harmonics, dead time, dead time design**

I. Introduction

Significant research has been completed on WPT systems, which generally use a resonant topology to maximize power transfer across an air gap, sometimes used in transportation electrification [1]–[5]. Advances have been made with more exotic architectures to achieve better control and lower losses [6]. Regardless of the architecture, for some applications, including WPT, the secondary side can be unknown or time-varying, leading to time-varying varying loading conditions seen by the primary.

Zero-volt switching (ZVS) is used to reduce switching losses in a full- or half-bridge inverter. In ZVS, a dead-time current discharges the parasitic output capacitance before the MOSFET begins to conduct. Work has been done to determine limits of ZVS, considering, modeling, and measuring the non-linearity of the MOSFET output capacitances [7]–[9]. Commonly, the compensation network is mistuned to be slightly inductive at the switching frequency. When this is the case, with sufficient dead time, the MOSFETs in the h-bridge leg will soft switch. Critically, however, the necessary dead time is load-dependent: when the load decreases, a longer dead time is needed to discharge the parasitic capacitance. When transferring power to a moving secondary, the load seen by a given primary system varies with time, resulting in similarly time-varying dead time requirements. Moreover, mistuning the compensation network decreases the power factor. Previous work has already analyzed several approaches to achieving ZVS with harmonics [10]–[12]. Beyond that, a large body of work exists on minimizing and modeling losses in resonant converters [13]–[15].

This research was supported in part by the ASPIRE (Advancing Sustainability through Powered Infrastructure for Roadway Electrification) Center, an NSF ERC, under award number 1941524.

In the proposed ZVS design, the compensation network of the resonant converter is not necessarily mistuned; the impedance at the switching frequency f_S must only be strictly non-capacitive. Instead, the third and higher harmonics are used to achieve ZVS on the bridge leg. With many topologies, when the compensation network is tuned for the switching frequency, the network is guaranteed to be inductive at the third harmonic and higher harmonics. The LCC compensation used here is one such topology. Thus, provided the magnitude of the compensation network impedance at the third and higher harmonics is sufficiently low, those higher harmonics are sufficient to soft-switch the H-bridge. Beyond the fundamental, the subsequent current harmonics are load-independent, and the inverter may soft switch regardless of the load.

The approach presented here uses LCC-compensated topology on the primary side, but no assumption is made on secondary topology. This approach is general to both WPT and DC/AC converters. In a dynamic system, including roadway–vehicle WPT, the secondary compensation network may differ in different instances. Secondary compensation network design, primary controller design, and secondary controller design are left to other research. This paper only discusses how a primary compensation network and fixed dead time may be designed to achieve ZVS, modeling the secondary as a reflected resistance on the primary. Any secondary design is thus applicable, and the approach may be modified trivially for a variety of primary topologies. In short, this paper uses harmonics to implement a charge-based approach to ZVS. Although the voltage waveforms during dead time are not directly calculable, this dead-time design method calculates an upper limit on the dead time necessary to achieve ZVS.

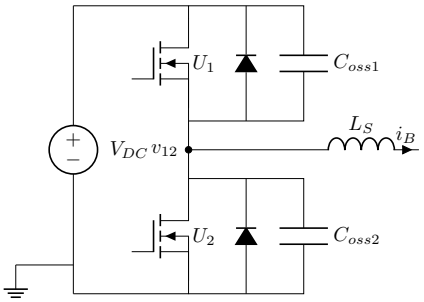

Fig. 1. Model of a half bridge. Note the body diode and output capacitance in parallel with each switch. The switch node voltage v_{12} is referenced relative to the source terminal of the low-side switch U_2

II. Background

A small-signal dead-time analysis of the switching transition can be modeled by removing the V_{DC} source and non-conducting elements (switches and diodes) seen in Figs. 1 and 3. With the DC voltage removed, the effective capacitance can be observed to be C_{oss}. The small-signal model contains three groups in series: 1) U_1 and U_2 in parallel, 2) The primary network, and 3) the parallel combination of U_3 and U_4. The effective parasitic capacitance C_{oss}, which acts with the primary network, is shown in (1). When all output capacitances are equal, $C_{oss} = C_{oss1} = C_{oss2}$....

$$\frac{(C_{oss1} + C_{oss2})\,(C_{oss3} + C_{oss4})}{C_{oss1} + C_{oss2} + C_{oss3} + C_{oss4}} \tag{1}$$

This small-signal model is appropriate, when v_1 and v_2 are the voltages across U_1 and U_2, respectively, $\Delta v_1 = -\Delta v_2$, as $v_1 + v_2 = V_{DC}$ at all instances during dead time. This constraint is reflected in the small-signal model. Assuming a linear C_{oss}, the equivalent dead-time model is a single capacitor with capacitance C_{oss} in series with L_S and the rest of the network. Assuming $C_P \gg C_{oss}$, the dead-time small-signal circuit can be approximated as C_{oss} in series with L_S. When the full bridge is operated at full phase angle, the rising edge of one half-bridge corresponds to the falling edge of the other. Further, at a full phase angle, by ensuring ZVS on one half-bridge, we ensure ZVS of the full bridge, assuming all four output capacitances, although nonlinear, are identical. Typical switching waveforms are shown in Fig. 2.

Numerous methods, such as state-plane modeling, exist to model dead-time transition with such a linear output capacitance. While the simplified model described above is still valid for a non-linear output capacitance, the effective capacitance in the small-signal model is simply $\frac{1}{2}\left(C_{oss}(v) + C_{oss}(V_{DC} - v)\right)$, the solution becomes intractable with a non-linear output capacitance. This paper presents a method to design for ZVS using only the charge-equivalent capacitance, as defined in [9]. Further, the method is load-independent, meaning ZVS will occur regardless of the load condition.

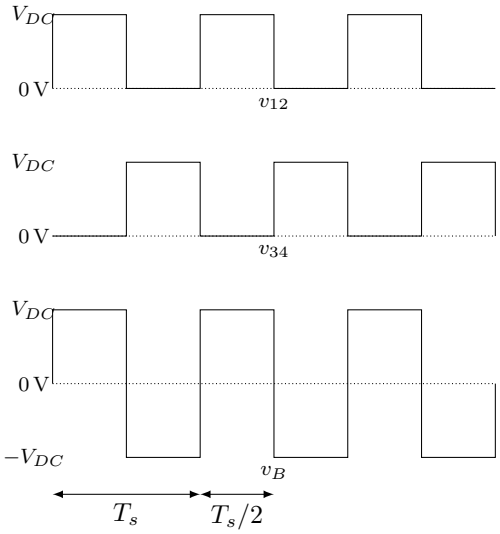

Fig. 2. Switch-node voltages. Note that v_{12} and v_{34} are switch-node voltages relative to ground, and $v_B = v_{12} - v_{34}$

III. Harmonic Dead Time Design Method

The harmonic dead time design method for ZVS predetermines a dead time. The following variables will be used, with lowercase letters indicating a complete signal, a bar indicating a phasor quantity, and a numeric subscript referencing that harmonic of the switching frequency, where f_S is the switching frequency. Note that all voltage harmonics are defined to have a phase of 0. Further note that these equations imply a well-tuned network.

$$v_B = v_{12} - v_{34}$$

$$\bar{Z}_n = \frac{\bar{V}_{Bn}}{\bar{I}_{1n}}$$

$$X = 2\pi f_S L_S = \frac{1}{2\pi f_S C_P} = 2\pi f_S L_{Coil} - \frac{1}{2\pi f_S C_C}$$

$$H = \frac{L_{Coil}}{L_S}$$

It can be shown that the predetermined dead time guarantees ZVS, provided the current does not lead voltage at the switching frequency, or $\angle \bar{Z}_1 \geq 0$. The equations here assume an LCCL primary network, as seen in Fig. 3, commonly used for wireless power transfer. To generalize for all secondary topologies, the reflected impedance of the secondary on the primary is modeled as a resistance, as seen in Fig. 3. Here, it is simply noted that R_{Load} can vary between some maximum value and $0\,\Omega$. This topology could also be used directly as an inverter. The phase difference between the two legs is assumed to be $180°$, generating a perfect square-wave voltage at v_B. The assumption of a perfect square wave is relaxed in Section IV-C. Referring to the notation used in Fig. 3, U_1 and U_4 switch in-phase with each other, $180°$ off of U_2 and U_3. This switching action is detailed in Fig. 2.

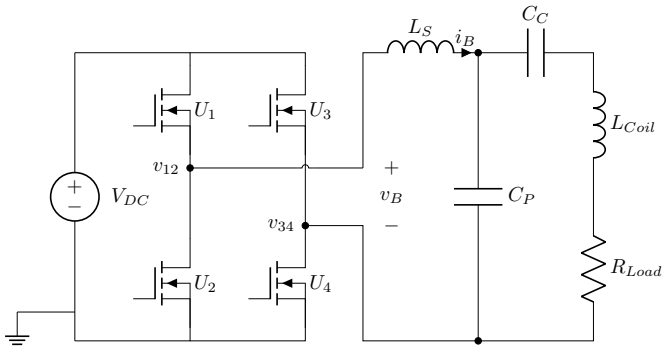

Fig. 3. LCC-compensated WPT system. Note that in a well-tuned network, $X = \omega L_S = \frac{1}{\omega C_P} = \omega L_{Coil} - \frac{1}{\omega C_C}$, where ω is the switching frequency in rad/sec. Often, the MOSFETs are modeled as an ideal switch with a parallel capacitance and antiparallel body diode, as in Fig. 1.

Typically, a network would be defined by its impedance over a range of frequencies. However, because we are concerned with only the out-of-phase current as discussed later, it is more convenient to define the network by its phasor admittance at each harmonic, $\bar{Y}_n$. Measuring the admittance allows us to separate the out-of-phase component while neglecting the in-phase component. For each harmonic, $\bar{I}_n = \bar{V}_{Bn}\bar{Y}_n$; the in-phase and out-of-phase components of the current will be proportional to the conductance and susceptance components of the admittance, respectively.

Now, we note the formula for any impedance is given by (2) and (3), which is exactly given by (4) when $n = 1$ and approximated by (4) when $n = 3, 5, 7....$ Note that since a square wave voltage observed at v_B only includes odd-numbered harmonics and the LCCL network is a linear system, (4) only need approximate (2) for those harmonics. Further justification for this simplification is given in Section IV-D. Note that in some cases, an induced voltage may be more appropriate than a resistor. This would be modeled by setting $R = 0\,\Omega$ and including an AC voltage source at f_S, but, as will be seen, such a change is immaterial for our purposes, provided $\angle\bar{I}_{B1} \leq 0$. If the secondary compensation causes R_{Load} to decrease as harmonic number n increases, the approximation in (4) becomes more accurate.

$$\bar{Z}_n = jXn - \frac{jX}{n} - \frac{jX^2}{n\left(HX\left(n^2-1\right) - jR_{Load}n\right)} \tag{2}$$

$$\bar{Y}_n = \frac{1}{\bar{Z}_n} \tag{3}$$

$$\bar{Y}_n \approx \begin{cases} \frac{R_{Load}}{X^2} & n = 1 \\ \frac{-j}{Xn} & n = 3, 5, 7... \end{cases} \tag{4}$$

Now, we note that the harmonics of a square-wave voltage are given as:

$$\bar{V}_{Bn} = \begin{cases} \frac{4V_{DC}}{\pi n} & n = 1, 3, 5, 7... \\ 0 & \text{otherwise} \end{cases} \tag{5}$$

Solving for current at each harmonic with (4) and (5) yields:

$$\bar{I}_{Bn} = \begin{cases} \frac{-j4V_{DC}}{\pi X n^2} & n = 3, 5, 7... \\ \frac{4V_{DC}R_{Load}}{\pi X^2} & n = 1 \\ 0 & \text{otherwise} \end{cases} \tag{6}$$

The phase of all higher harmonics $\angle\bar{I}_{Bn} = -90°, n = 3, 5, 7...$; the inductive currents at higher harmonics may be sufficient to achieve ZVS. For any dead-time length, the zero crossing of i_{B1} is aligned with the midpoint of the dead time — integrating i_{B1} over the dead time, regardless of dead time length, results in $\Delta Q = 0\,\mathrm{C}$. Significantly, for all harmonics, only the portion of i_{Bn} that is out-of-phase with v_{Bn} can affect ZVS. In other words, only the susceptance (imaginary portion of the admittance) and out-of-phase component of a current harmonic affect ZVS; the conductance (real portion of the admittance) and in-phase component of a current harmonic will have no net effect on ZVS during the dead time and can be neglected. This is true for all harmonics.

The argument can be summarized as follows:

- The square-wave voltage v_B contains odd-numbered harmonics
- The magnitude and phase of i_{B1} are set by R_{Load}, and are set by V_{DC} for higher harmonics $(n = 3, 5, 7...)$
- For all current harmonics, only the component out of phase with the voltage harmonic, proportional to the susceptance, affects ZVS.
- For all non-fundamental harmonics, the current lags the voltage by $90°$
- Higher current harmonics are independent of loading condition, or R_{Load}
- ZVS can be achieved independently from R_{Load}

We assume that the out-of-phase component of the current $\bar{I}_{B1}$ is zero, or that Y_1 is entirely real. Y_1 is entirely real under a few common simplifications: R_{Load} is purely resistive, the network is well-tuned, and the passive components do not have parasitic resistance. This assumption is relaxed in Section IV-A. Load independence is guaranteed by the independence of ZVS on any in-phase component of $\bar{I}_{1B}$. All real power is delivered by the component of I_{B1} in phase with $\bar{V}_{B1}$; which can be scaled arbitrarily without affecting ZVS.

For the following discussion, we will consider the transition lowering the voltage of v_{12} in Fig. 1, which coincides with the falling voltage transition of v_{34}. Note that when operating at $180°$ phase angle, achieving ZVS on one half-bridge guarantees ZVS on the other half-bridge. To guarantee ZVS according to this design method, the phase angle cannot be modulated.

We define the necessary charge moved as $\Delta Q = 2C_{oss}V_{DC}$, where C_{oss} is the charge-equivalent capacitance defined in [9]. Now we note that the maximum value of each harmonic current $i_{Bn}, n \neq 1$ occurs during the middle of dead time. Then, we solve the following, where t_d is the dead time and i' is the sum of all out-of-phase components of each of the higher current harmonics. As discussed previously, we can neglect all contributions from in-phase current components.

$$\Delta Q = \int_{-t_d/2}^{t_d/2} i'(\tau)\, d\tau \tag{7}$$

$$\Delta Q = \int_{-t_d/2}^{t_d/2} \sum_{n=3,5,7\ldots} \frac{4V_{DC}}{\pi X n^2} \cos\left(2\pi f_S n \tau\right) d\tau \tag{8}$$

Noting that the formulation in (8) resembles the Fourier series of a triangular wave, (8) can be reduced as:

$$\Delta Q = \frac{V_{DC}\pi}{2X}\left(t_d - f_S t_d^2 - \frac{16}{2\pi^3 f_S}\sin\left(2\pi f_S \frac{t_d}{2}\right)\right) \tag{9}$$

Using the small angle approximation, assuming $t_d \ll T_s$, and solving for t_d with the quadratic equation, we arrive at (10), where α is a conveniently defined constant, $\alpha = \frac{1}{2} - \frac{4}{\pi^2}$.

$$t_d = \frac{\alpha}{f_S} - \sqrt{\left(\frac{\alpha}{f_S}\right)^2 - \frac{2\Delta Q X}{\pi V_{DC} f_S}} \tag{10}$$

An alternative formulation of (10) referencing C_{oss}, the equivalent-charge capacitance, is given in (11)

$$t_d = \frac{\alpha}{f_S} - \sqrt{\left(\frac{\alpha}{f_S}\right)^2 - 8 L_S C_{oss}} \tag{11}$$

We neglect the other solution given by the quadratic equation. The other solution would indicate the maximum dead-time value; and would be less accurate due to the breakdown of the small-angle approximation.

When the dead time is set according to (10) or (11), ZVS will be achieved so long as the fundamental current does not interfere, or if the reactive portion of the fundamental current does not lead the fundamental voltage. A lagging fundamental current, a fundamental current at unity power factor, or 0 fundamental current all meet this condition.

IV. Consideration of Non-Idealities and Approximations

The ZVS design presented in Section III neglects several practical effects. The purpose of this section is to address those real-world considerations.

A. Non-Zero Out-of-Phase Series Inductor Current

In Section III, we assumed that the out-of-phase component of i_{B1} is zero. In implementation, it is difficult to guarantee that the out-of-phase component is 0. If the out-of-phase component is 0, the dead time calculated in (10) is accurate. If the out-of-phase component if I_{B1} is inductive, lagging V_{B1}, then the dead time calculated in (10) is conservative.

As long as the out-of-phase component of i_{B1} is not capacitive, not leading v_{B1}, (10) is accurate or conservative. Or, the dead-time design method introduced in this paper will be conservative, provided (12) is met. If (12) is not met, the dead-time design is not guaranteed to be conservative.

$$\Im\left\{\bar{Y}_1\right\} \leq 0 \tag{12}$$

B. Parasitic Series Resistance

All the passive components in Fig. 3 will have some parasitic series resistance or conductance. Here, we assume the $R_L \gg R_{DC,on}$, where R_L is the parasitic series resistance of L_S and $R_{DS,on}$ is the on resistance of a switch. If $R_{DS,on}$ is not negligible, let $R'_L = R_L + R_{DS,on}$. Generally, the most impactful parasitic effect on i_B will be R'_L, as its impedance contributes linearly to Z and the quality factor of inductors tends to be less than that of capacitors. Note that, since only the reactive current affects ZVS during the dead time, we need only quantify the effect of a series resistance on the reactive component of a current harmonic.

The ratio of reactive current with a series resistance $R'_L = \frac{X}{Q}$, where Q is the assumed quality factor of the inductor at f_S, to the reactive current when $R'_L = 0$ is given by:

$$\frac{\left(Q\left(Hn^4 - 2Hn^2 + H - 1\right)\right)^2}{\left(Q\left(Hn^4 - 2Hn^2 + H - 1\right)\right)^2 + \left(Hn\left(n^2 - 1\right)\right)^2} \tag{13}$$

As $n \to \infty$, the fraction in (13) approaches unity; if (13) can be approximated as unity when $n = 3$, the approximation is valid for all harmonics. When $n = 3$, it can be shown through manipulation of (13) that the condition in (14) is sufficient to show that the approximation is valid, or that the parasitic resistance on L_S can be neglected. For any reasonable Q, (14) should be easily met.

$$Q^2 \frac{441}{64} \gg 1 \tag{14}$$

C. Non-Square Voltage Waveforms

With any dead time, the voltage signal v_B will no longer be a pure square wave, which will impact the harmonic strength. Further, the voltage dynamics calculations during dead time are intractable due to the non-linear output capacitance C_{oss}. However, the effects of dead time on harmonic strength are minimal, as shown in Fig. 4. Two different approximations for dead time voltage are shown. In both cases, the dominant harmonics are negligibly affected by a reasonable dead time.

D. Impedance Approximations

By approximating (3) as (4), we slightly overestimate the impedance and underestimate the current available to achieve ZVS. This is particularly pronounced for the lower harmonics, which provide most of the current for ZVS. Thus, the approximation overestimates the necessary dead time. Here, we show that, although the estimate of necessary dead time is conservative, the estimate remains approximately accurate.

As discussed previously, any in-phase component of harmonic current will not affect necessary dead time. The only mechanism through which resistance at a harmonic affects necessary dead time is by increasing the magnitude of the impedance. As seen is (3), $\lim_{n\to\infty}\left(\bar{Y}_n\right) = \frac{-j}{nX}$. By proving that (4) approximates (3) for $n = 3$, we show that the two formulations are approximately equal for $n = 3, 5, 7 \ldots \infty$. Further, since only the susceptance, and not the conductance,

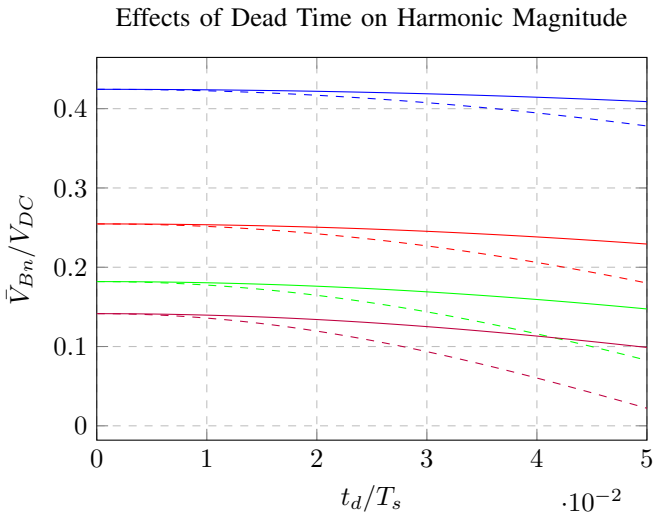

Fig. 4. Effects of dead time duration on harmonic magnitude. The y-axis is relative to V_{DC}. The blue, red, green, and purple lines correspond to the 3rd, 5th, 7th, and 9th harmonics, respectively. Solid lines correspond to a linear voltage during dead time, and dashed lines correspond to $v_B = 0\,\text{V}$ during dead time. Where $t_d \leq 0.01T_s$, the effects of dead time on harmonic magnitude are negligible.

represented in Y_n affects ZVS, we need only demonstrate that the imaginary components of the exact form and approximation are approximately equal, or that the susceptance of the exact form is roughly equal to the approximation in (4).

We observe that the imaginary part of Y_3, or $\Im\{Y_3\}$, the component that will aid in ZVS, is given below, where the value $w = \frac{X}{R_{Load}}$ and we let $n = 3$.

$$\Im\{Y_3\} = \frac{-1}{Xn}\left(\frac{w^2 72H\,(64H-1)+648}{w^2\,(64H-1)^2+576}\right) \tag{15}$$

This expression given in (4) underestimates the susceptance given in (15) by a factor between $\frac{8}{9}$ and $\frac{72}{63}$, provided $H \geq 1$, or the transmission coil has a higher inductance than the compensating inductor. By underestimating the susceptance at a lower harmonic, this model underestimates the current available to discharge the MOSFET output capacitance, and the required dead time is conservative. Further, because (4) approximates (15) with sufficient accuracy for $n = 3$, we conclude the approximation is valid for higher harmonics as well.

V. Simulation Validation

To test the ZVS design scheme in a simple application, the circuit in Fig. 3 was simulated with three values of R_{Load} in LTSpice. The simulation results, seen in Figs. 5 and 6, show the rising switch-node voltage v_{12} during the dead-time transition. Quantities are labeled the same as in Fig. 3. The time to soft switch should be independent of the test load. The simulated system was designed for a maximum power of 100 W. Values for various components are included in Table I. The switch was composed of an ideal switch, a diode, and a non-linear capacitor in parallel. The model for the non-linear capacitor was designed to fit the output capacitance of a Cree CCS050M12CM2 switch; although the nonlinear capacitor was used in simulation, the charge-equivalent capacitance C_{oss} is reported in Table I. The oversized switch was chosen to require a larger dead time, making the dead-time transition more observable. To model a real-world scenario more closely and to attenuate start-up transients, both inductors also have a $10\,\text{m}\Omega$ parasitic series resistance, and $R_{DS,on} = 10\,\text{m}\Omega$.

TABLE I
Component Values Used in Simulation

Component	Value
C_{oss}	2.24 nF
V_{DC}	40 V
f_S	85 kHz
L_S	9.998 µH
C_P	350.66 nF
C_C	941.63 nF
L_{Coil}	13.721 µH
R_{Load} (Test 1)	2.1984 Ω
R_{Load} (Test 2)	1.0992 Ω
R_{Load} (Test 3)	0 Ω

Given the calculated charge-equivalent capacitance C_{oss} and the parameters listed above, the necessary dead time was calculated with (10) as 84 ns. As discussed in Section IV-D, the method described in this paper underestimates the current available to achieve ZVS, thus the calculated dead time is conservative, and the body diodes should conduct for some time before the switch closes. With the fine resolution available in simulation, we can verify ZVS by observing the following conditions on a rising switch-node voltage transition:

1) A smooth, continuous switch-node voltage
2) At the end of dead time, the switch-node voltage is V_{DC} plus the forward voltage of the body diode
3) At the end of dead time, the switch-node voltage drops to V_{DC}

Further, as seen in Fig. 4, the dead time is sufficiently short to neglect any effect on voltage harmonic magnitudes, as $\frac{t_d}{T_s} = 0.00714$.

Each test condition was simulated in LTSpice unit steady-state was achieved. For the two higher load conditions (Tests 1 and 2), 25 switching periods was sufficient to reach steady state. For the no-load test (Test 3), 250 switching periods were required to reach steady state. The last rising-voltage transitions are shown for all three tests. Timescales for all the following plots are normalized to the start of dead time, with time given in nanoseconds.

Fig. 5 shows the switch-node voltage and high-side body diode current during a rising-voltage transition for the three tests. Although all three tests have slightly different waveform shapes during the dead time, we can observe the three indicators of ZVS. First, all waveforms are continuous; the lack of sudden voltage changes during the commutation indicates C_{oss} avoids sudden discharge. Second, at the end of dead time at $t_d = 84\,\text{ns}$, we observe the switch-node voltage has exceeded V_{DC} by the forward voltage drop of the body diode. Third,

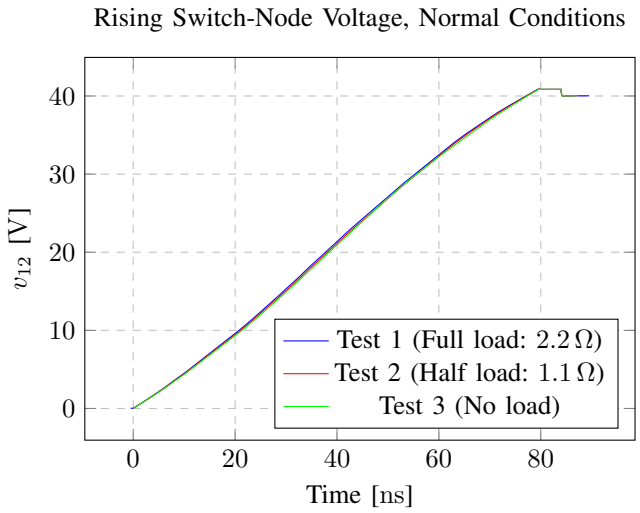

Fig. 5. Switch-node voltage waveforms during a rising transition. Note that the waveforms are nearly identical, with only minor variation due to i_1.

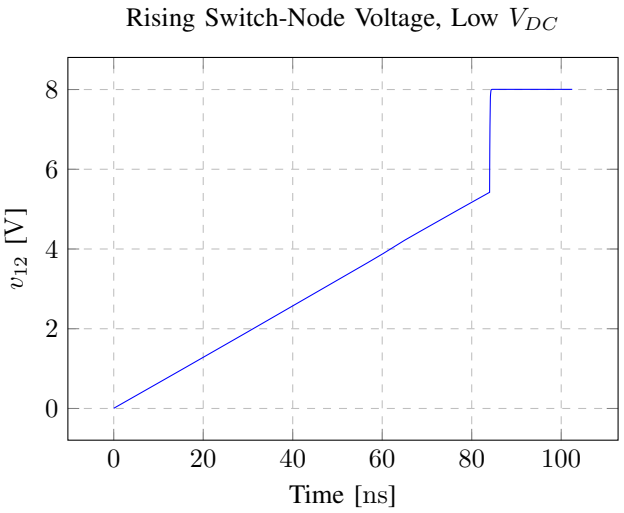

Fig. 6. Switch-node voltage waveform during a rising transition with low V_{DC} and high C_{oss}. Note the discontinuity of 2.6 V.

after dead time, we see the voltage drop to V_{DC}. All three conditions indicate ZVS for all three load cases. Additionally, we observe the waveforms are nearly identical, indicating the low dependence of switch-node voltage on I_1.

A. Validation by Comparison with Hard Switching

To further demonstrate the effectiveness of the design procedure, another test was included, contrasting the simulated ZVS waveforms with a hard-switching scenario. Hard switching was achieved by lowering DC voltage to 8 V while leaving the dead time unchanged. At $V_{DC} = 8\,\text{V}$, C_{oss} increases sufficiently to prevent ZVS when $t_d = 84\,\text{ns}$. As can be seen in Fig. 6, none of the three indicators of ZVS are shown when $V_{DC} = 8\,\text{V}$, as expected. The waveform shows a discontinuity at the end of dead time, suddenly jumping 2.6 V to V_{DC}, indicating hard switching.

VI. Hardware Validation

To validate the proposed dead-time design, a hardware implementation similar to the simulation was realized. The value of each component is listed in Table II, where the series resistance is noted along with each component. The value of C_{oss} is calculated from the datasheet; all other values were measured with an LCR meter at f_S. The reactive components were measured with an LCR meter at 85 kHz, parasitic series resistances are also shown. Whereas the simulated value of C_{oss} was derived from an existing MOSFET, the other hardware components were chosen to match the simulated values. As in simulation, the datasheet indicates $R_{DS,on} = 10\,\text{m}\Omega$.

As in simulation, we measure the switch-node voltage to determine ZVS. For ZVS, we expect the switch-node voltage waveform to:

1) Be smooth during the commutation
2) Exceed V_{DC} by some small voltage at the end of dead time

TABLE II
Component Values Used in Hardware Testing

Component	Value
C_{oss}	2.24 nF
V_{DC}	35 V
f_S	85 kHz
L_S	9.41 µH + 45 mΩ
C_P	336 nF + 3.6 mΩ
C_C	949 nF + 75 mΩ
L_{Coil}	14.4 µH + 61 mΩ
R_{Load} (Test 1)	2.1 Ω
R_{Load} (Test 2)	1.1 Ω
R_{Load} (Test 3)	0 Ω

3) Drop to V_{DC} after the end of dead time.

Any ringing observed should only be due to the discharge of the body diode forward voltage, which is typically between 1.5 V and 2.0 V.

As before, a contrasting, hard-switching example is discussed in Section VI-B, which shows the difference between an observed hard switch and an observed ZVS. That hard-switch characteristics are visible in that test suggests the ZVS characteristics we observe in Tests 1, 2, and 3 truly indicative of ZVS, and not artifacts of hardware or instrument limitations.

An FPGA generated an 85 kHz signal with 85 ns dead time, as in the simulation. The signal drove an evaluation board with a Cree CCS050M12CM2 H-bridge. The inverter output supplied a resonant tank with a resistive load, as in Fig. 3 and as in the simulation. The voltage at the switch node was measured for comparison with the simulated results.

A. Normal Condition Tests

The plots for each of the Test 1, Test 2, and Test 3 collected from the oscilloscope are shown superimposed in Fig. 7. As before, the time axis is referenced to the start of dead time.

First, we note that overall, the waveforms appear to match the simulation waveforms. All three tests are nearly identi-

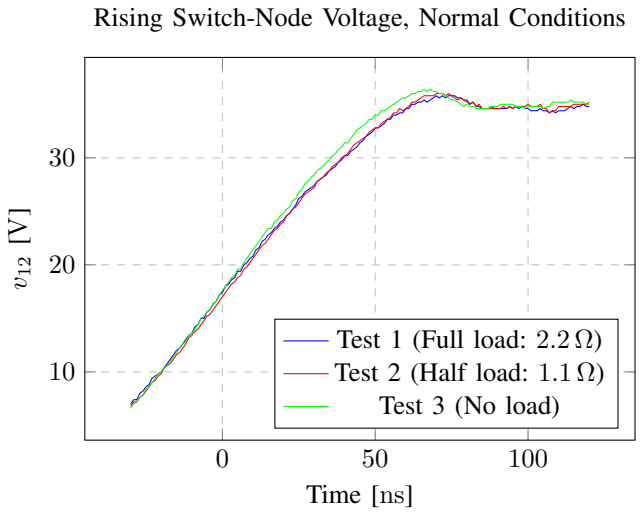

Fig. 7. Switch-node voltage waveforms during a rising transition. Note that the waveforms are nearly identical, with only minor variations.

cal, with only minor variation; all show a smooth voltage waveform, typical of ZVS. Second, we note that by 85 ns, all three waveforms appear to have reached and exceeded V_{DC}, further indicative of soft switching. We even observe the slight overshoot, due to the inclusion of the forward voltage drop of the diode. Finally, after roughly 85 ns, we observe that the switch-node voltage settles to V_{DC}. Given these observations, we conclude that 85 ns is sufficient dead time to achieve ZVS.

One discrepancy is noted between the hardware test and the simulation: at the start of dead time, $v_{12} \neq 0\,\text{V}$ in the hardware tests. This is due to the slow turn-off of the lower switch, U_2. With the gate driver used, the turn-off included roughly 200 ns ramp down of the gate–source voltage. This ramp-down of voltage increases $R_{DS,on}$, increasing switch-node voltage. The start of dead time is determined by when the gate-source voltage dropped below the threshold voltage provided by the manufacturer. The delay between turn-off and turn-on was observed to be approximately 85 ns.

B. Validation by Comparison with Hard Switching

The ideal waveforms observed in Figs. 5 are not precisely replicable in hardware, due to the instantaneous voltage changes in 5. The purpose of this subsection is to prove the design actually achieves ZVS by contrasting the results with a known hard-switching condition, as in Section V-A.

To verify ZVS in the Fig. 7, the supply voltage was intentionally decreased to force hard switching. As discussed in Section V-A and due to the non-linear nature of C_{oss}, a lower V_{DC} increases the charge-equivalent capacitance sufficiently to cause hard switching. However, the dead time remains the same, so no non-idealities from a shorter dead time are different from Tests 1, 2, and 3. A hard-switching transition has a discontinuity in the switch-node voltage waveform and significant ringing, which would contrast with the observations in Fig. 7. As observed in Section V-A, we expect the system to hard-switch when $V_{DC} = 8\,\text{V}$, after only charging to 5.4 V during dead time, or with an instantaneous voltage change of 2.6 V.

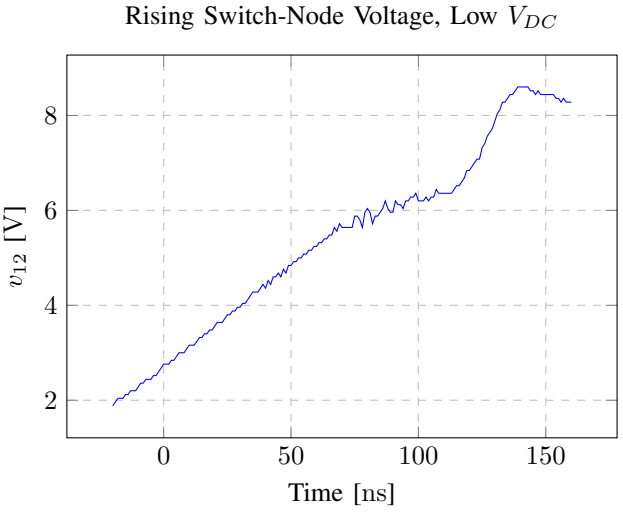

Fig. 8. Switch-node voltage waveform during a hard-switch rising-voltage transition. Note that the more data points are included than in Fig. 8, to highlight more the effects of hard switching.

In addition to the waveforms captured as part of Tests 1, 2, and 3 in Fig. 7, a hard-switching waveform was captured, shown in Fig. 8. In all cases, the timescale is referenced relative to the start of dead time, as in the simulation.

The waveform in Fig. 8 is visibly different from the ZVS waveforms shown in Fig. 7 in all three indicators of ZVS. The switch-node voltage is noticeably less smooth, with two corners in the rising voltage. Most telling, however, is the switch-node voltage at the end of dead time, occurring at 85 ns. The switch-node voltage only reaches 5.96 V during dead time, which aligns nicely with the simulated result of 5.4 V. After dead time, we observe v_{12} continuing to rise. After some time, near 140 ns, we observe the beginning of ringing. Taken together, these observations suggest that at $V_{DC} = 8\,\text{V}$, the inverter does not achieve ZVS, as expected.

C. Experimental Result Summary

As predicted by the dead time design model presented in this paper, the inverter achieved ZVS regardless of load, as long as V_{DC} was at or near the design V_{DC}. The observed waveforms for Tests 1, 2, and 3 indicate ZVS, as predicted by simulation and the dead time design model. However, when the V_{DC} is decreased to force hard switching, a completely different waveform is observed, indicative of the expected hard switching. We conclude that the harmonics dead time design model is accurate and does guarantee load-independent ZVS.

Note that no thermal dependence is noted in the data sheet, so thermal effects on C_{oss} are neglected. To account for a thermal dependency in C_{oss}, the necessary dead time would be calculated for the extreme values of C_{oss} possible over the temperature range. In this case, the value of C_{oss} determined from the data sheet was assumed to be accurate at

all temperatures. Due to the low power level, large heat sink, and short test duration, no noticeable temperature rise in the switches was observed during testing.

VII. Conclusion

This paper presents a technique to guarantee ZVS at a variety of load conditions, provided several conditions are met:

- The load at the switching frequency, f_S, is not capacitive. The load may be infinite, purely resistive, or inductive; so long as $\Im\{\bar{Z}_1\} \geq 0$.
- The bridge operates at a full 180° phase angle.
- The compensation network is well-tuned
- Parasitic inductor resistance is reasonable.
- A solution to (10) or (11) exists where $t_d f_S$ is sufficiently less than unity.
- The value of C_{oss} is bounded.

Given these constraints, we can guarantee that a resonant LCCL converter will achieve ZVS under all load conditions. Although the simulation and hardware tests illustrate the effectiveness of the dead time design method at $85\,\mathrm{kHz}$, this approach is applicable to any switching frequency. One promising application of this technology is dynamic wireless power transfer, where the load may vary with time. By designing the dead time as described here, we can guarantee the converter will operate in ZVS for all potential loads. Further, this approach does not require additional harmonics or additional reactive current, beyond those intrinsic to switch-mode resonant converters. Rather, this approach uses current harmonics intrinsic to switch-mode power supplies.

The theory was developed, demonstrated in simulation, and validated in hardware, with simple conditions and equations to guarantee ZVS. The calculated dead time is guaranteed to be conservative. Further, we demonstrated in theory, simulation, and hardware that the design is robust against non-ideal components and real-world conditions.

Perhaps the largest limitation of designing the dead time according to the theories presented here is the requirement that the bridge operate at a 180° phase angle, precluding primary phase-angle modulation for power regulation. The limitation that C_{oss} be bounded may further preclude cascading a DC converter with the resonant converter to regulate power transfer. However, no limitations of the proposed ZVS design preclude secondary power regulation and guaranteeing ZVS over a full power range may be possible with frequency modulation.

References

[1] C. C. Mi, G. Buja, S. Y. Choi, and C. T. Rim, "Modern advances in wireless power transfer systems for roadway powered electric vehicles," *IEEE Transactions on Industrial Electronics*, vol. 63, no. 10, pp. 6533–6545, 2016.

[2] Y. Sakayanagi, S. Togawa, K. Konagaya, and Y. Kuwahara, "Wireless power transmission for a traveling mobility scooter," in *2016 IEEE Wireless Power Transfer Conference (WPTC)*, 2016, pp. 1–3.

[3] A. Kamineni, M. J. Neath, A. Zaheer, G. A. Covic, and J. T. Boys, "Interoperable ev detection for dynamic wireless charging with existing hardware and free resonance," *IEEE Transactions on Transportation Electrification*, vol. 3, no. 2, pp. 370–379, 2017.

[4] U. K. Madawala and D. J. Thrimawithana, "A bidirectional inductive power interface for electric vehicles in v2g systems," *IEEE Transactions on Industrial Electronics*, vol. 58, no. 10, pp. 4789–4796, 2011.

[5] G. Buja, M. Bertoluzzo, and K. N. Mude, "Design and experimentation of wpt charger for electric city car," *IEEE Transactions on Industrial Electronics*, vol. 62, no. 12, pp. 7436–7447, 2015.

[6] M. Bojarski, E. Asa, K. Colak, and D. Czarkowski, "Analysis and control of multiphase inductively coupled resonant converter for wireless electric vehicle charger applications," *IEEE Transactions on Transportation Electrification*, vol. 3, no. 2, pp. 312–320, 2017.

[7] B. Liu, P. Davari, and F. Blaabjerg, "Nonlinear $c_{oss} - v_{DS}$ profile based zvs range calculation for dual active bridge converters," *IEEE Transactions on Power Electronics*, vol. 36, no. 1, pp. 45–50, 2021.

[8] R. Elferich, "General zvs half bridge model regarding nonlinear capacitances and application to llc design," in *2012 IEEE Energy Conversion Congress and Exposition (ECCE)*, 2012, pp. 4404–4410.

[9] D. Costinett, D. Maksimovic, and R. Zane, "Circuit-oriented treatment of nonlinear capacitances in switched-mode power supplies," *IEEE Transactions on Power Electronics*, vol. 30, no. 2, pp. 985–995, 2015.

[10] W. Su and C. Chen, "Zvs for pt backlight inverter utilizing high-order current harmonic," *IEEE Transactions on Power Electronics*, vol. 23, no. 1, pp. 4–10, 2008.

[11] X. Zhang, T. Cai, S. Duan, H. Feng, H. Hu, and J. Niu, "A harmonic-considered time domain model of lcc compensated wireless power transfer systems," in *2018 IEEE International Power Electronics and Application Conference and Exposition (PEAC)*, 2018, pp. 1–5.

[12] H. Hu, T. Cai, S. Duan, X. Zhang, J. Niu, and H. Feng, "An optimal variable frequency phase shift control strategy for zvs operation within wide power range in ipt systems," *IEEE Transactions on Power Electronics*, vol. 35, no. 5, pp. 5517–5530, 2020.

[13] Z. Pantic, S. Bai, and S. M. Lukic, "Zcs lcc-compensated resonant inverter for inductive-power-transfer application," *IEEE Transactions on Industrial Electronics*, vol. 58, no. 8, pp. 3500–3510, 2011.

[14] E. S. Glitz and M. Ordonez, "Mosfet power loss estimation in llc resonant converters: Time interval analysis," *IEEE Transactions on Power Electronics*, vol. 34, no. 12, pp. 11 964–11 980, 2019.

[15] H. Wu, T. Mu, X. Gao, and Y. Xing, "A secondary-side phase-shift-controlled llc resonant converter with reduced conduction loss at normal operation for hold-up time compensation application," *IEEE Transactions on Power Electronics*, vol. 30, no. 10, pp. 5352–5357, 2015.

CHAPTER 5

IMPROVEMENTS TO REAL-TIME SYNCHRONIZATION AND DETECTION FOR A DUAL-ACTIVE, SECONDARY-DRIVEN DYNAMIC WIRELESS POWER TRANSFER SYSTEM

This chapter is a replication of a journal article currently under review, submitted to IEEE Open Journal of Power Electronics [26]. The work is based on previous work by the same author [27, 28].

Improvements to Real-Time Synchronization and Detection for a Dual-Active, Secondary-Driven Dynamic Wireless Power Transfer System

Matthew Hansen, *Student Member, IEEE,* Azmeer Zahid, *Student Member, IEEE* Abhilash Kamineni, *Member, IEEE*

***Abstract*—A novel control scheme applicable to in-road inductive wireless charging pads in a dynamic system is presented. Primary inverter current sensing allows the primary pad to detect an approaching secondary pad. Zero-crossing detection of the same current allows the primary to synchronize to the secondary, functioning as a synchronous inverter with dual-active switching. Such primary synchronous inverters allow for independent primary pads. Necessary measures to ensure stable operation of the design are discussed. The control scheme only adds an analog filter hardware to the bare-bones open-loop design. The design is validated through simulation and hardware experimentation, with a strong demonstration of robustness.**

***Index Terms*—Power conversion, Resonant converters, Inverters, Electric vehicles, Inductive charging, Vehicle detection**

I. Introduction

DYNAMIC wireless power transfer (DWPT) in electric vehicles could increase the feasibility of vehicle electrification, potentially resulting in many environmental advantages. By electrifying a small portion of roadways, a majority of routes could be covered by electric vehicles (EVs) without stopping to recharge [1]. Although battery modeling, technology, and use optimization are improving [2], [3], [4] and novel battery charging solutions are being explored [5], [6], [7], battery limitations remain a weakness of EVs. With en-route, no-time-added charging through DWPT, electric vehicles could overcome two of the main weaknesses in a battery-centered approach to vehicle electrification: range anxiety and battery cost [8], [9]. The suitability of WPT for electric vehicles has been well-studied [10]. This paper further develops the real-time synchronization and detection, or synchronous inversion approach initially introduced in [11], [12], which in turn was an extension of the work in [13]. In comparison with [11], [12], the present paper includes a more rigorous proof of closed-loop stability, more thorough development of the underlying theory, and, critically, a hardware demonstration of the operating principle at $15\,\mathrm{kW}$.

Near-field wireless power transfer (WPT) is accomplished either through an electric field (capacitive power transfer, CPT) or a magnetic field (inductive power transfer, IPT). Although work in capacitive transfer shows promise [14], [15], [16], CPT still has limitations in air gap length and frequency that restrict the applicability of CPT to DWPT [17]. Most research on high-powered WPT for EVs uses IPT.

Work on stationary WPT has demonstrated the advantages of a bidirectional system, where the vehicle rectifier is active and therefore reversible [18]. We assume such an active rectifier on the secondary in the present work, which requires primary–secondary synchronization — a critical contribution of this work. In [18], [19], [20], control schemes have been developed to regulate power transfer on the secondary side of a WPT system. In [21], and [22], the control scheme is designed to ensure low-loss zero-volt switching. The work in [23] provides an accurate method to measure energy transferred, which is an essential step to the commercialization of WPT for EVs. In [24], a framework for stationary charging with rotating magnetic fields and less ferrite is presented. The work in [25] provides a framework for overcoming large air gaps, which could be present in DWPT. The extensive research environment around stationary WPT complements and enriches the present work, while highlighting the need to extend those advances to DWPT with a robust and simple detection and synchronization scheme.

Existing work describes how an in-road primary coil in a DWPT system can detect an approaching vehicle-mounted secondary coil with dedicated detection hardware [26], which relies on ultrasonic sensors to detect the secondary. Such an approach is too slow and insufficiently robust for high-speed DWPT, including in-motion EV applications. Other work uses extra coils to detect approaching vehicles [27], [28]. This approach is fast and reliable enough to achieve DWPT but increases complexity and cost by requiring additional components. In [13], a robust, fast detection scheme is presented without relying on additional detection hardware, but the parasitic losses in the approach requires constant pulsing and sampling, increasing system complexity and making each primary pad dependent on the preceding primary pad operation. In [13], [26], [28], all primary pads need a central synchronization signal, decreasing modularity and robustness.

An LCCL topology, visualized in Fig. 1, is among the commonly used approaches in WPT [13], [21], [22], [29], [30], in part due to a few key advantages. Unlike simple series compensation, the system can be perfectly tuned and operated with no load. Unlike basic parallel compensation, the LCCL system can achieve ZVS when perfectly tuned [30]. Finally, as discussed in [13], the inverter current and voltage are decoupled; more analysis of this decoupling is addressed

This research was supported in part by the ASPIRE (Advancing Sustainability through Powered Infrastructure for Roadway Electrification) Center, an NSF ERC, under award number 1941524, and by Utah State University College of Engineering.

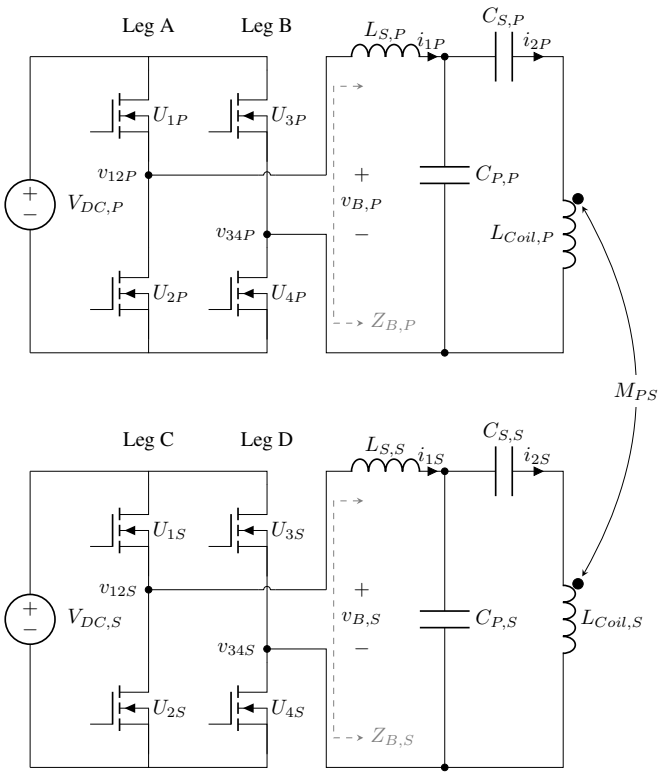

Fig. 1. System overview of primary and secondary pad architectures with LCC compensation.

in this paper. Although this approach may extend to other compensation topologies, this work assumes an LCCL system.

The contributions of this paper are expansions on previous research [11], [12] in six critical directions. First, the design simplifies the approach in [13] by allowing a single control law for the primary and open-loop control for the secondary, using one threshold to determine both turn-on and turn-off. Second, in this approach, the primary coils are activated by the secondary, rather than neighboring primary pads. The result is that the secondary can initiate and cease power transfer, as necessary. The third improvement over the previous work is a simplified primary controller with no switching clock; the primary switching is driven by a simple comparator and adapts to the frequency and phase of the secondary. In the future, this innovation could allow a secondary-based frequency-modulated controller that achieves ZVS with no required communication to the primary; removing the primary switching clock simplifies the primary control and eliminates a point of failure. All three of those innovations are implemented without a dedicated primary–secondary communication link or auxiliary coils, increasing system simplicity and robustness.

Those three innovations are discussed lightly in [11], [12], although this work presents a more thorough analysis than in [11], [12]. Compared to [11], [12], this work also includes three new and essential contributions. The first is the rigorous development of stability criteria, with analytical treatment of the nonlinear system components. The second new contribution is the consideration of imperfectly-tuned systems. The final, and perhaps most critical, new contribution of this paper is a high-power (15 kW) experimental validation of this approach.

This paper is organized as follows. Section II introduces pertinent characteristics of an LCCL WPT topology and introduces the basic concept, detailing how synchronous inversion on the primary can simplify the synchronization and detection operations. Section III presents practical considerations for implementing the system in a dynamic setting, including a discussion on stability. Section V demonstrates the effectiveness of the scheme through software simulation; Section VI mirrors Section V with hardware validation. A conclusion and discussion of potential impacts follows in Section VII. Appendix A works out the modeling of the nonlinear zero-crossing detector.

II. WPT in a Well-Tuned LCCL System and Basic Control Scheme

The work presented here expands on previous work [11], [12], [13]. As in those works, this paper assumes LCC compensation on both the primary and secondary side, although the control scheme could be adapted to other topologies as well. Quantities relevant to this discussion are defined in Table I and noted in Fig. 1. The notation for phasors, small-signal, DC, and large-signal quantities shown in Table I holds for all quantities. In the present system, the H-bridge switches at a fundamental frequency $f_f = 85\,\text{kHz}$, in line with SAE J2954 standards. This section gives some essential background on LCCL systems in Section II-A, and describes the essential principle of operation in Section II-B.

TABLE I
Referenced quantities in an LCCL system

Phasor	Complete Signal	Small Signal	Value
$\bar{V}_{B,P}$	$v_{B,P}$	$\hat{v}_{B,P}$	Primary bridge voltage
$\bar{V}_{B,S}$	$v_{B,S}$	$\hat{v}_{B,S}$	Secondary bridge voltage
$\bar{I}_{1P}$	i_{1P}	$\hat{i}_{1P}$	Primary inverter current
$\bar{I}_{1S}$	i_{1S}	$\hat{i}_{1S}$	Secondary inverter current
X_P			Primary branch impedance (1a)
X_S			Secondary branch impedance (1b)
$V_{DC,P}$			Primary DC voltage
$V_{DC,S}$			Secondary DC voltage
M_{PS}			Primary–secondary mutual inductance
f_f			Switching frequency
f_{z1}, f_{z2}			Primary natural response frequencies
f_{coil}			Resonant frequency of $L_{Coil,P}$ and $C_{S,P}$
$Z_{B,P}$			Output impedance seen by the primary inverter
f_{e1}, f_{e2}			Equilibrium frequencies of primary network and anti-resonance filter

A. WPT in a Well-Tuned LCCL System

In a well-tuned LCCL system operating at $f_f = \omega_f/2\pi$, the magnitude of the impedance of each branch in either the

primary or secondary (X_P and X_S, respectively) are given by

$$X_P = (\omega_f L_{S,P}) = \left(\frac{1}{\omega_f C_{P,P}}\right) = \left(\omega_f L_{Coil,P} - \frac{1}{\omega_f C_{S,P}}\right) \tag{1a}$$

$$X_S = (\omega_f L_{S,S}) = \left(\frac{1}{\omega_f C_{P,S}}\right) = \left(\omega_f L_{Coil,S} - \frac{1}{\omega_f C_{S,S}}\right) \tag{1b}$$

A brief explanation of the current–voltage decoupling phenomenon is given here. Consider the following equations defined by Kirchhoff's Voltage Law, where the total voltage around is calculated for each loop in Fig. 1:

$$\bar{V}_{B,P} = (-jX_P)\left(-\bar{I}_{2P}\right) \tag{2a}$$

$$j\omega_f M_{PS}\bar{I}_{2S} = (-jX_P)\left(\bar{I}_{1P}\right) \tag{2b}$$

$$j\omega_f M_{PS}\bar{I}_{2P} = (-jX_S)\left(\bar{I}_{1S}\right) \tag{2c}$$

$$\bar{V}_{B,S} = (-jX_S)\left(-\bar{I}_{2S}\right) \tag{2d}$$

Note that neither of the currents in (2a) and (2c) appear in (2b) and (2d), showing two decoupled systems. By solving the expressions in (2) for $\bar{I}_{1P}$ and $\bar{I}_{1S}$, we arrive at the expressions

$$\bar{I}_{1P} = \frac{j\omega_f M_{PS}\bar{V}_{B,S}}{X_S X_P} \tag{3a}$$

$$\bar{I}_{1S} = \frac{j\omega_f M_{PS}\bar{V}_{B,P}}{X_S X_P} \tag{3b}$$

As consequence of (3), $\bar{V}_{B,P}$ will not contribute to $\bar{I}_{1P}$, making the two quantities independent. The bridge impedance at f_f approaches infinity, implying that any small-signal change to $v_{B,P}$ at f_f will not affect i_{1P}

The analysis conducted here assumes a well-tuned system. While variations in system parameters may admit some mistuning, as long as the current $\bar{I}_{1P}$ is largely induced by $\bar{V}_{B,S}$, not $\bar{V}_{B,P}$, the essential principle holds.

B. Basic Control Scheme

The characteristics of the LCCL WPT topology described here allow for a simplified detection/synchronization scheme through synchronous inversion. Because power is transferred at the fundamental frequency f_f, we neglect higher harmonics. In synchronous rectification, the current and voltage of the fundamental harmonic are aligned such that $\angle\bar{V}_{B,S} = \angle\bar{I}_{1S} \pm 180°$, forcing the secondary to act as a load. Synchronous inversion is the complement; $\angle\bar{V}_{B,P} = \angle\bar{I}_{1SP}$, forcing the primary to act as a power source. Noting the decoupling between the voltage and current in (3a), the voltage and current can be aligned. This is synchronous inversion, the central thesis of this work. The remainder of this section details how synchronous inversion can be used to simplify and increase robustness in detection and synchronization. Because synchronous inversion injects power into a system, which tends to be unstable, some practical considerations for stable operation are made in Section III.

The present approach uses inherent characteristics of the WPT current waveforms to replace any other primary–secondary communication links, as all information necessary for primary control in the dual-active system is contained in the $\bar{I}_{1P}$ current.

1) Secondary Operation: The secondary H-bridge operates in two modes, as a synchronous rectifier and as an inverter. To request power, the secondary begins switching, which induces a signal on any coupled primary. After the secondary begins switching, but before primary–secondary coupling, the secondary-side H-bridge operates as an inverter, supplying only enough real current to counteract parasitic losses. When coupled to a primary, the secondary side operates as an open-loop synchronous rectifier. For both modes, the switches operate at a fixed fundamental frequency, f_f. The only difference between the two modes is the current i_{1S} induced by the primary pad.

The secondary side H-bridge maintains the same operation independent of the primary, but when the primary side injects power into the system, the change in $\bar{I}_{1S}$ causes the secondary H-bridge to begin functioning as a synchronous rectifier, rather than as an inverter. Although the system is effective with open-loop control of the secondary, the secondary can also control the total power transferred through voltage or phase modulation without additional hardware [20], or through a cascaded DC–DC converter. Previous work describes power transfer control of a similar system through current regulation, which can be simplified and applied here to regulate power on the secondary [18]. Because secondary power regulation is addressed in other works, a rigorous discussion is omitted here.

2) Primary Operation: Both the primary and secondary network are tuned for the same f_f. The primary inverter measures i_{1P}; the magnitude of the current determines when a vehicle is approaching. The primary inverter then synchronizes to i_{1P}, sending power into the secondary network. Because the primary inverter voltage $v_{B,P}$ is synchronized to i_{1P}, the primary H-bridge operates as a synchronous inverter. A synchronous rectifier tends to pull whatever power is available from a network, which is generally stable or stabilizable [31], [32]. In contrast, basic synchronous inversion tends to inject power into the network however possible, including at a natural response frequency of the primary network, f_z; considerations to avoid this phenomenon are discussed in Section III. Note the distinction between the switching frequency f_f, where $L_{S,P}$ and $C_{P,P}$ resonate, and the resonant frequency f_z, where the entire primary network resonates.

Initially, the primary inverter idles in a passive mode where $v_{B,P} = 0$, caused by closing both low-side switches U_{2P} and U_{4P}. The approaching AC magnetic field from the secondary pad induces a current i_{1P}, which flows through the primary inverter as described in Section II-A.

The magnitude of I_{1P} can be used to detect an approaching vehicle. As seen in (3a), I_{1P} is proportional to M_{PS} and $V_{B,S}$. When $M_{PS} \neq 0$, power transfer is possible. When $V_{B,S} \neq 0$, the secondary requests power from the primary by applying a voltage at $v_{B,S}$. Thus, some threshold, $I_{1crit,P}$ can be set, such that when $|\bar{I}_{1P}| > \bar{I}_{1crit,P}$, the primary determines power transfer is both possible and desired and begins to switch its H-bridge. To ensure power transfer is achievable, the threshold should be set below the typical current induced

by the secondary, i.e.,

$$I_{1crit,P} < \frac{4\omega_f V_{DC,S} M_{PS}}{\pi X_P X_S} \tag{4}$$

To avoid instability, $I_{1crit,P}$ should be sufficiently high that the induced current from a neighboring primary pad alone will not cause $I_{1P} > I_{1crit,P}$, which would result in system-level daisy-chain instability where a primary is activated by a neighboring primary, rather than a secondary. Where $V_{DC,P}$ is the maximum primary inverter voltage amplitude and M_{PP} is the maximum mutual inductance between neighboring primary pads, this is expressed as

$$I_{1crit,P} > \left| \frac{4\omega_f V_{DC,P} M_{PP}}{\pi X_P^2} \right|. \tag{5}$$

Two aspects of synchronization are relevant here. First, the primary H-bridge switching frequency needs to be synchronized to the secondary H-bridge switching frequency. Second, the phase of $\angle \bar{V}_{B,P}$ needs to be synchronized to the phase of $\angle \bar{I}_{1P}$. However, note that $|\bar{V}_{B,P}|$ and $|\bar{I}_{1P}|$ are irrelevant for synchronization. In effect, signal magnitude impacts detection, while signal phase impacts synchronization.

In the most simple case, the synchronization is accomplished by aligning the zero-crossings of $v_{B,P}$ with the zero-crossings of i_{1P}, or applying a positive voltage $v_{B,P}$ when a positive current i_{1P} is detected. We assume the angle between primary legs $\theta_{AB} = 180°$, so the switches all commute on exactly the zero crossings of i_{1P}. Figure 2 shows a sample switching action, with the voltage and current aligned. Synchronous inversion, in its most basic form, always injects power into the network. At f_f, the injected power will be pushed through the secondary's synchronous rectifier and to the load, and the current i_{1P} will be unaffected by the inverter voltage.

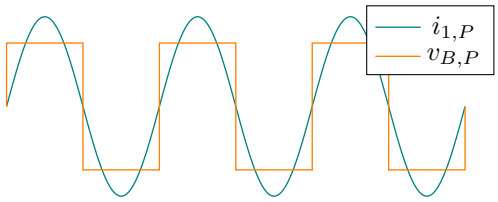

Fig. 2. Sample figure of synchronous inversion in action. Note that the voltage commutes at the exact zero crossing, such that the sign of the voltage and current are always the same.

C. Note on Robustness

Synchronous inversion allows the secondary to initiate power transfer with a primary pad, obviating the need for additional detection hardware. Both primary and secondary use active switching, lowering losses, but external synchronization between neighboring primary pads becomes unnecessary, as the synchronization signal is an inherent property of power transfer and always transmitted by the secondary during power transfer.

There are a number of phenomena that could potentially insert a phase shift into the system. However, any phase shift in the secondary will be matched by a phase shift in the primary, as demonstrated in Sections V and VI. Because the phase on a primary is always tied to the bridge current, the phase of the inverter will adapt in a dynamic system to send power. These features are all enabled over the wireless power transfer link, meaning that detection and synchronization will only fail when power transfer itself fails. This approach increases modularity and robustness of the system. As mentioned previously, the basic approach presented here tends to be unstable; slight modifications to the basic approach to guarantee stability are now detailed in Section III.

III. Practical Considerations and Stability

The approach presented up to this point is relatively simple, but any practical system designed only according to Section II will be unstable. Control of the primary inverter by detecting only the zero crossings of i_{1P} introduces instability to the LCC-compensated system. Qualitatively, synchronous inversion, tends to inject power at whatever frequency it can be absorbed, which may be dominated by either f_f or a natural response frequency of the primary network. In order for the system to behave as expected, considerations must be made to ensure power is only injected at f_f. Two filters, pictured in Fig. 3, affect the phase of the zero crossing detection (Section III-A) and implement the envelope detection filter (Section IV).

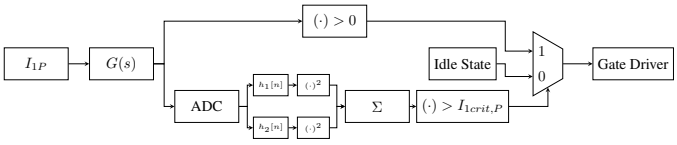

Fig. 3. Control system overview. The upper path implements the design discussed in Section III-A. The lower path implements the design discussed in Section IV.

A. Anti-Resonance Filter

Resonance, where a positive feedback loop causes the inverter to inject power at a frequency not equal to f_f, will naturally occur in the basic system. Any component of $v_{B,P}$ at a natural response frequency of the primary network, calculated below and given as f_z, will increase the in-phase component of i_{1P}. As the current at f_z increases, zero crossings of i_{1P} become dominated by that frequency, and the spectrum of $v_{B,P}$ becomes dominated by f_z. This positive feedback means that the approach in Section II-B will quickly become unstable unless another measure is taken. Besides significant parasitic losses, no power will be received by the secondary, as the primary and secondary bridges would switch at different frequencies. We introduce a filter that enforces a phase difference between i_{1P} and $v_{B,P}$ at some frequencies to avoid positive feedback. This section derives the design of that anti-resonance filter.

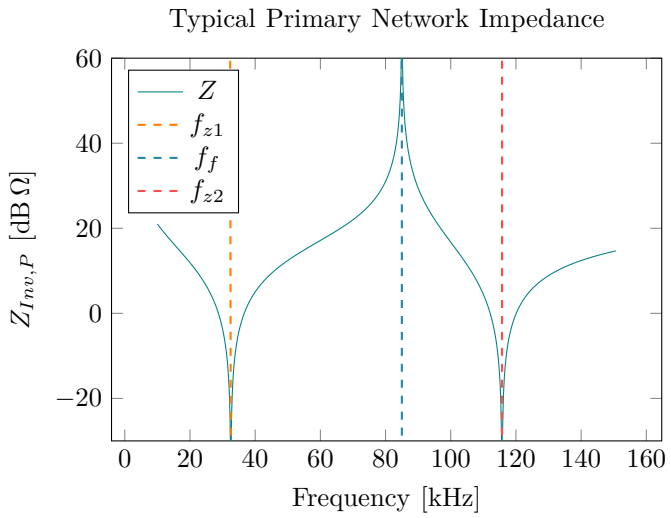

Fig. 4. Impedance of primary network $Z_{B,P}$. Note that relevant pole and zero frequencies are shown. There are two zeros at the corresponding negative frequencies. There is also a pole at the negative corresponding frequency, and at 0 and ∞.

The presence of four reactive components in the primary circuit guarantees that the impedance defined by:

$$Z_{B,P}(j2\pi f) = \frac{\hat{v}_{B,P}}{\hat{i}_{1P}} \tag{6}$$

has four poles and four zeros, with the finite, positive poles and zeros visualized in Fig. 4. One pole is clearly 85 kHz, where i_{1P} and $v_{B,P}$ are decoupled. The other poles are observed by inspection to be 0 and $\pm\infty$. There are also four frequencies where the impedance is zero, $\pm f_{z1}$ and $\pm f_{z2}$. Although the positive and negative frequencies are algebraic necessities, we only consider positive frequencies.

To simplify the calculation of f_{z1} and f_{z2}, consider the resonant frequencies of each loop of the primary circuit and the coil branch:

$$\begin{aligned} f_{l1} &= \frac{1}{2\pi\sqrt{L_{S,P}C_{P,P}}} \\ f_{l2} &= \frac{1}{2\pi\sqrt{L_{Coil,P}\frac{C_{P,P}C_{S,P}}{C_{P,P}+C_{S,P}}}} \\ f_{coil} &= \frac{1}{2\pi\sqrt{L_{Coil,P}C_{C,P}}} \end{aligned} \tag{7}$$

Given the frequencies defined in (7), the zero frequencies, at which the primary circuit will resonate, are calculated as:

$$\begin{aligned} f_{z1} &= \sqrt{\frac{f_{l1}^2+f_{l2}^2}{2}}\sqrt{1+\sqrt{1-\frac{4f_{l1}^2f_{coil}^2}{\left(f_{l1}^2+f_{l2}^2\right)^2}}} \\ f_{z2} &= \sqrt{\frac{f_{l1}^2+f_{l2}^2}{2}}\sqrt{1-\sqrt{1-\frac{4f_{l1}^2f_{coil}^2}{\left(f_{l1}^2+f_{l2}^2\right)^2}}} \end{aligned} \tag{8}$$

In a well-tuned system, where $f_{l1} = f_{l2} = f_f$, we simplify (8) as:

$$\begin{aligned} f_{z1} &= f_f\sqrt{1-\sqrt{1-\frac{f_{coil}^2}{f_f^2}}} \\ f_{z2} &= f_f\sqrt{1+\sqrt{1-\frac{f_{coil}^2}{f_f^2}}} \end{aligned} \tag{9}$$

A frequency spectrum can be introduced by noise, harmonics, or the natural response to energizing the primary. An anti-resonance filter ensures that $v_{B,P}$ only injects power at f_f, and draws power at f_{z1} and f_{z2}, guaranteeing that i_{1P} will not become dominated by a component at f_{z1} or f_{z2}. The small-signal, linearized relationship between the spectra of i_{1P} and $v_{B,P}$ is addressed more thoroughly in Appendix A. However, here it suffices to note that there is no safe attenuation, below which current at f_{z1} or f_{z2} will not cause resonance. This section defines an anti-resonance filter that avoids the positive feedback phenomenon at the resonant frequencies of the primary circuit.

1) Key Operating Principle: To avoid that instability, a first approach is to pass i_{1P} through an anti-resonance filter with the transfer function $G(s)$ and switch inverter states on the zero crossings of $G(i_{1P})$, rather than i_{1P}. The filter needs to be transparent at f_f, so the phase and frequency of $v_{B,P}$ match those of i_{1P}. However, the filter needs to alter the phase of the input signal at f_{z1} and f_{z2}; in all cases, the magnitude is unimportant. The conditions are expressed mathematically as.

$$|\angle G(j2\pi f_{z1})| > 90° \tag{10a}$$
$$|\angle G(j2\pi f_{z2})| > 90° \tag{10b}$$
$$|\angle G(j2\pi f_f)| = 0° \tag{10c}$$

The conditions in (10a) and (10b) ensure that the applied voltage will draw power from the network, reducing the current at f_{z1} and f_{z2} and preventing positive feedback. Any small noise at either resonant frequency will be reduced as the primary draws power at that frequency. Further, (10c) ensures the primary inverter will inject energy into the network at f_f at near-unity power factor.

We note that no second-order filter can realize the phase shift requirements expressed in (10a) and (10b). Earlier work gives an active filter solution [11] or a fully passive solution [12], both comprised of two cascaded second-order filters. However, both [11], [12] require inductors in the filters; to avoid the drawbacks of inductors, that filter can be redesigned as a three-ring-filter as described in [33].

The basic approach is to cascade two second-order filters, to achieve the phase required at f_{z1} and f_{z2}. Both filters have the same transfer function[1]:

$$G_{\frac{1}{2}}(s) = \frac{\frac{s}{\omega_f Q}}{1+\frac{s}{\omega_f Q}+\frac{s^2}{\omega_f^2}}, \tag{11}$$

[1]Note that the zero-crossing detection is independent of signal magnitude; $G_{\frac{1}{2}}(s)$ can be arbitrarily scaled without affecting operation. For simplicity, we assume a form with unity gain at f_f

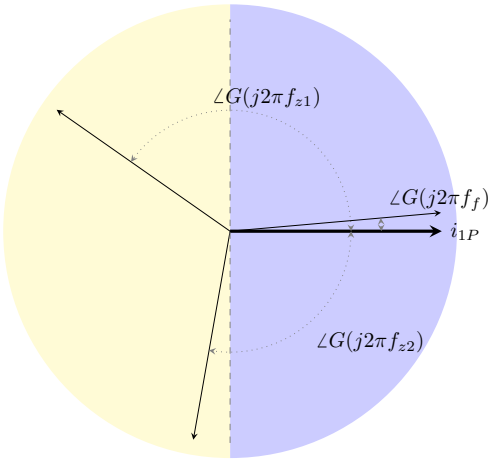

Fig. 5. Sample phase diagram of filter at f_{z1}, f_{z2} and f_f; the values shown here are not derived from any circuit but are merely illustrative. The current phase is assumed to be zero. The phase of the voltage is determined by the filter transfer function $G(s)$. On the right half, $|\angle G(s)| < 90°$ and the power factor is positive; meaning the inverter injects power. On the left half, $|\angle G(s)| > 90°$, the power factor is negative, and the inverter draws power.

and both are individually capable of achieving half the required phase shifts: $\pm 45°$ at f_{z1} and f_{z2}, while maintaining near-zero phase shift at f_f. To achieve those phase shifts, the minimum quality factor for each stage is given by

$$Q > \frac{f_f f_{z1}}{f_f^2 - f_{z1}^2} \tag{12a}$$

$$Q > \frac{f_f f_{z2}}{f_{z2}^2 - f_f^2}. \tag{12b}$$

It can be shown that (12b) guarantees (12a) when $L_{Coil,P} > L_{S,P}$. With the assumption of a well-tuned system and noting the redundancy of (12a), the conditions in (12) reduce to

$$Q > \sqrt{\frac{L_{Coil,P}}{L_{1P}} + \sqrt{\frac{L_{Coil,P}}{L_{1P}}}} \tag{13}$$

B. Stability Analysis

In Section III-A, an anti-resonance filter was introduced to ensure that the primary inverter draws power at f_{z1} and f_{z2}, rather than injecting power. This section addresses the effect of those measures quantitatively. In Section III-B1, the instability of the system without the anti-resonance filter is quickly proved through local linearization. Section III-B2 derives the the necessary conditions for system stability using a quasi-linearized model, which can be expressed as a modification of the linear portion of the loop gain. That section also discusses the characteristics of unstable system behavior. Section III-C summarized the stability criteria.

1) Proof of Instability without Anti-Resonance Filter: In Section III-A, an anti-resonance filter is developed to avoid positive feedback resonance. A more rigorous stability analysis is presented here, assuming a portion of i_{1P} is induced by the secondary; this section evaluates stability in the presence of a current-inducing secondary. A block diagram of the system with zero-crossing detection is shown in Fig. 6.

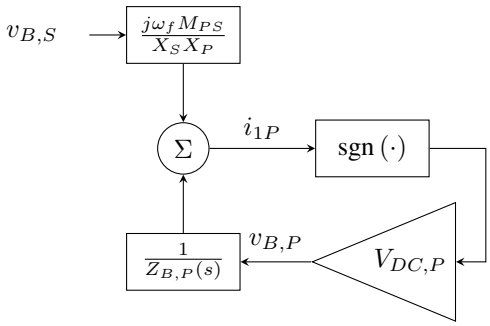

Fig. 6. Block diagram of the zero-crossing detection sgn $(\cdot)$ in the feedback path with no anti-resonance filtering. The contribution of the secondary voltage excitation $v_{B,S}$ to i_{1P} is determined by (3a), and the effect of the primary voltage $v_{B,P}$ is mediated through $Z_{B,P}$. Note that $v_{B,S}$ is assumed to be monoharmonic at f_f.

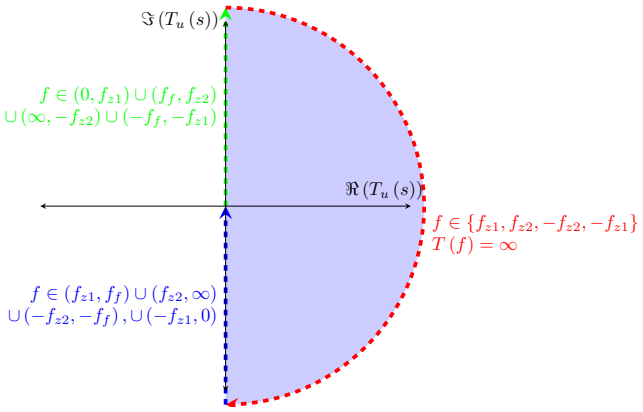

Fig. 7. Nyquist plot of uncompensated loop gain seen in Fig. 6. Note that since the loop in Fig. 6 shows positive feedback, instability is measured by encirclements about $1 + j0$. The entire shaded region is encircled four times, with two poles with positive frequency and two poles with negative frequency. The outer circumference is at infinity.

A fully-linear approximation of the zero-crossing detector is calculated in Appendix A, the result being that a small-signal, linear approximation of sgn $(\cdot)$ is a scalar gain of $2/(A\pi)$, where A is the magnitude of the carrier current at the dominant frequency; here, the portion of i_{1P} at f_f induced on the primary by the secondary. The linear system can demonstrate instability but may not guarantee stability. The major contribution of the secondary is in setting the steady-state amplitude A of the carrier component of i_{1P}. This gives a linearized open-loop gain of

$$\frac{2}{A\pi} \tag{14}$$

The instability of this system can be readily proved with a Nyquist plot. Note that the feedback is positive, so the encirclements should be counted about the critical point $1+j0$, rather than $-1+j0$. By inverting the impedance in Fig. 4, it can be observed that the open-loop transfer function has poles at f_{z1} and f_{z2}, and zeros at 0 and ∞. The phase at every frequency is $\pm 90°$ because there are only reactive elements in the circuit. The Nyquist plot of the uncompensated open-loop gain $T_u(s)$ is given in Fig. 7.

Both positive and negative frequencies are considered in Fig. 7. As expected, the loop gain pole frequencies f_{z1} and f_{z2}

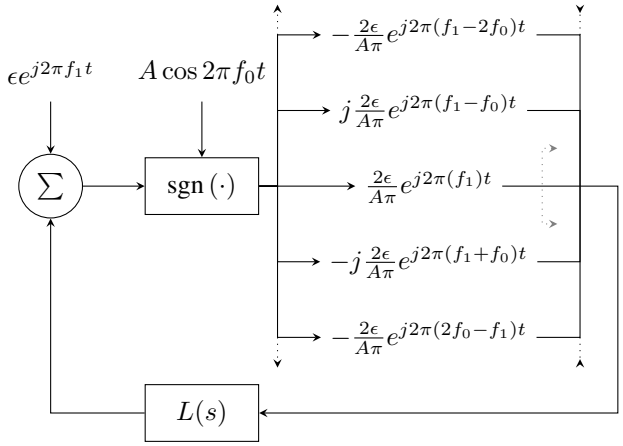

Fig. 8. Quasi-linear small signal model of the zero-crossing detector. Note the system is not linear: a perturbation at one frequency spreads to other frequencies, and the sidelobes are oddly symmetric about the carrier frequency. The loop gain is measured looking into the gray dashed line. Here, $L\left(s\right)$ represents the whole linear portion of the system; in the application discussed here, $L\left(s\right)$ includes the admittance $1/Z$ and the anti-resonance filter $G\left(s\right)$. For simplicity, only the dominant sidelobes are illustrated here.

cause four encirclements, and place poles of the closed-loop system in the right-hand plane. Without the anti-resonance filter, the system is unstable.

2) Stability Conditions with Anti-Resonance Filter: The inclusion of the anti-resonance filter $G\left(s\right)$ visualized in Fig. 9 can stabilize the system. Because the zero-crossing detector introduces additional frequencies, all relevant frequencies should be considered in any closed-loop analysis. The flaw with the fully-linearized model given in Appendix A is that it assumes an infeasible output of the zero-crossing detector, so any analysis done using only the fully linear model is inaccurate. Counterexamples exist where the fully-linearized model predicts stability, but a simulation demonstrates instability. In this section, the system is modeled with the full quasi-linearized model derived in Appendix A, where the "transfer function" of the zero-crossing detector is given by

$$H_n\left(\xi\right)=\sum_{k=-\infty}^{\infty}\left(\frac{2\left(-j\right)^k}{A\pi}G_n\left(\xi-kf_0\right)\right). \tag{15}$$

After the model is developed, a method to test for stability numerically is discussed, along with an approximate analytical method.

Here, the zero-crossing detector acts in the presence of the carrier signal (noted as $A\cos\left(2\pi f_0 t\right)$ in Fig. 8) and in a loop with a linear component $L(s)$. For our purposes, $L(s)=G(s)/Z_{B,P}(s)$. Assume that noise is injected before the current sensor, but the open-loop gain is measured after, visualized in Fig. 8 with the noise $\epsilon d^{j2\pi f_1 t}$ and the loop gain measured from the gray dashed line, where ϵ is an infinitesimally small scalar value.

We consider the spectrum of the noise signal as it passes through the loop. Let $i_0\left(\xi\right)$ be the small-signal spectrum of the noise signal at a frequency f, modeled as a Dirac function in the frequency domain:

$$i_0\left(\xi\right)=\epsilon\delta\left(\xi-f_1\right). \tag{16}$$

The small-signal zero-crossing detector output spectrum $v_0\left(\xi\right)$ is given by

$$v_0\left(\xi\right)=\epsilon\sum_{k=-\infty}^{\infty}\left(\frac{2\left(-j\right)^k}{A\pi}\delta\left(\xi-f_1-kf_0\right)\right) \tag{17}$$

In a feedback loop with a linear transfer function $L\left(s\right)$, the spectrum of the feedback input to the zero-crossing detector i_1 is given by

$$i_1\left(\xi\right)=\epsilon\sum_{k=-\infty}^{\infty}\left(\frac{2\left(-j\right)^k}{A\pi}\delta\left(\xi-f_1-kf_0\right)L\left(j2\pi\xi\right)\right) \tag{18}$$

The linear function $L\left(s\right)$ discussed here is includes the anti-resonance filter $G\left(s\right)$ and the admittance $1/Z\left(s\right)$.

The output of the zero-crossing detector is given by

$$\begin{gathered}v_1\left(\xi\right)=\epsilon\sum_{l=-\infty}^{\infty}\left(\frac{2\left(-j\right)^l}{A\pi}\sum_{k=-\infty}^{\infty}\left(\frac{2\left(-j\right)^k}{A\pi}\delta L(\xi,k,l)\right)\right)\\ \delta L(\xi,k,l)=\delta\left(\xi-f_1-kf_0-lf_0\right)L\left(j2\pi\xi-lf_0\right);\end{gathered} \tag{19}$$

comparing $v_1\left(f_1\right)$ and $v_0\left(f_1\right)$ gives

$$v_1\left(f_1\right)=v_0\left(f_1\right)\frac{2}{A\pi}\sum_{k=-\infty}^{\infty}L(j2\pi f_1+kf_0), \tag{20}$$

which suggests the open-loop transfer function has the periodic form

$$T\left(s\right)=\frac{2}{A\pi}\sum_{k\in\mathbb{Z}}L\left(s+j2\pi kf_0\right) \tag{21}$$

Note that the loop gain is inversely proportional to the amplitude of the carrier signal.

A precise, analytical stability test for an infinite-series transfer function is beyond the scope of this work. Here, stability tests are derived using a Nyquist plot[2], which can be generated with a truncated series[3]. Because the loop has positive feedback, encirclements are counted about the point $(1+j0)$.

With no parasitic resistance in the primary, two classes of encirclements are considered. First, those with infinite radius, where scaling the loop gain has no effect, and second, those with finite radius, where the loop gain can be scaled to stabilize the system.

3) Encirclements with Infinite Radius: Because the loop gain $T\left(s\right)$ is periodic, the number of poles in one period of $T\left(s\right)$ is equal to the number of poles in $L\left(s\right)$. Further, the behavior of $T\left(s\right)$ near any pole is dominated by the corresponding pole in $L\left(s\right)$. Mathematically,

$$\begin{gathered}L\left(s-j2\pi f_0\right)\to\infty\implies\\ T\left(s\right)\approx\frac{2}{A\pi}L\left(s-j2\pi kf_0\right)=\frac{2}{A\pi}L\left(j2\pi\left(\xi-f_0\right)\right),\end{gathered} \tag{22}$$

where k is any integer. So, it is sufficient to consider potential encirclements with infinite radius on the linear system $L\left(s\right)$.

[2]In this discussion, assume that there is no parasitic resistance in the system, so some portions of the Nyquist plot will have infinite radius.

[3]Because there are zeros at $\pm\infty$ in $L(s)$, the system can be truncated with reasonable accuracy by neglecting frequencies $|\xi|\gg|f_{z2}|$

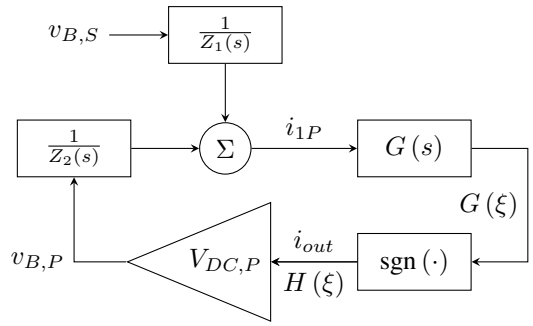

Fig. 9. Block diagram of the zero-crossing detection sgn $(\cdot)$ in the feedback path with no anti-resonance filtering. The contribution of the secondary voltage excitation $v_{B,S}$ to i_{1P} is mediated through the impedance Z_1, and the effect of the primary voltage $v_{B,P}$ is mediated through Z_2. The spectra of th input and output to the zero-crossing detector are shown as $G(\xi)$ and $H(\xi)$, respectively.

TABLE II
PHASE RESPONSE OF COMPENSATED LOOP

Frequency Range	Phase Range
$(0, f_{z1})$	$(270°, 90° + \angle G(j2\pi f_{z1}))$
f_{z1}	$(90° + \angle G(j2\pi f_{z1}), -90° + \angle G(j2\pi f_{z1}))$
(f_{z1}, f_f)	$(-90° + \angle G(j2\pi f_{z1}), -90°)$
(f_f, f_{z2})	$(90°, 90° + \angle G(j2\pi f_{z2}))$
f_{z2}	$(90° + \angle G(j2\pi f_{z2}), -90° + \angle G(j2\pi f_{z2}))$
(f_{z2}, ∞)	$(-90° + \angle G(j2\pi f_{z2}), -270°)$

The essential function of the anti-resonance filter is to modify the phase of the Nyquist plot in Fig. 7. The phase of the anti-resonance filter $G(s)$ varies on the range $(-180°, 180°)$.

The angle ranges of the compensated loop gain, including the zero-crossing detector, anti-resonance filter, DC voltage gain, and impedance in Fig. 9 are given in Table II.

To ensure the pole frequencies f_{z1} and f_{z2} do not encircle the critical point, the phase of $G(s)$ at f_{z1} and f_{z2} is restricted

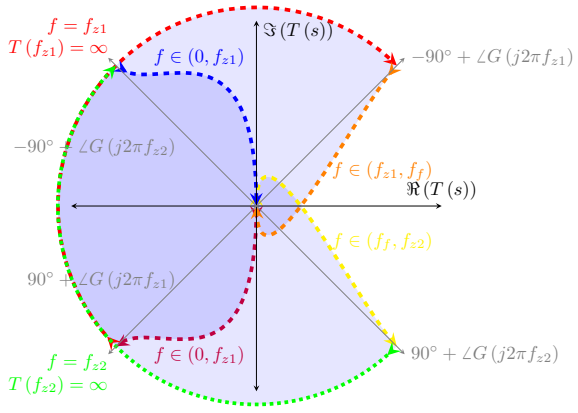

Fig. 10. Nyquist plot of the linear, compensated loop gain $L(s)$ seen in Fig. 9. Note that since the feedback is positive, instabilities are found by encirclements of the point $1 + j0$. Only positive frequencies are shown here, but the pertinent features of the Nyquist plot for negative frequencies are similar and easily extrapolated. Poles of $L(s)$ correspond exactly to poles of $T(s)$.

such that

$$-90° + \angle G(j2\pi f_{z1}) > 0 \tag{23a}$$
$$90° + \angle G(j2\pi f_{z2}) < 0 \tag{23b}$$

Note that the conditions in (23a) and (23b) are equivalent to (10a) and (10b), respectively; the inclusion of the anti-resonance filter as designed is sufficient to avoid encirclements of the critical point with infinite radius. This means that, once the anti-resonance filter is included, any encirclements can be avoided by sufficiently reducing the loop gain when the anti-resonance filter is included.

4) Encirclements with Finite Gain: The conditions in (23) ensure that there will not be an encirclement with infinite radius, but, as seen in Fig. 10, there can be an encirclement with finite radius. A sufficiently dominant carrier current reduces the small-signal loop gain; this section defines the minimum carrier current (induced by the secondary) to ensure there are no encirclements in the Nyquist plot and guarantee stability. In this section, a practical test is defined. Then, to gain more insight, an approximation of a sufficient condition is developed.

The most comprehensive test for stability is with a Nyquist plot of the quasi-linear loop, with the loop $T(s)$ defined in (21). Note that (21) implies that the open-loop transfer function is always periodic on f_0. Because

$$\lim_{s\to\infty} \frac{G(s)}{Z(s)} \to 0, \tag{24}$$

there must be a reasonable approximation of $T(s)$ by a finite series. A Nyquist-like plot can be constructed with that finite series on the interval $\xi \in [-f_f/2, f_f/2]$, and the plot measured for encirclements.

Setting the turn-on threshold forces $A > I_{1crit,P}$, with no feedback and no instability when $I_{1P} < I_{1crit,P}$. The threshold $I_{1crit,P}$ can be defined to force A to be sufficiently great that none of the x-axis crossings encircle the critical point $(1 + j0)$. That is, $I_{1crit,P} > A_{min}$, where A_{min} is the minimum carrier amplitude to move the real-axis crossings to the interval $[0, 1]$, removing any encirclements.

Given the graphical method to determine stability, it is desired to define a more informative and intuitive stability criterion. Because $T(s)$ is periodic, it is sufficient to consider potential encirclements on the range $\xi \in [0, f_f]$. On that range, consider the positive x-axis crossing of the Nyquist plot.

Let f_{e1} be a frequency where the phase of the anti-resonance filter is $90°$, and f_{e2} is the frequency where the phase of the anti-resonance filter is $-90°$. With a high-Q-factor anti-resonance filter, f_{e1} and f_{e2} will be near f_f, with $f_{e1} < f_f$ and $f_{e2} > f_f$. The linear gain $L(s)$ is $G(s)/Z_{B,P}(s)$, and the angles $\angle Z_{B,P}(j2\pi f_{e1}) = 90°$ and $\angle Z_{B,P}(j2\pi f_{e2}) = -90°$. Thus, $L(j2\pi f_{e1})$ and $L(j2\pi f_{e2})$ are real. Further, with a high-Q-factor anti-resonance filter,

$$f_{e1} + f_{e2} \approx 2f_f. \tag{25}$$

Because of the additional frequencies introduced by the zero-crossing detector, the Nyquist plot should be generated with $T(s)$, rather than $L(s)$. Because of the zeros at high

frequencies and 0, and because f_{e1} is close to f_f, most terms of (21) can be neglected:

$$T(j2\pi f_{e1}) \approx \frac{2}{A\pi}\left(L\left(j2\pi\left(f_{e1}-2f_f\right)\right)+L\left(j2\pi f_{e1}\right)\right). \tag{26}$$

Substituting (25) into (26) yields

$$T(j2\pi f_{e1}) \approx \frac{2}{A\pi}\left(L(-j2\pi f_{e2})+L\left(j2\pi f_{e1}\right)\right) \tag{27}$$

Because the system is real, $L(-s) = L(s)^*$. Further, because $L(-j2\pi f_{e2})$ is real,

$$T(j2\pi f_{e1}) \approx \frac{2}{A\pi}\left(L(j2\pi f_{e2})+L\left(j2\pi f_{e1}\right)\right). \tag{28}$$

By a similar argument,

$$T(j2\pi f_{e1}) \approx T(j2\pi f_{e2}), \tag{29}$$

so the stability condition refers to the system behavior at both frequencies.

The stability condition is the real axis crossings of $T\left(j2\pi\xi\right)$, occurring approximately at f_{e1} and f_{e2}, are less than one. This is expressed as

$$\frac{2}{A\pi}\left(\frac{G(j2\pi f_{e1})}{Z_{B,P}\left(j2\pi f_{e1}\right)}+\frac{G(j2\pi f_{e2})}{Z_{B,P}\left(j2\pi f_{e2}\right)}\right)<1 \tag{30}$$

This can be further simplified by noting that $G(s)$ is comprised of two second-order filters defined in (11). The anti-resonance filter gain at f_{e1} and f_{e2} is $\pm j/2$; the condition in (30) can be simplified and solved for A:

$$\frac{1}{\pi}\left(\frac{j}{Z_{B,P}\left(j2\pi f_{e1}\right)}+\frac{-j}{Z_{B,P}\left(j2\pi f_{e2}\right)}\right)<A \tag{31}$$

Note that the phase of $Z_{B,P}\left(j2\pi f_{e1}\right)$ is $90°$, and the phase of $Z_{B,P}\left(j2\pi f_{e2}\right)$ is $-90°$, so both summands are real and positive. The system will be stable when the carrier current (induced by the secondary at f_f) is greater than the threshold in (31). This can be guaranteed by detecting the carrier current envelope, and only initiating primary switching when I_{1P} satisfies the condition on A in (31).

C. Stability Conditions Summary

This section summarizes the conditions for system stability developed in Section III-B. To avoid instability, the anti-resonance filter should provide the phase characteristics in (10), which is assumed to be implemented as two cascaded second-order analog filters. Further, the turn-on threshold current $I_{1crit,P}$ should be high enough to avoid turn-on by a neighboring pad, addressed in (5), and should be high enough to avoid local instability, addressed in (31). These three conditions guarantee that during power transfer, the system is stable.

1) Note on Interference from the Secondary: The value of Z defined here typically considers only the primary network, not any effects from the secondary. The extra element theorem (EET) can be used to modify the expression in (31) to include the effects of the secondary [34]. The EET provides a scaling factor that relates the impedance with the extra element (in this case, impedance reflected from the secondary network to the primary network) to the impedance without it. The scaling factor γ for the expression in (31), which is inversely proportional to the impedance, is given by

$$\gamma = \frac{1-\frac{s^2M_{PS}^2}{Z_{secondary}Z_d}}{1-\frac{s^2M_{PS}^2}{Z_{secondary}Z_n}}, \tag{32}$$

where Z_n and Z_d are nulling and direct impedances and $Z_{secondary}$ is the impedance looking into the secondary from the coil, i.e.,

$$Z_{secondary} = sL_{Coil,S}+\frac{1}{sC_{S,S}}+\frac{sL_{S,S}}{1+s^2L_{S,S}C_{P,S}} \tag{33a}$$

$$Z_n = sL_{Coil,P}+\frac{1}{sC_{S,P}}+\frac{sL_{S,P}}{1+s^2L_{S,P}C_{P,P}} \tag{33b}$$

$$Z_d = sL_{Coil,P}+\frac{1}{sC_{S,P}}+\frac{1}{sC_{P,P}} \tag{33c}$$

Typically, at the f_{e1} and f_{e2}, the correction factor γ will be small, on the order of a few decibels. The effect should be considered but is not the main driving force of instability.

2) Note on Bounded Instability: Instability, as described here, represents any deviation away from the steady-state condition. Instability may not lead to system failure but may simply allow other frequencies to be introduced into $v_{B,P}$, which leads to some power oscillation. If the conditions described here are too exacting, some instability and power ringing may be allowed; especially if a strong EMI filter is included on the primary and secondary. For a conceptual argument for why instability is bounded, note that only the first-order effects have been discussed here. However, the gain decreases as the noise signal increases from an infinitesimal magnitude, bounding the gain and eventually placing the real-axis crossings of hte Nyquist plot with finite radius exactly at the critical point.

Instability presents as an increasing component of $v_{B,P}$ and i_{1P} at some frequency. However, as the component of i_{1P} at that frequency increases, that component becomes the carrier signal, and A begins to increase, which eventually causes (31) to be satisfied. The bounded nature of the instability can also be understood by noting that, when second-order effects are considered, the loop gain is decreased for non-infinitesimal ϵ. As the noise signal increases, the loop gain decreases, and eventually the system becomes stable. A more thorough analysis is beyond the scope of this work, but can easily be verified in simulation by allowing the condition in (31) to be violated by a small margin.

IV. Envelope Detection

So far in this work, references have been made to the turn-on condition

$$I_{1P} < I_{1crit,P}, \tag{34}$$

but no mention of how the envelope of I_{1P} can be measured, especially when i_{1P} contains multiple frequencies. The turn-on condition should be measured only on the component of i_{1P} at f_f, and should give a constant output, regardless of the phase of the input signal. This section describes a discrete-time

envelope detection filter, which can also attenuate other frequencies. The basic approach is highlighted in Section IV-A, with Section IV-B describing key frequency response characteristics of the filter, and Sections IV-B and IV-C discussing how the filter should be designed. Section IV-D summarizes the envelope detector design requirements.

A. Approach Overview

To achieve phase independence, the envelope detection filter is comprised of two discrete, orthogonal filters with complementary phases and equal magnitude gain at f_f; let the filters be defined as $h_1[n]$ and $h_2[n]$ and let the samples of i_{1P} be given as $x[n]$, and let the output of the envelope detector be given by $y[n]$. Then

$$y[n] = \sqrt{\left(\sum_k h_1[k]x[n-k]\right)^2 + \left(\sum_k h_2[k]x[n-k]\right)^2} \tag{35}$$

Suppose i_{1P} is monoharmonic with magnitude α and h_1 and h_2 have unity magnitude gain and complementary phase, such that

$$x[n] = \alpha\cos\left(2\pi f + \phi_1\right) \tag{36a}$$

$$\sum_n h_1[n]x[k-n] = \alpha\cos\left(\phi_1 + \phi_2\right) \tag{36b}$$

$$\sum_n h_2[n]x[k-n] = \alpha\cos\left(\phi_1 + (\phi_2 + 90^\circ)\right) \tag{36c}$$

for some angles ϕ_1 and ϕ_2. Substituting (36b) and (36c) into (35) yields

$$y[k] = |\alpha|, \tag{37}$$

which demonstrates the desired phase-independence properties. A simple approach is let $h_1[n]$ and $h_2[n]$ be derived from a basic low-pass filter $w[n]$, as

$$h_1[n] = 2w[n]\cos\left(2\pi F_{conv} n\right) \tag{38a}$$

$$h_2[n] = 2w[n]\sin\left(2\pi F_{conv} n\right), \tag{38b}$$

where F_{conv} is a discrete-time frequency, and the necessary properties of $w\left[n\right]$ are addressed in Sections IV-B and IV-C. If $F_{conv} = 0.25$, then half the terms in both $h_1[n]$ and $h_2[n]$ are eliminated, simplifying the filters. In that case, both filters will have the strongest response when f_f aliases to $F_{conv} = 0.25$, which requires the sampling frequency f_{sam} to be selected:

$$f_{sam} = \frac{4}{k} f_f, k = 1, 3, 5, ... \tag{39}$$

With the filter structure defined, consideration is now given characteristics and implementation of the low-pass filter.

B. Self-Induced Current Attenuation

It is possible that the primary continues switching even after the secondary is removed; to avoid that, the low-pass filter should attenuate current induced only by the primary. This section defines at what frequencies such a phenomenon may occur and defines a necessary characteristic of the low-pass filter.

Consider the case where some current $\bar{I}_{ind}$ is induced in $\bar{I}_{1P}$; some component of the current is induced from the secondary and some component is induced by $\bar{V}_{B,P}$. Without loss of generality, let the angle $\angle\bar{I}_{1P} = 0$. Let $Z_{B,P}$ again be the impedance seen by the primary inverter. Note that with no resistive elements, $\angle Z_{B,P} = \pm 90^\circ$. Then, we observe the relationship:

$$\bar{I}_{1P} = \bar{I}_{ind} + \frac{|\bar{V}_{B,P}|\angle G(s)}{Z_{B,P}} \tag{40}$$

If there is no induced current, (40) only has a solution when $\angle G(s) = \angle Z_{B,P}$. For convenience, let us define the following quantities:

$$\theta_{Zf} = \angle Z_{B,P}(j2\pi f) \tag{41a}$$

$$\theta_{Gf} = \angle G\left(j2\pi f\right) \tag{41b}$$

Both quantities describe the how much the voltage leads the current at the primary inverter, although both refer to different portions of the current i_{1P}.

When the secondary does not induce any component of the current $\bar{I}_{1P}$ and $\theta_{Zf} \neq \theta_{Gf}$, the frequency is unstable and there is no solution to (40). That instability is observed by letting the current $A \to 0$ in the stability criterion (31). Consider a moment where $\theta_{Zf} > \theta_{Gf}$. In that moment, the current forced by the inverter leads the total current, and the phase of the total current increases. The rate of change is beyond the scope of this paper, suffice it to note that the phases of the voltage and current are unstable and increasing. A continuously increasing phase is equivalent to a higher frequency; thus, when $\theta_{Zf} > \theta_{Gf}$, the frequency will increase.

Similarly, when $\theta_{Zf} < \theta_{Gf}$, the frequency decreases. We refer to the equilibrium frequencies f_{e1} and f_{e2} defined previously where $\theta_{Zf} = \theta_{Gf}$, and define them in terms of the anti-resonance filter quality factor Q:

$$f_{e1} = \frac{f_f}{2Q}\left(\sqrt{1+4Q^2} - 1\right) \tag{42a}$$

$$f_{e2} = \frac{f_f}{2Q}\left(\sqrt{1+4Q^2} + 1\right). \tag{42b}$$

With f_{e1} and f_{e2} defined and the frequency drift phenomena as describe that at those frequencies, the equilibrium frequencies are stable when the condition:

$$\lim_{f \to f_e} \frac{(\theta_{Zf} - \theta_{Gf})}{(f - f_e)} < 0 \tag{43}$$

is met; otherwise, they are unstable.

Note that the frequencies defined in (42) depend on Q. To preserve the integrity of the signal at f_f, Q should generally be as high as possible to minimize the contribution of $v_{B,P}$ to i_{1P} at f_{e1} or f_{e2}. Further note that as $Q \to \infty$, $f_{e1}, f_{e2} \to f_f$ and $Z_{B,P}(f_f) \to \infty$. Thus, a sufficiently high Q will ensure that during steady state operation, the current at f_f dominates the current at either equilibrium frequency.

The steady-state current is determined by the magnitudes $|Z_{B,P}(j2\pi f_{e1})|$ and $|Z_{B,P}(j2\pi f_{e2})|$. When the secondary no longer induces a current i_{1P} at f_f, the primary inverter will drift to operate at f_{e1} or f_{e2}, given in (42). At either of those operating points, the primary network may consume a

large amount of reactive power, and the current i_{1P} may be high, possibly perpetuating operation of the primary inverter. The envelope filter described in (35) should attenuate any contributions from current at f_{e1} or f_{e2}. Let f_{e1} and f_{e2}, continuous-time frequencies, alias to F_{e1} and F_{e2}, discrete-time frequencies. Then let the discrete-time frequency bandwidth β be

$$\beta_1 = \min\left(|F_{conv} \pm F_{e1} + n|\right), n \in \mathbb{Z} \tag{44a}$$

$$\beta_2 = \min\left(|F_{conv} \pm F_{e2} + n|\right), n \in \mathbb{Z} \tag{44b}$$

If F_{e1} and F_{e2} are near 0 or 0.25, $\beta_1 \approx \beta_2 \approx 0.25$, which is the maximum possible value.

The first property of the low-pass filter is that the stopband should begin at most by β, with a maximum stopband gain of $W(\beta)$:

$$W\left(\beta_1\right) <= \frac{\pi}{4V_{DC,P}}(2)Z_{B,P}\left(2\pi f_{e1}\right)I_{1crit,P} \tag{45a}$$

$$W\left(\beta_2\right) <= \frac{\pi}{4V_{DC,P}}(2)Z_{B,P}\left(2\pi f_{e2}\right)I_{1crit,P}; \tag{45b}$$

those expressions are inversely proportional to the AC bridge voltage and the gain of the anti-resonance filter at f_{e1}, and proportional to the impedance and the turn-on threshold. This ensures the primary cannot be active without a secondary.

C. DC Offset and Phase Sensitivity

The sensitivity of the discrete-time filter to a DC offset is determined by the the sensitivity of the lowpass filter to the frequency $F = 0.25$. The required attenuation depends on the maximum expected DC offset; here, let the maximum desired DC gain of the final filter be W_{DC}. Then the design requirement for the lowpass filter is

$$W\left(0.25\right) \leq W_{DC} \tag{46}$$

The DC gain can interfere constructively or destructively with the signal gain, resulting in output variance. Ideally, the DC sensitivity is 0, but that may not be perfectly achievable.

Similarly, any response of the lowpass filter at $F = 0.5$ will also manifest as a phase dependence in the envelope detector. Even if there is no DC offset, any sensitivity will cause a phase dependence on the envelope detector. The attenuation at $F = 0.5$ should be as low as possible while limiting the filter length to a reasonable size.

The passband should be sized to include some robustness to frequency differences; a few hundred hertz is generally sufficient. Some variance in filter passband sensitivity affects the effective turn-on threshold current but does not affect system performance as much as other lowpass filter design parameters.

D. Envelope Detector Summary

The envelope detector can be implemented by multiplying a lowpass filter $w[n]$ with two orthogonal filters to generate $h_1[n]$ and $h_2[n]$, as in (38). Letting $F_{conv} = 0.25$ simplifies the implementation.

The lowpass filter should be designed to:

- Have a relatively small passband, on the order of a few hundred Hertz. Moderate variation is allowed within the passband.
- Have a gain at β that satisfies (45).
- Have the DC gain sensitivity at $F = 0.25$
- Have as low sensitivity as possible at $F = 0.5$, while keeping the filter length reasonable.

Within these rough design parameters, the design and choice of the lowpass filter is beyond the scope of this work.

V. Simulation Validation

The design approach presented thus far is aims to apply for any LCCL system; that is, the coils and compensation are defined to satisfy power transfer, EMI, or other requirements, and the proposed synchronous inversion control scheme is wrapped around an existing design. To validate the synchronous inversion approach to detection and synchronization, the proposed scheme is tailored for an existing hardware system with a primary pad and a secondary pad. The relevant inductances have been simulated in a FEM solver, and the entire system is simulated in a Simulink/Plecs environment. In Section V-A, the basic system parameters are defined. Section V-B assesses the system stability as discussed in Section III-B. Sections V-D to V-F describe the results of various tests.

A. System Overview

The primary coils are a DD design, with the magnetic field orthogonal to the direction of travel. Using the axes defined in the static WPT SAE standard [35], the primary coils measure $2\,\mathrm{m}$ in the y-dimension and $1\,\mathrm{m}$ in the x-dimension. The secondary coils have a complementary DD geometry, measuring $1\,\mathrm{m}$ in the x-dimension by $1\,\mathrm{m}$ in the y-dimension. The system values are given Table III. Note that a small, practical resistance has been included on the inductors for simulation.

The self- and mutual- inductances are measured at a variety of y-misalignments, replicating the varying coupling as a vehicle passes over several subsequent primary pads. In the simulation, the vehicle passes over the primary pads at $30\,\mathrm{km/h}$. The simulations include representative DC bus inductance, resistance, and capacitance values, which tend to filter out the power ripple at double the switching frequency, seen in Fig. 11; the DC bus is assumed to be identical for both the primary and the secondary and the values are also reported in Table III. To simplify the graphs and remove the power ripple, the power is passed through a second-order low-pass filter with a corner frequency of $500\,\mathrm{Hz}$; extensive work exists on eliminating the power ripple; that work is not replicated here.

With (9), the resonant frequencies are determined to be

$$f_{z1} = 41.3\,\mathrm{kHz} \tag{47a}$$

$$f_{z2} = 114\,\mathrm{kHz}, \tag{47b}$$

The design discussed to this point is fixed before the control scheme is implemented. The discussion now turns to the requirements to ensure stability.

TABLE III
SIMULATED COMPONENT VALUES

Component	Value	Component	Value
$V_{DC,P}$	565 V	$V_{DC,S}$	565 V
$L_{S,P}$	$5.62\,\mu\text{H} + 5\,\text{m}\Omega$	$L_{S,S}$	$3.35\,\mu\text{H} + 5\,\text{m}\Omega$
$C_{P,P}$	631 nF	$C_{P,S}$	1.04 µF
$C_{C,P}$	415 nF	$C_{C,S}$	990 nF
$L_{Coil,P}$	$14.2\,\mu\text{H} + 5\,\text{m}\Omega$	$L_{Coil,S}$	$8.10\,\mu\text{H} + 5\,\text{m}\Omega$
$\max(M_{PS})$	1.61 µH	$\min(M_{PS})$	534 pH
$\max(M_{PP})$	−35.3 nH	$\min(M_{PP})$	−73.7 nH
L_{bus}	100 nH	R_{bus}	1 mΩ
C_{bus}	200 µF		

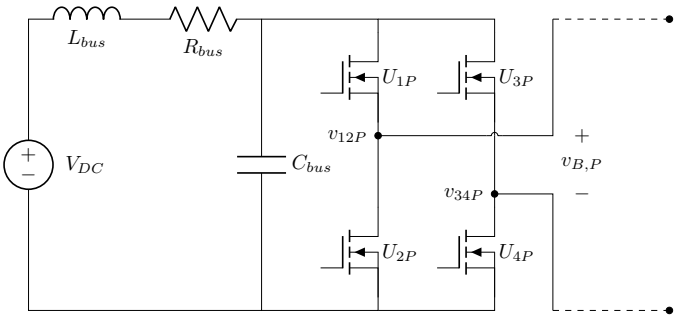

Fig. 11. Diagram of H-bridge with bus capacitance and parasitic inductance and resistance

B. Stability Analysis

Given those design requirements, the stability can be analyzed. Given the resonant frequencies defined in (47), the minimum quality factor is determined to be $Q = 1.67$, as per (13). Ensuring the quality factor exceeds 1.67 meets the first of the three conditions discussed in Section III-C. A quality factor of $Q = 5$ is selected for the anti-resonance filter, satisfying that condition and placing the equilibrium frequencies f_{e1} and f_{e2} at

$$f_{e1} = 76.9\,\text{kHz} \tag{48a}$$
$$f_{e2} = 93.9\,\text{kHz}. \tag{48b}$$

The other stability requirements are that the conditions in (5) and (31) are satisfied, requiring the following, respectively:

$$I_{1crit,P} > 1.67\,\text{A} \tag{49a}$$
$$I_{1crit,P} > 33.8\,\text{A} \tag{49b}$$

Although only one primary pad was used in the simulation, M_{PP} was calculated for a reasonably-placed hypothetical second primary pad for (49a). As discussed in Section III-C1, the secondary can reduce the impedance somewhat, and the current threshold $I_{1cirt,P}$ should be somewhat higher. The system parameters described here imply that an additional 1.4 dB on the turn-on threshold should ensure stability; we let

$$I_{1crit,P} = 40\,\text{A} \tag{50}$$

Recall the the condition in (31) is only approximate, and a Nyquist plot is necessary to confirm stability. The Nyquist plot described in Section III-B4 with $A = I_{1crit,P} = 75\,\text{A}$ is shown in Fig. 12, with a zoomed-in version shown in Fig. 13. As the magnitude of the carrier increases, the x-axis crossings will move towards the origin, with no effect on the stability of the system[4]. By assuming a small series resistance, the Nyquist plot differs slightly from that shown in Fig. 10, replacing the infinite radius with a finite radius. However, the four sections with infinite radius in Fig. 10 correspond to the large loops in Fig. 12. In Figs. 12 and 13, the both primary inductors are assumed to have the 5 mΩ resistance shown in Table III.

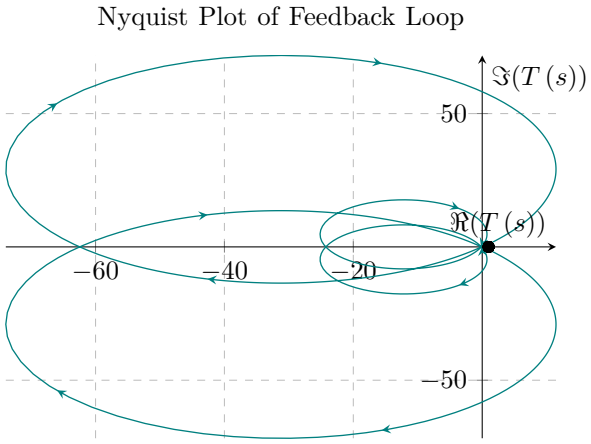

Fig. 12. Nyquist plot of the loop gain. As discussed in Section III-C1, the loop gain is periodic. From this perspective, it is clearly observed that there are no encirclements with infinite or near-infinite (restricted only by parasitic resistance) radius.

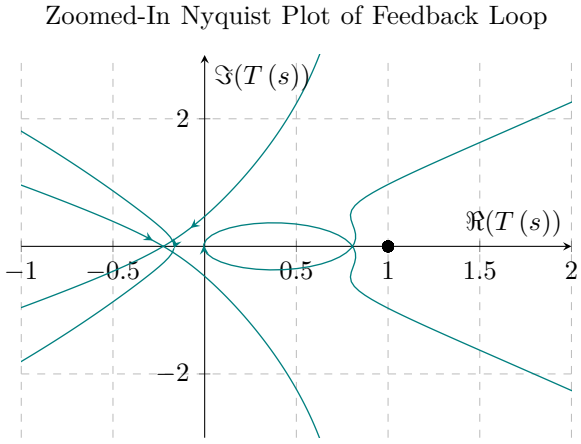

Fig. 13. Zoomed-in Nyquist plot with $A = I_{1crit,P} = 40\,\text{A}$. The chosen value of $I_{1crit,P}$ forces the x-axis crossings occur to the left of unity, guaranteeing there are no encirclements of the critical point and guaranteeing stability.

Four tests are completed here, described more fully in Sections V-C to V-F, respectively:

- Benchmark pulse test: The primary and secondary continuously operate on a shared clock. This has no synchronization or detection, and the shared clock is unrealizable.

[4]While the system remains stable, as the carrier magnitude further increases, the increasing margin between the real axis crossing and the critical points suggests a faster transient attenuation.

- Standard pulse test: The system runs as described thus far; typical operation.
- Half pulse test: While coupled to the primary pad, the secondary pad suddenly stops switching to stop requesting power transfer.
- Phase shift pulse test: Some control schemes may introduce a slight secondary phase shift; in this test, the secondary implements a 180° phase shift during power transfer.

C. Benchmark Pulse Test

The benchmark test simulated ideal laboratory conditions, without the contributions included in this paper and therefore unsuitable for DWPT. Two key differences distinguished the benchmark test from subsequent tests. First, the primary pad remained active during the whole simulation, as it lacked a clear turn-on/turn-off signal. For such a system to be practically realizable, an additional system to detect an approaching secondary and turn on the primary is needed.

Second, the secondary system operated with passive rectification, increasing losses and decreasing total power flow. In effect, this simulation reflected a common paradigm, where the primary drives the power transfer, and the secondary responds.

The waveforms of power transferred through the primary and secondary are shown in Fig. 14a. Note that the primary power and secondary power waveforms are nearly superimposed, with the primary power slightly higher, indicating some system losses. Power transferred and power received are included in Table IV. Generally, the pulse shape is as expected, with a linear ramp up and a relatively flat profile during power transfer. There is an impulse as the secondary powers on, but the profile is otherwise smooth.

D. Standard Pulse Test

The standard operation test simulated the expected operation of the system as described in this paper. All synchronization and detection information was transmitted solely through the induced primary inverter current. The primary and secondary power waveforms are shown in Fig. 14b. Relevant values are shown in Table IV. With this test, a clear turn-on and turn-off transition was expected and observed. Further, the power transfer was expected to be nearly identical to that in the control test, as the primary remained active when the induced voltage was high enough to transfer appreciable power. Finally, as the data link is an intrinsic characteristic of the power link, the data link is as robust and reliable as the power link — a desirable effect of this system.

E. Half Pulse Test

The half pulse test and the phase shift test demonstrate the reliability of the control algorithm against disturbances. In the half pulse, the secondary inverter closes both low-side switches (U_{2S} and U_{4S}) and opens both high-side switches (U_{1S} and U_{3S}), forcing $v_{B,S} = 0\,\mathrm{V}$. As discussed previously, $i_{B,P}$ at f_f is proportional to $v_{B,S}$, so setting $v_{B,S} = 0\,\mathrm{V}$ should stop power transfer. This tests the response of the primary to a bang-bang secondary control scheme. When the secondary H-bridge stops commutation, we expect the $\bar{I}_{B,P}$ to rapidly decay to zero, causing the primary to shut off.

As seen in Fig. 14c, the desired operation is observed. The power transfer follows the first half of the pulse seen in Fig. 14b. Halfway through the pulse, the power drops to 0 and the primary inverter shuts off, as expected. The total power transfer is expected to be roughly half that in the other tests, which is observed in Table IV.

TABLE IV
SIMULATED TEST RESULTS

Test	Primary Energy	Secondary Energy	Efficiency
Benchmark	3.66 kJ	3.53 kJ	96.60 %
Standard	3.13 kJ	3.01 kJ	96.20 %
Half	1.63 kJ	1.57 kJ	96.43 %
Phase Shift	3.13 kJ	3.01 kJ	96.19 %

F. Phase Shift Pulse Test

The third test instantaneously shifted the secondary H-bridge phase by 180°. Some control schemes introduce a small phase shift; the goal of this test is to demonstrate robustness against any phase effects that may occur, and further demonstrate that the primary will always send power to the secondary. Immediately after the phase shift, we expect the flow of power to be reversed. In a successful test, however, the primary will quickly respond and begin sending power to the secondary once again.

As seen in the power transfer plot in Fig. 14d, the power flow direction quickly responds to the phase shift. In fact, the low-pass filter attenuates negative power flow; the total transient duration is very short. Further, total power transferred is nearly as high as in the standard pulse test, as seen in Table IV.

G. Summary

As can be seen in Table IV, no appreciable difference in efficiency exists between the benchmark test and the standard operation test, indicating that the synchronization and detection algorithm presented here works as designed, with each primary pad responding independently to the secondary pad. Further, we observe that the energy transferred during both robustness tests (half pulse and phase shift pulse) are as expected. The efficiency and power transferred vary less than $0.1\,\%$ between the standard test and the phase shift test.

As discussed in Section V-B, the turn-on limit is set sufficiently high to ensure stable operation at turn on. However, this reduces total power transfer. Without changing the power transfer system, this could be fixed by lowering the turn-on current $I_{1crit,P}$. While this would transfer power at $85\,\mathrm{kHz}$ for a longer interval, this would also introduce a component of $v_{B,P}$ at one or both of the equilibrium frequencies f_{e1} and f_{e2}, increasing power ripple and potentially reducing efficiency. The designer must consider whether that instability and potential efficiency reduction, or a shorter power transfer interval, is more acceptable.

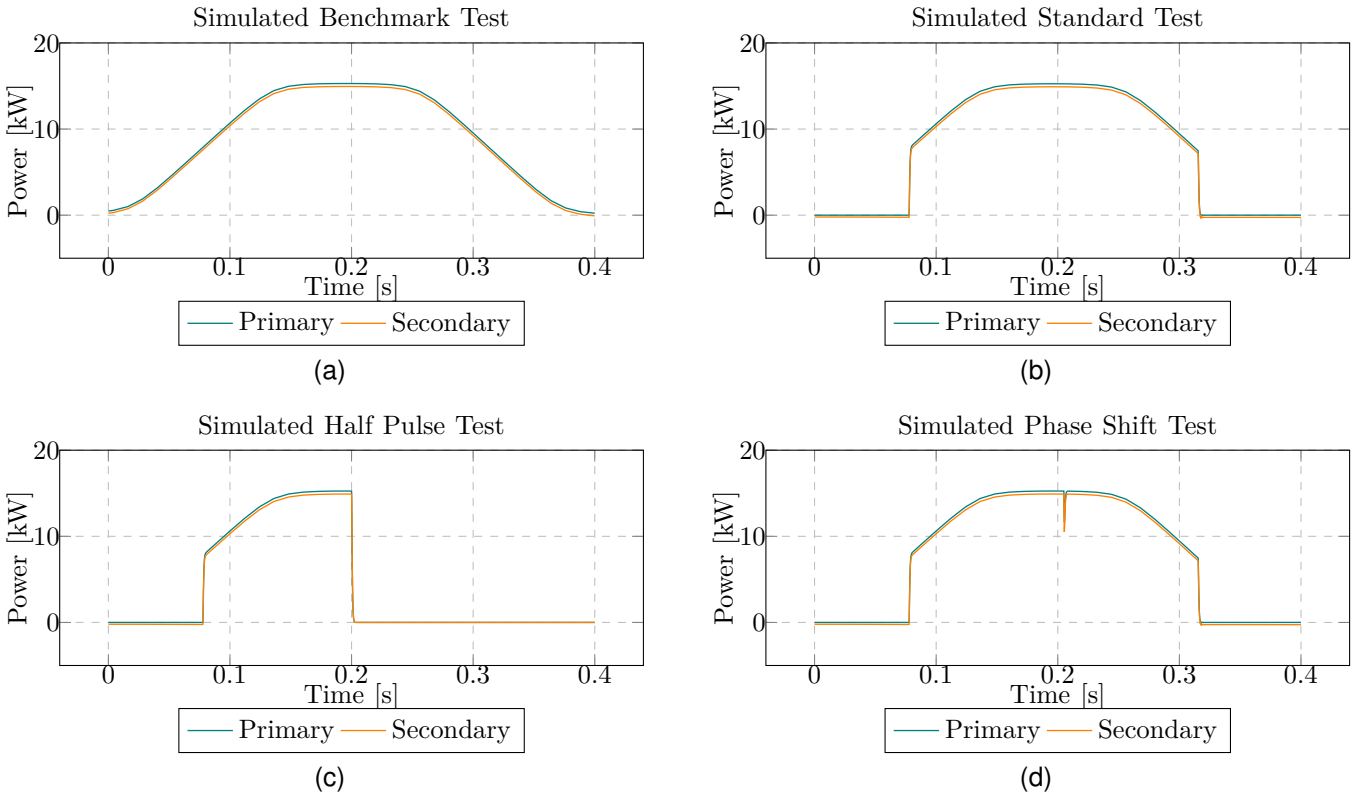

Fig. 14. Plots of simulated primary power (blue) and secondary power (orange) for the four tests. The vertical axis is power in kilowatts; the horizontal axis, time in seconds.

The simulated tests also show a robust primary–secondary communication link. Because all necessary information for synchronization and detection is inherent in power transfer, the communication link is the power link, and both share a strong degree of robustness. The standard operation and robustness tests did not require any additional, weaker communication link, such as a hard-wired connection or an optical coupler.

Finally, the simulation demonstrates that the proposed design is robust against system disturbances. Both the phase-shift pulse and the half-pulse test simulate the extremes in secondary control strategies. In both cases, the primary responds as expected, shutting off when the secondary did, or matching the secondary phase. The simulated results show a comparable performance to an omniscient primary controller, but with no dedicated communication link and significant robustness built into the system.

VI. Hardware Validation

Three hardware tests were run to validate the simulated results: first, a standard test; second, a half-pulse test; and finally, a phase shift test.

This scheme was tested on an existing DWPT system, demonstrating the adaptability of the proposed approach to an arbitrary topology. As in the simulation, an analog anti-resonance filter sensed the primary inverter current to insert the appropriate phase shift. A digital filter, implemented on an FPGA, sampled the filtered, sensed, current to determine the on/off thresholds. The digital turn on/off filter sampled the primary inverter current at 31 kHz.

Due to some hardware limitations, a few minor modifications differentiated the simulated test from the hardware tests:

- Hardware and propagation delays added some phase to the system; to counteract that lag and still achieve ZVS, the system operated at 84.25 kHz, rather than 85 kHz. ZVS, not a concern in simulation, was achieved with current harmonics, as in [30].
- To counteract some jitter in the comparator, the comparator output was not sampled for roughly 700 ns after a transition.
- The setup moved at roughly 1.5 MPH
- Due to space constraints, the secondary reversed direction over the primary pad, rather than passing over the entire pad in a continuous motion.
- To counteract noise in the envelope detector, the system did not begin switching until 25 consecutive iterations of the envelope detector indicated sufficient coupling. Likewise, the primary did not stop switching until 25 consecutive iterations of the envelope detector suggested insufficient coupling. A long buffer was necessary to counteract the relatively slow speed of the setup and some noise in the envelope detector.

The current recirculated, with bus inductances and capacitances as in Fig. 15. The system parameters of the hardware test, on which the simulated design was based, are included in Table V. Note that the benchmark test detailed in Section V-C assumes an unrealizable system, where the secondary and primary are perfectly synchronized. Because the simulated

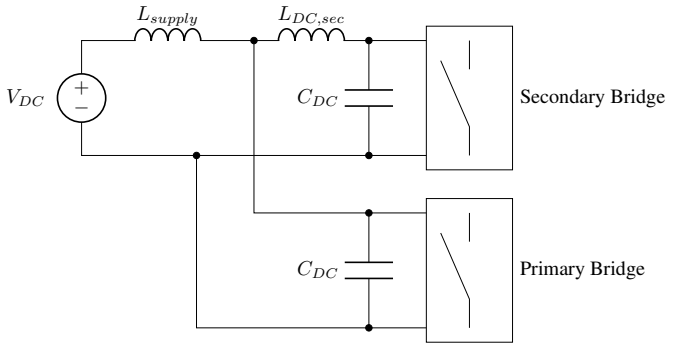

Fig. 15. Diagram of recirculating current with bus capacitances and inductances

system is unrealizable, an experimental verification of the benchmark test is omitted.

A sample oscilloscope screen capture during power transfer is shown in Fig. 16. In that image, the inverted current shows a sharp angle when the voltage inverts; the direction of the current corner indicates inversion, rather than rectification. The setup is shown in Fig. 17.

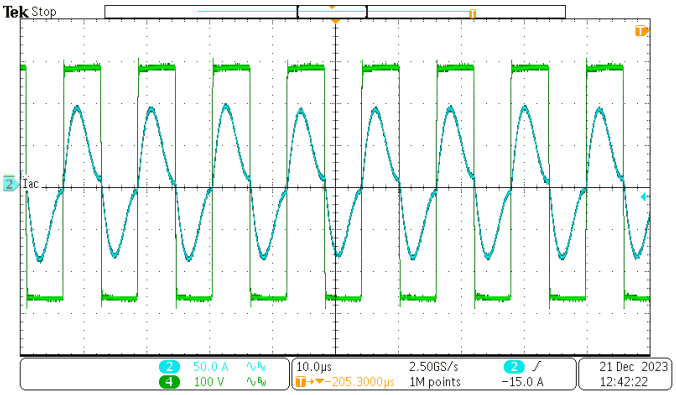

Fig. 16. Oscilloscope screen capture of the primary side during typical operation, with voltage $v_{B,P}$ and current i_{1P} represented.

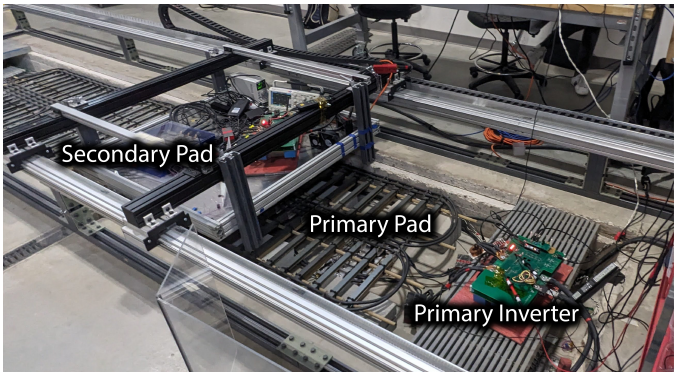

Fig. 17. Picture of the experimental setup. The wireless power transfer coils, inverters, and control board are clearly seen.

The remainder of this section gives results for each hardware test in Sections VI-A to VI-C, with comparison in Section VI-D.

TABLE V
EXPERIMENTAL COMPONENT VALUES

Component	Value	Component	Value
$V_{DC,P}$	300 V	$V_{DC,S}$	300 V
$L_{S,P}$	5.62 µH	$L_{S,S}$	3.35 µH
$C_{P,P}$	631 nF	$C_{P,S}$	1.04 µF
$C_{C,P}$	415 nF	$C_{C,S}$	990 nF
$L_{Coil,P}$	14.2 µH	$L_{Coil,S}$	8.10 µH
$\max(M_{PS})$	1.61 µH	$\min(M_{PS})$	534 pH
$\max(M_{PP})$	−35.3 nH	$\min(M_{PP})$	−73.7 nH
L_{supply}	≈1 µH	$L_{DC,sec}$	960 µH
R_{bus}	1 mΩ	C_{DC}	200 µF

A. Standard Pulse Test

The hardware standard pulse test mirrored the simulated test described in Section V-D. The power waveforms are shown in Fig. 18a, and the energy transferred during both consecutive pulses is shown in Table VI.

Note relatively lower efficiency and power transfer compared to the simulated results. These values could clearly be improved with more ideal components; however, we note an effective proof of concept observed in hardware. In response to an induced current, the primary inverter switches to inject power into the system; while controlling an inverter to inject power could introduce instability, the analog and digital filters work as expected to stabilize the system. The primary only injects power at the switching frequency and turns on and off correctly as the secondary conduction angle is modulated.

B. Half Pulse Test

A hardware half pulse test reflected the simulation described in Section V-E. The secondary inverter operates normally through the first part of the test. Halfway through the pulse, the secondary stops switching its inverter.

The experimental results, plotted in Fig. 18b, match the simulated results in Fig. 14c. For the first portion of the pulse, the power transfer profile closely matches the standard simulation. However, at the midpoint of the pulse, the power drops to zero. The primary shuts off in response to the secondary inverter de-energizing the circuit, demonstrating the ideal primary response to a secondary control. There is some ringing due to the resonance of the DC system, with the DC bus capacitance and line inductance seen in Fig. 15.

C. Phase Shift Pulse Test

As in Section V-F, instantaneous phase shifts in the secondary H-bridge were introduced during power transfer. The primary and secondary power waveforms for the phase shift test, shown in Fig. 18c, match the simulated results shown in Fig. 14d. The total measured energy transferred during both pulses is shown in Table VI.

Note that the power transfer briefly reverses, but quickly recovers, as expected. The most critical issue is the large spike; however, this is due to the under-damped DC bus, rather than the control scheme presented here. Because the DC bus is

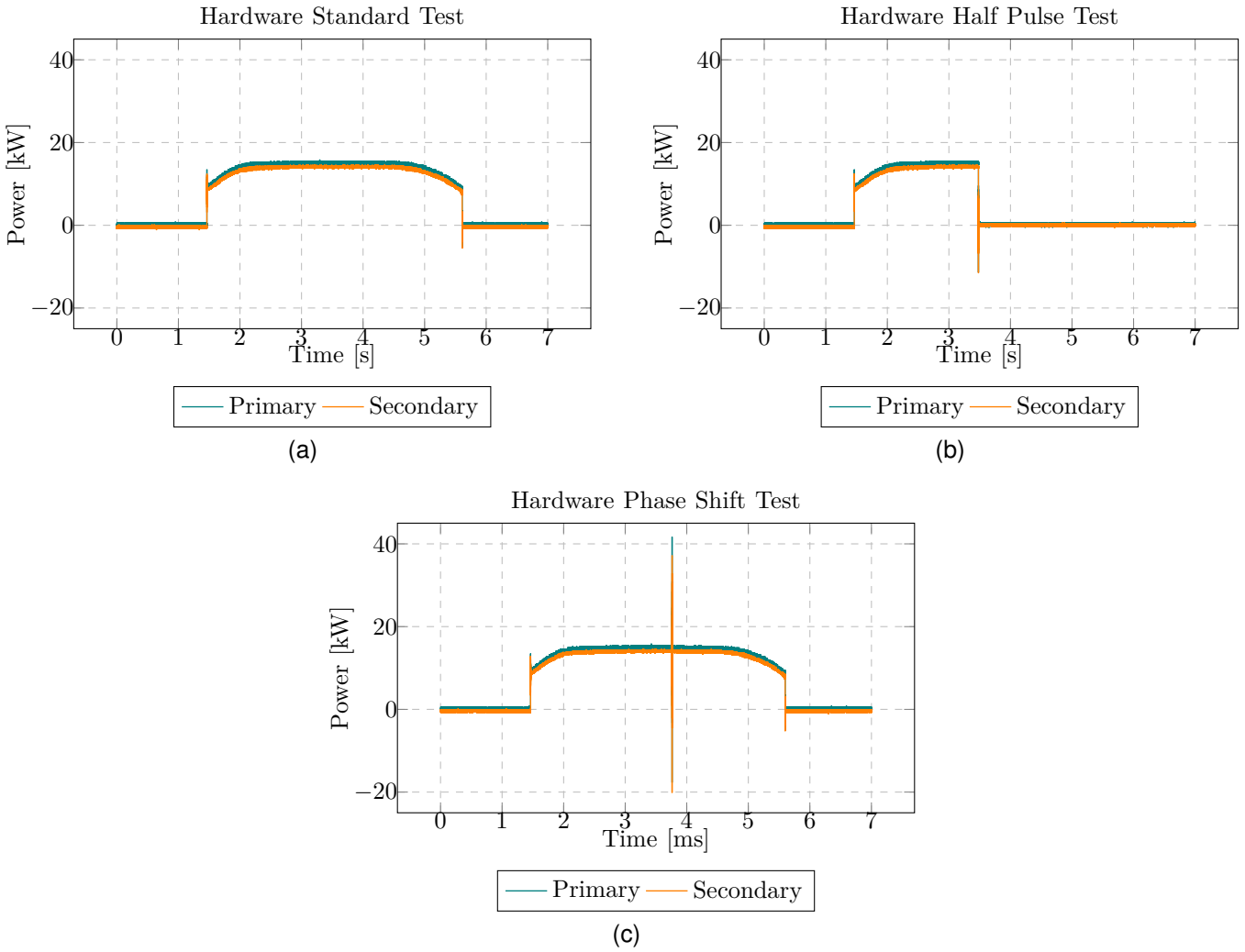

Fig. 18. Plots of experimental primary power (blue) and secondary power (orange) for the three tests. The vertical axis is power in kilowatts; the horizontal axis, time in seconds.

under-damped, there is ringing with nearly a 100 % overshoot. As power reverses direction, the primary and secondary DC currents overshoot, causing a large negative current. As the primary responds and the power again begins to flow in the typical direction, the currents again overshoot. The response time of the system is the delay between the downward spike and the upward spike and is typically on the order of a few cycles. Better damping on the DC bus could eliminate the overshoot, as seen in the simulated results.

The strong robustness against an instantaneous, dramatic phase shift demonstrates that the proposed system will be unaffected by any minor aberration in secondary frequency or phase. The robustness does not simply extend to independence of each primary coil, but also to robustness against secondary aberrations. The simulated results suggest the rinign is an issue with eh DC bus, and not the synchronous inversion control scheme.

D. Summary

The strongest conclusion of the experimental results is the close match between the experimental and simulated results, with only minor deviations. This strong relationship suggests that any simulated design may be implemented in hardware and demonstrates that the results in Section V do not rely on timing precision or numerical precision available only in simulation.

TABLE VI
HARDWARE TEST RESULTS

Test	Primary Energy	Secondary Energy	Efficiency
Standard	58.36 kJ	52.94 J	90.72 %
Half	28.89 kJ	26.00 kJ	89.98 %
Phase Shift	57.91 kJ	52.664 kJ	90.94 %

The experimental standard operation test has some oscillation at turn-on and turn-off, which is not present in the simulated test. Even with those transients, the system performed as expected, turning on and off correctly with the primary accurately synchronizing to the secondary. The transients are due to ringing on the DC bus, where power is measured. A better damping design on the DC bus would eliminate much of the ringing.

With the half-pulse test, the hardware test modeled the simulation while demonstrating the efficacy and robustness of the system. When the secondary stops switching to stop requesting power transfer, the primary responds in kind and both bridges are shorted.

Finally, in the phase-shift test, the primary quickly and correctly responded to a dramatic phase shift in the secondary, demonstrating the robustness of the system to dramatic and minor changes in secondary phase.

VII. Conclusion

The approach to WPT presented here permits a variety of improvements, compared to current technologies. Those advantages are immediately applicable to DWPT scenarios, although certainly not limited to that application. The proposed approach is demonstrated in both simulation and hardware to be responsive to variations in induced primary inverter current.

The responsiveness to dynamic conditions is demonstrated by synchronization to and detection of secondary switching. The primary responds appropriately to differences in the phase and conduction angle of the secondary, demonstrating independence from any open-loop control law, and suggesting independence from a secondary closed-loop control law. Any modulations of the current induced on the primary coil by the secondary are handled well. Thus, effective operation across a range of coupling factors is similarly demonstrated.

Further, because synchronization and detection are realized over the power link, the robustness of the synchronization/detection communication link is inherently as strong as the robustness of the power link. Thus, unlike an optical coupler or a wired connection, a dual-active, secondary-driven DWPT is possible whenever any appreciable wireless power transfer is possible. That is, the proposed system is as robust as the wireless power transfer itself.

This system was developed specifically to reduce the hardware needed for realizable DWPT. Current technologies require external hardware or additional coils to detect an approaching vehicle [27]. A conceptually similar approach segmenting the primary pads has similarly been considered [36].

Such approaches may gather more data for the primary side, but the primary system only needs to detect the presence, not location, of an approaching secondary system. That single bit of information can be determined by measuring the magnitude of the induced primary inverter current, obviating the need for external hardware. Simplifying the primary-side detection to a single-bit choice places responsibility for alignment on the secondary side, which can be accomplished with previously developed technology [37].

By using the synchronous inversion control scheme, both synchronization and detection are accomplished without external hardware. The benefits of a dual-active WPT system, including power regulation and lower losses, are realized without requiring any additional synchronization signal.

The main improvements of this design are as follow:

- The design simplifies the control scheme, with a single turn-on/off condition on the primary and open-loop operation on the secondary.
- The primary coils are activated by the secondary, rather than neighboring primary pads. The active switching on the secondary allows secondary power regulation and lowers semiconductor losses.
- The primary control is simplified by removing the primary clock.
- A rigorous stability criterion is established.
- Imperfectly tuned systems are addressed.
- The principle is demonstrated on a hardware system, transferring $15\,\mathrm{kW}$.

Other approaches exist that can achieve some of these objectives, but no other approach allows all the above objectives to be met simultaneously and robustly. These objectives, essential for dynamic wireless power transfer, are also useful in a variety of other applications. Although there remains space for further advancement of this technology, the development of synchronous inversion has proven possible. With regards to dynamic wireless power transfer, the synchronous inversion technology enables increased elegance in the design and could facilitate future deployment of dynamically, wirelessly powered electric vehicles.

References

[1] B. J. Limb, Z. D. Asher, T. H. Bradley, E. Sproul, D. A. Trinko, B. Crabb, R. Zane, and J. C. Quinn, "Economic viability and environmental impact of in-motion wireless power transfer," *IEEE Trans. Transport. Electrific.*, vol. 5, no. 1, pp. 135–146, March 2019.

[2] S. N. Motapon, E. Lachance, L.-A. Dessaint, and K. Al-Haddad, "A generic cycle life model for lithium-ion batteries based on fatigue theory and equivalent cycle counting," *IEEE Open Journal of the Industrial Electronics Society*, vol. 1, pp. 207–217, 2020.

[3] K. Smith, A. Saxon, M. Keyser, B. Lundstrom, Z. Cao, and A. Roc, "Life prediction model for grid-connected li-ion battery energy storage system," in *2017 American Control Conference (ACC)*, 2017, pp. 4062–4068.

[4] A. Millner, "Modeling lithium ion battery degradation in electric vehicles," in *2010 IEEE Conference on Innovative Technologies for an Efficient and Reliable Electricity Supply*, Sep. 2010, pp. 349–356.

[5] J. V. Barreras, C. Pinto, R. de Castro, E. Schaltz, S. J. Andreasen, P. O. Rasmussen, and R. E. Araújo, "Evaluation of a novel bev concept based on fixed and swappable li-ion battery packs," *IEEE Trans. Ind. Appl.*, vol. 52, no. 6, pp. 5073–5085, Nov 2016.

[6] S. Manzetti and F. Mariasiu, "Electric vehicle battery technologies: From present state to future systems," *Renewable and Sustainable Energy Reviews*, vol. 51, pp. 1004–1012, 2015. [Online]. Available: https://www.sciencedirect.com/science/article/pii/S1364032115006577

[7] A. Fotouhi, D. J. Auger, K. Propp, S. Longo, and M. Wild, "A review on electric vehicle battery modelling: From lithium-ion toward lithium–sulphur," *Renewable and Sustainable Energy Reviews*, vol. 56, pp. 1008–1021, 2016. [Online]. Available: https://www.sciencedirect.com/science/article/pii/S1364032115013921

[8] H. Ambrose, N. Pappas, and A. Kendall, "Exploring the costs of electrification for California's transit agencies," *ITS Reports, 2017(03)*, vol. 03, Oct 2017.

[9] N. Lutsey and M. Nicholas, "Update on electric vehicle costs in the United States through 2030," *The International Council on Clean Transportation*, vol. 2, 04 2019.

[10] A. Ahmad, M. S. Alam, and R. Chabaan, "A comprehensive review of wireless charging technologies for electric vehicles," *IEEE Trans. Transport. Electrific.*, vol. 4, no. 1, pp. 38–63, 2018.

[11] M. Hansen, A. Kamineni, and R. Zane, "Zero-crossing current detection for modular and robust dynamic wireless power transfer," in *2020 IEEE Energy Conversion Congress and Exposition (ECCE)*, Oct 2020, pp. 5207–5214.

[12] M. J. Hansen, R. A. Zane, and A. Kamineni, "Zero-crossing current detection for modular and robust dynamic wireless power transfer," U.S. Patent 11 218 026, Jan. 4, 2022.

[13] A. Kamineni, M. J. Neath, A. Zaheer, G. A. Covic, and J. T. Boys, "Interoperable EV detection for dynamic wireless charging with existing hardware and free resonance," *IEEE Trans. Transport. Electrific.*, vol. 3, no. 2, pp. 370–379, 2017.

[14] S. Li, Z. Liu, H. Zhao, L. Zhu, C. Shuai, and Z. Chen, "Wireless power transfer by electric field resonance and its application in dynamic charging," *IEEE Trans. Ind. Electron.*, vol. 63, no. 10, pp. 6602–6612, 2016.

[15] E. Abramov and M. M. Peretz, "Multi-loop control for power transfer regulation in capacitive wireless systems by means of variable matching networks," *IEEE Trans. Emerg. Sel. Topics Power Electron.*, vol. 8, no. 3, pp. 2095–2110, Sep. 2020.

[16] F. Lu, H. Zhang, H. Hofmann, and C. Mi, "A double-sided lclc-compensated capacitive power transfer system for electric vehicle charging," *IEEE Trans. Power Electron.*, vol. 30, no. 11, pp. 6011–6014, Nov 2015.

[17] J. Dai and D. C. Ludois, "A survey of wireless power transfer and a critical comparison of inductive and capacitive coupling for small gap applications," *IEEE Trans. Power Electron.*, vol. 30, no. 11, pp. 6017–6029, 2015.

[18] U. K. Madawala and D. J. Thrimawithana, "A bidirectional inductive power interface for electric vehicles in v2g systems," *IEEE Trans. Ind. Electron.*, vol. 58, no. 10, pp. 4789–4796, Oct 2011.

[19] H. Wu, T. Mu, X. Gao, and Y. Xing, "A secondary-side phase-shift-controlled llc resonant converter with reduced conduction loss at normal operation for hold-up time compensation application," *IEEE Trans. Power Electron.*, vol. 30, no. 10, pp. 5352–5357, Oct 2015.

[20] G. Buja, M. Bertoluzzo, and K. N. Mude, "Design and experimentation of WPT charger for electric city car," *IEEE Trans. Ind. Electron.*, vol. 62, no. 12, pp. 7436–7447, 2015.

[21] H. Hu, T. Cai, S. Duan, X. Zhang, J. Niu, and H. Feng, "An optimal variable frequency phase shift control strategy for zvs operation within wide power range in ipt systems," *IEEE Trans. Power Electron.*, vol. 35, no. 5, pp. 5517–5530, 2020.

[22] X. Zhang, T. Cai, S. Duan, H. Feng, H. Hu, and J. Niu, "A harmonic-considered time domain model of lcc compensated wireless power transfer systems," in *2018 IEEE International Power Electronics and Application Conference and Exposition (PEAC)*, 2018, pp. 1–5.

[23] S. Y. Chu, X. Cui, X. Zan, and A.-T. Avestruz, "Transfer-power measurement using a non-contact method for fair and accurate metering of wireless power transfer in electric vehicles," *IEEE Trans. Power Electron.*, vol. 37, no. 2, pp. 1244–1271, Feb 2022.

[24] J. Pries, V. P. N. Galigekere, O. C. Onar, and G.-J. Su, "A 50-kw three-phase wireless power transfer system using bipolar windings and series resonant networks for rotating magnetic fields," *IEEE Trans. Power Electron.*, vol. 35, no. 5, pp. 4500–4517, May 2020.

[25] C. Cheng, F. Lu, Z. Zhou, W. Li, C. Zhu, H. Zhang, Z. Deng, X. Chen, and C. C. Mi, "Load-independent wireless power transfer system for multiple loads over a long distance," *IEEE Trans. Power Electron.*, vol. 34, no. 9, pp. 9279–9288, Sep. 2019.

[26] Y. Sakayanagi, S. Togawa, K. Konagaya, and Y. Kuwahara, "Wireless power transmission for a traveling mobility scooter," in *2016 IEEE Wireless Power Transfer Conference (WPTC)*, 2016, pp. 1–3.

[27] A. N. Azad, A. Echols, V. A. Kulyukin, R. Zane, and Z. Pantic, "Analysis, optimization, and demonstration of a vehicular detection system intended for dynamic wireless charging applications," *IEEE Trans. Transport. Electrific.*, vol. 5, no. 1, pp. 147–161, 2019.

[28] G. R. Nagendra, L. Chen, G. A. Covic, and J. T. Boys, "Detection of EVs on ipt highways," *IEEE Trans. Emerg. Sel. Topics Power Electron.*, vol. 2, no. 3, pp. 584–597, Sep. 2014.

[29] Z. Pantic, S. Bai, and S. M. Lukic, "Zcs *lcc*-compensated resonant inverter for inductive-power-transfer application," *IEEE Trans. Ind. Electron.*, vol. 58, no. 8, pp. 3500–3510, Aug 2011.

[30] M. Hansen, A. Kamineni, and R. Zane, "Current harmonics dead time design method to achieve ZVS with non-linear output capacitance," in *2021 IEEE Energy Conversion Congress and Exposition (ECCE)*, Oct 2021, pp. 2189–2196.

[31] O. Yu, C. Yeh, and J. Lai, "Synchronous rectifier design considerations for solid-state transformer light-load stability," in *2018 Asian Conference on Energy, Power and Transportation Electrification (ACEPT)*, 2018, pp. 1–5.

[32] O. Yu, C.-S. Yeh, and J.-S. Lai, "Sequential parallel switching for drain-source synchronous rectifier efficiency and light-load stability improvement," in *2019 IEEE Applied Power Electronics Conference and Exposition (APEC)*, March 2019, pp. 463–467.

[33] M. E. V. Valkenburg, *Analog filter design*. Holt, Rinehart, and Winston, 1982.

[34] R. Middlebrook, "Null double injection and the extra element theorem," *IEEE Trans. Educ.*, vol. 32, no. 3, pp. 167–180, Aug 1989.

[35] "Wireless power transfer for light-duty plug-in/electric vehicles and alignment methodology," *SAE Standard J2954_202208*, Aug 2022. [Online]. Available: https://www.sae.org/standards/content/j2954_202208

[36] Q. Deng, J. Liu, D. Czarkowski, M. Bojarski, J. Chen, W. Hu, and H. Zhou, "Edge position detection of on-line charged vehicles with segmental wireless power supply," *IEEE Trans. Veh. Technol.*, vol. 66, no. 5, pp. 3610–3621, 2017.

[37] P. Sukprasert, B. M. Nguyen, and H. Fujimoto, "Estimation of lateral displacement of electric vehicle to an alignment of wireless power transmitters," in *2014 IEEE/SICE International Symposium on System Integration*, 2014, pp. 542–547.

APPENDIX

Although the zero-crossing detection is nonlinear, it can be locally linearized. Consider a carrier signal g_c with amplitude A at frequency f_0, summed with some infinitesimal noise signal g_n at frequency f_1:

$$\begin{aligned} g_c(x) &= A\cos\left(2\pi f_0 x\right) \\ g_n(x) &= \epsilon\cos\left(2\pi f_1 x\right) \\ g(x) &= g_c(x) + g_n(x), \end{aligned} \tag{51}$$

where ϵ is some infinitesimally small value. The signals in (51) have corresponding Fourier decompositions

$$\begin{aligned} G_c(\xi) &= \frac{A}{2}\left(\delta(\xi - f_0) + \delta(\xi + f_0)\right) \\ G_n(\xi) &= \frac{\epsilon}{2}\left(\delta(\xi - f_1) + \delta(\xi + f_1)\right) \\ G(\xi) &= G_c(\xi) + G_n(\xi). \end{aligned} \tag{52}$$

Let the zero-crossing detection be modeled by the sign function,

$$h(g(x)) = \operatorname{sgn}\left(g(x)\right), \tag{53}$$

with values in the set $\{-1, 0, 1\}$. It is desired to determine the spectrum of $h(g(x))$, to analyze local stability.

When ϵ is sufficiently small, the only effect of the noise on the sign of $f(x)$ is some small shift in the zero crossings. Let

$$h(g(x)) = h_c\left(g_c\left(x\right)\right) + h_n\left(g_c\left(x\right), g_e\left(x\right)\right), \tag{54}$$

where h_c is a square wave, with a Fourier decomposition of

$$H_c\left(\xi\right) = \frac{2}{\pi}\left(\delta(\xi - f_0) + \delta(\xi + f_0)\right), \tag{55}$$

and $h_n\left(g_c\left(x\right), g_e\left(x\right)\right)$ is some correction function, with values in the set $\{-2, 0, 2\}$. Naturally, h_c contains other harmonics, but in the linearized model, only the fundamental component is considered. The function h_n can be visualized as a series of peaks, as in Fig. 19. The Fourier transform of h^* can be calculated by

$$\int_{-\infty}^{\infty} h_n(g_c(x), g_e(x)) e^{-j2\pi\xi x} dx \tag{56}$$

It is necessary to formulate the integral in (56) as a summation of the peaks in h_n on the edges of the carrier signal $g_c(x)$. Let $\Delta_{n,f}$ be the width of the n^{th} pulse in h_n, occurring on a falling edge of $g_c\left(x\right)$; similarly, let $\Delta_{n,r}$ be the width of the n^{th} pulse in h_n, occurring on a rising edge of $g_c\left(x\right)$. The falling edges of $g_c\left(x\right)$ occur at

$$x = \frac{n + 0.25}{f_0}, \tag{57}$$

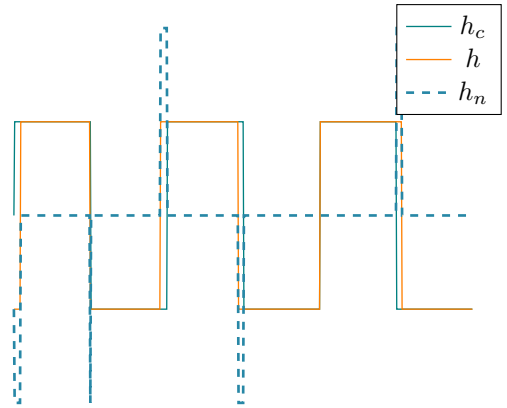

Fig. 19. Sample figure of synchronous inversion in action. Note that the voltage commutes at the exact zero crossing, such that the sign of the voltage and current are always the same.

with the rising edges occurring at

$$x = \frac{n - 0.25}{f_0}, \tag{58}$$

where $n \in \mathbb{Z}$.

On the falling edges, if $\Delta_{n,f} > 0$, the value of h_n on that interval is 2. If $\Delta_{n,f} < 0$, the value of h_n on that interval is -2. Regardless of the sign of $\Delta_{n,f}$, the portion of (56) corresponding to falling edges can be expressed as

$$\sum_n \left(\int_{x=\frac{n+0.25}{f_0}}^{x=\frac{n+0.25}{f_0}+\Delta_{n,f}} 2e^{-j2\pi\xi x} dx \right). \tag{59}$$

This can also be expressed as

$$\sum_n E\left[\int_{x=\frac{n+0.25}{f_0}}^{x=\frac{n+0.25}{f_0}+\Delta_{n,f}} 2e^{-j2\pi\xi x} dx \right]. \tag{60}$$

Note that in the linearized system, we can ignore the harmonics. As will be discussed later, two frequencies are required to represent the pulses. We can replace the pulses seen in Fig. 19 with a series of sinusoids, with coefficients α_k to be determined hereafter, such that pulses are equivalently approximated by the series:

$$s(x) = \sum_k \alpha_k e^{j2\pi f_k x}, \tag{61}$$

which has the spectrum

$$\sum_k \alpha_k \delta(\xi - f_k). \tag{62}$$

In (60), the expectation is calculated over a period of the carrier signal. Over one period and neglecting harmonics, the expectation with the sinusoidal approximation can be calculated as

$$E\left[\int_{\frac{n}{f_0}}^{\frac{n1}{f_0}} s(x) e^{-j2\pi\xi x} dx \right] = \begin{cases} \frac{\alpha_k}{f_0}, & \xi = f_k \\ 0, & \text{otherwise} \end{cases} \tag{63}$$

The zero-crossing detector output spectrum, defined in (62), can be calculated by equating the expectation in (63) to the summand in (60), which will yield the values of α_1 and α_2. Combined with the definition in (62), those values produce spectrum of the zero-crossing detector output.

The balance of this appendix solves for α_1 and α_2. To that end, it is necessary to define the values $\Delta_{n,f}$; a similar process can be used to determine the values of $\Delta_{n,r}$. We solve for

$$\begin{aligned} A\cos(2\pi f_0 x) + \epsilon\cos(2\pi f_1 x) &= 0 \\ x &= \frac{n + 0.25}{f_0} + \Delta_{n,f}. \end{aligned} \tag{64}$$

It can be shown that (64) is exactly equal to

$$\begin{aligned} 0 = &- A\sin(2\pi f_0 \Delta_{n,f}) \\ &+ \epsilon\cos\left(\frac{2\pi f_1 (n + 0.25)}{f_0}\right)\cos(2\pi f_1 \Delta_{n,f}) \\ &- \epsilon\sin\left(\frac{2\pi f_1 (n + 0.25)}{f_0}\right)\sin(2\pi f_1 \Delta_{n,f}) \end{aligned} \tag{65}$$

for $n \in \mathbb{Z}$. Because $\Delta_{n,f}$ is small for an infinitesimal ϵ, the small-angle approximation can be used to simplify (65) as

$$\begin{aligned} 0 = &- 2A\pi f_0 \Delta_{n,f} + \epsilon\cos\left(\frac{2\pi f_1 (n + 0.25)}{f_0}\right) \\ &- \epsilon\sin\left(\frac{2\pi f_1 (n + 0.25)}{f_0}\right) 2\pi f_1 \Delta_{n,f} \end{aligned} \tag{66}$$

Noting that $|\epsilon f_1 \sin(\cdot)| \ll |f_0|$ for an infinitesimal ϵ, it is observed that (66) has an approximate solution at

$$\Delta_{n,f} = \frac{\epsilon}{A} \frac{\cos\left(\frac{2\pi f_1 (n+0.25)}{f_0}\right)}{2\pi f_0}. \tag{67}$$

Now, we can equate the summand in (60) to (63), in order to solve for α_1. and α_2. Because $\Delta_{n,f}$ is infinitesimal, the Leibniz integral rule and first-order approximation reduce the summand in (60) to

$$E\left[\Delta_{n,f} 2e^{-j2\pi\xi\frac{n+0.25}{f_0}}\right]. \tag{68}$$

Substituting (67) into the expression yields

$$\frac{\epsilon}{A\pi f_0} E\left[\cos\left(2\pi\frac{f_1}{f_0}(n + 0.25)\right) e^{-j2\pi\xi\frac{n+0.25}{f_0}}\right]. \tag{69}$$

which expands to

$$\frac{\epsilon}{2A\pi f_0} E\left[e^{j2\pi(n+0.25)\left(\frac{f_1}{f_0} - \frac{\xi}{f_0}\right)} + e^{-j2\pi(n+0.25)\left(\frac{f_1}{f_0} + \frac{\xi}{f_0}\right)}\right]. \tag{70}$$

This reduces to

$$E\left[\Delta_{n,f} 2e^{-j2\pi\xi\frac{n+0.25}{f_0}}\right] = \begin{cases} \frac{\epsilon(-j)^k}{2A\pi f_0}, & \xi = \pm f_1 + k f_0, k \in \mathbb{Z} \\ 0 & \text{otherwise} \end{cases} \tag{71}$$

In assuming the pulses could be approximated by a series of sinusoids, additional frequencies were introduced. Those additional frequencies can be defined by equating (74) with (63) and substituting into (62), which yields the output spectrum

$$\sum_{k\in\mathbb{Z}} \frac{\epsilon(-j)^k}{2A\pi} \left(\delta(\xi - f_1 - k f_0) + \delta(\xi + f_1 - k f_0)\right). \tag{72}$$

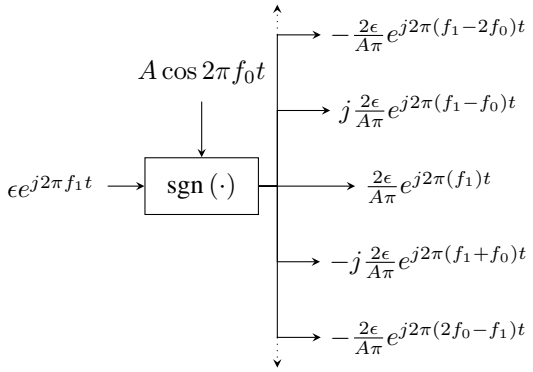

Fig. 20. Small-signal model for a zero-crossing detector, including additional sidelobe frequencies, due to the non-linearity of the sign function. For simplicity, only 2 sidelobe frequencies are shown on each side, although an infinite number are present. Distinct paths exist for each central and sidelobe frequency. Note that a real input signal will still produce a real output signal.

However, (72) only considers the effects of the noise signal on the falling edges of the carrier wave; a similar effect can be shown to be effected on the rising edges of the carrier wave. Thus, the effect should be doubled to account for both effects. The quasi-linear, small-signal model of the zero-crossing detector is given by

$$H_n(\xi) = \sum_{k\in\mathbb{Z}} \left(\frac{2(-j)^k}{A\pi} G_n(\xi - kf_0) \right) \tag{73}$$

which is illustrated in Fig. 20. This can only be quasi-linear, as additional frequencies are introduced. However, accounting for these additional frequencies is essential; it is possible for an additional frequency to couple with a base frequency and increase the effective loop gain, resulting in system instability.

Although (71) includes components across an infinite spectrum of frequencies, some of the higher frequencies can be neglected if the gain of the transfer function is sufficiently low at frequencies near or above $2f_0$. In such cases, (73) can be approximated by:

$$H_n(\xi) = \sum_{k=-2}^{2} \left(\frac{2(-j)^k}{A\pi} G_n(\xi - kf_0) \right) \tag{74}$$

The fully linear system, excluding all frequencies not present in the noise spectrum, is further simplified to

$$H_n(\xi) = \frac{2}{A\pi} G_n(\xi) \tag{75}$$

CHAPTER 6

ARTIFICIAL NEURAL NETWORK MODELING OF WPT MAGNETIC FIELDS IN AN EV APPLICATION

This chapter is a replication of a journal article currently under review, submitted to IEEE Transactions on Magnetics [29]. The work is based on previous work by the same author [30].

Artificial Neural Network Modeling of WPT Magnetic Fields in an EV Application

Matthew J. Hansen[1], *Student Member, IEEE*, Seho Kim[2], *Member, IEEE*, and Abhilash Kamineni[1], *Member, IEEE*
[1]Department of Electrical and Computer Engineering, Utah State University, Logan, UT, 84322 USA
[2]Department of Electrical, Computer and Software Engineering, University of Auckland, Auckland, New Zealand

One promising approach to reducing range anxiety in electric vehicles (EVs) is wireless power transfer (WPT), which includes in-motion or dynamic wireless power transfer (DWPT). Many different classes of EVs could potentially use the same infrastructure. With the rapid development of WPT solutions, and with many classes of EVs potentially leveraging the same infrastructure, there is a need to rapidly qualify and optimize WPT coil designs, and compare tradeoffs inherent in the design. To that end, an artificial neural network (ANN) is trained to estimate 4,203 magnetic parameters of a wireless power transfer (WPT) system. The network is trained on 12,855 unique combinations of coil geometries and coil alignments. Appropriate data representation schemes and cost functions to train the ANN are introduced. The trained ANN is shown to effectively reproduce data generated by a finite element method (FEM); comparison of FEM data to experimental results is outside the scope of this work.

***Index Terms*—wireless power transfer, inductive power transfer, artificial neural network, machine learning, electric vehicle**

I. Introduction

THE adoption of electric vehicles (EVs) represents a significant opportunity to reduce greenhouse gas (GHG) and other pollutant emissions. However, EVs require a paradigm shift to power the vehicles. Many approaches to power delivery have been considered, including wireless power transfer. In this work, we detail the design and training of an artificial neural network (ANN) to improve coil design for wireless power transfer (WPT), including multiple classes of EVs. The focus of this paper is on the training of and data representation within a neural network, and questions of training data reliability, which is generated by finite element method (FEM) analysis, are beyond the scope of this work.

WPT is used in a variety of applications, including electric vehicles (EVs) [1], [2], medical devices, and consumer electronics [3]. In some cases, a single primary coil may need to send power to secondary coils with varying geometries, power levels, air gaps, and misalignments [3], which may be the case for next-gen EV. In those applications, powering multiple vehicle classes from a single primary coil may be possible.

WPT can be broadly classified into two groups: capacitive power transfer (CPT) and inductive power transfer (IPT). While significant research has been completed in the field of CPT [4]–[7], especially for EVs, currently only IPT is supported by the SAE J2954 standard [8], which defines static WPT (SWPT, or WPT to a parked vehicle). A standard is currently in progress to define dynamic WPT (DWPT, or WPT to an in-motion vehicle).

Significant work has been done in the EV WPT space, including developing control algorithms [1], [9]–[16], topologies [1], [17] and coil design [16], [18], [19]. This work aims to inform developing standards and aid coil design once the standard is finalized. In recent years, ANNs have been used to control WPT systems [20], [21]. Here, we build on the rich work on coil design and ANNs in WPT to complement previous work on control algorithms; the result is an ANN that can aid in designing an optimal coil geometry.

To design an optimal coil geometry, many candidate geometries need to be quickly characterized. If the characterization is differentiable, gradient-descent algorithms can aid the optimization process. Thus, there is a need for a fast, differentiable function to characterize WPT coil geometries as a necessary first step to determine optimal, interoperable coil geometries. An ANN is an ideal tool for this end; it can improve simulation time compared to industry-standard FEM techniques (forward propagation), and the gradient of a given objective function with respect to the coil geometry parameters can be easily calculated (backpropagation). Both forward- and back-propagation in ANNs are well-researched and well-understood [22].

ANN characterization of inductors and WPT coils for EVs is well-studied. In [23], an ANN is trained to model the performance parameters of a simple converter. In [24], an ANN is trained to model 40 inductor parameters. One limitation of [23], [24] is that only one inductor is considered, not a pair of coupled coils.

The work in [25] does consider both a transmitter and receiver, but the focus is somewhat different from the focus here; the work only attempts to output the coupling coefficient, and the ANN input is the primary coil current. The work in [26] similarly considers two coils but optimizes to reduce the stray magnetic field. However, the approach in [26] is of limited applicability to EVs, as field-guiding ferrite is typically present in EV applications.

In [2], [27], [28], an ANN is trained to model coupled inductors for WPT, while a genetic algorithm uses the trained ANN to determine an optimal coil geometry, and the coil design is experimentally validated. However, the model presented in [2], [28] condenses information on the output stray field. This work aims to expand on that work, without simplifying the stray field representation.

However, in this work, a neural network is developed with significantly more output values than in any of [2], [23]–[26], [28]. While the specific figure of merit is beyond the scope of this work, a good figure of merit minimizes the stray magnetic field, copper losses, and ferrite losses, while maximizing primary–secondary coupling (especially when the primary and secondary pads are misaligned). Thus, we train an ANN to characterize self and mutual inductances, loss-inducing magnetic fields, and stray magnetic fields for a range of coil geometries used in WPT for EVs.

The goal of this approach is to define a neural network that models relevant parameters for a double-D (DD) pad topology. This work expands upon previous scholarship in its scope; the quantity of data this model represents exceeds that in existing scholarship. The neural network model also has 4,203 outputs, providing a powerful tool for analyzing coil geometries. Another key contribution of this work is in the data representation and ANN training algorithms. Decisions on how to represent key values, and how the accuracy of the ANN should be measured, and non-trivial. This work defines appropriate data representation techniques and ANN training cost functions to achieve high-accuracy results.

II. Data Structure

A neural network is simply a nonlinear function, mapping an input space to an output space. In this case, the function maps from nine independent variables, which describe the coil geometry, to $4{,}203$ dependent variables, which describe the magnetic values in a WPT system. This section describes the coil geometry parameters and the dependent variables generated by the ANN.

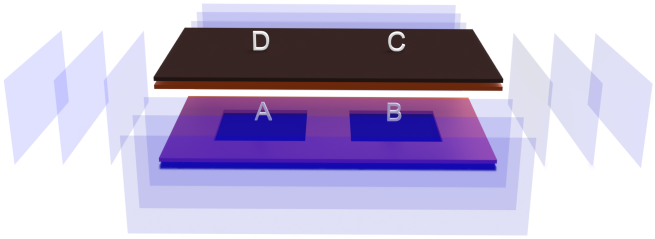

Fig. 1. WPT coil illustration with stray fields visualized. The Litz wire is modeled as a copper track with current evenly distributed through the track volume. Magnetic flux typically flows in a loop through A, B, C, and D in turn.

A. Model Simplification

This section describes how the 9 independent variables were determined. A multitude of variables could be used to describe a coil geometry. An incomplete list includes:

- Vehicle coil length
- Ground coil length
- Vehicle coil width
- Ground coil width
- Vehicle wire width
- Ground wire width

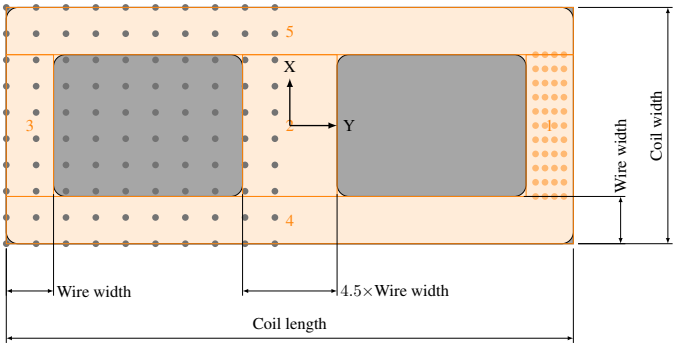

Fig. 2. Coil dimensioning. The gray dots on the left show where the magnetic field is measured in the ferrite; similar measurement points exist on the right but are not shown. The orange dots show where the magnetic field in the copper is measured; similar images corresponding to each orange box are also measured.

- X misalignment
- Y misalignment
- Air gap (Z misalignment)
- Vehicle/ground coil excitation current magnitude
- Vehicle/ground coil excitation current phase
- Vehicle/Ground ferrite width
- Vehicle/Ground ferrite length
- Vehicle/Ground ferrite thickness
- Vehicle/ground ferrite fill pattern e.g., ferrite sheets or bars
- Vehicle/ground conductor thickness
- Vehicle/ground conductor number of strands
- Vehicle/ground conductor strand diameter

In that list, 27 distinct parameters are identified. A comprehensive parameter sweep over so many parameters is afflicted by the curse of dimensionality — over 134 million geometries are needed to consider all the combinations of two variations of each parameter, an infeasibly large search space with very low resolution. In this section, the least-significant parameters are identified, to reduce the parameters to a manageable space.

1) Excitation Parameters

To reduce the search space and simplify the neural network's learning task, the effects of the primary and secondary coils are separated, as in [2]. Maximum power transfer will occur when the phases of the primary and secondary currents are offset by $90°$; it is therefore assumed that $100\,\mathrm{A}$ (peak–neutral) of real current excites the primary, and $100\,\mathrm{A}$ (peak–neutral) of imaginary current, out of phase from the primary by $90°$, excites the secondary, with a single turn on both the primary and secondary. While the assumption of $90°$ of separation between the primary and secondary current phases ensures maximum power transfer, this section justifies the arbitrary excitation current.

To improve simulation time, the FEM only records the magnitude of the real component of the magnetic field and the magnitude of the imaginary component of the magnetic field. The magnetic field scales proportionally with the excitation current and the turns. Consider a field in a FEM simulation where the X-component $x(t)$ is given by $a\cos(\omega t) + \alpha\sin(\omega t)$, the Y-component $y(t)$ by $b\cos(\omega t) + \beta\sin(\omega t)$, and the Z-component $z(t)$ by $c\cos(\omega t) + \gamma\sin(\omega t)$. The

magnitude of the real ($\|\mathbb{R}\|_{rms}$) and imaginary ($\|\mathbb{I}\|_{rms}$) portions of the field calculated by the FEM are

$$\begin{aligned} \|\mathbb{R}\| &= \sqrt{a^2+b^2+c^2} \\ \|\mathbb{I}\| &= \sqrt{\alpha^2+\beta^2+\gamma^2} \end{aligned} \tag{1}$$

Consider a design with a different number of turns or current excitation. Assuming i_g and i_v excitations on the ground and vehicle pads, respectively[1], and n_g and n_v turns on the ground and vehicle pads, respectively, the field strength squared $M(t)^2$ at time t is given by

$$\begin{aligned} M(t)^2 &= x(t)^2 + y(t)^2 + z(t)^2 \\ x(t) &= a i_g n_g \cos\omega t + \alpha i_v n_v \sin\omega t \\ y(t) &= b i_g n_g \cos\omega t + \beta i_v n_v \sin\omega t \\ z(t) &= c i_g n_g \cos\omega t + \gamma i_v n_v \sin\omega t \end{aligned} \tag{2}$$

The expression in (2) can be expressed as

$$\begin{aligned} M(t)^2 &= \left(a^2+b^2+c^2\right)\left(i_g^2 n_g^2\right)\cos^2(\omega t) \\ &+ (a\alpha+b\beta+c\gamma)\left(i_g i_v n_g n_v\right)\cos(\omega t)\sin(\omega t) \\ &+ \left(\alpha^2+\beta^2+\gamma^2\right)\left(i_v^2 n_v^2\right)\sin^2(\omega t) \end{aligned} \tag{3}$$

From the expression in (3), it can be observed that the RMS value $\|M\|_{rms}$ of $M(t)$ is given by

$$\|M\|_{rms} = \sqrt{\frac{\left(a^2+b^2+c^2\right)\left(i_g^2 n_g^2\right)+\left(\alpha^2+\beta^2+\gamma^2\right)\left(i_v^2 n_v^2\right)}{2}} \tag{4}$$

Because the stray field is sinusoidal, the magnitude $\|M\|$ is easily determined by scaling (4) and substituting the expressions in (1).

$$\|M\| = \sqrt{\|\mathbb{R}\|^2\left(i_g n_g\right)^2 + \|\mathbb{I}\|^2\left(i_v n_v\right)^2} \tag{5}$$

The expression in (5) shows that it is sufficient to extract only the magnitude of the real ($\|\mathbb{R}\|$) and imaginary ($\|\mathbb{I}\|$) portions of the field from the FEM, with a given current excitation. The total field strength can then be calculated for an arbitrary number of turns and an arbitrary excitation. Further, it is well-known that the ground coil inductance scales by n_g^2, the vehicle pad inductance scales by n_v^2, and the mutual inductance scales by $n_g n_v$.

2) Ferrite Parameters

In this section, a reduction of several ferrite variables is considered. While this section provides an intuitive justification for the simplifications present in the ANN model, a justification using a reasonable design is addressed in Section V-C. In a DD coil design, a typical magnetic circuit diagram is seen in Fig. 3, which neglects cross-coupling terms for simplicity. Here, we ignore the fact that the MMF induced at loop A is typically the same as the MMF induced at loop B. Applying the superposition principle to each MMF source in turn, it can be seen that

$$\begin{bmatrix}\Phi_A\\ \Phi_B\\ \Phi_C\\ \Phi_D\end{bmatrix} = \begin{bmatrix} L_A & L_{AB} & 0 & L_{AD} \\ L_{AB} & L_B & L_C & 0 \\ 0 & L_{BC} & L_C & L_{CD} \\ L_{AD} & 0 & L_{CD} & L_D \end{bmatrix} \begin{bmatrix}\mathcal{F}_A\\ \mathcal{F}_B\\ \mathcal{F}_C\\ \mathcal{F}_D\end{bmatrix} \tag{6}$$

[1]These values are relative to the FEM current excitations

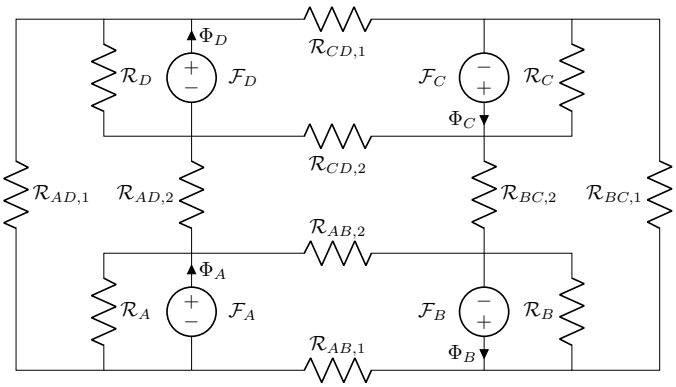

Fig. 3. Magnetic circuit diagram with ferrite planes, corresponding to the coils depicted in Fig. 1. Note that the cross-coupling effects are neglected, that is, this diagram assumes the mutual inductance $M_{AC} = M_{BD} = 0$. Reluctance paths for pole A are illustrated in Fig. 4. Magnetomotive force is denoted by $\mathcal{F}$.

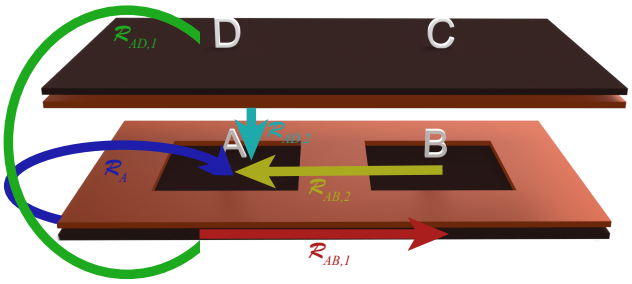

Fig. 4. Illustration of reluctance paths for magnetomotive force $\mathcal{F}_A$. The reluctance path $\mathcal{R}_{AB,1}$ flows through the ferrite, while $\mathcal{R}_{AB,2}$, $\mathcal{R}_{AD,2}$ flow through air, and $\mathcal{R}_{AD,1}$ and $\mathcal{R}_A$ flow through some ferrite and some air.

with

$$\begin{aligned} L_A &= \frac{1}{\mathcal{R}_A} + \frac{1}{\mathcal{R}_{AD,1}+\mathcal{R}_{AD,2}} + \frac{1}{\mathcal{R}_{AB,1}+\mathcal{R}_{AB,2}} \\ L_{AB} &= \frac{1}{\mathcal{R}_{AB,1}+\mathcal{R}_{AB,2}} \\ L_{AD} &= \frac{1}{\mathcal{R}_{AD,1}+\mathcal{R}_{AD,2}} \\ L_B &= \frac{1}{\mathcal{R}_B} + \frac{1}{\mathcal{R}_{AB,1}+\mathcal{R}_{AB,2}} + \frac{1}{\mathcal{R}_{BC,1}+\mathcal{R}_{BC,2}} \\ L_{BC} &= \frac{1}{\mathcal{R}_{BC,1}+\mathcal{R}_{BC,2}} \\ L_C &= \frac{1}{\mathcal{R}_C} + \frac{1}{\mathcal{R}_{BC,1}+\mathcal{R}_{BC,2}} + \frac{1}{\mathcal{R}_{CD,1}+\mathcal{R}_{CD,2}} \\ L_{CD} &= \frac{1}{\mathcal{R}_{CD,1}+\mathcal{R}_{CD,2}} \\ L_D &= \frac{1}{\mathcal{R}_D} + \frac{1}{\mathcal{R}_{AD,1}+\mathcal{R}_{AD,2}} + \frac{1}{\mathcal{R}_{CD,1}+\mathcal{R}_{CD,2}} \end{aligned} \tag{7}$$

It can be observed that the matrix defined by (6) and (7) is the inductance matrix when both primary and secondary coils consist of a single turn.

Changes to the ferrite that do not appreciably affect any element in the matrix will not affect the power transfer properties of a coil design, and modifications with non-desirable effects are not considered. Consider the effects of altering the ferrite shape or, to a lesser extent, fill pattern. Both modifications

affect the cross-sectional area of the ferrite, which is inversely proportional to the reluctances $\mathcal{R}_{AB,1}$ or $\mathcal{R}_{CD,1}$. However, because the permittivity of ferrite is much higher than free space,

$$\frac{1}{\mathcal{R}_{AB,1}+\mathcal{R}_{AB,2}} \approx \frac{1}{\mathcal{R}_{AB,2}}. \tag{8}$$

The effects of increasing the ferrite thickness are greatly reduced beyond a minimum thickness. Optimizing the ferrite thickness is a second-order decision left for future work, while the ANN presented here is appropriate for analyzing tradeoffs of more influential, first-order parameters. The same argument can be extended to defer decisions on ferrite thickness for a finer optimization over a smaller region.

Increasing ferrite overhang affects some of the reluctances, but the effect is a second-order effect, while the ferrite and coil dimensions tend to have a dominant effect.

3) Conductor Properties

The effects of the conductor geometry parameters are divided between DC resistance and AC resistance; DC resistance is inversely proportional to the conductor cross-sectional area and directly proportional to the conductor length. WPT applications typically use Litz wire, so it is reasonable to assume the skin effect is negligible. AC proximity effect losses scale with power level, and the magnetic fields inducing the losses scale as described in (5). Decisions on strand count and diameter can be made after the conductor layout is determined.

Altering the conductor thickness may have a small effect on some magnetic values, but the X- and Y- dimensions are expected to have a much greater effect. The DC losses are controlled by the shape of the conductor and can be calculated without the ANN. The result is that conductor thickness has a minimal effect on magnetic properties, and other conductor parameters' effects can be determined directly.

B. Independent Variables

The independent variables are those defining the coil geometry. With a DD coil design, three parameters are used for each coil: coil width, length, and track width. Three additional variables describe the location of the secondary relative to the primary: X-dimension offset, Y-dimension offset, and Z-dimension offset (air gap). The step sizes, maximum, and minimum values for each independent variable are shown in Table I.

TABLE I
INDEPENDENT VARIABLES

Parameter	Minimum Value	Maximum Value	Step Size
Vehicle coil length	400 mm	1,000 mm	200 mm
Ground coil length	600 mm	2,000 mm	467 mm
Vehicle coil width	200 mm	1,000 mm	267 mm
Ground coil width	600 mm	2,000 mm	467 mm
Vehicle wire width	20 mm	200 mm	60 mm
Ground wire width	40 mm	200 mm	53 mm
X misalignment	0 mm	200 mm	100 mm
Y misalignment	0 mm	300 mm	100 mm
Air gap	150 mm	300 mm	75 mm

To reduce the search space, the corners of the 9-dimensional hyperspace described by Table I are all sampled. In addition, rather than sampling on the grid, each subsection of the hyperspace is randomly sampled three times. This helps the neural network learn to interpolate across the space, and reduces the search space by roughly a factor of 3, compared to sampling on all grid intersections. A 2-dimensional visualization of this approach is illustrated in Fig. 5.

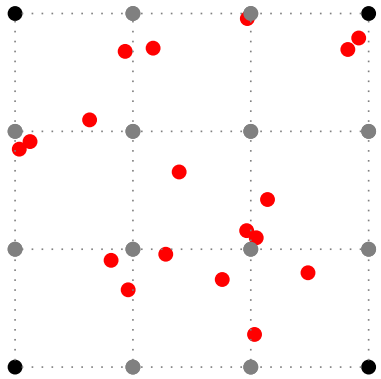

Fig. 5. Diagram of 2-dimensional analog of independent variable selection. The corner points (black) are all sampled, along with a few randomly chosen points (red) within each sub-region (defined by step sizes, shown as gray nodes).

In this paper, 13,927 feasible geometries are generated, meaning that the inner coil dimensions are at least $50\,\mathrm{mm}$ in both the X- and Y- directions. Those are separated into a 12,855-element training set and a 1,072-element test set. Every 13^{th} element from the FEM simulations is separated into the test set. The dimensions given in Table I are diagrammed in Fig. 2.

C. Dependent Variables

Given the nine input variables, the following description is generated for each geometry, where the following items 1 to 3 are separated into real and imaginary components

1) A description of the magnetic field in the ferrite, used to calculate losses, given as a 10×20 image of the B-field in the primary and secondary ferrite plates
2) A description of the magnetic field in the copper, used to calculate proximity effect losses as in [29]. These data are represented as 5 images per coil.
3) A description of stray magnetic field data, used to ensure compliance with leakage field standards and given as the B-field in 10×10 images. Each image corresponds to one of 3 distances from the coils, in either the positive or negative X- or Y- direction.
4) A measurement of relevant inductances.

These data points are sufficient to analyze a set of coil geometries, based on ferrite losses, copper losses, magnetic stray field, and coupling stability with respect to coil misalignment. Discussion of an appropriate figure of merit is left to future work; in Section V a reasonable figure of merit is arbitrarily chosen. Regardless, the present work lays the foundation for future optimization.

III. Neural Network Structure and Training

This section describes the training data generation and segregation into training and testing sets, the neural network structure, and the training algorithm and cost functions. For each of the 13,927 geometries, the nine independent variables are inputs to the ANN, which generates 4,203 variables that describe the magnetic field.

A. Data Generation and Training/Testing Sets

One concern with ANNs is over-fitting, where the ANN learns a function that matches well the data points on which it was trained, but poorly approximates other data points. This is especially possible in large ANNs; however, larger ANNs can also approximate more complex functions. Over-fitting can largely be avoided, or at least measured, by the segregation of data into a training set and a test set. While an ANN learns from the training set, an ANN never learns from the test set. Thus, the performance of the ANN on the test set is indicative of how well the ANN can generalize to new data points, as long as those points are within the same bounds as the training and test sets.

In the present work, every 13$^{\text{th}}$ geometry was placed in the testing set; the test set equally represents all combinations of air gaps, coil widths, and other independent variables.

B. Neural Network Structure

The ANN structure is composed of 4 independent neural networks, or branches, which all share the same nine input variables; the ANN was implemented in PyTorch [30]. The number of layers used to model each characteristic varies, as seen in Fig. 6. Throughout the network, a ReLu activation function is used on all except the last layer of the stray field branch and the last layer of the inductance branch, as explained in Section III-C. Nonlinear activation functions, such as ReLu, allow the neural network to learn nonlinear functions; the ReLu activation function is defined element-wise on a vector as:

$$R(x) = \begin{cases} x & x > 0 \\ 0 & x \leq 0 \end{cases} \tag{9}$$

The ANN learned to represent values in the units shown in Table II. Note that better results were obtained when the ANN learned to represent the natural logarithm of the flux density, rather than the direct value. This is addressed further in Section III-C, but note that the last layer of the stray field branch allows negative values, and so is not passed through a ReLu activation function. Additionally, while the inductance values are given in units of nanohenries, recall that a single turn is assumed. When the number of turns on both the primary and secondary are increased, the inductance values will increase proportionally to the square of the turns.

TABLE II
Units used in ANN training. Note that ANN learned to represent the stray field strength as the natural logarithm of the value.

Measured Value	Unit
Ferrite magnetic flux density	millitesla
Copper magnetic field strength	Amperes per meter
Self- and mutual-inductance	nano henry
Stray field magnetic flux density	ln(microtesla)

C. Training Algorithm and Cost Functions

A gradient descent algorithm trains an ANN to minimize a cost, which is some measure of the difference between the training data and the output of the ANN. For this application, the Adam gradient descent algorithm modifies the ANN parameters to replicate the FEM-generated training data [31].

Typically, the ANN is trained on a *minibatch* of inputs, in this case, a set of 50 coil geometries randomly selected from the training set. By averaging the ANN parameter modifications over several geometries, training speed, and accuracy are improved. Each time the ANN is trained on the full training data is considered an *epoch*. The entire structure was trained for 6,000 epochs. The number of training iterations was chosen after attempting several different values.

The choice of cost function and data representation is of critical importance to the ANN's efficacy; the cost function describes how well the ANN approximates the target function, in this case, the FEM data. The data representation scheme also affects how the distance is measured. The definition of the distance between the ANN and FEM data should be tailored to maximize accuracy where it is most important; as an example, a 50 % error in the stray field may be more tolerable than a 1 % error in the same plane, if the former point does not affect compliance with standards and the latter does. The most typical cost function for ANNs that output continuous values is a mean squared error (MSE); an MSE cost typically limits very poor fits. Where there is a very poor fit, the cost gradient is dominated by poorly fit points, and the optimizer adjusts the ANN parameters to better fit those points. The cost functions used in training the neural network are discussed below.

1) Inductance

An MSE cost function is appropriate when the goal is to minimize the square of the error between data points, or when the importance of the error does not depend on the function value. In this case, we want to minimize the square of the error in the inductance values, and an error of 5 nH is equally important whether it be on a 5 µH measurement or a 1 µH measurement. Further, by focusing on the poorly-fit points, representation across the entire domain is improved. Thus, when training the ANN to estimate the inductance values, an MSE cost is used:

$$c_L = \left\langle (\mathbf{l}_O - \mathbf{l}_T)^T (\mathbf{l}_O - \mathbf{l}_T) + 50 \left(\mathbf{l}_O^M - \mathbf{l}_T^M\right)^T \left(\mathbf{l}_O^M - \mathbf{l}_T^M\right) \right\rangle, \tag{10}$$

where c_L is the cost corresponding to the inductance values, $\mathbf{l}_O$ is a vector of inductance values predicted by the ANN, $\mathbf{l}_T$ is a vector of FEM-calculated inductance values, the superscript M refers to mutual-inductance values, and $\langle \cdot \rangle$ averages the cost over a minibatch.

In (10), special emphasis is given to the mutual inductance, rather than the self inductances; a few reasons justify this

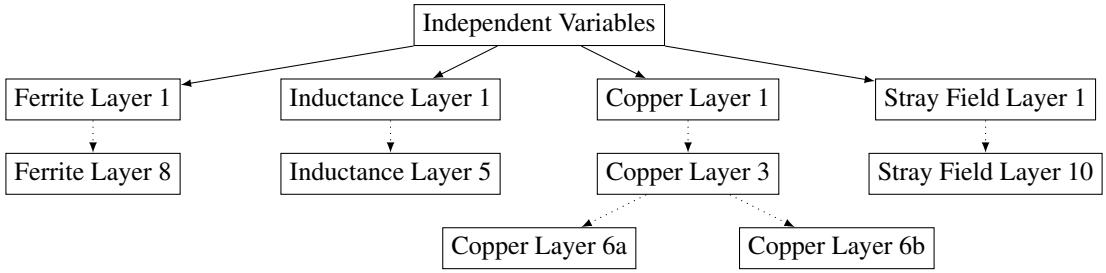

Fig. 6. ANN structure. The network has 4 main outputs, as described in Section II-C. The first layers in each branch are linear, followed by transpose convolutional layers and convolutional layers for the magnetic field branches, i.e., the ferrite, copper, and stray field branches. Note that the copper layer splits; this is because the copper magnetic field images are in two different shapes.

focus. First, the mutual inductance is of more critical importance to the power transfer capability. The power transferred depends directly on the mutual inductance, depending only on the combination of the GA or VA inductance with a capacitance elsewhere in the circuit. Second, the value of the mutual inductance is less than the value of either of the self-inductances — a greater emphasis on mutual inductance is needed to achieve a roughly similar relative error. Finally, the mutual inductance is more variable, and so more difficult for the ANN to model. Without an added emphasis on the mutual inductance, the ANN would likely shift more error onto those measurements, rather than onto the self-inductance.

2) Magnetic Field and Copper Losses

When training the ANN on the magnetic field strength in both the ferrite and copper, a simple MSE cost is inadequate. The direct measurement of the magnetic field is not as important as the energy lost; ferrite losses are roughly proportional to the square of the flux density and copper proximity effect losses are strictly proportional to the square of the magnetic flux density. Thus, to get a good fit for energy losses, the ferrite cost c_F is given by

$$c_F = \left\langle \left(\mathbf{f}_O^2 - \mathbf{f}_T^2\right)^T \left(\mathbf{f}_O^2 - \mathbf{f}_T^2\right) \right\rangle, \tag{11}$$

where $\mathbf{f}_O$ is a vector of magnetic flux density values predicted by the ANN, $\mathbf{f}_T$ is a vector of FEM-calculated magnetic flux densities, the $(\cdot)^2$ operator squares each element in a vector, and $\langle\cdot\rangle$ averages the cost over each channel, or image, in a batch of geometries. For each geometry, there is a channel corresponding to the real component and imaginary component of the field in both the vehicle and ground assemblies. In effect, (11) defines the cost function as the MSE of the magnetic flux density squared.

Note that while the structure of (11) suggests that $\mathbf{f}_O = \pm\mathbf{f}_T$ is a valid solution, the ReLu activation function ensures $\mathbf{f}_O \geq 0$, while by definition, $\mathbf{f}_T \geq 0$. Thus, there is a single optimum.

Similarly, the copper cost c_{Cu} is given by

$$c_{Cu} = \left\langle \left(\mathbf{c}_O^2 - \mathbf{c}_T^2\right)^T \left(\mathbf{c}_O^2 - \mathbf{c}_T^2\right) \right\rangle, \tag{12}$$

where $\mathbf{c}_O$ is a vector of magnetic field strengths predicted by the ANN and $\mathbf{c}_T$ is a vector of FEM-calculated field strengths. In both (11) and (12), the ANN is trained to minimize the MSE between the expected and calculated energy loss, rather than between the field measurements.

A more rigorous justification for the cost function is the following. Any ANN will represent the training data x with y. However, that representation is imperfect, with some error distribution $N(x)$:

$$y = x + N(x) \tag{13}$$

Note that the error is not assumed to be independent of x. One assumption we will make is that the mean squared value of a random variable is minimized when the random variable is zero-mean, for any error distribution.

If the cost function c is calculated as the MSE of the field strength

$$c = (x - (x + N(x)))^2, \tag{14}$$

then the expectation to be minimized is

$$E\left[N(x)^2\right], \tag{15}$$

which, by our assumption above, implies $N(x)$ is zero-mean.

However, consider the expected difference between the ANN-generated power loss and the FEM-generated power loss. The expected energy error is given as

$$E\left[x^2 - (x + N(x))^2\right], \tag{16}$$

which reduces to

$$-E\left[2xN(x) + N(x)^2\right]. \tag{17}$$

The probability that the error distribution that minimizes $N(x)^2$ also happens to set (17) equal to 0 exists, but is vanishingly small, and requires a precise correlation between $N(x)$ and x to happen by minimizing $N(x)$. There is a very high probability of a systematic offset in the energy consumption calculations.

Conversely, consider the cost function

$$c = (x^2 - y^2)^2. \tag{18}$$

The ANN minimizes the expectation

$$E[c] = E\left[\left(x^2 - x^2 - 2xN(x) - N(x)^2\right)^2\right], \tag{19}$$

which is assumed to be minimized when

$$-E\left[2xN(x) + N(x)^2\right] = 0, \tag{20}$$

which forces the expected energy error defined in (17) to be 0. With the assumption that the mean squared value of a random variable is minimized when the random variable is zero-mean, the proposed cost function is guaranteed to produce a zero-mean energy error.

3) Stray Magnetic Field Intensity

The natural way to qualify the stray field ANN approximation is to measure the relative accuracy because the stray fields scale arbitrarily with current and the values in the stray fields vary enormously. With magnetic field strength represented on a linear scale, as the Ampere-turns in either the primary or secondary vary, the total error varies proportionally. Further, because some stray magnetic field strength measurements are very high, while many are very low, a relative error ensures that every measurement is reasonable. However, an MSE cost function on linear values causes the ANN to learn to represent the high-strength and low-strength stray magnetic field points with roughly the same linear error but vastly different relative errors.

Because the stray field strengths are represented on a logarithmic scale, minimizing the relative error in the field strength is equivalent to minimizing the MSE of the error in the logarithmic domain. Note that the logarithmic values may sometimes be negative, this requires that the last ANN layer of the stray field branch not be passed through the ReLu activation function.

The cost function in (11) and (12) biases the ANN to higher accuracy when the magnetic field is higher; this effect should be exaggerated for the stray field. Although ferrite and copper proximity losses are largely dominated by points with a strong magnetic field, the magnetic field throughout the entire ferrite or copper volume continues to contribute to losses. However, to ensure compliance with IEEE exposure standards [32], only the peak magnetic field, including both the real and complex components, in each measurement plane is important.

Let s_O be the ANN-predicted stray field and s_T be the FEM-calculated stray field, which are both expressed on a logarithmic scale. Because only the maximum value of the stray field is of importance, when calculating the cost at a single point, it is assumed that the complementary field ϵ is sufficiently strong at that point to dominate all other points in the plane. The value ϵ is included when comparing the realized (ANN) and expected (FEM) field strengths to represent that complementary field strength. Let ϵ also be represented as a logarithm.

Let s_{TM} be the maximum field strength of all s_T in a plane, either real or imaginary. If it is assumed that the point represented by s_T defines the maximum field strength within a plane, then

$$\sqrt{e^{2s_T} + e^{2\epsilon}} \geq e^{s_{TM}}, \tag{21}$$

which gives a lower bound that

$$\epsilon \geq \frac{1}{2} \ln \left(e^{2s_{TM}} - e^{2s_T} \right). \tag{22}$$

With the assumption that a given point dominates the stray field, and using an MSE of logarithm, the cost c_S is

$$c_S^* = \left\langle \left(\ln \sqrt{e^{2s_O} + e^{2\epsilon}} - \ln \sqrt{e^{2s_T} + e^{2\epsilon}} \right)^2 \right\rangle. \tag{23}$$

Note that as $\epsilon \to \infty$, $c_S^* \to 0$; if the stray field at a point is very low relative to the maximum in that plane, it does not contribute significantly to the cost. Because $\epsilon \to \infty \implies c_S \to 0$, this paper only considers the lower bound of ϵ.

Note that the expression given in (23) is computationally intensive. A 2nd-order Taylor expansion of (23) about $s_O = s_T$ can be defined to reduce complexity. With the lower bound of ϵ defined in (22), (23) is approximated as

$$c_S^* \approx c_S = r^4 \left(s_O - s_T \right)^2, \tag{24}$$

where $r = e^{s_T - s_{TM}}$. This is essentially MSE in the logarithmic domain, which optimizes for relative error, but it is weighted to value points more likely to contribute to the peak field in a plane.

Another approach to relative error is with a cost function like

$$c = \frac{(x-y)^2}{x}, \tag{25}$$

provided x is positive. While this does not require expression in the logarithmic domain, the training becomes unstable. The derivative of (25) near $x = 0$ varies wildly, complicating training and creating huge, variable partial derivatives. This results in very large values in the update step, slow training, and numerical errors.

PyTorch allows only one cost function for training. Because the four branches are independent, the costs can be summed: $c_S + c_L + c_F + c_{Cu}$. The back-propagation ANN training step for any ANN parameter will only refer to one of the summands.

IV. ANN Training Results

In this section, the performance of the ANN is considered for each of the four principal neural network tasks. In this section, unless noted otherwise, all performance metrics are evaluated with the test set, rather than the training set.

A. Inductance Measurements

The ANN learned to predict the inductance values with a high degree of accuracy. Here, the R^2 value is an appropriate measure of neural network accuracy. By the end of training, the R^2 value is well above $99\,\%$ for all inductance measurements. Figure 7 illustrates the efficacy of the ANN in learning inductances, showing a close alignment between the FEM-calculated values and the ANN-calculated values. The problem of predicting inductances with a neural network is essentially solved, although that is perhaps the easiest problem to solve.

B. Stray Field Measurements

To validate the effectiveness of the ANN in estimating the stray magnetic fields, a sample excitation of 1 amp-turn in both the primary and secondary is assumed, and the resulting peak value in each plane for each geometry is compared between the ANN-generated fields and the FEM-generated fields.

Two metrics validate the effectiveness of the ANN for the assumed excitation: first, the R^2 value relates the MSE to the total signal energy, and second, the pass rate, or the percentage of fields for which the ANN-determined peak field strength is within $10\,\%$ of the FEM-determined peak field strength. Both metrics are given in Fig. 8. Note that both metrics are taken on the field strength, not the logarithm of the field strength.

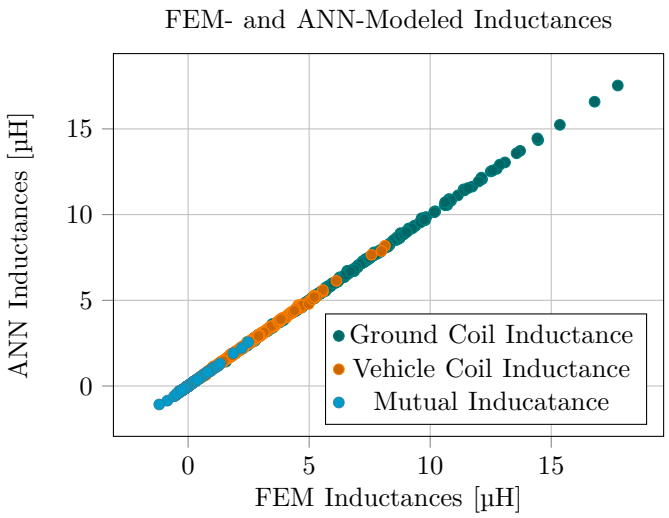

Fig. 7. Comparison of ANN-calculated and FEM-calculated inductance values. Recall that these values are for a single-turn inductor.

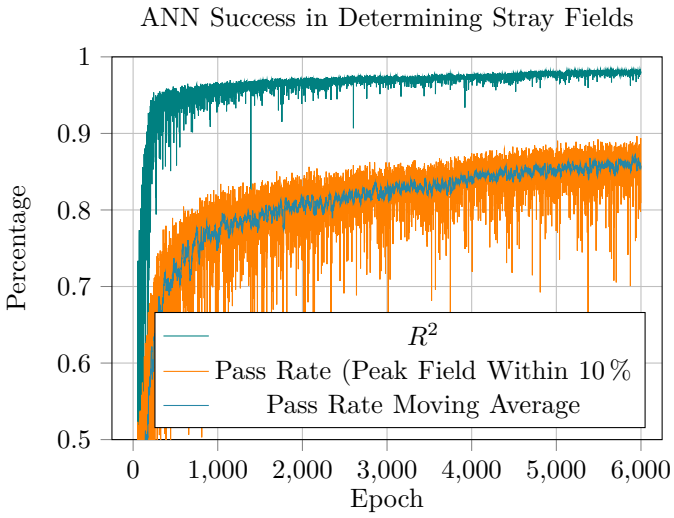

Fig. 8. Measures of the effectiveness of the ANN in representing stray fields. Included are the R^2 values, which is a proxy for relative MSE; pass rate, which shows how frequently the ANN-generated peak field strength values are within 10 % of the FEM-generated values, and the 20-sample moving average of the pass rate.

After 6000 training epochs, the R^2 values on the training set was 98 % and the 20-epoch moving average pass rate was 85.8 %. The data from which those percentages are drawn are shown in Fig. 9, which compares the FEM-calculated peak magnetic flux density in each sampling plane of the test set with the corresponding ANN-calculated values.

C. Ferrite and Copper Field Measurements

When calculating the effectiveness of the ANN in modeling ferrite magnetic fields, an approximate energy loss for each geometry was calculated, based on the FEM-generated data and the ANN-generated data. The ferrite energy losses are assumed to be proportional to the average of the flux density

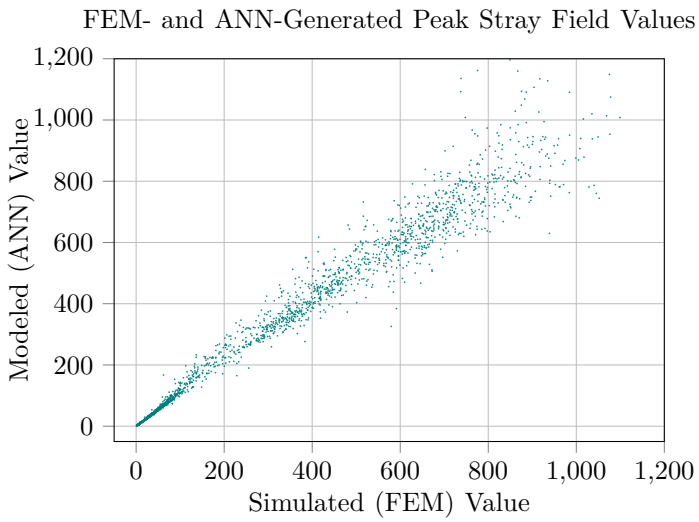

Fig. 9. Scatterplot comparing FEM- and ANN-generated peak magnetic flux density values. Note that the relative error is minimized; larger errors are permitted on larger measurements.

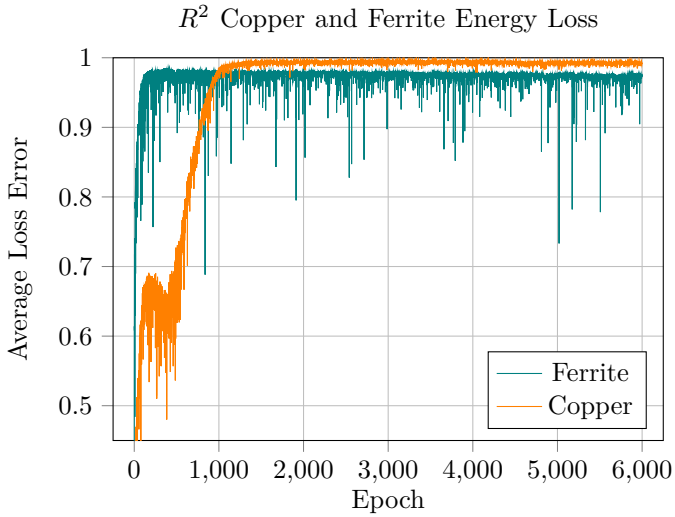

Fig. 10. Improvements in the power of the ANN to predict magnetic field losses through training. Both values are represented with excellent accuracy.

squared. After 6000 training epochs, $R^2 = 97.6\,\%$. Figure 10 shows the improvements in the ANN during training.

The ANN copper magnetic field accuracy was calculated identically to the ferrite magnetic field accuracy, by comparing the ANN-calculated and FEM-calculated energy losses. After 6000 epochs, the $R^2 = 99.2\%$, also seen in Fig. 10.

V. Validation of Assumptions and ANN Efficacy

This section describes the experiments used to validate the ANN training, by comparing FEM and ANN results for a "good" coil design, which is not included in the training set or the test set. This paper focuses on replacing a FEM model with an ANN model, and any discrepancies between the ANN and the underlying physics are beyond the scope of this paper.

First, a combined gradient descent/genetic algorithm is used to determine a good design in Section V-A. Then, in Section V-B, the optimal design is compared to a FEM model. Section V-C analyzes the validity of the simplifications in Section II-A, while Section V-D addresses the inclusion of aluminum shielding in other applications.

A. Simple Coil Design Optimization

While the trained ANN generates a multitude of potential inputs to an objective function, a thorough development of such a function is beyond the scope of this work. However, here we introduce a simple optimization problem so that the validation of the ANN is completed on a reasonable design outside the training and testing sets. Let the vector x include both the 9 ANN input variables and the excitation of both coils in Ampere-turns ($i_g n_g$ and $i_v n_v$). Ferrite loss densities $P(B_F)$ are calculated with the power loss density given by

$$P(B_F) = 0.07 f^{1.7} B^{2.5}, \tag{26}$$

where f is the frequency and B is the B-field magnitude. Copper losses are calculated according to [33], where the loss $P(B_{Cu})$ on each strand of Litz wire is given by

$$P(B_{Cu}) = \frac{\pi l d^4}{64 \rho_c} \overline{\left(\frac{dB_{Cu}}{dt} \right)^2}, \tag{27}$$

where l is the length of the strand represented by the B_{Cu} measurement, d is the diameter of each Litz wire strand (assumed to be $100\,\mu\mathrm{m}$), ρ_c the conductivity of copper, and $\bar{\cdot}$ averages over time. Here, it is assumed that there are $20{,}000$ strands of Litz wire on both coils.

When the power transfer $P(x)$ with coupling factor $L_M(x)$ for a given x is assumed to be

$$P(x) = \frac{L_M(x) i_g n_g i_v n_v}{2}, \tag{28}$$

and the stray fields determined according to (4), the optimization is expressed as

$$\begin{aligned} &\max_x \ P(x) \\ \text{s.t. } &\max \|M\|_{rms} \leq 15\,\mu\mathrm{T} \\ &lb \leq x \qquad\quad \leq ub, \end{aligned} \tag{29}$$

where the maximum magnetic flux density along any of the sampled planes is constrained to be less than $15\,\mu\mathrm{T}$, per ANSI standards for exposure by persons with implantable medical devices to magnetic fields at $85\,\mathrm{kHz}$ [34]. Further, lb and ub are the bounds described in Table I, with the additional constraint that the X misalignment be $0\,\mathrm{mm}$ and that the Y misalignment be $100\,\mathrm{mm}$. Finally, the excitation currents were restricted to 350 ampere-turns. The excitation currents were used in the optimization, with the values scaled appropriately in the neural network output (magnetic fields scaled proportionally to the excitation current).

The PyTorch library [30] includes automatic differentiation, allowing the gradient of the constraint and cost to be easily calculated. The cost function and constraints, together with their gradients, are passed into a simple optimization procedure. Initially, 30 geometries are chosen at random; those geometries are then locally optimized with a SciPy optimization package [35].

Subsequently, 10 *generations* of a genetic algorithm refine the designs further. In each generation, 10 random geometries are locally optimized, the best 10 previous designs (*elites*) are passed directly to the next generation, and 10 mutated recombinations of traits from the elites are locally optimized. The aim of this optimization is not to define a specific coil design, but rather to demonstrate the utility of the ANN in optimization and evaluate the ANN on a reasonable design. Therefore, the problem as presented does not consider all factors that may be relevant to a practical optimization. Regardless, this optimization presents a reasonable design on which to validate the ANN performance. The design generated by the above-described algorithm is given in Table III. Note that the excitations are in ampere-turns, so $350\,\mathrm{A-turns}$ could be a single turn with $350\,\mathrm{A}$ or three turns with $117\,\mathrm{A}$ each.

TABLE III
OPTIMIZED DESIGN

Parameter	Value
Vehicle coil length	$658\,\mathrm{mm}$
Ground coil length	$693\,\mathrm{mm}$
Vehicle coil width	$931\,\mathrm{mm}$
Ground coil width	$1{,}056\,\mathrm{mm}$
Vehicle track width	$93.6\,\mathrm{mm}$
Ground track width	$98.9\,\mathrm{mm}$
X misalignment	$0\,\mathrm{mm}$
Y misalignment	$100\,\mathrm{mm}$
Air gap	$150\,\mathrm{mm}$
Primary excitation	$141\,\mathrm{A-turns}$
Secondary excitation	$338\,\mathrm{A-turns}$

B. Comparison of ANN with FEM models

The optimized design presented in Table III was compared with a high-resolution FEM model. In the model, the convergence threshold was set to $1\,\%$, rather than the $5\,\%$ used to generate the training data.. Ferrite and copper losses are calculated by (26) and (27). The DC copper loss does not rely on the magnetics, but is easily calculated with the winding cross-sectional area, length, current, and copper resistivity; the Litz wire assumption causes the skin effect to be negligible. The DC copper losses are included for comparison with the AC copper losses. Note that because Litz wire is assumed to be used, bundle-level AC copper losses are neglected as in [33]. Power is calculated according to (28). As mentioned previously, the ANN-generated values are scaled by the optimal current excitations, while the FEM-generated values are simulated directly with the optimal excitation currents.

As seen in Table IV, the ANN compares favorably with the FEM model. The losses, inductances, and maximum stray fields are presented. Note that the DC copper losses are calculated directly, so no difference is observed between the ANN and FEM values. For simplicity, only the peak values in the four stray field planes closest to the transmission pads are considered.

TABLE IV
COMPARISON OF ANN AND FEM MODELS FOR OPTIMIZED DESIGN

Parameter	ANN Value	FEM Value	Relative Error
GA Inductance (per turn)	2,564 nH	2,616 nH	2.0 %
VA Inductance (per turn)	2,402 nH	2,279 nH	5.4 %
Mutual Inductance (per turn)	661.9 nH	662.0 nH	0.01 %
GA Proximity Effect Copper Loss	2.85 W	4.94 W	42.4 %
VA Proximity Effect Copper Loss	15.9 W	16.7 W	4.5 %
GA DC Copper Loss	4.94 W		N/A
VA DC Copper Loss	25.1 W		N/A
Ferrite Loss	14.7 W	12.9 W	13.9 %
Total Loss	63.6 W	64.6 W	1.6 %
Max Stray Field ($y = 0.8\,\mathrm{m}$)	15 µT	13.8 µT	8.3 %
Max Stray Field ($y = -0.8\,\mathrm{m}$)	15.0 µT	13.6 µT	9.9 %
Max Stray Field ($x = 0.8\,\mathrm{m}$)	15 µT	12.9 µT	16.7 %
Max Stray Field ($x = -0.8\,\mathrm{m}$)	12.9 µT	12.9 µT	0.6 %

Generally, the ANN serves as a reasonable surrogate model for the FEM. Most of the essential values are within a reasonable error bound of $10\,\%$; some of the individual measurements are outside that bound, but the total loss estimate error only sums to $10\,\%$. The inductance values are accurate to within roughly $6\,\%$, reasonable enough to consider trade-offs, especially with the very high accuracy exhibited on the mutual inductance measurement. Even the stay fields are reasonably accurate, which is very difficult to achieve with a neural network. Interestingly, the optimizer found a solution where the peak field intensity was met in two locations.

The results also suggest another approach to coil design, by including current excitation in design. The compensation and excitations around the GA and VA coils can be altered without varying the power transfer, provided that the product of the Ampere-turns of the GA and VA remains unchanged. Typically, the efficiency is maximized by matching losses on the GA and VA. This optimization, however, suggests a modest reduction in efficiency to maximize power transfer capabilities within magnetic field exposure limits.

C. Validation of Simplifying Assumptions

All of the results in this section are informed by FEM simulations, rather than ANN-generated data. It is shown in Section II-A that there is an intractable number of parameters to sweep for a full optimization; the ANN presented here simply provides a first estimate, which can then be further optimized by subsequent training in a neighborhood region. This section provides a richer justification for the parameters excluded from consideration in Section II-A. The base geometry, or original value, is the optimized design, although the current excitations are set to $100\,\mathrm{A} - \mathrm{turn}$ on both the primary and secondary. The goal of this section is to demonstrate that several of the simplifying assumptions discussed in Section II are valid; that is, that losses and efficiency vary in negligible or predictable ways with different geometries.

In this section, several versions of the optimized design are simulated. The losses discussed here are calculated directly by the FEM solver, so they vary somewhat from the estimations generated by the neural network. Relevant results from the FEM solver are given by Table V.

A few variations of the optimized design considered here were simulated, to demonstrate the limited or well-understood effect those modifications have on the overall result. Those variations are:

1) Ferrite Bars

The ferrite plates are replaced with 11 ferrite bars on both the GA side and the VA side, with a $50\,\%$ reduction in total ferrite volume[2]. As seen in Fig. 1, the bars lie along the axis between *A* and *B* on the GA, and along the axis between *D* and *C* on the VA. As discussed in Section II-A2, this should have no significant effect on the inductances, stray field, or copper losses.

However, by focusing the magnetic flux into $50\,\%$ of the ferrite volume, the flux density within the ferrite will scale by a factor of 2. Assuming all the flux is concentrated in the ferrite bars, rather than the the air gaps, and according to (26), the power loss density will increase by a factor of 5.66; with the reduced volume, the ferrite power loss should increase by a factor of 2.83. Given that $1.36\,\mathrm{W}$ of power was lost in the ferrite with the original design, there is expected to be $3.85\,\mathrm{W}$ of ferrite loss with this variation. Other results should remain essentially unchanged.

2) Thick Ferrite

In Section II, it was noted that $16\,\mathrm{mm}$ thick ferrite is modeled. While that thickness is reasonably common, it was suggested in Section II-A2 that the ferrite thickness fails to contribute significantly to the important parameters. This variation addresses that assumption by setting both primary and secondary ferrite thicknesses to $32\,\mathrm{mm}$. Following the same reasoning as before, the flux density should decrease by a factor of 2, decreasing loss by a factor of 2.83 to $481\,\mathrm{mW}$. Other results should remain essentially unchanged.

3) Thick Copper

In Section II, it was noted that the copper is assumed to be $20\,\mathrm{mm}$ thick, with the thought that copper thickness was not a significant contributor. This variation sets the copper thickness to $30\,\mathrm{mm}$, without altering the number of strands. Because this affects conductor spacing, there might be slightly lower conduction losses, but the effect should be relatively small — the track width remains unchanged and is greater than the copper width, so the B-field strength within the copper will have only a small reduction. Additionally, the thicker copper results in a farther average distance between GA and VA coils and the ferrite plates, potentially having a small effect on coupling. Beyond those effects, there should be no appreciable difference between this variation and the base case.

4) Results

The results for each of the variations on the optimal design are shown in Table V. As seen there, each of the variations only had a moderate effect on the performance of the WPT system, validating the simplifications used throughout this paper for first-approximation designs. That is, in analyzing a WPT design, the nine parameters are among the most

[2]The outermost bars are half as wide as the others, resulting in 10 gaps and 9 ferrite bars of equal sizes, with two half-sized ferrite bars.

critical, while other considerations can be reasonably delayed for further refinement. As before, the assumption of Litz wire forces the skin effect to be negligible. DC, or regular resistive losses, are not included here.

For the most part, the inductance values vary as expected — inductances are slightly higher in the variation with more ferrite and slightly lower in the variation with less ferrite. In variation 3, where the average distance between the conductor and the ferrite is increased, the self-inductances are reduced. However, the thicker copper also decreases the gap between the VA and GA conductors, increasing the coupling coefficient and resulting in a minimal net effect on mutual inductance.

The losses also vary as expected. The conductor losses show very little variation across the different setups. More ferrite tends to correlate to stronger conductor magnetic fields, inducing greater proximity effect losses. Conversely, less ferrite or thicker copper weakens or dilutes the conductor's magnetic fields, lowering proximity effect losses. However, those effects are minimal — the copper losses only vary by around $10\,\%$ across the variations.

Ferrite losses vary as expected. Applying the reasoning in Sections V-C1 and V-C2, the ferrite losses are expected to be $3.85\,\mathrm{W}$ in variation 1 and $481\,\mathrm{mW}$ in variation 2. Those are reasonable approximations for the measured values.

While not precisely accurate, decisions on ferrite geometry and conductor thickness have small or predictable effects on losses and coupling. The exclusion of those decisions from the ANN is justified to allow for a reasonable training set and defer less significant decisions to a smaller sample space.

D. Inclusion of Aluminum Plates

It may be noted that in a practical system, there would be a conductive body behind the secondary ferrite. That body could be either an aluminum plate, as in the SAE J2954 standard [8], or the body of a vehicle, or both. However, the conductive body's shape is not clearly defined, e.g., the metallic steps on the side of a semi-truck shape the magnetic fields differently from how a small sedan shapes the magnetic fields. Therefore, an ANN trained with a given conductive body would be invalid for other vehicles.

A different approach is required, of which this work represents the first step. The effects of a given conductive body on the magnetic fields can be well-understood, regardless of the body. A modularized approach is proposed, where the magnetic field generated by this ANN is *translated* by a subsequent ANN, trained on a smaller dataset, that replicates the modifications a conductive body applies to a magnetic field. That is, the basic ANN, presented here, defines the basic magnetics. Then, for each variation, a new, proposed ANN modifies the outputs appropriately.

A full consideration of the effects of the vehicle body on the magnetic fields is beyond the scope of this work but is a logical future extension of this work.

VI. Conclusion

An ANN is designed and trained to estimate 4,093 variables in a DD WPT scheme. The dependent variables are sufficient to determine an interoperable, optimal design, given a quality metric. The ANN is trained to estimate self-inductances of both the primary and secondary coils, mutual inductance, stray magnetic fields, and magnetic fields in the copper and ferrite. The copper and ferrite magnetic fields can be used to determine proximity and ferrite losses, respectively.

The ANN is shown to be highly effective at generating data very closely aligned with the FEM data. The ANN estimations closely mirror the FEM data, even on coil geometries the ANN has not been trained on. Of the four areas the ANN is trained on, the ANN performs worst when measuring the stray fields, most likely due to the extreme variation in the stray magnetic field strength measurements and the number of field measurements required for each coil geometry. A more powerful ANN could improve this, although the ANN performance is ultimately limited by the allowable tolerance in the FEM data.

The most obvious application of this ANN is in coil design optimization; the ANN quickly simulates the WPT system and when a figure of merit is developed, gradient descent techniques can suggest candidate optimal solutions. Future tasks could include determining a ground coil design that maximizes power transfer to many secondary designs, over a variety of air gaps and misalignments, while minimizing parasitic losses. The speed and gradient descent algorithms allowed by an ANN would allow quick and accurate optimization.

The two key contributions of this work are 1) the scope of data, both the number of geometries used to train the ANN and the data points collected for each coil geometry; and 2) the identification of appropriate cost functions to train the ANN and data representation schemes. The work presented here will allow engineers to leverage next-gen EV technology, by designing WPT systems that work with a variety of EV classes. The ANN described here will allow engineers to quickly ensure a proposed primary design is sufficiently robust to transfer power to a range of secondary coil geometries, at a range of misalignments. Beyond the applicability of the ANN presented here, the data representation schemes and cost functions will be broadly applicable to other coil designs; ANNs trained with the same cost functions could represent ferrite-less designs or circular or polyphase coils. The advancements of this work extend beyond the immediate applicability to DD coils.

References

[1] M. Bojarski, E. Asa, K. Colak, and D. Czarkowski, "Analysis and control of multiphase inductively coupled resonant converter for wireless electric vehicle charger applications," vol. 3, no. 2, pp. 312–320, 2017.

[2] S. Inoue, D. Goodrich, S. Saha, R. Nimri, A. Kamineni, N. S. Flann, and R. A. Zane, "Fast design optimization method utilizing a combination of artificial neural networks and genetic algorithms for dynamic inductive power transfer systems," *IEEE Open Journal of Power Electronics*, vol. 3, pp. 915–929, 2022.

[3] H. Oh, S. Oh, H. Koo, W. Choi, J. Shin, K. C. Hwang, K.-Y. Lee, and Y. Yang, "Mid-range wireless power transfer system for various types of multiple receivers using power customized resonator," vol. 9, pp. 45 230–45 241, 2021.

[4] H. Zhang, F. Lu, H. Hofmann, W. Liu, and C. C. Mi, "A four-plate compact capacitive coupler design and lcl-compensated topology for capacitive power transfer in electric vehicle charging application," vol. 31, no. 12, pp. 8541–8551, Dec 2016.

TABLE V
VALIDATION OF SIMPLIFYING ASSUMPTIONS

Parameter	Original Value	Variation 1	Variation 2	Variation 3
GA Inductance (per turn)	2,615 nH	2,460 nH	2,637 nH	2,456 nH
VA Inductance (per turn)	2,282 nH	2,154 nH	2,301 nH	2,132 nH
Mutual Inductance (per turn)	662 nH	605 nH	674 nH	665 nH
GA AC Copper Loss	4.50 W	4.21 W	4.54 W	4.11 W
VA AC Copper Loss	4.25 W	3.97 W	4.29 W	3.86 W
Ferrite Loss	1.36 W	3.53 W	518 mW	1.29 W

[5] F. Lu, H. Zhang, H. Hofmann, and C. Mi, "A double-sided lclc-compensated capacitive power transfer system for electric vehicle charging," vol. 30, no. 11, pp. 6011–6014, Nov 2015.

[6] H. Zhang, F. Lu, H. Hofmann, W. Liu, and C. C. Mi, "An lc-compensated electric field repeater for long-distance capacitive power transfer," vol. 53, no. 5, pp. 4914–4922, Sep. 2017.

[7] E. Abramov, I. Zeltser, and M. M. Peretz, "A network-based approach for modeling resonant capacitive wireless power transfer systems," *CPSS Transactions on Power Electronics and Applications*, vol. 4, no. 1, pp. 19–29, Mar 2019.

[8] "Wireless power transfer for light-duty plug-in/electric vehicles and alignment methodology," *SAE Standard J2954_202208*, Aug 2022. [Online]. Available: https://www.sae.org/standards/content/j2954_202208

[9] U. K. Madawala and D. J. Thrimawithana, "A bidirectional inductive power interface for electric vehicles in v2g systems," vol. 58, no. 10, pp. 4789–4796, Oct 2011.

[10] B. Sanftl, C. Joffe, M. Trautmann, R. Weigel, and A. Koelpin, "Reliabe data link for power transfer control in an inductive charging system for electric vehicles," in *2016 IEEE MTT-S International Conference on Microwaves for Intelligent Mobility (ICMIM)*, 2016, pp. 1–3.

[11] C. C. Mi, G. Buja, S. Y. Choi, and C. T. Rim, "Modern advances in wireless power transfer systems for roadway powered electric vehicles," vol. 63, no. 10, pp. 6533–6545, 2016.

[12] O. C. Onar, G.-J. Su, E. Asa, J. Pries, V. Galigekere, L. Seiber, C. White, R. Wiles, and J. Wilkins, "20-kw bi-directional wireless power transfer system with energy storage system connectivity," in *2020 IEEE Applied Power Electronics Conference and Exposition (APEC)*, 2020, pp. 3208–3214.

[13] S. Y. Chu, X. Cui, X. Zan, and A.-T. Avestruz, "Transfer-power measurement using a non-contact method for fair and accurate metering of wireless power transfer in electric vehicles," vol. 37, no. 2, pp. 1244–1271, Feb 2022.

[14] M. Hansen, A. Kamineni, and R. Zane, "Zero-crossing current detection for modular and robust dynamic wireless power transfer," in *2020 IEEE Energy Conversion Congress and Exposition (ECCE)*, Oct 2020, pp. 5207–5214.

[15] R. Zeng, V. P. Galigekere, O. C. Onar, and B. Ozpineci, "Grid integration and impact analysis of high-power dynamic wireless charging system in distribution network," vol. 9, pp. 6746–6755, 2021.

[16] G. Buja, M. Bertoluzzo, and K. N. Mude, "Design and experimentation of WPT charger for electric city car," vol. 62, no. 12, pp. 7436–7447, 2015.

[17] C. Cheng, F. Lu, Z. Zhou, W. Li, C. Zhu, H. Zhang, Z. Deng, X. Chen, and C. C. Mi, "Load-independent wireless power transfer system for multiple loads over a long distance," vol. 34, no. 9, pp. 9279–9288, Sep. 2019.

[18] J. Pries, V. P. N. Galigekere, O. C. Onar, and G.-J. Su, "A 50-kw three-phase wireless power transfer system using bipolar windings and series resonant networks for rotating magnetic fields," vol. 35, no. 5, pp. 4500–4517, May 2020.

[19] A. Ahmad, M. S. Alam, and A. A. S. Mohamed, "Design and interoperability analysis of quadruple pad structure for electric vehicle wireless charging application," vol. 5, no. 4, pp. 934–945, Dec 2019.

[20] T. Bai, B. Mei, L. Zhao, and X. Wang, "Machine learning-assisted wireless power transfer based on magnetic resonance," vol. 7, pp. 109 454–109 459, 2019.

[21] Z. Zhang, S. Shen, Z. Liang, S. H. K. Eder, and R. Kennel, "Dynamic-balancing robust current control for wireless drone-in-flight charging," vol. 37, no. 3, pp. 3626–3635, March 2022.

[22] W. Liu, Z. Wang, X. Liu, N. Zeng, Y. Liu, and F. E. Alsaadi, "A survey of deep neural network architectures and their applications," *Neurocomputing*, vol. 234, pp. 11–26, 2017. [Online]. Available: https://www.sciencedirect.com/science/article/pii/S0925231216315533

[23] R. Rajamony, S. Wang, G. Calderon-Lopez, I. Ludtke, and W. Ming, "Artificial neural networks-based multi-objective design methodology for wide-bandgap power electronics converters," *IEEE Open Journal of Power Electronics*, vol. 3, pp. 599–610, 2022.

[24] T. Guillod, P. Papamanolis, and J. W. Kolar, "Artificial neural network (ANN) based fast and accurate inductor modeling and design," *IEEE Open Journal of Power Electronics*, vol. 1, pp. 284–299, 2020.

[25] S. Shen, Z. Zhang, Y. Wu, R. Wang, and Z. Liang, "Modeless prediction of variable coupling effect for multiple-load wireless power transfer," vol. 58, no. 2, pp. 1–5, Feb 2022.

[26] A. O. Hariri, T. Youssef, A. Elsayed, and O. Mohammed, "A computational approach for a wireless power transfer link design optimization considering electromagnetic compatibility," vol. 52, no. 3, pp. 1–4, March 2016.

[27] S. Inoue, R. Nimri, A. Kamineni, and R. Zane, "A new design optimization method for dynamic inductive power transfer systems utilizing a neural network," in *2021 IEEE Energy Conversion Congress and Exposition (ECCE)*, 2021, pp. 1496–1501.

[28] ——, "High-resolution design optimization for ipt including stray field and coupling coefficient," in *2021 IEEE Applied Power Electronics Conference and Exposition (APEC)*, June 2021, pp. 1573–1579.

[29] M. Lu and K. D. T. Ngo, "Analytical calculation of proximity-effect resistance for planar coil with litz wire and ferrite plate in inductive power transfer," vol. 55, no. 3, pp. 2984–2991, May 2019.

[30] A. Paszke, S. Gross, S. Chintala, G. Chanan, E. Yang, Z. DeVito, Z. Lin, A. Desmaison, L. Antiga, and A. Lerer, "Automatic differentiation in PyTorch," in *NIPS-W*, 2017.

[31] D. P. Kingma, J. Ba, D. P. Kingma, and J. Ba, "Adam: A method for stochastic optimization," in *3rd International Conference on Learning Representations, ICLR 2015, San Diego, CA, USA, May 7-9, 2015, Conference Track Proceedings*, Y. Bengio and Y. LeCun, Eds. arXiv, 2014. [Online]. Available: https://arxiv.org/abs/1412.6980

[32] "IEEE standard for safety levels with respect to human exposure to electric, magnetic, and electromagnetic fields, 0 Hz to 300 GHz," *IEEE Std C95.1-2019 (Revision of IEEE Std C95.1-2005/ Incorporates IEEE Std C95.1-2019/Cor 1-2019)*, pp. 1–312, Oct 2019.

[33] C. Sullivan, "Computationally efficient winding loss calculation with multiple windings, arbitrary waveforms, and two-dimensional or three-dimensional field geometry," vol. 16, no. 1, pp. 142–150, Jan 2001.

[34] *Active implantable medical devices - Electromagnetic compatibility - EMC test protocols for implantable cardiac pacemakers, implantable cardioverter defibrillators and cardiac resynchronization devices*, ANSI/AAMI/ISO 14117:2019, Oct. 2019.

[35] P. Virtanen, R. Gommers, T. E. Oliphant, M. Haberland, T. Reddy, D. Cournapeau, E. Burovski, P. Peterson, W. Weckesser, J. Bright, S. J. van der Walt, M. Brett, J. Wilson, K. J. Millman, N. Mayorov, A. R. J. Nelson, E. Jones, R. Kern, E. Larson, C. J. Carey, İ. Polat, Y. Feng, E. W. Moore, J. VanderPlas, D. Laxalde, J. Perktold, R. Cimrman, I. Henriksen, E. A. Quintero, C. R. Harris, A. M. Archibald, A. H. Ribeiro, F. Pedregosa, P. van Mulbregt, and SciPy 1.0 Contributors, "SciPy 1.0: Fundamental Algorithms for Scientific Computing in Python," *Nature Methods*, vol. 17, pp. 261–272, 2020.

CHAPTER 7

GRAPH-BASED MODELING AND OPTIMIZATION OF WPT SYSTEMS

This chapter is a replication of a paper submitted to Electronics [31].

MDPI

Article

Graph-Based Modeling and Optimization of WPT Systems for EVs

Matthew J Hansen [1,†]*, Greg Droge [1,†] and Abhilash Kamineni [1,†]

[1] Utah State University; matthew.hansen@usu.edu [1], greg.droge@usu.edu [2], abhilash.kamineni@usu.edu [3]
* Correspondence: matthew.hansen@usu.edu
† These authors contributed equally to this work.

Abstract: A model of a system of wireless power transfer (WPT) pads is developed, where each WPT pad is modeled as a node and the coupling between pads is modeled as graph edges. This modeling approach is generalized to admit primary, secondary, and booster coils, where power can flow among the pads and a pad can fill multiple roles. An excitation in one pad induces voltage and current in all neighboring pads, causing each pad to act as both a booster coil and either a transmitter or a receiver. Power flow through the entire system can be modeled with the graph structure; the power flow can then be optimized by alternating the phases of the WPT excitations to maximize power transfer. An example is shown where exploiting the graph-based WPT system modeling increases total energy transfer by 25% compared to another method. This increase occurs without altering the geometry of the pads or the magnitude of the pad excitations.

Keywords: wireless power transfer, graphs, optimization, inductive power transfer

Citation: Hansen, M.; Droge, G.; Kamineni, A. Graph-Based Modeling and Optimization of WPT Systems. *Electronics* **2024**, *1*, 0. https://doi.org/

Received:
Revised:
Accepted:
Published:

1. Introduction

Wireless power transfer (WPT) is becoming increasingly common in various applications, including electric vehicles (EVs). The application of WPT to EVs may alleviate range anxiety [1], reduce battery and EV upfront costs, and preserve battery lifetime. WPT transmits power from a *primary coil*, also called a transmitter or Tx, to a *secondary coil*, also called a receiver or Rx. An *excitation*, either a voltage source or current source, forces the creation of an electric field (capacitive power transfer, CPT) or a magnetic field (inductive power transfer, IPT) between the primary and secondary; the field draws power from the primary and injects power into the secondary. Emerging WPT applications often employ multiple coils, but the design and control of such applications only consider interactions between two coils. In this work, interactions between all the coils in a system are modeled, and those interactions are exploited to maximize power transfer.

Typically, IPT can achieve greater power transfer over a larger air gap at lower frequency [2], and so is more commonly used. Consequently, this work assumes IPT, although the principles could be transferred to a CPT system. For an EV application, the primary and secondary coils are generally poorly coupled; a coupling coefficient[1] of $k = 0.3$ is generally near the upper limit. High power transfer requires a high mutual inductance, which implies very large self-inductances. To counteract some of the reactive power consumed by primary and secondary coils, a WPT circuit usually includes *compensation*, a capacitive load that supplies reactive power; many different compensation schemes have been developed [3–5]. The assembly of the coil, compensation, and inverter is sometimes referred to as a *pad*. As

[1] The coupling coefficient is a value that indicates how much magnetic flux is shared between two coils. By convention, the coupling coefficient varies between 0, indicating no net shared flux, and 1, indicating identical magnetic fields. Sometimes it is also convenient to consider negative coupling factors between 0 and −1 to reflect the reference polarity. The coupling factor is only tangentially related to efficiency; a lower coupling factor requires more inductor current to transmit the same power; while that current can incur resistive losses, the coupling coefficient does not directly correspond to radiative or conductive losses.

WPT pad design [6–8], control [9], and IPT modeling [10,11] are well-studied topics, the questions of dynamic control, compensation, and pad design and not considered herein. Rather, the sequel investigates the interconnectedness of multiple WPT nodes to optimize power transfer.

Existing literature tends to describe WPT in terms of point-to-point wireless power transfer, with a single primary or a single secondary, rather than as power transfer through an interconnected graph of WPT nodes. Even in DWPT systems that typically include multiple primaries, it is often assumed that primary–primary interactions are negligible and each primary operates more or less independently [12,13]. WPT systems are generally designed to have good primary–secondary coupling, but also generally have *parasitic coupling*; in IPT systems, the parasitic coupling is the mutual inductance that is not designed for power transfer, i.e., primary–primary or secondary–secondary inductance. This parasitic coupling is always present when there are multiple primaries or secondaries, and while it is generally ignored, its effects can be harmful, negligible, or beneficial.

Some emerging WPT applications make use of a WPT network with multiple primaries and secondaries, whether that is to extend the WPT range in dynamic WPT (DWPT), transfer power to various targets, provide 3-phase power, or increase the WPT range [3,5,7,14,15]. However, none of these works aim to provide a generalized framework for modeling and exploiting parasitic coupling. The work in [5] uses changes in the parasitic primary–primary coupling to detect an approaching vehicle, but power is not transferred along the primary–primary link. In [14,15], multiple primaries and secondaries are considered, but primary–primary coupling and secondary–secondary coupling are not considered. Booster coils, or coils without a conductive connection to an excitation source that are placed between a primary and a secondary coil, are discussed in [3], which increase the distance over which power transfer is achieved. However, there is still a single transmitter coil and a single receiver coil. Other work estimates the existence or position of multiple secondaries, but using parasitic coupling to maximize power transfer is outside the scope of [14,16,17]. The work in [18], although only considering a single WPT pad, bears conceptual and mathematical similarities to the approach developed herein. In [18], current distribution through multiple parallel windings within a single coil is discussed and modeled. Each winding is coupled with the secondary coil, but also with the other, parallel windings; this affects current distribution, losses, and overall primary–secondary coupling. However, multiple primary pads and parasitic coupling are not discussed.

This work aims to exploit parasitic coupling to improve power transfer and present a model that unifies the varying modeling methods for complex WPT systems. This improves the current state-of-the-art in two ways. First, it allows for more accurate modeling of the WPT system, modeling power flow through the network, rather than simply from one primary to one secondary. This results in a unified model that can be used on booster coils, parallel windings, or complex WPT systems with multiple primaries and secondaries. Second, this work also develops a technique to optimize power transfer by altering the phase of each primary in the system. Brief discussions of distributed controllability and multiple-secondary systems are included. To those ends, WPT through a complex system of mutually-coupled coils is described with a graph, where each node represents a WPT unit, and the edges represent mutual coupling. This graph structure allows the practitioner to model and optimize power flow from one point to another throughout the network, rather than through two coupled coils. Multiple applications of this approach exist; the work focuses on an in-motion or dynamic WPT (DWPT) system represented as a series of stationary WPT (SWPT) systems. The system of each SWPT set point can be modeled and optimized with a graph, leading to an optimization of the DWPT system as a whole. This approach yields richer insights than observation at a single set point.

The paper is organized as follows. Section 2 defines the mathematical background of the system, and describes a method to account for all the paths from one node to another. Section 3 discusses optimal control of a multi-pad system, and addresses some of the capabilities and challenges of this approach. An example of this modeling technique is

discussed in Section 4. Section 5 concludes this paper, reiterating key contributions and improvements with this modeling approach.

2. Basic Model

With multiple primaries and secondaries, the interactions become complicated. In Section 2.1, some notation is defined, followed by a discussion of the complexities of complex WPT systems with three or more WPT pads in Section 2.2. In Section 2.3 A graph is developed to model power flow through the complex systems, for which a mathematical model is defined.

2.1. Definition of States

First, note that with any compensation and excitation, a WPT pad can be modeled as either a Norton or Thévenin equivalent circuit; here it is assumed that the WPT pads are represented as Thévenin circuits, which are excited by a voltage source. Consider a system with Thévenin equivalent circuits on two primary pads and two secondary pads, as seen in Figure 1, where each pad is represented as a graph node. Pad n is excited by a phasor voltage source $\bar{v}_{X,n}$, which drives a current $\bar{i}_n$ through the Thévenin equivalent impedance Z_n and the power transfer coil. The voltage across the Thévenin impedance, $\bar{v}_{Z,n}$ plus the voltage across the coil $\bar{v}_{L,n}$ sums to $\bar{v}_{X,n}$.

Similar quantities can be gathered into a single vector. Assume there are N WPT coils in a system, then define the vectors

$$\begin{aligned} \mathbf{v}_L &= \begin{bmatrix} \bar{v}_{L,1} & \bar{v}_{L,2} & \cdots & \bar{v}_{L,N} \end{bmatrix}^T \\ \mathbf{v}_Z &= \begin{bmatrix} \bar{v}_{Z,1} & \bar{v}_{Z,2} & \cdots & \bar{v}_{Z,N} \end{bmatrix}^T \\ \mathbf{v}_X &= \begin{bmatrix} \bar{v}_{X,1} & \bar{v}_{X,2} & \cdots & \bar{X}_{X,N} \end{bmatrix}^T \\ \mathbf{i} &= \begin{bmatrix} \bar{i}_1 & \bar{i}_2 & \cdots & \bar{i}_N \end{bmatrix}^T \end{aligned} \tag{1}$$

Also, define an *inductance matrix*, noted as L, that collects that self- and mutual-inductance values. The inductance $L_{m,n}$ relates the current through coil m to the voltage induced across coil n. Note that $L_{m,n} = L_{n,m}$.

$$L = \begin{bmatrix} L_{1,1} & L_{1,2} & \cdots & L_{1,N} \\ L_{2,1} & L_{2,2} & \cdots & L_{2,N} \\ \vdots & \vdots & \ddots & \vdots \\ L_{N,1} & L_{N,2} & \cdots & L_{N,N} \end{bmatrix} \tag{2}$$

The problem can be mapped to a graph, as in Figure 1, which uses the notation defined above. Each node corresponds to a single pad, and the coupling between pads is expressed as an edge. The coupling can be interpreted with magnetic flux, induced voltage, or power flowing along the edges of the graph, with each primary or secondary pad represented with a node. States at each node are the relevant quantities in the pad, i.e., current through the coils and voltages across the inductors, and the input to each node is the excitation voltage.

In Figure 1, there are multiple power transmission paths from Primary 1 to Secondary 1 and multiple paths from Primary 2 to Secondary 1. The net effect of all the transmission paths is captured in the equation above. With this formulation, the matrices Z and L are both symmetric, implying that the inverse matrix is also symmetric.

2.2. Difficulties of Complex WPT Systems

Most literature considers a system with only a single primary pad and a single secondary pad, where the number of WPT pads $N = 2$. In that case, the power flow is

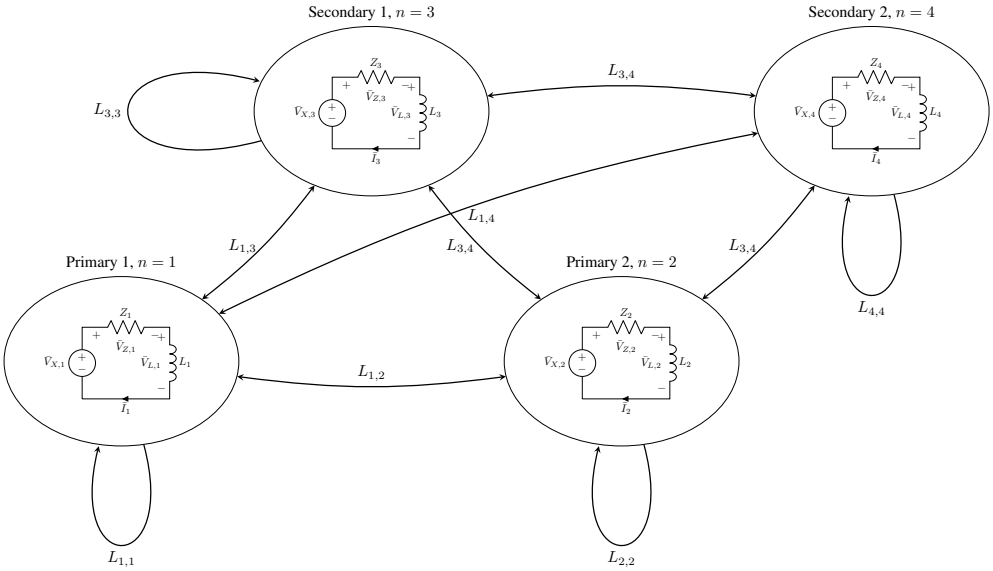

Figure 1. Diagram of WPT system as a graph, with each edge representing an inductance and each oval corresponding to a node in the graph or a WPT pad in the circuit.

straightforward and can be analyzed with tools like the transformer T-model or the reflected impedance.

However, those tools are not appropriate for a more complex network. Consider the WPT system shown in Figure 1, which has two primary pads and two secondary pads. Each coil couples with the others, and the interactions can be difficult to model. For example, suppose Primary 1 ($n = 1$) is excited with an excitation voltage $\bar{v}_{X,1}$, which induces currents in all the other pads, which reflect a voltage back to $\bar{i}_{L,1}$. However, the current $\bar{i}_2$ also affects the current $\bar{i}_3$, which affects the voltage seen at $\bar{v}_{L,1}$. Because the pads interact with each other through their neighbors, the interactions between a pad and each of its neighbors cannot be analyzed in isolation and the interactions across the system must be analyzed at once.

Some pads may be poorly coupled to others, and the system may be reasonably represented by a partially connected graph, where low-value edges are rounded to 0. In very complex systems, there may be an improvement in computational load with a partially connected graph, or it might be computationally heavy to generate all the edge weights. However, if all the relevant inductance values are generated by a FEM solver, or if the graph is small, there may not be an appreciable advantage to pruning low-weight edges.

In this paper, the edge weight is inductance between coils in each node/pad; inductance is defined as the ratio of voltage across a coil to the frequency and current through a coupled coil[2]. Each edge of the graph in Figure 1 corresponds to one or two[3] elements of L; the edges between distinct nodes are represented twice in L, i.e., $L_{m,n}$ and $L_{n,m}$, and the edges leading to and from the same node are represented only once each in L, i.e, $L_{n,n}$. The graph structure is encoded within the symmetric inductance matrix L, and the interactions between states at any node are mediated through an impedance matrix Z.

2.3. Mathematical Model

Consider the WPT system shown in Figure 1, with representative coupling values. This represents a snapshot of a dynamic WPT (DWPT) system, where two secondaries

[2] Each coil is coupled perfectly with itself. When the voltage and current are measured on the same coil, the ratio is self-inductance

[3] The edges represented twice in L imply that current through coil m induces a voltage on n, and the same current through n induces the same voltage on m.

move across two primary pads. Let the switching frequency or the frequency of the AC voltage excitation, be given as ω with units of radians per second.

Even in a DWPT scenario, the dynamics are typically dominated by the switching: The voltages across the inductors in a dynamic system are given by

$$\mathbf{v} = L\frac{d\mathbf{i}}{dt} + \frac{dL}{dt}\mathbf{i}. \tag{3}$$

Expressing the voltage and current quantities as phasors, Equation (3) can be expressed as

$$\mathbf{v} = \left(j\omega L + \frac{dL}{dt}\right)\mathbf{i}. \tag{4}$$

Typically, the switching frequency is high relative to the inductance values. A reasonable mutual inductance value in a DWPT system is 5 µH, and pads could be spaced on 1 m intervals. If a vehicle travels at 30 m/s, then

$$\left\|\frac{dL}{dt}\right\| \approx 0.2\,\mu\text{H/s}. \tag{5}$$

However, according to existing standards, a common switching frequency is 85 kHz [19]; assuming the same typical inductance value of 5 µH yields

$$\|j\omega L\| \approx 2\,\text{H/s}. \tag{6}$$

Although very approximate, Equations (5) and (6) show that the dynamics due to switching are roughly six orders of magnitude more important than dynamics due to changing inductances; therefore, Equation (3) can be approximated as

$$\mathbf{v} = L\frac{d\mathbf{i}}{dt} \tag{7}$$

and the DWPT system can be analyzed as a series of stationary WPT systems. For simplicity, only one secondary is considered in this paper, except for the discussion on multiple secondaries in Section 3.3.

The defining equations are voltage-balancing and the inductance equation. Using the vectors defined in Equation (1), the relevant equations are:

$$\begin{aligned} \mathbf{v}_L &= j\omega L\mathbf{i} \\ \mathbf{v}_Z &= Z\mathbf{i} \\ \mathbf{v}_X &= \mathbf{v}_L + \mathbf{v}_Z \end{aligned} \tag{8}$$

The defining equations can be solved for $\mathbf{i}$:

$$\mathbf{i} = (j\omega L + Z)^{-1}\mathbf{v}_X. \tag{9}$$

The expression in Equation (9) shows that $\mathbf{v}_X$ is an input to the system; the excitation voltages can be arbitrarily, independently, and directly selected. The current vector $\mathbf{i}$ represents a state, which cannot be directly set but is a consequence of the inputs. Note that $(j\omega L + Z)$ is assumed to be invertible; this is addressed more fully in Section 3.2 For convenience, define the matrix

$$B = (j\omega L + Z)^{-1} \tag{10}$$

and let $b_{m,n}$ be the element in row m and column n of B.

This approach is general enough to model most linear WPT systems, but the graph underlying this structure is powerful enough to quickly and powerfully model complicated systems, like that discussed in [3]. Even for a system for which this approach may not directly work, simple modifications to the equations presented here may make this

approach applicable. One example is the LCC-compensated circuit used in [5,12,20], where the Thévenin equivalent impedances and excitation voltages are all infinite. In such a case, a very similar approach to that taken herein, but using Norton equivalent circuits, could be used to model the system.

3. Control Optimization

The utility of the WPT graph is highlighted with an optimization of power flow. That is, given a fixed secondary phase, it is desired to control the phase of each primary pad to maximize power transfer. As mentioned earlier, most of this section assumes two primary pads and one secondary pad.

Consider the case where the secondary operates at the reference phase, meaning that the phasor values in the voltage excitation vector $\mathbf{v}_X$ corresponding to the secondary excitations are entirely real. Letting $v_{X,s}$ be the element of $\mathbf{v}_X$ corresponding to the secondary,

$$v_{X,s} \in \mathcal{R} \tag{11}$$

Because all impedances in the system are typically purely reactive, any real excitation voltages induce imaginary currents, and any imaginary excitation voltages correspond to real currents. In a general case, the primaries should each operate at $\pm 90^\circ$ relative to the phase of the secondary, so that the current induced on the secondary voltage source is in phase with that voltage source. However, there remains the question of whether a given primary should lead or lag the secondary; that determination is the focus of this section.

3.1. Omniscient Optimal Control

With an omniscient controller, calculating the optimal control is straightforward. Without loss of generality, let the excitation voltage of the secondary be defined by the real, positive phasor $\bar{v}_{X,s}$, where s is the index of the secondary pad. With the voltages and currents defined as in Figure 1, the complex power supplied by the voltage source is given by

$$\bar{v}_{X,s}\bar{i}_s^*, \tag{12}$$

where $\bar{i}_s^*$ is the complex conjugate of the current $\bar{i}_s$. Here $\bar{v}_{X,s}$ is a real constant, and the other quantities in $\mathbf{v}_X$ are the variables of optimization. Maximizing the real power transferred is expressed as:

$$\max_{\mathbf{v}_X \setminus v_{X,s}} \Re\left(-\bar{i}_s^* \bar{v}_{X,s}\right) \tag{13}$$

Two constraints are necessary. First, it is necessary that the circuit equations encoded in Equation (9) are satisfied, so that the optimization result is realizable. Second, the voltages must be bounded. There are two reasons for the excitation voltages to be bounded. First, the excitation voltages are typically physically bounded by the DC bus voltage[4]; the voltage applied across the system at any moment may not exceed the DC supply voltage. Second, without a constraint on the norm of the excitation voltages, the optimization would maximize the norms of the voltages, rather than optimizing the phase. An optimizer is unlikely to solve the problem, and no insight into the system is gained by noting that infinite excitation voltages can transfer infinite power. Letting α_n be a real-positive value describing the maximum excitation current for node n in the graph (either a primary or secondary pad), the full optimization can be expressed mathematically as

$$\begin{aligned} \max_{\mathbf{v}_X} \ & \Re\left(-\bar{i}_s^* \bar{v}_{X,s}\right) \text{ s.t.} \\ & \|\bar{v}_{X,n}\| \leq \alpha_n \forall n \\ & \mathbf{i} = B\mathbf{v}_X. \end{aligned} \tag{14}$$

[4] the Thévenin equivalent voltage can be unbounded, but such a case would best be modeled by a Norton equivalent circuit.

This optimization is trivial, once the inverse matrix B is found. Using the element-wise notation for B, the objective function is expanded to consider each voltage excitation separately:

$$\Re\left(-\bar{i}_s^* \bar{v}_{X,s}\right) = \sum_n \Re\left(-\bar{v}_{X,s} b_{s,n}^* \bar{v}_{X,n}^*\right). \tag{15}$$

The product $\bar{v}_{X,s} b_{s,n}^*$ is determined by the circuit and does not depend on the variables of optimization. It is observed that the objective function will be maximized when the norm of the excitation is maximized, as

$$\|\bar{v}_{X,n}\| = \alpha_n \tag{16}$$

and $\bar{v}_{X,n}$ is anti-parallel to the product $\bar{v}_{X,s} b_{s,n}^*$, or

$$\bar{v}_{X,n} = \frac{-\alpha_n \bar{v}_{X,s} b_{s,n}^*}{\left\|\bar{v}_{X,s} b_{s,n}^*\right\|} \tag{17}$$

Note that the secondary excitation voltage $\bar{v}_{X,s}$ is given, and not a variable of optimization in this case. An alternative interpretation is that $V_{X,n}$ should lag $-V_{X,s}$ by the angle of $b_{s,n}$.

Recall that the phase of $\bar{v}_{X,s}$ is chosen, and other phases are measured relative to $\bar{v}_{X,s}$. Let $\bar{v}_{X,s}$ be defined as positive and real, i.e.

$$\bar{v}_{X,s} \in \mathbb{R}_{>0}. \tag{18}$$

Typically, the impedance in a WPT system is dominated by the reactance, meaning the system is essentially lossless. In such a system,

$$\Re(b_{m,n}) = 0; \tag{19}$$

in that case, $\bar{v}_{X,n}$ should be parallel to $b_{s,n}$ for $n \neq s$, or

$$\bar{v}_{X,n} \parallel b_{s,n}. \tag{20}$$

Consider some implications of the assumptions in Equations (18)–(20):

$$\begin{aligned} \bar{v}_{X,s} \in \mathbb{R}_{>0} &\implies \bar{v}_{X,s} = \|\bar{v}_{X,s}\| \\ \Re(b_{m,n}) = 0 &\implies {b_{m,n}}^* = -b_{m,n} \\ \bar{v}_{X,n} \parallel b_{s,n} &\implies \bar{v}_{X,s}^* b_{s,n} = \|\bar{v}_{X,s}\| \|b_{s,n}\|. \end{aligned} \tag{21}$$

Substituting into Equation (15) yields:

$$\begin{aligned} \Re\left(-\bar{v}_{X,s} b_{s,n}^* \bar{v}_{X,n}^*\right) &= \Re\left(-\|\bar{v}_{X,s}\| b_{s,n}^* \bar{v}_{X,n}^*\right) \\ &= \Re\left(\|\bar{v}_{X,s}\| b_{s,n} \bar{v}_{X,n}^*\right) \\ &= \Re\left(\|\bar{v}_{X,s}\| \|b_{s,n}\| \left\|\bar{v}_{X,n}^*\right\|\right), \end{aligned} \tag{22}$$

which is the maximum possible value subject to the constraints.

Note that $\bar{v}_{X,s}$ is fixed before the optimization, and is not included in the optimization. In a lossless system,

$$\Re\left(\bar{v}_{X,s} \bar{v}_{X,s}^* b_{s,s}^*\right) = 0, \tag{23}$$

and the optimization need only consider the other voltage excitations.

3.2. Comments on Invertibility

In Equation (14), it is assumed that the matrix B is invertible. The discussion on invertibility follows two tracks; in Section 3.2.1, it is shown that a realizable, solvable system implies the existence of B. In Section 3.2.2, sufficient conditions for invertibility are discussed.

3.2.1. Existence of B in a Realizable System

To prove the existence of B, the logical contrapositive will be used. Let $(Z, L, \omega) \in Y$ mean that Z, L, and ω define a realizable, solvable system. This section proves

$$\nexists B \implies (Z, L, \omega) \notin Y \tag{24}$$

to demonstrate that

$$(Z, L, \omega) \in Y \implies \exists B, \tag{25}$$

which means that B must exist in any solvable, realizable system.

In the counterexample, where $(j\omega L + Z)$ is non-invertible, it is known that $(j\omega L + Z)$ is necessarily rank-deficient:

$$\exists \mathbf{i} \neq 0 | \mathbf{v}_x = (j\omega L + Z)\mathbf{i} = 0. \tag{26}$$

That statement can be interpreted as "there exists a state where there is current through some inductors, but there is no excitation voltage", which means that current flows through the system with no excitation current. Practically, such a system is unrealizable due to parasitic resistances; any system with parasitic resistances is guaranteed to produce a viable B.

However, when the parasitic resistance is very small or unknown, it may be reasonable to model the system with ideal conductors. Even in such a system, Equation (26) implies that the effective impedance around any of the Thévenin circuits is zero. As long as the effective impedance around any loop is non-zero, the necessary matrix will be invertible.

3.2.2. Tests and Necessary Conditions for Invertibility

Future research should further develop sufficient conditions, but for now, three tests can guarantee the existence of B. If either of the following sufficient conditions are met, the system is guaranteed to be realizable with non-zero impedance, and B is guaranteed to exist.

Typically, the WPT system can be modeled as lossless, meaning that Z is imaginary. In that case, consider the reactance matrix X such that

$$Z = jX, X \in \Re. \tag{27}$$

The matrix B can be expressed as

$$B = -j(\omega L + X)^{-1}, \tag{28}$$

which is specialized form of Equation (10) assuming purely reactive impedance. Note that L is an inductance matrix, which is necessarily positive definite, real, and symmetric. Let $\lambda_{L,1}$ be the lowest eigenvalue of ωL. Further, let $\lambda_{X,1}$ be the lowest diagonal element of X; since X is diagonal, $\lambda_{X,1}$ is the lowest eigenvalue. Let $\lambda_{B^{-1}}$ be the lowest eigenvalue of $(\omega L + X)$. The sufficient condition is that

$$\lambda_{X,1} \geq 0, \tag{29}$$

which implies

$$\lambda_{X,1} \geq 0 \implies \lambda_{L,1} + \lambda_{X,1} > 0 \implies \lambda_{B^{-1}} > 0, \tag{30}$$

therefore, none of the eigenvalues of $(\omega L + X)$ are zero, so $(\omega L + X)^{-1}$ and B must exist. The first sufficient condition is that in a lossless system, the compensating reactances are non-negative. This will occur when the Thévenin impedance is not present or generated by an inductor or a resistor; normally, however, the compensation is capacitive, requiring a different sufficient condition.

A less-restrictive interpretation of Equation (30) allows negative Thévenin reactance, or capacitive compensation. If the eigenvalues of ωL are known, then a looser sufficient

condition can be derived from Equation (30). Let the Thévenin impedance be capacitive, but be bounded by the eigenvalues of ωL:

$$\lambda_{X,1} > -\lambda_{L,1}. \tag{31}$$

This leads to the conclusion

$$\lambda_{X,1} > -\lambda_{L,1} \implies \lambda_{L,1} + \lambda_{X,1} > 0 \implies \lambda_{B^{-1}} > 0 \tag{32}$$

This condition guarantees no eigenvalues of 0, proving the existence of B. The lower limit on the reactance also establishes a lower limit on the capacitor size. This allows for more realistic compensation, but can be unnecessarily restrictive when pad sizes are dissimilar: the capacitance for all pads is essentially restricted by the least-inductive coil.

One approach that defines a compensation limit per pad is using Gershgorin circles, which also allows for resistive elements in the circuit. The Gershgorin circle theorem states that each eigenvalue of a matrix A must lie within a circle on the complex plane, with center points a_{ii} given as the diagonal elements of A, and radii R_i given by the sum of the absolute value of off-diagonal elements in each row. Using the Gershgorin circle theorem on the matrix $(j\omega L + Z)$ with $\lambda_{B^{-1},k}$ being an eigenvector of that matrix and z_{ii} the i^{th} diagonal of Z yields

$$\forall \lambda_{B^{-1},k} \exists i : \left|\lambda_{B^{-1},k} - j\omega L_{i,i} - z_{ii}\right| \leq \sum_{m \neq i} |L_{i,m}|. \tag{33}$$

This states that each eigenvalue of $(j\omega L + Z)$ must be within a circle; as long as

$$\forall i, |j\omega L_{i,i} + z_{ii}| > \sum_{m \neq i} |L_{i,m}|, \tag{34}$$

none of the eigenvalues are 0 and the matrix must be invertible. The value of the compensation on each pad can be modified such that Equation (34) is always satisfied. In a poorly-coupled system, the Gershgorin circle theorem is especially powerful. The three sufficient conditions described here are summarized:

- Non-negative compensation reactance, $\lambda_{X,1} \geq 0$. This essentially prohibits capacitive compensation and assumes lossless circuits, but can be applied without knowing the inductance matrix.
- Limited negative reactance, $\lambda_{X,1} \geq -\lambda_{L,1}$. This allows capacitive compensation but assumes lossless circuits and applies the same compensation restriction to all pads.
- Gershgorin circle limitation, $\forall i, |j\omega L_{i,i} + z_{ii}| > \sum_{m \neq i} |L_{i,m}|$. This allows lossy components and assigns a different compensation limit to each pad.

3.3. Extension to Multiple Secondaries

The approach in Section 3.1 can be modified to account for multiple secondary pads. Some high-power WPT applications use multiple secondary pads to maximize power transfer, or some drone applications have multiple disparate secondary coils [14]. There are many ways to define an objective function, weighting power transfer to a given coil, or optimizing for total power transfer. For a DWPT application where all secondaries are connected to the same battery, the objective of optimization may be defined as the total power transferred to all secondaries. In some cases, there may be a constraint that power to any given secondary does not exceed some hardware rating, although the hardware should generally be rated high enough that such a constraint is unnecessary. For a system with n

pads and k secondaries, where the secondaries are represented in the last rows of L, the optimization can be expressed as:

$$\begin{aligned} \max_{\mathbf{v}_x \setminus v_{X,n}} \ & \Re\left(\sum_{l=n-k+1}^{n} -\bar{i}_l^* \bar{v}_{X,l}\right) \text{ s.t.} \\ & \bar{v}_{x,n} \text{ is given} \\ & \|\bar{v}_{X,n}\| \leq \alpha_n \ \forall n \\ & \mathbf{i} = B\mathbf{v}_X. \end{aligned} \tag{35}$$

In Equation (35), the magnitudes of all the excitation voltages are fixed, and the phase of one secondary is fixed. Although there are multiple secondaries, it is only necessary to fix the excitation voltage corresponding to one; the phase of the other secondary may vary. Two immediate consequences follow. First, the problem is no longer linear, but quadratic: there is a quadratic term in the objective function summation corresponding to each unfixed secondary excitation voltage. Second, the other secondaries have the freedom to operate at different phase angles; each of the unfixed secondaries may alter its phase to reduce reactive power or maximize power transfer to itself. The result of these two consequences is that the simple closed-form solution developed in Section 3.1 is no longer applicable, and the correlation between real/complex currents and primary/secondary excitations breaks down. However, the quadratic problem can still be easily solved by most optimizers.

A convenient closed-form solution still exists for the special case where all the secondaries are operating at fixed excitations; that is, when the secondary voltage excitations are excluded from the variables of optimization. In that case, the objective function is given by:

$$\begin{aligned} \max_{\mathbf{v}_x} \ & \Re\left(\sum_{l=n-k+1}^{n} -\bar{i}_l^* \bar{v}_{X,l}\right) \text{ s.t.} \\ & \bar{v}_{x,k} \text{ is given for all } k \geq n-k+1 \\ & \|\bar{v}_{X,n}\| \leq \alpha_n \ \forall n \\ & \mathbf{i} = B\mathbf{v}_X. \end{aligned} \tag{36}$$

Note that the problem is linear when all the secondary excitations are fixed.

Similar to the calculations in Equation (15), the objective function can be expressed as:

$$\begin{aligned} & \Re\left(\sum_{l=n-k+1}^{n} \left(-\bar{v}_{X,l}\bar{i}_l^*\right)\right) \\ &= -\Re\left(\sum_{l=n-k+1}^{n}\left(\bar{v}_{X,l}\sum_n b_{l,n}^* \bar{v}_{X,n}^*\right)\right) \\ &= -\sum_n \Re\left(\left(\sum_{l=n-k+1}^{n} \bar{v}_{X,l} b_{l,n}^*\right)\bar{v}_{X,n}^*\right) \end{aligned} \tag{37}$$

Similar to the single-secondary case, the objective function will be maximized when

$$\bar{v}_{x,n} = \frac{-\alpha_n \sum_{l=n-k+1}^{n} \bar{v}_{X,l} b_{l,n}^*}{\left\|\sum_{l=n-k+1}^{n} \bar{v}_{X,l} b_{l,n}^*\right\|} \tag{38}$$

3.4. A Note on Local Optimization

The graph-based structure is critical to understanding potential false assumptions about the system; such assumptions may be valid for a simple system with a single primary and a single secondary but break down in more complex systems. One such assumption is that power transfer can be maximized by individually maximizing the power transferred by each primary pad; such an assumption is briefly disproven here.

Consider a system with inductance and admittance matrices defined as:

$$\begin{aligned} \omega &= 1 \\ L &= \begin{bmatrix} 1 & \frac{1}{2} & \frac{1}{3} \\ \frac{1}{2} & 1 & \frac{1}{2} \\ \frac{1}{3} & \frac{1}{2} & 1 \end{bmatrix} \\ Z &= 0, \end{aligned} \tag{39}$$

where $n = 3$ corresponds to the secondary. Note that L is positive definite, so the system is realizable. $Z = 0$ implies a system with no series compensation. Assuming the $\bar{v}_{X,3} = 1$, and $\forall n, \alpha_n = 1$, the optimization yields

$$\begin{aligned} \mathbf{v}_X &= \begin{bmatrix} j & j & 1 \end{bmatrix}^T \\ \mathbf{i} &= \begin{bmatrix} -0.75 + j0.15 & -1 + j0.6 & 0.75 - j1.35 \end{bmatrix}^T \end{aligned} \tag{40}$$

with the vector of apparent power delivered by each pad

$$\mathbf{s} = \begin{bmatrix} 0.15 + j0.75 & 0.6 + j1 & -0.75 + j1.35 \end{bmatrix}^T, \tag{41}$$

so the secondary receives 0.75 W of real power.

However, consider the case where the excitations for the secondary and first primary are fixed, and then optimize the other primary ($n = 2$) excitation to maximize real power transfer from that primary. If the primary pad only optimizes the total power it sends, regardless of whether that is to another primary or a secondary, the formulation is equivalent to the multiple-secondary approach in Equation (38). The resulting excitation currents, voltages, and apparent powers are

$$\begin{aligned} \mathbf{v}_X &= \begin{bmatrix} j & -\frac{1}{\sqrt{2}} - j\frac{1}{\sqrt{2}} & -1 \end{bmatrix}^T \\ \mathbf{i} &= \begin{bmatrix} 1.774 - j0.574 & -1.731 + j0.531 & 0.274 + j0.926 \end{bmatrix}^T \\ \mathbf{s} &= \begin{bmatrix} -0.574 + j1.774 & 0.849 + j1.6 & -0.274 + j0.926 \end{bmatrix}^T. \end{aligned} \tag{42}$$

Comparing Equation (42) with Equation (41), it can be seen that the primary $n = 2$ does transfer more real power but does so at the expense of power transfer to the secondary. That is, optimizing power transfer locally at each primary pad is not sufficient to guarantee optimal power transfer.

4. Example

To demonstrate the effectiveness of this approach, a DWPT test simulated the graph-based optimization described here. As approximated in Equations (5)–(7), the dynamics due to the changing geometry are insignificant compared to the AC dynamics, and the DWPT system can be approximated by a series of stationary WPT systems. The power transferred during a DWPT test is indicative of the graph-based approach over a range of feasible graph configurations.

Three different systems were simulated; visualized in Figures 2–4; all three systems are roughly in line with a DWPT system for electric vehicles. All tests have four primary pads, the first two systems have one secondary pad, and system three has two secondary pads. All the pads in all the systems are square. In all cases, the DC excitation voltage is 500 V. The air gap is 140 mm, and the vehicle assembly moves across the series of primary pads at 50 km/h. Note that the switching frequency is 85 kHz, in line with [19]. All systems

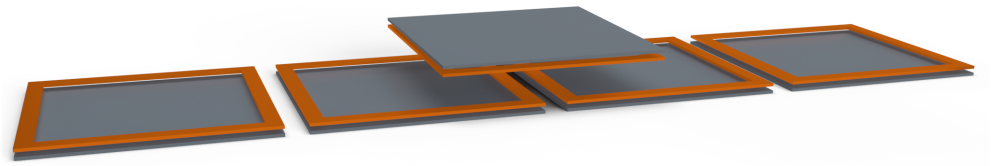

Figure 2. Illustration of example WPT System 1. Four primary (roadway) pads transfer power to a single, moving secondary (vehicle) pad.

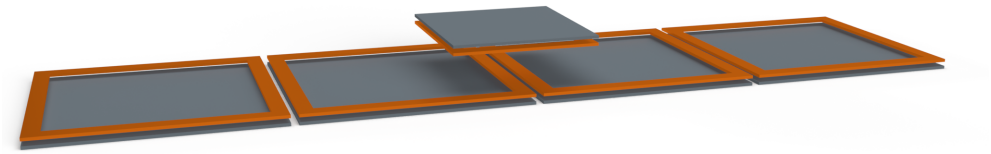

Figure 3. Illustration of example WPT System 2. Four primary (roadway) pads transfer power to a single, moving secondary (vehicle) pad. The vehicle pad is smaller than in System 1, and the pads are closer together.

are modeled in a FEM solver to determine the inductance matrix as the secondary pad moves across a range of motion, centered above the assembly.

Series compensation is used, with a slight mistuning to avoid an AC short circuit and ensure the potential for zero-volt switching; the compensation impedance is a 350 nF capacitor in all cases. The inductance is boosted by including a ferrite plate outside each coil, of the same dimensions as the coil. The gap between the coil and ferrite is 15 mm, and the thickness of both the ferrite and the coil is 10 mm. The circuit diagram for each pad in all systems is given in Figure 5, and values are shown in Table 1, respectively.

Three different control schemes are compared here. The first control scheme is the naive approach, where each pad operates at a set phase and the primary pads lead the secondary pads by 90°. The second control scheme is the inductor-based approach, where the phase of each primary excitation corresponds to the sign of the primary–secondary coupling at that point. In the absence of other primary pads, this approach would be optimal. Note that the inductor-based control scheme is ambiguous in the multi-secondary system, and so is excluded from consideration. The third control scheme is the optimal approach described in detail in this paper, which accounts for power flow through the network. For Systems 1 and 2, the closed-form solution in Equation (17) is used; for the multi-secondary System 3, the quadratic optimization in Equation (35) is used.

The plots of power with all three approaches are shown in Figures 6–8, with the total power transferred given in Table 2. From Table 2, it can be seen that the graph-based method outperforms the other methods. This performance boost is achieved without increasing the excitation voltages, but simply by exploiting the parasitic coupling. This exemplifies the thesis of this paper; that the graph-based approach allows an engineer to

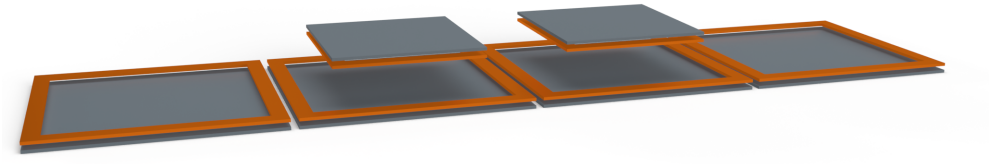

Figure 4. Illustration of example WPT System 3. Four primary (roadway) pads transfer power to two moving secondary (vehicle) pads. The pad design is the same as in System 2, but with an additional secondary pad.

Table 1. Typical WPT parameters for each geometry.

System Number	Primary Pad Dimension	Secondary Pad Dimension	Pad Spacing	Primary Turns	Secondary Turns
1	750 mm	750 mm	850 mm	3	3
2	750 mm	500 mm	775 mm	3	4
3	750 mm	500 mm	775 mm	3	4

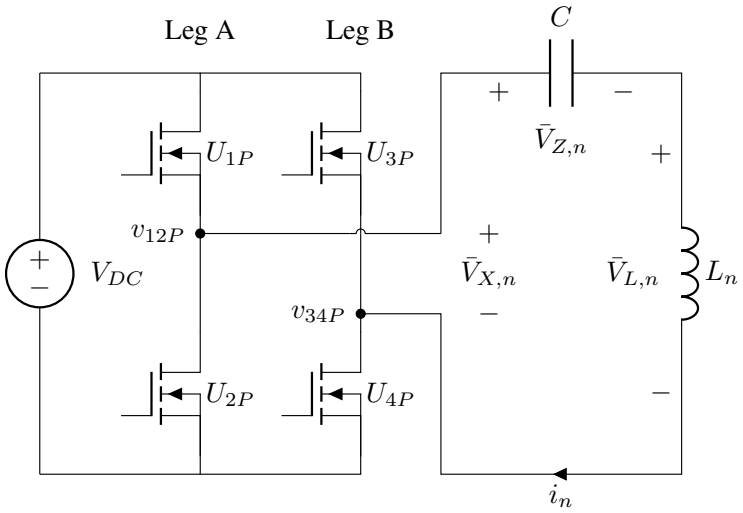

Figure 5. Circuit diagram; note that the primary and secondary pads are all identical.

push maximum power to the secondary pad and that such an approach is guaranteed to outperform other control strategies.

In Figure 6, observe that the inductance-based approach under-performs the other approaches; at those brief moments, the naive approach happens to correspond with the optimal approach. Similarly, at the beginning and the end, the naive approach causes a primary pad to pull power from the negatively-coupled secondary pad, while the inductor-based approach coincides with the graph-based, optimal approach. In those regions, the naive approach underperforms the other two approaches. Only the graph-based approach accounts for both phenomena. However, the difference between the approaches is relatively small, with only a 6.3 % improvement over the worst-case scenario.

In Figure 7, the inductance-based approach under-performs worse across nearly the entire range. In a system with only one primary pad and one secondary, the inductance-based approach is optimal. However, with the graph structure derived from the geometry depicted in Figure 3, the parasitic couplings play a greater role. The graph-based approach and the naive approach coincide over most possible graph structures. However, at the extrema, when the secondary is only coupled strongly to one primary pad, the inductor-based and graph-based models suggest the same strategy. As in the first system, the graph-based model can be optimized to transmit more power than either alternative.

There are five peaks in Figure 8; the addition of another secondary pad introduces another position where power can be transferred. The inductance-based method is ambiguous with two secondaries, so only the naive and graph-based approaches are considered. As in the others, power transfer is improved with the graph-based model. Recall that in all cases, the magnitudes of the excitation voltages are constant.

As noted in [3], a lower total impedance (including the coil and the compensation) allows higher power transfer levels. Each coil, acting as a primary, has a lower impedance between the excitation voltage and the induced voltage, forcing more current through

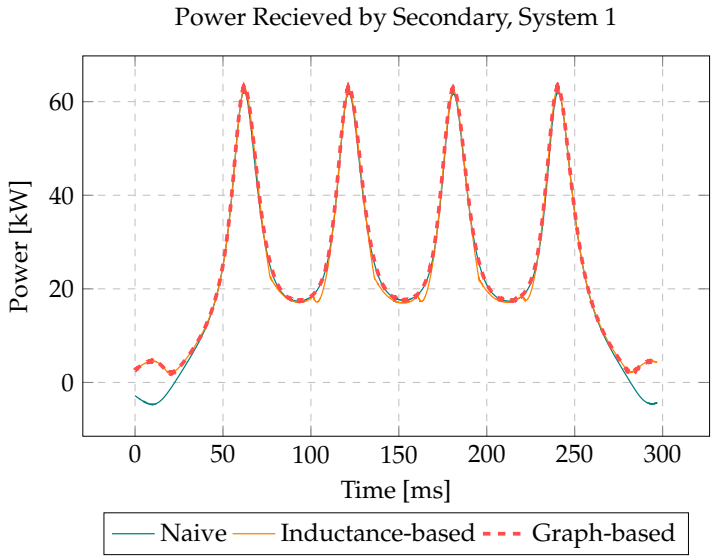

Figure 6. Comparison of three approaches. Power is smoothed by a low-pass filter with a corner frequency of 42.5 Hz. Note that the inductance-based method underperforms on the troughs, and the basic method underperforms at the beginning and the end.

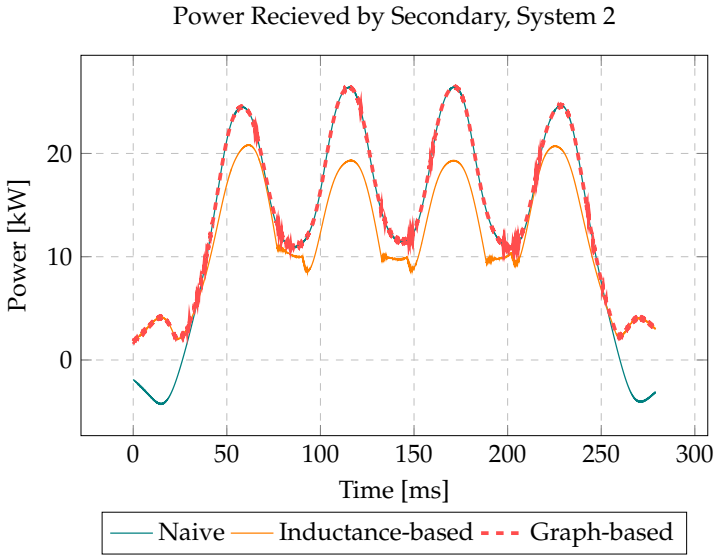

Figure 7. Comparison of three approaches. Power is smoothed by a low-pass filter with a corner frequency of 42.5 Hz. Note that the inductance-based method underperforms on the troughs, and the basic method underperforms at the beginning and the end.

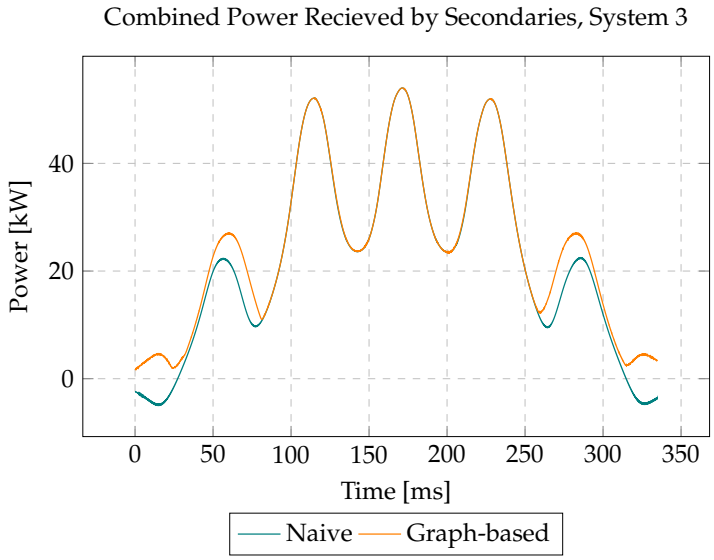

Figure 8. Comparison of three approaches. Power is smoothed by a low-pass filter with a corner frequency of 42.5 Hz. Note that the inductance-based method underperforms on the troughs, and the basic method underperforms at the beginning and the end.

Table 2. Energy transferred to secondary pad(s) for each system and control algorithm. The "Relative Improvement" field relates the total energy transferred to the lowest-energy variant of the same system.

System Number	Control Scheme	Energy Transferred	Relative Improvement
System 1	Naive	7.00 kJ	N/A
System 1	Inductance-based	7.24 kJ	3.5 %
System 1	Graph-based	7.44 kJ	6.3 %
System 2	Naive	3.71 kJ	12.7 %
System 2	Inductance-based	3.30 kJ	N/A
System 2	Graph-based	4.04 kJ	22.3 %
System 3	Naive	7.49 kJ	N/A
System 3	Graph-based	8.27 kJ	10.4 %

the circuit. Similarly, each coil, acting as a booster coil, amplifies the current with a lower impedance, which amplifies the booster-coil properties. Any change to the system that boosts primary–primary coupling or lowers impedance will transfer more power, disproportionately affecting the graph-based approach presented here.

Systems that emphasize one primary–secondary link above others, such as with a smaller secondary coil, also highlight the power of the approach described in this work. In that case, the single strong primary–secondary link focuses the impact of all the primary voltage excitations through a single edge, which is more powerfully modeled by this approach.

5. Conclusion

The approach presented here allows the complex interactions of mutually-coupled WPT pads to be modeled with a graph. This allows pads to simultaneously act as primaries, secondaries, and booster coils. The parasitic primary–primary coupling can be exploited to force each primary pad to behave like a booster coil, acting as a via and a source.

Stability conditions for compensation are discussed, with two definitions of maximum compensating inductance established. Increasing the compensating impedance helps transfer power, but if the compensating impedance increases beyond some threshold, the power transfer may become unstable.

An omniscient, optimal controller is developed. Exploiting that model allows the primary pads to switch smartly, increasing the total power transfer by up to 25 % compared to an inductance-based approach. That increase in power comes with no additional excitation voltages. Considerations are included for a multi-secondary system. The resulting system is stable and more effective than either of the other two approaches considered, as demonstrated in a simulation.

The approach is developed within an EV charging paradigm but promises utility in other applications, as well. Charging a swarm of drones, for example, could use the approach developed here. Modeling or optimizing the placement of booster coils could also use the tools developed here. Within DWPT and other potential applications, this work opens new avenues of research; the two most prominent of which are: first, evaluating the controllability and stability of a graph-based WPT system, and second, measuring or controlling transient response. While both discussions are beyond the scope of the present work, the present work lays the foundation for future work, which will enrich the present contributions.

References

1. Limb, B.J.; Asher, Z.D.; Bradley, T.H.; Sproul, E.; Trinko, D.A.; Crabb, B.; Zane, R.; Quinn, J.C. Economic Viability and Environmental Impact of In-Motion Wireless Power Transfer **2019**. *5*, 135–146. https://doi.org/10.1109/TTE.2018.2876067.
2. Dai, J.; Ludois, D.C. A Survey of Wireless Power Transfer and a Critical Comparison of Inductive and Capacitive Coupling for Small Gap Applications **2015**. *30*, 6017–6029. https://doi.org/10.1109/TPEL.2015.2415253.
3. Ota, Y.; Takura, T.; Sato, F.; Matsuki, H. Wireless power transfer by low coupling electromagnetic induction — LC booster. In Proceedings of the 2012 IEEE MTT-S International Microwave Workshop Series on Innovative Wireless Power Transmission: Technologies, Systems, and Applications, May 2012, pp. 175–178. https://doi.org/10.1109/IMWS.2012.6215779.
4. Wu, H.; Mu, T.; Gao, X.; Xing, Y. A Secondary-Side Phase-Shift-Controlled LLC Resonant Converter With Reduced Conduction Loss at Normal Operation for Hold-Up Time Compensation Application **2015**. *30*, 5352–5357. https://doi.org/10.1109/TPEL.2015.2418786.
5. Kamineni, A.; Neath, M.J.; Zaheer, A.; Covic, G.A.; Boys, J.T. Interoperable EV Detection for Dynamic Wireless Charging With Existing Hardware and Free Resonance **2017**. *3*, 370–379. https://doi.org/10.1109/TTE.2016.2631607.
6. Ahmad, A.; Alam, M.S.; Mohamed, A.A.S. Design and Interoperability Analysis of Quadruple Pad Structure for Electric Vehicle Wireless Charging Application **2019**. *5*, 934–945. https://doi.org/10.1109/TTE.2019.2929443.
7. Pries, J.; Galigekere, V.P.N.; Onar, O.C.; Su, G.J. A 50-kW Three-Phase Wireless Power Transfer System Using Bipolar Windings and Series Resonant Networks for Rotating Magnetic Fields **2020**. *35*, 4500–4517. https://doi.org/10.1109/TPEL.2019.2942065.
8. Hariri, A.O.; Youssef, T.; Elsayed, A.; Mohammed, O. A Computational Approach for a Wireless Power Transfer Link Design Optimization Considering Electromagnetic Compatibility **2016**. *52*, 1–4. https://doi.org/10.1109/TMAG.2015.2492922.
9. Buja, G.; Bertoluzzo, M.; Mude, K.N. Design and Experimentation of WPT Charger for Electric City Car **2015**. *62*, 7436–7447. https://doi.org/10.1109/TIE.2015.245552.

10. Hansen, M.; Poddar, S.; Ahmed, H.; Kim, S.; Kamineni, A. Artificial Neural Network Modeling of WPT Magnetic Fields in an EV Application. In Proceedings of the 2023 IEEE Wireless Power Technology Conference and Expo (WPTCE), June 2023, pp. 1–6. https://doi.org/10.1109/WPTCE56855.2023.10215940.
11. Shen, S.; Zhang, Z.; Wu, Y.; Wang, R.; Liang, Z. Modeless Prediction of Variable Coupling Effect for Multiple-Load Wireless Power Transfer **2022**. *58*, 1–5. https://doi.org/10.1109/TMAG.2021.3089784.
12. Hansen, M.; Kamineni, A.; Zane, R. Zero-Crossing Current Detection for Modular and Robust Dynamic Wireless Power Transfer. In Proceedings of the 2020 IEEE Energy Conversion Congress and Exposition (ECCE), Oct 2020, pp. 5207–5214. https://doi.org/10.1109/ECCE44975.2020.9236045.
13. Azad, A.N.; Echols, A.; Kulyukin, V.A.; Zane, R.; Pantic, Z. Analysis, Optimization, and Demonstration of a Vehicular Detection System Intended for Dynamic Wireless Charging Applications **2019**. *5*, 147–161. https://doi.org/10.1109/TTE.2018.2870339.
14. Zhang, Z.; Shen, S.; Liang, Z.; Eder, S.H.K.; Kennel, R. Dynamic-Balancing Robust Current Control for Wireless Drone-in-Flight Charging **2022**. *37*, 3626–3635. https://doi.org/10.1109/TPEL.2021.3111755.
15. Sarin, A.; Avestruz, A.T. A Framework for Code Division Multiple Access Wireless Power Transfer **2021**. *9*, 135079–135101. https://doi.org/10.1109/ACCESS.2021.3116114.
16. Oh, H.; Oh, S.; Koo, H.; Choi, W.; Shin, J.; Hwang, K.C.; Lee, K.Y.; Yang, Y. Mid-Range Wireless Power Transfer System for Various Types of Multiple Receivers Using Power Customized Resonator **2021**. *9*, 45230–45241. https://doi.org/10.1109/ACCESS.2021.3067023.
17. Bai, T.; Mei, B.; Zhao, L.; Wang, X. Machine Learning-Assisted Wireless Power Transfer Based on Magnetic Resonance **2019**. *7*, 109454–109459. https://doi.org/10.1109/ACCESS.2019.2933679.
18. Bono, J.; Ahmed, H.; Nimri, R.; Kamineni, A. Current Distribution in Multifilar Wireless Charging Pads. In Proceedings of the 2023 IEEE Wireless Power Technology Conference and Expo (WPTCE), 2023.
19. Wireless Power Transfer for Light-Duty Plug-in/Electric Vehicles and Alignment Methodology. *SAE Standard J2954_202208* **2022**.
20. Pantic, Z.; Bai, S.; Lukic, S.M. ZCS *LCC*-Compensated Resonant Inverter for Inductive-Power-Transfer Application **2011**. *58*, 3500–3510. https://doi.org/10.1109/TIE.2010.2081954.

CHAPTER 8

ADDITIONAL COMMENTS TO THE PRACTITIONER

One important purpose of the dissertation is to collect and transmit knowledge to future researchers; allowing subsequent researchers to build on the present work. Where journal articles tend to document successes, those articles may only lightly address potential pitfalls or may skim over the realities of implementation. Those exclusions from the journal articles might prove invaluable to future practitioners aiming to replicate or expand on these efforts; to aid those future efforts, a selection of implementation notes are collected in this chapter. Comments are organized by paper, following the order in Chapters 3 to 7 with Sections 8.1 to 8.5, respectively. Within each section, comments tend to be discussed in order of impact, although that sequence is admittedly subjective. Notation in each section is defined in the corresponding chapter.

8.1 A Network Flow Approach to Battery Electric Bus Scheduling and Battery Health Conscious Optimization

This work builds on the work in [9] in two critical directions. First, the work presented in Chapter 3 accounts for battery degradation, and second, the work includes a method to speed up the optimization. The adaptation of the battery model in [35] to the MILP is well-described in Chapter 3, and no further discussion is needed here.

8.1.1 Algorithm for MILP Matrix Generation

Some comments on the search space reduction algorithm are merited here, which necessitates a discussion on graph generation and optimization matrix definition. Although any algorithm to determine the relevant matrices will necessarily result in the same optimum, the algorithm to determine the null space of the incidence matrix is non-trivial. It is possible for the computation of the null space matrix $N_{(l)}$ to take longer than the algorithm

itself saves; this is increasingly likely as the null space matrix is calculated later relative to the other matrices.

Ideally, the null space matrix is built with the underlying graph. Each charging node can be mapped to a unique column of $N_{(l)}$, and new rows of $N_{(l)}$ can be calculated quickly with each new charging node.

To generate the graph and define the relevant matrices from a BEB schedule, a simple algorithm can be defined as follows:

1. Define the rest nodes and edges. Define the first column of $N_{(l)}$ to select those edges.
2. For each potential charging interval, also assign a group index and do the following:
   (a) If charging was not available in the previous time interval, start assigning charging nodes to a new group index
   (b) Let the duration property be 1
   (c) Let the time property be the time interval in question
   (d) Create a new charging node with the correct, bus ID, duration, and time interval properties
   (e) Create edges leading to and from that charging node
   (f) Define a nullspace basis vector that passes through both new edges
   (g) If there is a charging interval at the previous time step, then increase the duration, decrease the time interval, and repeat Items 2d to 2g
3. Create the group constraint matrix
4. Create $N_{(l)}$
5. Create an entry in the charging matrix $S_{(l)}$ for each charging edge
6. Define other necessary matrices and vectors

Other algorithms may work, but the algorithm presented above may speed processing time before the optimization occurs. If the code to define the optimization variables uses Matlab © functions like

```
k=find(X)
```

the processing will be unnecessarily slowed. The structure of the graph is very predictable and regular, rendering such functions unnecessarily slow. The code used in this dissertation does use the slower implementation, but future developments should use a faster algorithm. The constraints were developed from a comma-separated values (CSV) file containing the bus schedules with a Matlab script. The optimization was done in Python script with the Gurobi optimization library [98]. Code snippets are included as associated files.

8.1.2 Sensitivity of Results

The MILP in Chapter 3 has some sensitivity to the assumed parameters, which are discussed briefly here. First, the ToU energy charge can play a significant role in the efficacy of the battery-health-conscious (BHC) approach. If the ToU profile is relatively flat, the naive optimizer (ignoring battery health) is heavily incentivized to push all charging into the off-peak hours for minimal cost savings. Accounting for the deleterious effects of battery degradation shows the naive optimizer to be penny-wise and pound-foolish, incurring larger battery degradation costs than energy savings. However, a more varied ToU rate schedule may dominate the cost of charging, forcing the BHC to approximate the naive approach.

The cost savings of the BHC approach are also heavily dependent on battery size. Calendar aging will always dominate the degradation of a sufficiently large battery, and the results BHC approach showed no cost savings for the largest battery size. A smaller battery may need to be charged frequently to meet the constraints, limiting the effective search space of an optimizer to prevent battery degradation.

The discussed approach is also sensitive to the battery model. Variations in the battery chemistry will undoubtedly alter the battery degradation parameters. Further, it is noted in Chapter 3 that the battery capacity Q is the minimum of $\{Q_{Li}, Q_{neg}, Q_{pos}\}$. Different battery models may begin with different initial values of Q_{Li} or Q_{neg}, which may minimize the cost due to cycling or due to calendar fade. When the initial value of Q_{neg} is very high, Q_{Li} and its degradation through calendar capacity fade will tend to dominate battery

degradation and a BHC optimization will have minimal benefit. Conversely, when the initial value of Q_{neg} is low, cycling will tend to dominate battery degradation.

8.2 Current Harmonics Dead Time Design Method to Achieve ZVS with Non-linear Output Capacitance

The practitioner may note some limitations to the approach presented in Chapter 4, which are addressed in greater detail here. First, the rise-times of the switches may be on the order of the deadtime, second, that the load be non-capacitive, and third, that the H-bridge operates at 180° phase angle. Those three concepts are discussed in Sections 8.2.1 to 8.2.3, respectively.

8.2.1 Notes on Deadtime and Rise Time Length

In experimentation, the exact switch node voltage rise time was hard to determine, due to a slow-rising tail. Compare the experimental and simulated results in Figs. 8.1a and 8.1c: note that the DC voltage at the beginning of the deadtime interval is not precisely 0 V. This is most likely due to the rise/fall time of the gate drive circuits, although the behavior is difficult to observe on the nanosecond timescale. In practice, the deadtime should be further adjusted to account for the delay in the gate drive circuits.

8.2.2 Notes on Non-Capacitive Load Requirement

The second caution meriting discussion here is the strict requirement that the load at the switching frequency is not capacitive. Because the current at the switching frequency tends to dominate the current at the harmonics, it has an outsize impact on the switch-node voltage during deadtime. Even though a power factor near unity implies the fundamental component of the bridge current will be near zero during deadtime, the fundamental current can still invalidate the conclusions of Chapter 4. An example of this is discussed more fully in Section 8.3.

When the circuit states are entirely determined by the primary H-bridge, a non-capacitive fundamental current can be readily guaranteed. This could be a system with a resistive load,

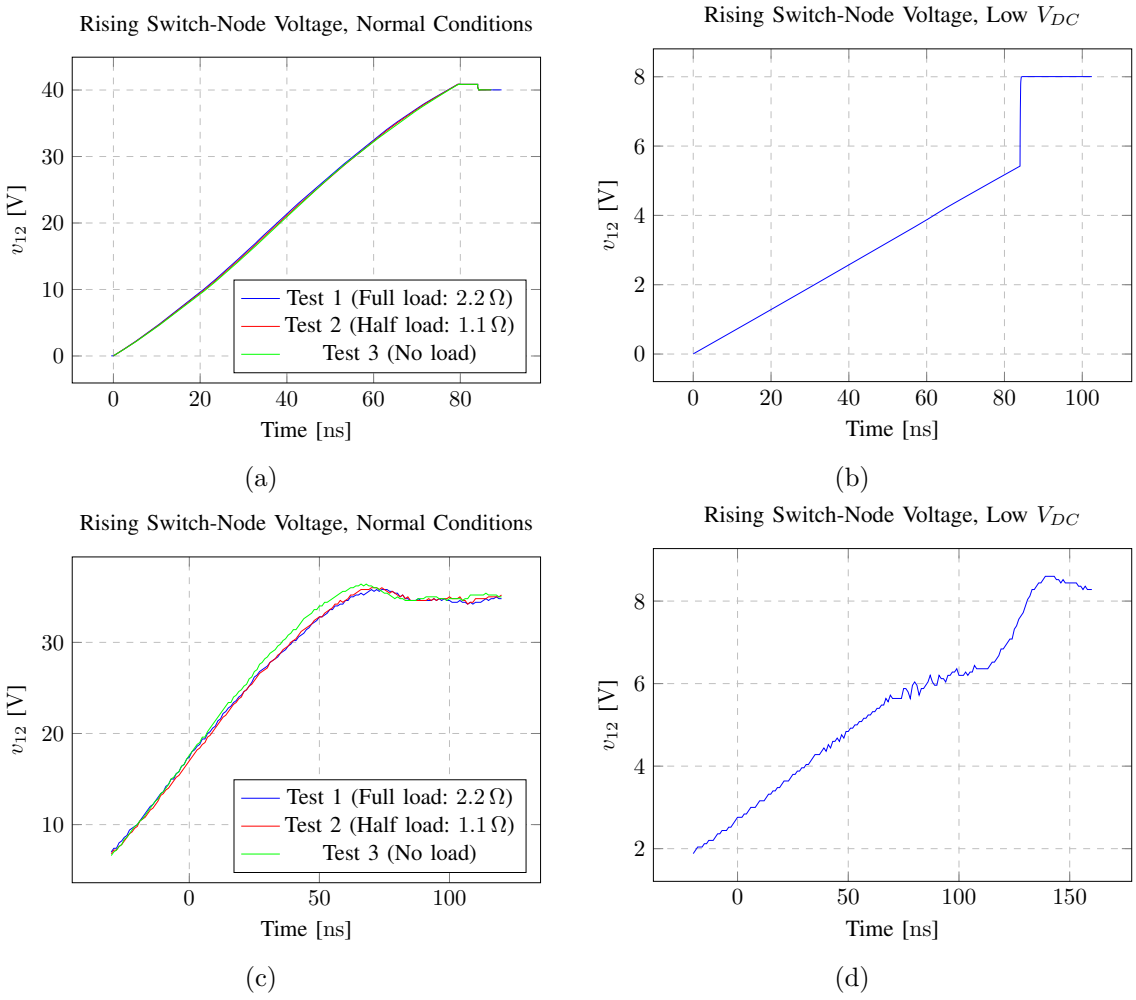

Fig. 8.1: Plots of switch-node voltages from Chapter 4. The upper plots are simulated results; the lower plots, experimental. The left-hand plots show ZVS; the right hand, hard switching. All plots ©2021 IEEE

a WPT system with a passive secondary, or a WPT system where the secondary and primary phases are locked relative to each other, i.e., driven by the same controller. However, in a WPT system with dual-active switching, this can be more complicated. Delays in rise time or signal propagation can delay the switch node voltage relative to the switch node current, resulting in hard switching.

Two possible solutions can ameliorate the hard switching. First, if any delays can be counteracted, the power factor may be driven to unity. A phase-locked loop (PLL), similar

to existing solutions [99], can easily be advanced temporally to counteract system delays[1]. Alternatively, the fundamental current can be assumed to be linear during dead time. Let I_f be the inductive portion of the fundamental current, present during the middle of deadtime. Then (7) from Chapter 4 should be written as

$$\Delta Q = \int_{t_d/2}^{td/2} I_f + i'(\tau)\, d\tau, \tag{8.1}$$

which implies, borrowing the notation from Chapter 4

$$\Delta Q = \int_{-t_d/2}^{t_d/2} I_f + \sum_{n=3,5,7...} \frac{4V_{DC}}{\pi X n^2} \cos\left(2\pi f_S n\tau\right) d\tau. \tag{8.2}$$

The expression in (8.2) may be further simplified by replacing the summation with a triangle wave.

$$\Delta Q = t_d I_f + \frac{V_{DC}\pi}{2X}\left(t_d - f_S t_d^2 - \frac{16}{2\pi^3 f_S}\sin\left(2\pi f_S \frac{t_d}{2}\right)\right), \tag{8.3}$$

resulting in the expression

$$t_d = \left(\frac{I_f X}{V_{DC}\pi f_s} + \frac{\alpha}{f_s}\right) - \sqrt{\left(\frac{I_f X}{V_{DC}\pi f_s} + \frac{\alpha}{f_s}\right)^2 - \frac{2\Delta Q X}{V_{DC}\pi f_s}}. \tag{8.4}$$

This will not have a solution when

$$I_f < \sqrt{\frac{V_{DC}\pi f_s 2\Delta Q}{X}} - \frac{\alpha V_{DC}\pi}{X}, \tag{8.5}$$

which implies a fundamental limit to the maximum capacitive current (or minimum inductive current) that can be tolerated to achieve ZVS. Of course, this approximation assumes that the average fundamental current during deadtime is known, which may not be the case for very long deadtimes.

Of course, the exact implementation of these proposed fixes is beyond the scope of the present work. A few qualitative suggestions are presented here only to guide the practitioner

[1] In Chapter 5, the anti-resonance filter is rudimentary PLL. Lowering the switching frequency effectively advances the PLL temporally

toward a feasible solution, but the designer should be aware of the limitations discussed here.

8.2.3 Notes on Phase Angle Requirement

A natural follow-up question to the work in Chapter 4 is if the work can be applied to other phase angles. While a full response to that question is beyond the scope of this work, some ink is spent here pointing the practitioner toward a reasonable approach. With a 180° phase angle, the rising edge of one switch node occurs exactly at the same time as the falling edge of the complementary switch node, which is the situation discussed in Chapter 4. When the rising and falling edges do not correspond exactly, each bridge leg should be considered an independent voltage source. The current (including harmonics) due to both voltage sources can be summed, and t_d solved for.

The solution would be straightforward, but there will be a dependence on the phase between the legs, and the small-angle approximation reducing (9) to (10) in Chapter 4 would need to be replaced by a second-order model. Again, the path is relatively straightforward, but the mathematical derivation is beyond the scope of this work.

8.3 Improvements to Real-Time Synchronization and Detection for a Dual-active, Secondary-driven Dynamic Wireless Power Transfer System

Chapter 5 describes a method for a primary (roadway) pad to detect an approaching vehicle and synchronize its switching to the secondary's switching. There are a few concepts that, due to space limitations, could not be fully addressed in the paper, but may be helpful for a practitioner. First, regarding the difference between the quasi-linear and fully-linear approximations of the zero-crossing detector, it is noted rather vaguely that "Counterexamples exist where the fully-linearized model predicts stability, but a simulation demonstrates instability." Section 8.3.1 addresses this phenomenon more fully. It is also noted in Chapter 5 that some instability may be acceptable; Section 8.3.2 addresses this comment. As with any design, a working model is much easier to build in simulation than realize in hardware; Sections 8.3.3 and 8.3.4 address some of the difficulties of realization.

8.3.1 Notes on Linearization of Zero-Crossing Detector

In this section, a simulation is shown, where the linear model of the zero-crossing detector predicts a stable system but the simulation demonstrates instability. Following that demonstration, a discussion ensues on why the quasi-linearization system, rather than the full linearization, must be used.

Consider the system shown in Fig. 8.2. The fully-linear approximation of the zero-crossing detector gain is derived as

$$\frac{2}{A\pi}, \tag{8.6}$$

where A is the magnitude of the primary bridge current. The loop gain, consequently, is approximated as

$$\frac{V_{DC,P} G(s) X_S X_P}{2\omega_f Z_{B,P}(s) M_{PS} V_{DC,S}}, \tag{8.7}$$

with variables defined in Chapter 5. As described in Chapter 5, we are concerned with the magnitude of the loop gain when

$$\angle G(s) = \angle Z_{B,P}(s), \tag{8.8}$$

which occurs when the frequency is f_{e1} or f_{e2}.

Let the circuit have the component values given in Table 8.1, which is typical of a poorly coupled system. Then the equilibrium frequencies, magnitudes of anti-resonance filter gain, magnitudes of the impedance, and loop gain magnitude are given in Table 8.2.

By the loop gain in Table 8.2, we would expect the system to be stable. However, a simulation of the system shows a beat pattern, as in Fig. 8.3. The beat pattern implies the existence of multiple frequencies in the current waveform, which do not include transients; the waveforms in Fig. 8.3 begin after 35 ms. The fast Fourier transform (FFT) of the voltage and current is shown in Fig. 8.4; for higher resolution, the FFT data is collected from roughly 12 ms.

The beat pattern in Fig. 8.3 and the sidelobes in Fig. 8.4 demonstrate that the switching frequency is dominated by f_{e2}, and the current induced by the secondary acts as a noise sig-

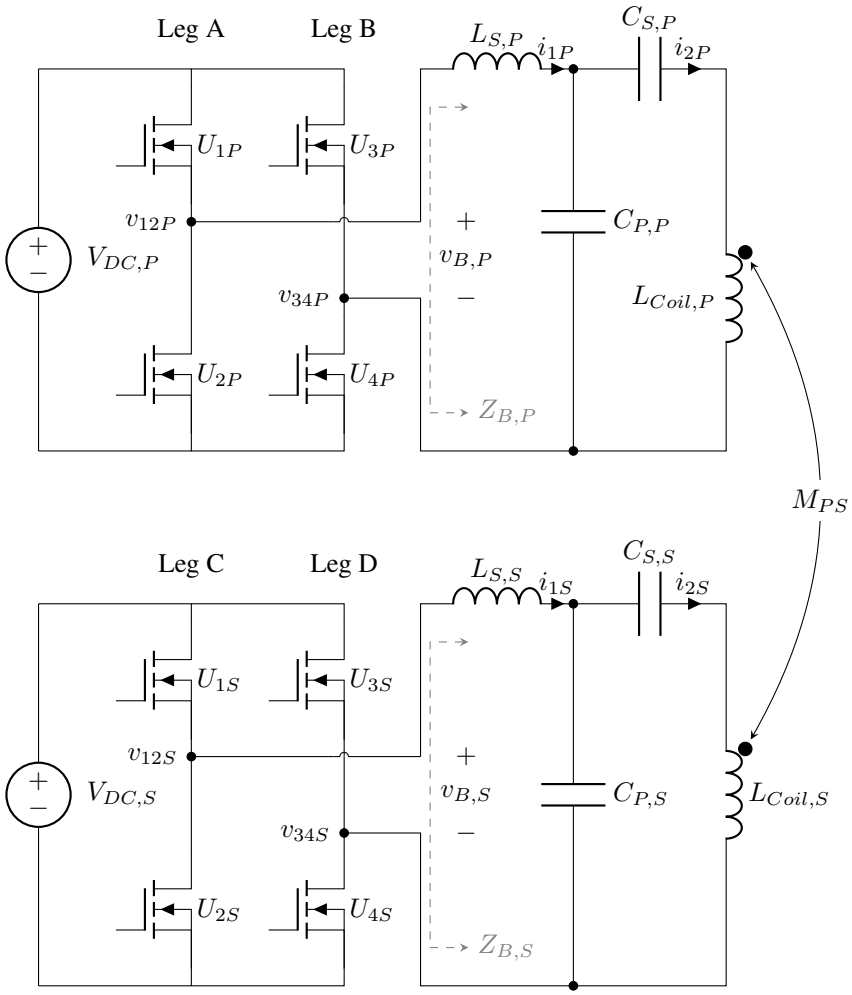

Fig. 8.2: System diagram of a WPT system. Replicated from Chapter 5.

Table 8.1: WPT system parameters. Based on those in Chapter 5.

Component	**Value**	**Component**	**Value**
$V_{DC,P}$	565 V	$V_{DC,S}$	565 V
$L_{S,P}$	5.62 µH + 5 mΩ	$L_{S,S}$	3.35 µH + 5 mΩ
$C_{P,P}$	631 nF	$C_{P,S}$	1.04 µF
$C_{C,P}$	415 nF	$C_{C,S}$	990 nF
$L_{Coil,P}$	14.2 µH + 5 mΩ	$L_{Coil,S}$	8.10 µH + 5 mΩ
M_{PS}	858 nH	Q	5
f_f	85 kHz		

Table 8.2: Fully-linear loop gain parameters

Equilibrium frequency f_e	**Anti-resonance filter gain** $G(s)$	**Impedance** $Z(s)$	**Linear loop gain**
$f_{e1} = 76.9\,\text{kHz}$	$j/2$	$j7.11$	0.4121
$f_{e2} = 93.9\,\text{kHz}$	$-j/2$	$-j3.844$	0.7622

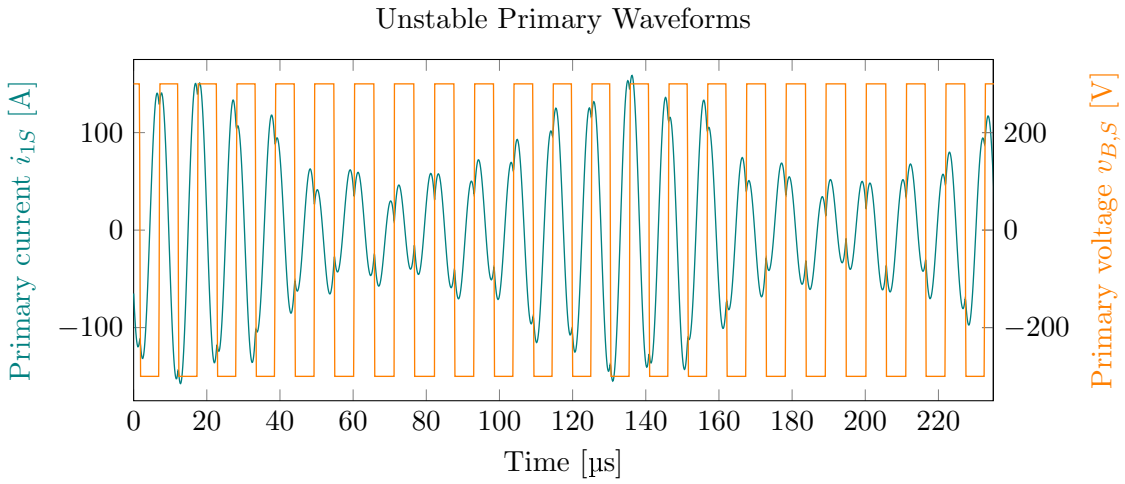

Fig. 8.3: Quasi-steady-state secondary current and voltage waveforms. Even after a long time, the current waveform is not stable over each switching period.

nal. Clearly, the system is unstable, although the linearization of the zero-crossing detector predicts stability.

As described in Chapter 5, the linear model of the zero-crossing detector assumes an infeasible zero-crossing detector output. Consider the FFT of the voltage in Fig. 8.4. The dominant frequency is f_{e2}, but there are symmetric sidelobes at 85 kHz and 101 kHz. The restriction that the primary voltage $v_{B,P} \in \{-V_{DC,P}, V_{DC,P}\}$ introduces a sidelobe complementary to the noise signal. That complementary sidelobe can reinforce the noise signal, increasing the gain predicted by the linearized zero-crossing detector.

The minor discrepancy between the calculated and observed values of f_{e2} (given in Table 8.2 and Fig. 8.4, respectively) because the calculated value of f_{e2} is determined uniquely by the anti-resonance filter while the observed value is determined by real-axis-crossing of the Nyquist plot with the quasi-linear model. The marginal difference in dominant frequency

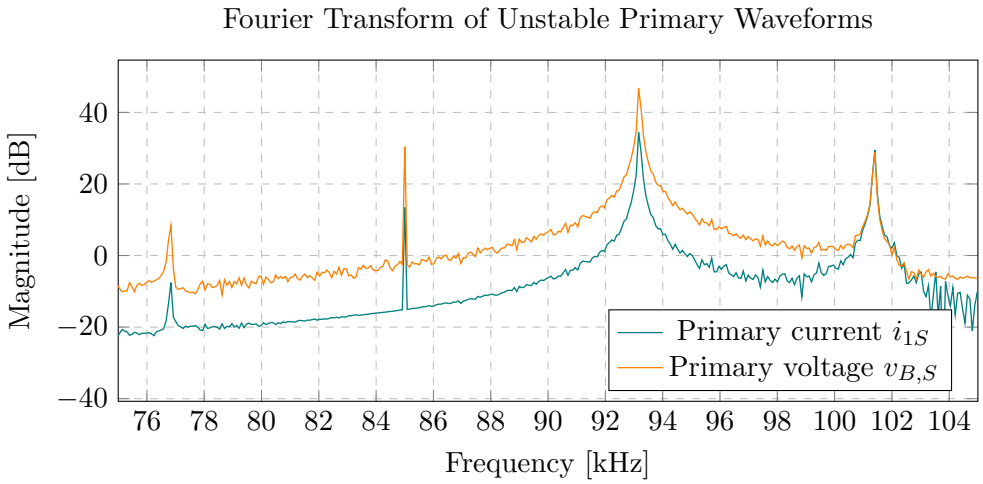

Fig. 8.4: FFT of the waveforms represented in Fig. 8.3. Note the dominant frequency around 93 kHz.

is secondary, however, to the fact this system is fundamentally unstable when the linear model of the zero-crossing detector predicts stability.

8.3.2 Acceptability of an Unstable System

In Chapter 5, it is mentioned in passing that some instability may be tolerable. The example described in Section 8.3.1 has a Nyquist plot shown in Fig. 8.5 with the quasi-linear model of the zero-crossing detector, clearly demonstrating instability. That instability is verified in simulation; Fig. 8.3 are not dominated by the induced current at 85 kHz.

However, although the system is unstable, there is still some power transferred. The peaks in Fig. 8.4 at 85 kHz transfer some real power, even while the dominant effect is reactive power. Further, the instability is fundamentally limited — the calculations in Chapter 5 assume an infinitesimal noise signal, but two other effects limit instability. First, a second-order model of the zero-crossing detector would yield a second-order effect that counteracts the linear term. Second, once a frequency becomes dominant, the gain is limited by $V_{DC,P}$. Increasing the magnitude of the dominant current does not change the zero crossings, and so the loop gain is 0. Both of those phenomena have the same effect: the loop gain decreases as a noise signal increases, and the instability is ultimately bounded.

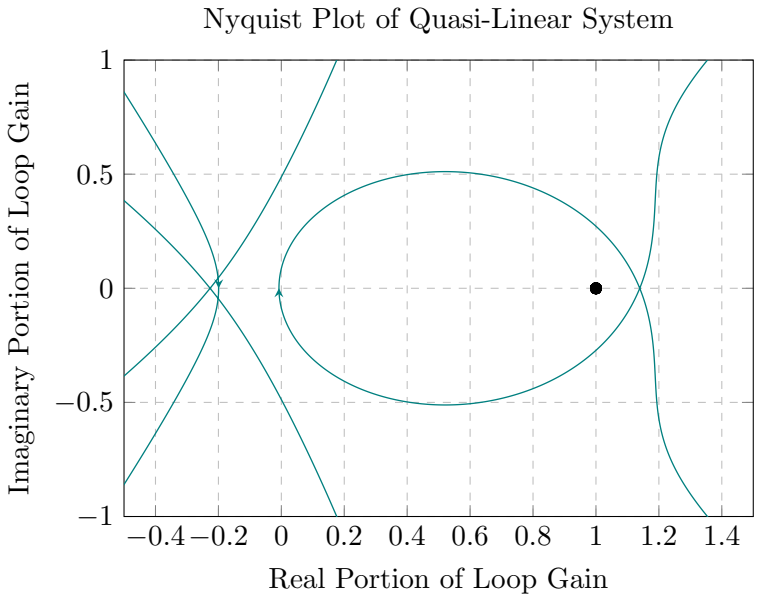

Fig. 8.5: Nyquist plot of the system with the quasi-linear approximation of the zero-crossing detector. Note that since the loop has positive feedback, the critical point is $(1, 0)$. Also, note that the quasi-linear model accurately predicts the observed instability.

Further discussion of the acceptability of an unstable system presents an interesting avenue for further research. Questions on how much instability may be tolerated, or a quantization of the exchange of real power for reactive power in an unstable system are interesting but are beyond the scope of this thesis.

8.3.3 Realization Difficulties, Phase

As with many innovations, there was a significant hurdle in realizing a design after thorough simulation testing. Noise, parasitic coupling, and other effects affect a hardware realization but are not apparent in simulation. This section describes best practices to match hardware results to simulation results, specifically as regards phase fidelity.

Information about the phase of the induced current passed through several stages before being manifested as a bridge voltage; many of those stages individually add a negligible amount of delay, but the total delay can be significant. In this section, causes of delay are treated individually. The delay causes the voltage to lag the current, resulting in an apparent capacitive load and potentially eliminating the possibility of ZVS.

First, the current is measured by a current transformer (CT), which passes a current to the control board, where it is forced over a 50 Ω resistor. The CT used in hardware has a phase delay of less than 2 m°; the delay is insignificant here but could become significant with a lower-quality CT.

The anti-resonance filter also presents an opportunity for delay, although the filter can alternatively be tuned for a negative delay. Careful tuning of the filter is critical for the correct phase response; the biquad filter is convenient as the filter parameters can be tuned independently, ensuring the center frequency and quality factor are accurate. An inaccurate quality factor affects the equilibrium frequencies; even if the quality factor is sufficiently high to avoid positive feedback, the envelope detector may not perform as designed.

In the system, an analog-to-digital converter (ADC) driver was placed between the filter and the comparator, acting as a comparator driver. The comparator driver had little effect on the phase, but conventionally, the comparator driver would have a low-impedance return path for high frequencies. The parallel feedback capacitor will alter the phase of the signal if present, adding to the delay. However, removing the feedback capacitor can add high-frequency noise to the signal, affecting the behavior of the comparator.

The comparator can be a significant source of delay. First, there is some propagation delay in the comparator. Although it may be only a few nanoseconds, the total delay can become significant when each component introduces a small delay. Further, a comparator typically has some hysteresis; hysteresis always introduces delay, and that delay will be especially pronounced at low power levels. Finally, a bounce in the comparator output, combined with noise induced on the input, results in an exceptionally jittery signal. The jitter has a strong effect on the falling edge, of the gate drive signals. With some deadtime/shoot-through control schemes, the gate drive signal will flip between high and low for a significant amount of time after the signal should have dropped. Conversely, the rising gate drive signal is delayed, because the jitter and deadtime prevent the gate drive signal from going high until after the jitter is over. The effect can be significant. In the hardware results presented in Chapter 5, the jitter added between 200 ns and 400 ns of delay — amounting to roughly

10° of lag. High-quality components and low-noise circuit design play a part in minimizing this noise, but in Chapter 5, a software solution is employed. The incoming, jittery signal is passed through a state machine that flips state at the jitter events and then does not sample for roughly 600 ns until the jitter even has passed. This preserves the quick response of the original design and minimizes delay, but it is somewhat lacking in elegance and is non-deterministic. A phase-locked loop would be a logical next step.

The comparator output signal passes through a level shifter and isolator, which can add some delay. Ideally, the part should be chosen to minimize delay. The FPGA can latch on to the signal rapidly, although the software solution to jitter requires an additional clock cycle. Overall, the isolator and FPGA introduce some delay, but that delay is small and essentially inevitable.

The last major cause of delay is the gate drive signal. This delay can be significant, but the gate-driver design is beyond the scope of this paper. Care should be taken to minimize the gate driver delay, and counteract it if necessary.

If the quality factor of the anti-resonance filter is higher than required, the anti-resonance filter may be tuned for a slightly higher frequency. This will counteract the delay in the system, including the delay at the zero-impedance frequency. This may be a feasible approach but is not explored here.

8.3.4 Realization Difficulties, Signal Fidelity

Beyond the delays that are present in a physical system, some issues with signal integrity became apparent. This section aims to note some of those issues, that the practitioner may create a working design for the first time.

Early designs sought to use a passive anti-resonance filter with capacitors and inductors. However, that design was prone to parasitic coupling with the inductors and was impossible to tune. However, it did achieve some results with a 100 W system. A later iteration, designed for a 50 kW system, still used a two-stage passive filter design. However, this design used a first stage near the CT, with a second stage on the control board. An attempt to combine the inductors for a second stage of the CT and the filter inductor failed; although

the design worked in simulation, the air gap required to tune the inductance degraded the second-stage CT coupling, rendering the whole system inoperable. The design used to generate the results in Chapter 5 avoided these issues, although the design still had some inductance in the loop, introducing noise into the system. Future designs should further shrink the anti-resonance filter footprint and should consider placing the anti-resonance filter in a Faraday cage.

Often, solving one problem with signal fidelity introduced another. The successful design of the active anti-resonance filter created the necessary phase response; however, the active version of the filter also introduces a small (roughly 5 mV). The comparator driver amplified this offset, and the pulses were asymmetric or non-existent if the input signal was small enough. To resolve this, a low-pass filter was introduced after the anti-resonance filter, and the comparator driver inputs were the anti-resonance filter output and the low-pass filter output, rather than the anti-resonance filter output and ground. This ensured that only the high-frequency component of the anti-resonance filter output reached the comparator. The low-pass filter was designed to be low impedance, to not affect the input impedance of the comparator driver. However, this had the undesired effect of overloading the anti-resonance filter in some cases. The filter demonstrated strong non-linearity, but only in the second stage. When the low-pass filter was replaced with a high-impedance version, the anti-resonance filter worked. However, the input impedance of the driver was then asymmetric, resulting in an offset on the driver output and a flat comparator output. Eventually, the input impedance of the driver was reduced to account for the impedance of the low-pass filter, and the system performed well.

One final issue worth mentioning here is the envelope detector. The filter can be designed to have an insignificant error, but imprecision and noise in the ADC values can still cause some variance in the output. If the variance in the envelope detector output is not dominated by the trend towards higher or lower values (as coupling increases or decreases), the *enable* state in the primary can jitter, introducing dramatic transients. A simple solution is to only set the primary enable state after n outputs of the envelope detector are all above or

below the threshold. As the vehicle speed increases, the value of n can decrease.

Design Principles

Ideally, the gain in the comparator driver would be incorporated into the first stage of the anti-resonance filter; this would eliminate the need for the comparator driver and potentially reduce noise. An active filter should be used to minimize parasitic coupling, the filter should have a minimal footprint, potentially even a Faraday cage around the filter circuit. Through the 6 op-amps of a biquad filter, some small DC offset may be introduced. A high-impedance low-pass filter should be used to isolate the DC offset. The comparator driver may be omitted, and the comparator may use the biquad and subsequent low-pass filter outputs directly. Care should be taken to ensure the low-pass filter impedance does not affect the comparator operation.

8.4 Artificial Neural Network Modeling of WPT Magnetic Fields in an EV Application

By its nature as a simulation-heavy project, the author has fewer comments to the practitioner related to Chapter 6 than other, more experimental chapters. Parametric variations were generated in Matlab and saved in CSV files. Those were processed into PyTorch tensor files and processed with the PyTorch library [100]. Code snippets included as associated files.

The practitioner should consider the tradeoffs of data set size, accuracy, and model size. If the training data set is too large for the model, accuracy gains will be left on the table. If the data set size is too small for the model size, the neural network will overfit the data, causing a loss of accuracy in the test data set. The complexity of each branch of the neural network should be tuned to maximize test accuracy.

With the stray field, there are some few values that seem odd, with much higher error than expected. There are a few possible explanations for this:

- The training data has inaccuracies, due to loose convergence criteria or a maximum

number of FEM iterations. The neural network will either correctly replicate the noisy data or an error will appear due to neural network smoothing.

- The neural network is ill-suited for processing the stray fields. The stray fields are especially difficult to calculate, but the huge variations may perform better with more linear layers and fewer convolutional layers. Experimentation with different network topologies may produce better results, although there is quite a bit of experimentation behind the results in Chapter 6.

Some more exotic approaches would be interesting to consider, such as a physics-informed neural network (PINN). However, the PINN approach does not fit nicely with ferrite plates, especially when the positions of the ferrite may change. A DWPT system would most likely have ferrite, so a PINN approach is interesting but beyond the achievable scope of this work.

8.5 Graph-Based Modeling and Optimization of WPT Systems

As in Section 8.4, the relevant work is analysis- and simulation-heavy, and there are no comments on a practical implementation; there are only a few comments on the analysis. First, some avenues towards distributed control may rely on primary inductances remaining stable. While this is a reasonable first-order approximation, the moving ferrite in the secondary affects primary–primary coupling. It would be interesting to evaluate the sensitivity of real power transfer to variations in inductance, but that is beyond the scope of this work.

CHAPTER 9
CONCLUSION

Increasing adoption of EVs will allow for a shift to cleaner energy in the transportation sector, with the potential for reduced GHG and pollution emissions. However, a major impediment to EVs efficacy in reducing emissions is the battery, which hampers EV adoption by increasing EV cost and requiring slower or more frequent refueling stops than ICE vehicles.

This concluding chapter is organized into four sections. A summary of this work's contributions is given in Section 9.1. Section 9.2 demonstrates that the contributions addressed in Chapters 3 to 7 fulfill the objectives introduced in Chapter 1 and the tasks given in the proposal defense. The contributions are bound together in a single narrative in Section 9.3, and Section 9.4 addresses the implications of this work.

9.1 Summary of Contributions

A brief summary of the novel contributions is given as:

- A graph to represent possible charger allocations during a planning horizon is defined, along with the constraints to express the graph search as a MILP.
- A battery degradation model is adapted to estimate battery degradation costs for each possible charging event.
- A space-reduction method is introduced to reduce the optimization space and the number of constraints in the MILP
- Justification is introduced for a charge-equivalent capacitance model of parasitic output capacitance in a resonant converter
- The conditions under which the harmonic current is sufficient to achieve ZVS without added reactive power are determined

- A method for a primary to detect a secondary in a DWPT system is developed. The method is novel in that it:
  - Allows active switching on both the primary and the secondary sides
  - Turns on the primary pad only in response to a secondary pad
  - Requires no additional sensing coils
  - Includes sufficient robustness for roadway deployment
- The stability requirements for that method are introduced
- Determine conditions for correct turn-on/turn-off of the primary, avoiding a permanent on-condition
- The proposed design is validated in hardware
- A FEM dataset, richer than what exists in the literature currently, is generated.
- The optimal cost functions to most accurately train an ANN to represent magnetic field quantities are determined.
- A graph-based model of WPT in a system with multiple primary/secondary pads is developed.
- A method, relying on the graph-based model, is developed that exploits parasitic coupling in WPT systems.

9.2 Completion of Objectives

This section describes how each objective and task in Section 1.2 is fulfilled by this dissertation. Each task within an objective corresponds to a chapter of this dissertation.

9.2.1 Objective 1

Objective 1 is to define a planning tool to reduce battery costs in an EV bus fleet by reducing battery degradation and deferring battery replacement costs. This objective is described in a single task, which corresponds to Chapter 3.

Task 1

Task 1 is to formulate the allocation of chargers to an EV fleet as a MILP. The formulation considers ToU energy costs and battery degradation costs with limited charging resources. As defined in the proposal, key milestones for this task include:

1. Define a graph to represent possible charger allocations during a planning horizon with the constraints to express the graph search as a MILP

2. Adapting a battery degradation model to estimate battery degradation costs for each possible charging event

3. Introduce a space-reduction method to reduce the optimization space and the number of constraints in the MILP

The work in Chapter 3 expresses the allocation of chargers as a graph search problem, which is then mapped to a MILP. The battery costs referenced in the objective are derived from a model of battery degradation [35]; the model is disassembled to isolate different forms of battery degradation and a graph is structured to express the calculated cycling-dependent battery damage as an edge cost. The cycling edge costs depend on the power level of the EV power supply equipment (EVPSE) and the length of the charging interval. The total battery cost for each bus is the minimum of the cycling cost assessed along graph edges and a minimum daily cost.

The other component of cost is a ToU energy charge, assessed along each edge. The costs associated with ToU energy charges and battery degradation comprise the objective of the MILP. The number of EVPSEs can be arbitrarily set in the MILP, allowing for limited charging resources. Chapter 3 also includes definitions of constraints to express the graph search as a MILP.

The contributions of Chapter 3 described thus far fulfill the requirements of Objective 1 and Task 1 and complete the first two milestones. However, Chapter 3 also includes another contribution, completing milestone three. A method is defined to reduce the optimizer search space, which tends to reduce the optimization time by roughly 50 %. Considerations

are also made for multiple power levels of EVPSE, which is also relevant but beyond the scope of Objective 1.

The work in Chapter 3 is complete on its own, but also presents interesting questions for follow-up research. At some point, the BEB fleet would become too complex for the MILP to solve. In that case, what heuristic algorithm can best approximate the MILP? What is the tradeoff between accuracy and speed? The work can easily be applied to different battery models, but work remains to arbitrarily scale BEB fleet size.

9.2.2 Objective 2

This section describes how the work in Chapters 4 and 5 completes Tasks 2 and 3, respectively, in fulfillment of Objective 2, which is to reduce up-front and operational costs of DWPT systems by reducing system complexity and system losses. The two tasks to achieve this objective and the corresponding papers are discussed in continuation.

Task 2

Task 2, which is to describe a method to achieve ZVS in a resonant converter or WPT circuit without added reactive power, is addressed in Chapter 4. That work describes how the current harmonics can be used to achieve ZVS, and provides deadtime criteria. Specific milestones corresponding to this task in the approved proposal are

1. Model the harmonic current in a resonant converter
2. Determine an appropriate model of parasitic switch output capacitance
3. Determine conditions under which the harmonic current is sufficient to achieve ZVS without added reactive power.

Each of those milestones is addressed in Chapter 4.

The sum of the harmonic current is modeled as a modified triangular wave, and the effects of deadtime length on harmonic strength are considered. Further, because the voltage is effectively fixed (even accounting for variable deadtime), the total current during deadtime

can be easily calculated, and the charge-equivalent capacitance model is appropriate. Because the method uses current harmonics to charge and discharge parasitic capacitance, no inductive current at the fundamental frequency is required. That is, the proposed method does achieve ZVS at a unity power factor

Section 8.2 goes beyond those contributions, modifying the condition to account for a slightly capacitive load. Section 8.2 also suggest paths for future research analyzing the limits of the approach to a phase-shift modulated voltage. In such a scenario, the switching action of the two inverter legs is offset by some other angle than 180°, adding phase to one leg and subtracting phase from another leg. For any system that can ZVS at 180° phase between the inverter legs, there is some range of phase angles over which the inverter will ZVS, future work should clearly define that range as a step to high-efficiency, low-component power regulation.

Task 3

Task 3, corresponding to Chapter 5, is to develop a synchronization and detection algorithm for DWPT. The requirements for this algorithm are that it:

1. Allows active switching on both the primary and the secondary sides
2. Turns on the primary pad only in response to a secondary pad
3. Requires no additional sensing coils
4. Includes sufficient robustness for roadway deployment

Here, the fulfillment of each algorithm requirement is discussed, with a brief discussion of future research paths.

The algorithm described in Chapter 5 does allow active switching on both sides. The algorithm requires the secondary to switch to request power transfer and requires the primary to switch to allow power transfer. Chapter 5 also includes a condition to ensure that a primary pad is only enabled in response to a secondary pad, not by another primary, although that constraint is rarely active. Further, the design does not require any auxiliary sensing

coils, requiring instead only a simple bandpass filter. Finally, the system was proven to be sufficiently robust for roadway deployment. Hardware tests verified the DWPT system behaved appropriately, even with harsh tests, like the phase shift test. The proposed design therefore met all the requirements of Task 3 and, together with the work in Chapter 4, fulfill the requirements of Objective 2.

In the proposal, several milestones are also listed. They are:

1. Develop a theory where a primary coil detects and synchronizes to an approaching secondary coil
2. Determine conditions for primary stability, avoiding resonance
3. Determine conditions for correct turn-on/turn-off of the primary, avoiding a permanent on-condition
4. Test the design in hardware

The work described in Chapter 5 also demonstrates that each milestone is met. The primary coil does detect and synchronize to a secondary, and the requirements for stability are well-addressed. The conditions for a stable turn-on condition are related to the general stability conditions and also addressed in Chapter 5. Finally, Chapter 5 does describe a high-power (15 kW) hardware test.

Several avenues for future research are apparent from Chapter 5. First, the transients are intense because the primary responds so quickly to changes in induced current, both in phase and magnitude. The anti-resonance filter is a simple PLL, but its response is too quick. A digital PLL could be used to ramp up the primary phase angle when power transfer begins, tamping down transients. Similarly, a PLL could be tuned to achieve a 180° phase shift over some number of cycles, eliminating the transient seen in the phase shift test. Even a 10-cycle delay would significantly reduce the transients while having negligible effects on the power transferred. However, it is unknown how a PLL would affect the stability of the system. Further research is required.

9.2.3 Objective 3

Objective 3 is to facilitate the adoption of DWPT systems by improving the modeling of DWPT systems. The two tasks corresponding to this objective are discussed in continuation.

Task 4

Task 4, fulfilled in Chapter 6, is to train a neural network to describe the characteristics of a DD coil topology. Specifically, given nine variables describing the geometry of the primary and secondary coils and their locations relative to each other, the neural network will model

1. Stray magnetic fields, which are used to ensure compliance with IEEE standards for electromagnetic (EM) exposure
2. Ferrite magnetic fields, from which ferrite losses are estimated
3. Copper magnetic fields, from which copper proximity losses are estimated
4. Primary and secondary self-inductances and mutual inductance

The key milestones for this task are:

1. Collect training and testing data through the finite element method (FEM), which include a representative sample of coil design parameters and associated measurements
2. Determine optimal cost functions to most accurately train an ANN
3. Design and implement an ANN capable of representing the measurements collected through FEM

The work detailed in Chapter 6 satisfies all the requirements and meets all the milestones described for this task. The neural network achieves reasonable accuracy in predicting stray fields, high accuracy in predicting ferrite and copper magnetic fields, and very high accuracy in predicting relevant inductances.

Chapter 6 also describes how each of the milestones is met. The training and testing data collection are described, along with the separation of the two datasets. Appropriate cost

functions are defined, and the optimality of the cost functions to accurately characterize a WPT pad design is discussed. Finally, the ANN is compared to a high-accuracy FEM model, and the ANN is shown to be sufficiently accurate.

Task 5

Task 5, fulfilled in Chapter 7, is to develop a graph-based model to evaluate steady-state interactions between multiple primary and secondary coils, including possible benefits of parasitic coupling. The key milestones of this task are:

1. Develop a graph-based model to quantify steady-state WPT in a system with multiple primary/secondary pads
2. Determine a necessary or sufficient condition for the existence of an equilibrium point
3. Define how a benefit from parasitic primary–primary or secondary–secondary coupling may be achieved. One potential benefit is reduced inverter current for a given power level.
4. Validate results through simulation in PLECS/Spice

Because Task 5 was proposed before the model was developed, the resultant work differed slightly from the proposed work. Chapter 7 does develop a graph-based model for a WPT network and steady-state power transfer can be measured between nodes. A benefit of parasitic coupling is also identified, as the full consideration of the system, including such parasitic coupling, allows a higher power transfer level than without parasitic coupling. The results were validated with a PLECS model.

The most significant difference between the proposed work and the work in Chapter 7 is that Chapter 7 does not focus on the existence of an equilibrium point. It was determined that an omniscient optimal controller was more interesting, which assumes open-loop control and implies an equilibrium point. When the research on an equilibrium point was proposed, it was assumed that a locally-maximized power transfer control (similar to that in Chapter 5) would be employed, but when it was proven that such a controller is generally sub-optimal,

the existence of an equilibrium point with that control scheme became moot. Thus, the definition of an omniscient, optimal controller, including multiple secondary coils, became a more interesting, relevant question.

9.3 Contribution Cohesion

Beyond alignment in the purpose of each objective, there is strong technical cohesion among the various contributions detailed in this work. That cohesion can best be understood by looking backward from the last task; the work in the dissertation yielded the tools and expertise to solve new problems, like the work in Chapter 7. While the framework developed in Chapter 7 does provide some utility to the practitioner, the principal value of Chapter 7 lies in the contributions the model can be used to generate; this section describes how the contributions of this dissertation all are necessary precursors to the full utilization of the contributions of Chapter 7. The work discussed in Chapter 7 is intended to be both a capstone of the dissertation and a launching point for future research.

The work relies on knowledge of graphs developed in gained while developing Chapter 3. The constrained graph flow optimization problem in Chapter 7 also calls to mind the constrained graph flow optimization in Chapter 3, although the optimization in Chapter 7 is simpler.

A successful implementation of this approach will require soft switching on all the WPT pads. If limits on the fundamental frequency current phase are established, the work in Chapter 4 can prove the feasibility of soft switching. The work in Chapter 4 may not be a prerequisite to Chapter 7, but the future, successful hardware test of Chapter 7 may require the contributions of Chapter 4.

The concept of graph-based WPT modeling was engendered during the development of the synchronous inverter discussed in Chapter 5. The approach in Chapter 5 will cause each primary to push as much power as possible, which is the local optimization discussed in Chapter 7. The modeling technique developed in Chapter 7 is the best way to evaluate system stability with the synchronous inverter. It is possible that primary–primary synchronous inverter interactions could introduce instability into the system, and the graph-based modeling method is necessary to determine what form an instability would take.

Finally, the neural network developed in Chapter 6 can be used to best design the pads for graph-based power transfer, or a neural network could be trained as a reinforcement learning agent to maximize power transfer with a minimal agent. The synergy between the two tasks in Objective 3 allows for more insightful future development. Conceptually, both tasks also required thoughtful and novel approaches to modeling characteristics of a WPT system; in Chapter 6, this is manifested by the training cost functions and representation of the stray fields on a logarithmic scale. In Chapter 7, this is manifested as the mapping of the system onto a graph.

That is to suggest that the scholar who developed Chapter 7 must necessarily be capable of making all the contributions in Chapters 3 to 6. Beyond a strong cohesion in aim, each task defined here demonstrates a proficiency of the author, and those proficiencies are mutually reinforcing.

9.4 Final Comments

In 2020, transportation accounted for 26 % of energy consumption in the United States, with petroleum accounting for 90 % of energy used in transportation [2]. While EVs can allow greater penetration of clean energy sources into transportation, displacing some of the GHG-emitting petroleum, several technical hurdles remain to spur EV adoption and use. One of the most prominent obstacles to EV adoption is range anxiety, with a secondary concern on EV cost [6]. Overcoming energy storage limitations is key to alleviating those concerns, spurring EV adoption, and ultimately replacing petroleum-based energy with cleaner energy sources.

Three objectives were proposed to overcome EV energy storage limitations; the completion of those objectives is detailed in this dissertation. Those objectives are:

1. Define a planning tool to reduce battery costs in an EV bus fleet by reducing battery degradation and deferring battery replacement costs. This objective is described in a single task:

   (a) Formulate the allocation of chargers to an EV fleet as a MILP. The formulation

considers time of use (ToU) energy costs and battery degradation costs with limited charging resources.

2. Reduce up-front and operational costs of DWPT systems, by reducing system complexity and system losses. The two tasks to achieve this objective are:

   (b) Describe a method to achieve ZVS in a resonant converter or WPT circuit without added reactive power.

   (c) Develop a synchronization and detection algorithm for DWPT.

3. Facilitate the adoption of DWPT systems by improving the modeling of DWPT systems. The two tasks corresponding to this objective are:

   (d) Train a neural network to describe the characteristics of a DD coil topology.

   (e) Develop a graph-based model to evaluate steady-state interactions between multiple primary and secondary coils, including possible benefits of parasitic coupling.

The technological innovations necessitated by the three objectives may play some role in overcoming energy storage limitations, allowing better utilization of EV batteries, and minimizing EV battery size and cost. With fewer energy storage limitations, EVs may allow an increasingly greater portion of the transportation section to be powered by non-polluting energy sources, ultimately improving the quality of life for many people.

REFERENCES

[1] P. Jochem, S. Babrowski, and W. Fichtner, "Assessing co2 emissions of electric vehicles in Germany in 2030," *Transportation Research Part A: Policy and Practice*, vol. 78, pp. 68–83, 2015. [Online]. Available: https://www.sciencedirect.com/science/article/pii/S0965856415001354

[2] S. C. Davis and R. G. Boundy, "Transportation energy data book: Edition 39," 2 2021. [Online]. Available: https://www.osti.gov/biblio/1767864

[3] N. Rietmann, B. Hügler, and T. Lieven, "Forecasting the trajectory of electric vehicle sales and the consequences for worldwide co2 emissions," *Journal of Cleaner Production*, vol. 261, p. 121038, 2020. [Online]. Available: https://www.sciencedirect.com/science/article/pii/S0959652620310854

[4] B. Wolkinger, W. Haas, G. Bachner, U. Weisz, K. W. Steininger, H.-P. Hutter, J. Delcour, R. Griebler, B. Mittelbach, P. Maier, and R. Reifeltshammer, "Evaluating health co-benefits of climate change mitigation in urban mobility," *International Journal of Environmental Research and Public Health*, vol. 15, no. 5, 2018. [Online]. Available: https://www.mdpi.com/1660-4601/15/5/880

[5] K. Forrest, M. Mac Kinnon, B. Tarroja, and S. Samuelsen, "Estimating the technical feasibility of fuel cell and battery electric vehicles for the medium and heavy duty sectors in California," *Applied Energy*, vol. 276, p. 115439, 2020. [Online]. Available: https://www.sciencedirect.com/science/article/pii/S030626192030951X

[6] J. Kester, G. Zarazua de Rubens, B. K. Sovacool, and L. Noel, "Public perceptions of electric vehicles and vehicle-to-grid (v2g): Insights from a nordic focus group study," *Transportation Research Part D: Transport and Environment*, vol. 74, pp. 277–293, 2019. [Online]. Available: https://www.sciencedirect.com/science/article/pii/S1361920918306916

[7] B. J. Limb, Z. D. Asher, T. H. Bradley, E. Sproul, D. A. Trinko, B. Crabb, R. Zane, and J. C. Quinn, "Economic viability and environmental impact of in-motion wireless power transfer," *IEEE Trans. Transport. Electrific.*, vol. 5, no. 1, pp. 135–146, March 2019.

[8] K. Gkiotsalitis, "Bus holding of electric buses with scheduled charging times," *IEEE Trans. Intell. Transp. Syst.*, vol. 22, no. 11, pp. 6760–6771, Nov 2021.

[9] J. Whitaker, G. Droge, M. Hansen, D. Mortensen, and J. Gunther, "A network flow approach to battery electric bus scheduling," *IEEE Trans. Intell. Transp. Syst.*, pp. 1–12, 2023.

[10] J. Lee, H. Shon, I. Papakonstantinou, and S. Son, "Optimal fleet, battery, and charging infrastructure planning for reliable electric bus operations," *Transportation Research Part D: Transport and Environment*, vol. 100, p. 103066, 2021. [Online]. Available: https://www.sciencedirect.com/science/article/pii/S1361920921003631

[11] A. Hoke, A. Brissette, K. Smith, A. Pratt, and D. Maksimovic, "Accounting for lithium-ion battery degradation in electric vehicle charging optimization," *IEEE Trans. Emerg. Sel. Topics Power Electron.*, vol. 2, no. 3, pp. 691–700, 2014.

[12] G. Buja, M. Bertoluzzo, and K. N. Mude, "Design and experimentation of WPT charger for electric city car," *IEEE Trans. Ind. Electron.*, vol. 62, no. 12, pp. 7436–7447, 2015.

[13] A. Ahmad, M. S. Alam, and R. Chabaan, "A comprehensive review of wireless charging technologies for electric vehicles," *IEEE Trans. Transport. Electrific.*, vol. 4, no. 1, pp. 38–63, 2018.

[14] S. Y. Chu, X. Cui, X. Zan, and A.-T. Avestruz, "Transfer-power measurement using a non-contact method for fair and accurate metering of wireless power transfer in electric vehicles," *IEEE Trans. Power Electron.*, vol. 37, no. 2, pp. 1244–1271, Feb 2022.

[15] W. Su and C. Chen, "ZVS for PT backlight inverter utilizing high-order current harmonic," *IEEE Trans. Power Electron.*, vol. 23, no. 1, pp. 4–10, 2008.

[16] S. Lim, A. J. Hanson, J. A. Santiago-González, and D. J. Perreault, "Bus converter using isolation capacitance for zvs and invariant operation," *IEEE Trans. Emerg. Sel. Topics Power Electron.*, vol. 8, no. 3, pp. 1971–1982, 2020.

[17] R. Elferich, "General zvs half bridge model regarding nonlinear capacitances and application to llc design," in *2012 IEEE Energy Conversion Congress and Exposition (ECCE)*, 2012, pp. 4404–4410.

[18] A. Kamineni, M. J. Neath, A. Zaheer, G. A. Covic, and J. T. Boys, "Interoperable EV detection for dynamic wireless charging with existing hardware and free resonance," *IEEE Trans. Transport. Electrific.*, vol. 3, no. 2, pp. 370–379, 2017.

[19] A. N. Azad, A. Echols, V. A. Kulyukin, R. Zane, and Z. Pantic, "Analysis, optimization, and demonstration of a vehicular detection system intended for dynamic wireless charging applications," *IEEE Trans. Transport. Electrific.*, vol. 5, no. 1, pp. 147–161, 2019.

[20] T. Guillod, P. Papamanolis, and J. W. Kolar, "Artificial neural network (ANN) based fast and accurate inductor modeling and design," *IEEE Open Journal of Power Electronics*, vol. 1, pp. 284–299, 2020.

[21] S. Shen, Z. Zhang, Y. Wu, R. Wang, and Z. Liang, "Modeless prediction of variable coupling effect for multiple-load wireless power transfer," *IEEE Trans. Magn.*, vol. 58, no. 2, pp. 1–5, Feb 2022.

[22] S. Inoue, D. Goodrich, S. Saha, R. Nimri, A. Kamineni, N. S. Flann, and R. A. Zane, "Fast design optimization method utilizing a combination of artificial neural networks and genetic algorithms for dynamic inductive power transfer systems," *IEEE Open Journal of Power Electronics*, vol. 3, pp. 915–929, 2022.

[23] A. Sarin and A.-T. Avestruz, "A framework for code division multiple access wireless power transfer," *IEEE Access*, vol. 9, pp. 135 079–135 101, 2021.

[24] M. J. Hansen, G. Droge, and J. Gunther, "A network flow approach to battery electric bus scheduling and battery health conscious optimization," *Under Review*.

[25] M. Hansen, A. Kamineni, and R. Zane, "Current harmonics dead time design method to achieve ZVS with non-linear output capacitance," in *2021 IEEE Energy Conversion Congress and Exposition (ECCE)*, Oct 2021, pp. 2189–2196.

[26] M. J. Hansen, A. Zahid, and A. Kamineni, "Improvements to real-time primary synchronization in a dual-active DWPT system," *Under Review*.

[27] M. J. Hansen, R. A. Zane, and A. Kamineni, "Zero-crossing current detection for modular and robust dynamic wireless power transfer," U.S. Patent 11 218 026, Jan. 4, 2022.

[28] M. Hansen, A. Kamineni, and R. Zane, "Zero-crossing current detection for modular and robust dynamic wireless power transfer," in *2020 IEEE Energy Conversion Congress and Exposition (ECCE)*, Oct 2020, pp. 5207–5214.

[29] M. J. Hansen, S. Kim, and A. Kamineni, "Artificial neural network modeling of WPT magnetic fields in an ev application," *Under Review*.

[30] M. Hansen, S. Poddar, H. Ahmed, S. Kim, and A. Kamineni, "Artificial neural network modeling of WPT magnetic fields in an EV application," in *2023 IEEE Wireless Power Technology Conference and Expo (WPTCE)*, June 2023, pp. 1–6.

[31] M. J. Hansen, G. Droge, and A. Kamineni, "Graph based modeling and optimization of wpt systems," *Electronics*, 2024.

[32] H. Ambrose, N. Pappas, and A. Kendall, "Exploring the costs of electrification for California's transit agencies," *ITS Reports, 2017(03)*, vol. 03, Oct 2017.

[33] A. Millner, "Modeling lithium ion battery degradation in electric vehicles," in *2010 IEEE Conference on Innovative Technologies for an Efficient and Reliable Electricity Supply*, Sep. 2010, pp. 349–356.

[34] J. S. Edge, S. O'Kane, R. Prosser, N. D. Kirkaldy, A. N. Patel, A. Hales, A. Ghosh, W. Ai, J. Chen, J. Yang, S. Li, M.-C. Pang, L. Bravo Diaz, A. Tomaszewska, M. W. Marzook, K. N. Radhakrishnan, H. Wang, Y. Patel, B. Wu, and G. J. Offer, "Lithium ion battery degradation: what you need to know," *Phys. Chem. Chem. Phys.*, vol. 23, pp. 8200–8221, 2021. [Online]. Available: http://dx.doi.org/10.1039/D1CP00359C

[35] K. Smith, A. Saxon, M. Keyser, B. Lundstrom, Z. Cao, and A. Roc, "Life prediction model for grid-connected li-ion battery energy storage system," in *2017 American Control Conference (ACC)*, 2017, pp. 4062–4068.

[36] N. Lutsey and M. Nicholas, "Update on electric vehicle costs in the United States through 2030," *The International Council on Clean Transportation*, vol. 2, 04 2019.

[37] S. Manzetti and F. Mariasiu, "Electric vehicle battery technologies: From present state to future systems," *Renewable and Sustainable Energy Reviews*, vol. 51, pp. 1004–1012, 2015. [Online]. Available: https://www.sciencedirect.com/science/article/pii/S1364032115006577

[38] X. Chen, W. Shen, T. T. Vo, Z. Cao, and A. Kapoor, "An overview of lithium-ion batteries for electric vehicles," in *2012 10th International Power & Energy Conference (IPEC)*, Dec 2012, pp. 230–235.

[39] Q. Wang, W. Liu, X. Yuan, H. Tang, Y. Tang, M. Wang, J. Zuo, Z. Song, and J. Sun, "Environmental impact analysis and process optimization of batteries based on life cycle assessment," *Journal of Cleaner Production*, vol. 174, pp. 1262–1273, 2018. [Online]. Available: https://www.sciencedirect.com/science/article/pii/S0959652617327178

[40] A. Abdollahi, X. Han, G. Avvari, N. Raghunathan, B. Balasingam, K. Pattipati, and Y. Bar-Shalom, "Optimal battery charging, part i: Minimizing time-to-charge, energy loss, and temperature rise for ocv-resistance battery model," *Journal of Power Sources*, vol. 303, pp. 388–398, 2016. [Online]. Available: https://www.sciencedirect.com/science/article/pii/S0378775315003092

[41] L.-R. Chen, R. C. Hsu, and C.-S. Liu, "A design of a grey-predicted li-ion battery charge system," *IEEE Trans. Ind. Electron.*, vol. 55, no. 10, pp. 3692–3701, Oct 2008.

[42] L.-R. Chen, J.-J. Chen, C.-M. Ho, S.-L. Wu, and D.-T. Shieh, "Improvement of li-ion battery discharging performance by pulse and sinusoidal current strategies," *IEEE Trans. Ind. Electron.*, vol. 60, no. 12, pp. 5620–5628, Dec 2013.

[43] F. Zinnari, S. Strada, M. Tanelli, S. Formentin, and S. M. Savaresi, "Electrification potential of fuel-based vehicles and optimal placing of charging infrastructure: A large-scale vehicle-telematics approach," *IEEE Trans. Transport. Electrific.*, vol. 8, no. 1, pp. 466–479, March 2022.

[44] T. Zhang, W. Chen, Z. Han, and Z. Cao, "Charging scheduling of electric vehicles with local renewable energy under uncertain electric vehicle arrival and grid power price," *IEEE Trans. Veh. Technol.*, vol. 63, no. 6, pp. 2600–2612, July 2014.

[45] C. Zhang, Y. Liu, F. Wu, B. Tang, and W. Fan, "Effective charging planning based on deep reinforcement learning for electric vehicles," *IEEE Trans. Intell. Transp. Syst.*, vol. 22, no. 1, pp. 542–554, Jan 2021.

[46] W. Su and M.-Y. Chow, "Performance evaluation of an EDA-based large-scale plug-in hybrid electric vehicle charging algorithm," *IEEE Trans. Smart Grid*, vol. 3, no. 1, pp. 308–315, 2012.

[47] L. Yan, X. Chen, J. Zhou, Y. Chen, and J. Wen, "Deep reinforcement learning for continuous electric vehicles charging control with dynamic user behaviors," *IEEE Trans. Smart Grid*, vol. 12, no. 6, pp. 5124–5134, 2021.

[48] N. A. El-Taweel, A. Zidan, and H. E. Z. Farag, "Novel electric bus energy consumption model based on probabilistic synthetic speed profile integrated with hvac," *IEEE Trans. Intell. Transp. Syst.*, vol. 22, no. 3, pp. 1517–1531, March 2021.

[49] J. Wang, L. Kang, and Y. Liu, "Optimal scheduling for electric bus fleets based on dynamic programming approach by considering battery capacity fade," *Renewable and Sustainable Energy Reviews*, vol. 130, p. 109978, 2020. [Online]. Available: https://www.sciencedirect.com/science/article/pii/S1364032120302690

[50] Y. Zhou, X. C. Liu, R. Wei, and A. Golub, "Bi-objective optimization for battery electric bus deployment considering cost and environmental equity," *IEEE Trans. Intell. Transp. Syst.*, vol. 22, no. 4, pp. 2487–2497, 2021.

[51] N. A. El-Taweel, H. E. Z. Farag, and M. Mohamed, "Integrated utility-transit model for optimal configuration of battery electric bus systems," *IEEE Syst. J.*, vol. 14, no. 1, pp. 738–748, March 2020.

[52] G.-J. Zhou, D.-F. Xie, X.-M. Zhao, and C. Lu, "Collaborative optimization of vehicle and charging scheduling for a bus fleet mixed with electric and traditional buses," *IEEE Access*, vol. 8, pp. 8056–8072, 2020.

[53] A. Bagherinezhad, A. D. Palomino, B. Li, and M. Parvania, "Spatio-temporal electric bus charging optimization with transit network constraints," *IEEE Trans. Ind. Appl.*, vol. 56, no. 5, pp. 5741–5749, Sep. 2020.

[54] J. He, N. Yan, J. Zhang, Y. Yu, and T. Wang, "Battery electric buses charging schedule optimization considering time-of-use electricity price," *Journal of Intelligent and Connected Vehicles*, vol. 5, no. 2, pp. 138–145, 2022.

[55] Y. Wang, C. Lu, J. Bi, Q. Sai, and X. Qu, "Lifecycle cost optimization for electric bus systems with different charging methods: Collaborative optimization of infrastructure procurement and fleet scheduling," *IEEE Trans. Intell. Transp. Syst.*, vol. 24, no. 3, pp. 2842–2861, March 2023.

[56] M. Lu, X. Zhang, J. Ji, X. Xu, and Y. Zhang, "Research progress on power battery cooling technology for electric vehicles," *Journal of Energy Storage*, vol. 27, p. 101155, 2020. [Online]. Available: https://www.sciencedirect.com/science/article/pii/S2352152X19311193

[57] O. C. Onar, G.-J. Su, E. Asa, J. Pries, V. Galigekere, L. Seiber, C. White, R. Wiles, and J. Wilkins, "20-kw bi-directional wireless power transfer system with energy storage system connectivity," in *2020 IEEE Applied Power Electronics Conference and Exposition (APEC)*, 2020, pp. 3208–3214.

[58] C. C. Mi, G. Buja, S. Y. Choi, and C. T. Rim, "Modern advances in wireless power transfer systems for roadway powered electric vehicles," *IEEE Trans. Ind. Electron.*, vol. 63, no. 10, pp. 6533–6545, 2016.

[59] J. Dai and D. C. Ludois, "A survey of wireless power transfer and a critical comparison of inductive and capacitive coupling for small gap applications," *IEEE Trans. Power Electron.*, vol. 30, no. 11, pp. 6017–6029, 2015.

[60] H. Yang and J. Lee, "Wireless power transfer techniques for cell balancing of battery management systems," in *2014 IEEE Wireless Power Transfer Conference*, May 2014, pp. 162–165.

[61] J. Sun, T. Jiang, G. Yang, Y. Tang, S. Chen, S. Qiu, and K. Song, "A novel charging and active balancing system based on wireless power transfer for lithium-ion battery pack," *Journal of Energy Storage*, vol. 55, p. 105741, 2022. [Online]. Available: https://www.sciencedirect.com/science/article/pii/S2352152X22017297

[62] M. P. Theodoridis, "Effective capacitive power transfer," *IEEE Trans. Power Electron.*, vol. 27, no. 12, pp. 4906–4913, Dec 2012.

[63] E. Abramov, I. Zeltser, and M. M. Peretz, "A network-based approach for modeling resonant capacitive wireless power transfer systems," *CPSS Transactions on Power Electronics and Applications*, vol. 4, no. 1, pp. 19–29, Mar 2019.

[64] E. Abramov and M. M. Peretz, "Multi-loop control for power transfer regulation in capacitive wireless systems by means of variable matching networks," *IEEE Trans. Emerg. Sel. Topics Power Electron.*, vol. 8, no. 3, pp. 2095–2110, Sep. 2020.

[65] C. Chen, C. Li, C. Liao, and L. Wang, "Parameter identification of capacitive power transfer system based on spectrum analysis," *CPSS Transactions on Power Electronics and Applications*, vol. 3, no. 3, pp. 181–186, 2018.

[66] H. Zhang, F. Lu, H. Hofmann, W. Liu, and C. C. Mi, "An lc-compensated electric field repeater for long-distance capacitive power transfer," *IEEE Trans. Ind. Appl.*, vol. 53, no. 5, pp. 4914–4922, Sep. 2017.

[67] S. Li, Z. Liu, H. Zhao, L. Zhu, C. Shuai, and Z. Chen, "Wireless power transfer by electric field resonance and its application in dynamic charging," *IEEE Trans. Ind. Electron.*, vol. 63, no. 10, pp. 6602–6612, 2016.

[68] B. Regensburger, S. Sinha, A. Kumar, S. Maji, and K. K. Afridi, "High-performance multi-MHz capacitive wireless power transfer system for EV charging utilizing interleaved-foil coupled inductors," *IEEE Trans. Emerg. Sel. Topics Power Electron.*, vol. 10, no. 1, pp. 35–51, Feb 2022.

[69] "Wireless power transfer for light-duty plug-in/electric vehicles and alignment methodology," *SAE Standard J2954_202208*, Aug 2022. [Online]. Available: https://www.sae.org/standards/content/j2954_202208

[70] "IEEE standard for safety levels with respect to human exposure to electric, magnetic, and electromagnetic fields, 0 Hz to 300 GHz," *IEEE Std C95.1-2019 (Revision of IEEE Std C95.1-2005/ Incorporates IEEE Std C95.1-2019/Cor 1-2019)*, pp. 1–312, Oct 2019.

[71] U. K. Madawala and D. J. Thrimawithana, "A bidirectional inductive power interface for electric vehicles in v2g systems," *IEEE Trans. Ind. Electron.*, vol. 58, no. 10, pp. 4789–4796, Oct 2011.

[72] B. Sanftl, C. Joffe, M. Trautmann, R. Weigel, and A. Koelpin, "Reliabe data link for power transfer control in an inductive charging system for electric vehicles," in *2016 IEEE MTT-S International Conference on Microwaves for Intelligent Mobility (ICMIM)*, 2016, pp. 1–3.

[73] A. Ahmad, M. S. Alam, and A. A. S. Mohamed, "Design and interoperability analysis of quadruple pad structure for electric vehicle wireless charging application," *IEEE Trans. Transport. Electrific.*, vol. 5, no. 4, pp. 934–945, Dec 2019.

[74] J. Pries, V. P. N. Galigekere, O. C. Onar, and G.-J. Su, "A 50-kw three-phase wireless power transfer system using bipolar windings and series resonant networks for rotating magnetic fields," *IEEE Trans. Power Electron.*, vol. 35, no. 5, pp. 4500–4517, May 2020.

[75] C. Cheng, F. Lu, Z. Zhou, W. Li, C. Zhu, H. Zhang, Z. Deng, X. Chen, and C. C. Mi, "Load-independent wireless power transfer system for multiple loads over a long distance," *IEEE Trans. Power Electron.*, vol. 34, no. 9, pp. 9279–9288, Sep. 2019.

[76] H. Oh, S. Oh, H. Koo, W. Choi, J. Shin, K. C. Hwang, K.-Y. Lee, and Y. Yang, "Mid-range wireless power transfer system for various types of multiple receivers using power customized resonator," *IEEE Access*, vol. 9, pp. 45 230–45 241, 2021.

[77] Y. Sakayanagi, S. Togawa, K. Konagaya, and Y. Kuwahara, "Wireless power transmission for a traveling mobility scooter," in *2016 IEEE Wireless Power Transfer Conference (WPTC)*, 2016, pp. 1–3.

[78] M. S. Ahmed, M. A. Hoque, and A. J. Khattak, "Demo: Real-time vehicle movement tracking on android devices through bluetooth communication with dsrc devices," in *2016 IEEE Vehicular Networking Conference (VNC)*, 2016, pp. 1–2.

[79] J. B. Kenney, "Dedicated short-range communications (dsrc) standards in the United States," *Proc. IEEE*, vol. 99, no. 7, pp. 1162–1182, July 2011.

[80] G. R. Nagendra, L. Chen, G. A. Covic, and J. T. Boys, "Detection of EVs on ipt highways," *IEEE Trans. Emerg. Sel. Topics Power Electron.*, vol. 2, no. 3, pp. 584–597, Sep. 2014.

[81] R. Zeng, V. P. Galigekere, O. C. Onar, and B. Ozpineci, "Grid integration and impact analysis of high-power dynamic wireless charging system in distribution network," *IEEE Access*, vol. 9, pp. 6746–6755, 2021.

[82] Z. Zhang, S. Shen, Z. Liang, S. H. K. Eder, and R. Kennel, "Dynamic-balancing robust current control for wireless drone-in-flight charging," *IEEE Trans. Power Electron.*, vol. 37, no. 3, pp. 3626–3635, March 2022.

[83] Z. Pantic, S. Bai, and S. M. Lukic, "Zcs *lcc*-compensated resonant inverter for inductive-power-transfer application," *IEEE Trans. Ind. Electron.*, vol. 58, no. 8, pp. 3500–3510, Aug 2011.

[84] O. Yu, C.-S. Yeh, and J.-S. Lai, "Sequential parallel switching for drain-source synchronous rectifier efficiency and light-load stability improvement," in *2019 IEEE Applied Power Electronics Conference and Exposition (APEC)*, March 2019, pp. 463–467.

[85] O. Yu, C.-W. Chen, C.-S. Yeh, and J.-S. Lai, "Sequential parallel switching for drain-source synchronous rectification efficiency boost in parallel switch rectifiers," *IEEE Transactions on Circuits and Systems II: Express Briefs*, vol. 67, no. 11, pp. 2637–2641, Nov 2020.

[86] S. Ben-Yaakov, S. Glozman, and R. Rabinovici, "Envelope simulation by spice-compatible models of linear electric circuits driven by modulated signals," *IEEE Trans. Ind. Appl.*, vol. 37, no. 2, pp. 527–533, March 2001.

[87] D. P. Kingma, J. Ba, D. P. Kingma, and J. Ba, "Adam: A method for stochastic optimization," in *3rd International Conference on Learning Representations, ICLR 2015, San Diego, CA, USA, May 7-9, 2015, Conference Track Proceedings*, Y. Bengio and Y. LeCun, Eds. arXiv, 2014. [Online]. Available: https://arxiv.org/abs/1412.6980

[88] T. P. Lillicrap, J. J. Hunt, A. Pritzel, N. Heess, T. Erez, Y. Tassa, D. Silver, and D. Wierstra, "Continuous control with deep reinforcement learning," 2015. [Online]. Available: https://arxiv.org/abs/1509.02971

[89] T. Q. Chen, Y. Rubanova, J. Bettencourt, and D. Duvenaud, "Neural ordinary differential equations," *CoRR*, vol. abs/1806.07366, 2018. [Online]. Available: http://arxiv.org/abs/1806.07366

[90] A. Krizhevsky, I. Sutskever, and G. E. Hinton, "Imagenet classification with deep convolutional neural networks," in *Advances in Neural Information Processing Systems*, F. Pereira, C. J. C. Burges, L. Bottou, and K. Q. Weinberger, Eds., vol. 25. Curran Associates, Inc., 2012. [Online]. Available: https://proceedings.neurips.cc/paper/2012/file/c399862d3b9d6b76c8436e924a68c45b-Paper.pdf

[91] A. O. Hariri, T. Youssef, A. Elsayed, and O. Mohammed, "A computational approach for a wireless power transfer link design optimization considering electromagnetic compatibility," *IEEE Trans. Magn.*, vol. 52, no. 3, pp. 1–4, March 2016.

[92] R. Rajamony, S. Wang, G. Calderon-Lopez, I. Ludtke, and W. Ming, "Artificial neural networks-based multi-objective design methodology for wide-bandgap power electronics converters," *IEEE Open Journal of Power Electronics*, vol. 3, pp. 599–610, 2022.

[93] T. Bai, B. Mei, L. Zhao, and X. Wang, "Machine learning-assisted wireless power transfer based on magnetic resonance," *IEEE Access*, vol. 7, pp. 109 454–109 459, 2019.

[94] N. Soltani, M. ElAnsary, J. Xu, J. S. Filho, and R. Genov, "Safety-optimized inductive powering of implantable medical devices: Tutorial and comprehensive design guide," *IEEE Trans. Biomed. Circuits Syst.*, vol. 15, no. 6, pp. 1354–1367, Dec 2021.

[95] J. Bono, H. Ahmed, R. Nimri, and A. Kamineni, "Current distribution in multifilar wireless charging pads," in *2023 IEEE Wireless Power Technology Conference and Expo (WPTCE)*, Jun. 2023.

[96] W. Liu, Z. Wang, X. Liu, N. Zeng, Y. Liu, and F. E. Alsaadi, "A survey of deep neural network architectures and their applications," *Neurocomputing*, vol. 234, pp. 11–26, 2017. [Online]. Available: https://www.sciencedirect.com/science/article/pii/S0925231216315533

[97] O. Russakovsky, J. Deng, H. Su, J. Krause, S. Satheesh, S. Ma, Z. Huang, A. Karpathy, A. Khosla, M. Bernstein, A. C. Berg, and L. Fei-Fei, "Imagenet large scale visual recognition challenge," *Int. J. Comput. Vision*, vol. 115, no. 3, p. 211–252, dec 2015. [Online]. Available: https://doi.org/10.1007/s11263-015-0816-y

[98] Gurobi Optimization, LLC, "Gurobi Optimizer Reference Manual," 2023. [Online]. Available: https://www.gurobi.com

[99] H. Miura, S. Arai, F. Sato, H. Matsuki, and T. Sato, "A synchronous rectification using a digital pll technique for contactless power supplies," *IEEE Trans. Magn.*, vol. 41, no. 10, pp. 3997–3999, Oct 2005.

[100] A. Paszke, S. Gross, S. Chintala, G. Chanan, E. Yang, Z. DeVito, Z. Lin, A. Desmaison, L. Antiga, and A. Lerer, "Automatic differentiation in PyTorch," in *NIPS-W*, 2017.

CURRICULUM VITAE

Matthew J. Hansen

Awarded Patent

- **M. Hansen**, A. Kamineni, and R. Zane, "Zero-crossing current detection for modular and robust dynamic wireless power transfer" *U.S. Patent 11 218 026*, Jan 2022

Published Journal Article

- J. Whitaker, G. Droge, **M. Hansen**, D. Mortensen and J. Gunther, "A Network Flow Approach to Battery Electric Bus Scheduling," in *IEEE Transactions on Intelligent Transportation Systems*, vol. 24, no. 9, pp. 9098-9109, Sept. 2023, doi: 10.1109/TITS.2023.3276269.

Published Conference Papers

- **M. Hansen**, S. Poddar, H. Ahmed, S. Kim and A. Kamineni, "Artificial Neural Network Modeling of WPT Magnetic Fields in an EV Application," *2023 IEEE Wireless Power Technology Conference and Expo (WPTCE)*, San Diego, CA, USA, 2023, pp. 1-6, doi: 10.1109/WPTCE56855.2023.10215940.

- **M. Hansen**, A. Kamineni and R. Zane, "Current Harmonics Dead Time Design Method to Achieve ZVS with Non-Linear Output Capacitance," *2021 IEEE Energy Conversion Congress and Exposition (ECCE)*, Vancouver, BC, Canada, 2021, pp. 2189-2196, doi: 10.1109/ECCE47101.2021.9595311.

- **M. Hansen**, A. Kamineni and R. Zane, "Zero-Crossing Current Detection for Modular and Robust Dynamic Wireless Power Transfer," *2020 IEEE Energy Conversion Congress and Exposition (ECCE)*, Detroit, MI, USA, 2020, pp. 5207-5214, doi: 10.1109/ECCE44975.2020.9236045.

Journal Articles Under External Review

- **M. Hansen**, G. Droge, and A. Kamineni, "Graph-Based Modeling and Optimization of WPT Systems" *Electronics*
- **M. Hansen** and A. Kamineni, "Artificial Neural Network Modeling of WPT Magnetic Fields in an EV Application," *IEEE Transactions on Magnetics*
- **M. Hansen**, A. Zaheed, and A. Kamineni, "Improvements to Real-Time Synchronization and Detection for a Dual-active, Secondary-driven Dynamic Wireless Power Transfer System," *IEEE Open Journal of Power Electronics*
- **M. Hansen**, G. Droge, and J. Gunther, "A Network Flow Approach to Battery Electric Bus Scheduling and Battery Health Conscious Optimization," *IEEE Transactions on Intelligent Transportation Systems*

Patent Filing in Preparation

- **M. Hansen**, "Auxiliary Coils and a Linear Support Vector Machine to Detect Foreign Objects in Wireless Power Transfer," Expected filing Summer 2024